DOE/ER-0046/6

Damage Analysis and Fundamental Studies

Quarterly Progress Report
April-June 1981

August 1981

U.S. Department of Energy
Assistant Secretary for Energy Technology
Office of Fusion Energy
Washington, DC 20545

NOTICE

Printed in the United States of America
Available from .
National Technical Information Service
U.S. Department of Commerce
5285 Port Royal Road
Springfield, VA 22161

NTIS price codes
Printed copy: A11
Microfiche copy: A01

DOE/ER-0046/6
UC-20,20c

Damage Analysis and Fundamental Studies

Quarterly Progress Report
April-June 1981

August 1981

U.S. Depattment of Energy
Assistant Secretary for Energy Technology
Office of Fusion Energy
Washington, DC 20545

DOE Richland, WA

FOREWORD

This report is the fourteenth in a series of Quarterly Technical Progress Reports on Damage Analysis and Fundamental Studies (OAFS), which is one element of the Fusion Reactor Materials Program, conducted in support of the Magnetic Fusion Energy Program of the U. S. Department of Energy (DOE). The first eight reports in this series were numbered DOE/ET-0065/1 through 8. Other elements of the Materials Program are:

- Alloy Development for Irradiation Performance (ADIP)
- Plasma-Materials Interaction (PMI)
- Special Purpose Materials (SPM).

The DAFS proqram element is a national effort composed of contributions from a number of National Laboratories and other government laboratories, universities, and industrial laboratories. It was organized by the Materials and Radiation Effects Branch, Office of Fusion Energy, DOE, and a Task Group on Damage Analysis and Fundamental Studies, which operates under the auspices of that Branch. The purpose of this series of reports is to provide a working technical record of that effort for the use of the proqram participants, the fusion energy program in qeneral, and the DOE.

This report is organized along topical lines in parallel to a Program Plan of the same title so that activities and accomplishments may be followed readily, relative to that Program Plan. Thus, the work of a given laboratory may appear throuqhout the report. The Table of Contents is annotated for the convenience of the reader.

This report has been compiled and edited under the guidance of the Chairman of the Task Group on Damage Analysis and Fundamental Studies, D. G. Doran, Hanford Enqineerinq Oevelopment Laboratory (HEDL). His efforts, those of the supporting staff of HEDL, and the many persons who made technical contributions are gratefully acknowledged. M. M. Cohen, Materials and Radiation Effects Branch, is the DOE counterpart to the Task Group Chairman and has responsibility for the DAFS Proqram within DOE.

T. C. Reuther, Acting Chief
Materials and Radiation Effects Branch
Office of Fusion Energy

CONTENTS

	Page
Foreword	iii
Figures	xi
Tables	xix
CHAPTER 1: IRRADIATION TEST FACILITIES	1
1. RTNS-II Irradiations and Operations (LLNL)	3
Irradiations were done on a totul of six different experiments. No major unscheduled outages occurred.	
2. Nuclear Data for Damage Studies and FMIT (HEDL)	6
Calculations of the transmission spectm of FMIT-like neutrons through thick iron were completed; they are in good agreement with revised experimental datu.	
An evaluation was completed of proton and deuteron-induced activation and neutron production from graphite beam stops for both the FMIT prototype and full energy accelerators.	
CHAPTER 2: DOSIMETRY AND DAMAGE PARAMETERS	15
1. Fission Reactor Dosimetry (ANL)	17
Neutron fluence and damage parameters are reported for *the ORR-MFEZ and Omega West-HEDL1 irradiations. Analysis is in progress* for *the EBRII-XZ87 and ORR-MFE4A experiments.*	
2. Helium Generation Cross Sections for Fast Neutrons (RIES)	29
An initial three-dimensional neutron fluence map has been constructed for the high-flux region of the RTNS-II neutron field, and helium analyses are nearing completion for the RTNS-11-irradiated separated isotopes of Fe, Ni, and Cu.	

Page

3. Calculation of Damage Parameters (HEDL) 32

The damage energy cross sections (E <20 MeV) processed from ENDF/B-V by the DISCS and NJOY codes were found to have only slight differences.

CSEWG has established a charged particle format for *ENDF/B which will also be used* for *neutron evaluations above 20 MeV.*

Helium production cross sections from ENDF/B-V were processed.

4. Solid and Gas Transmutation Production Code Development (HEDL) 36

The computer code REAC with its associated libraries has been developed and successfully used.

5. Computer Simulation of High Energy Recoils in fcc Metals: Cascade Shapes and Sizes (HEDL) 39

In the energy range from 30 keV to 50 keV in copper there is a transition from compact single damage regions to chains of *generally closely spaced, but distinct multiple damage regions. The average spacing between multiple damage regions remains constant with energy. Only a small fraction* of *the recoils from fusion neutrons is expected to produce widely separated subcascades.*

6. The Effect of Irradiation on the Order/Disorder Transformation in CuPd (U. of Wis.) 52

Irradiation of *CuPd with 14-MeV copper ions at 10^{-3} dpa/s causes the ordered structure to disappear at temperatures below 200°C after 0.2 dpa. postirradiation annealing indicates that the reordering process is a classical nucleation and growth type.*

Low temperature (4.1 °K) 14.8-MeV neutron irradiation of *ordered and disordered CuPd provides a replacement to displacement ratio* of *70. Postirradiation annealing indicates that interstitial migration is responsible* for *some reordering, but vacancy migration is the main mechanism.*

7. Effects of Heavy-Ion Irradiation on the Phase Stability of a Cu-3.4 at% Be Alloy (U. of Wis.) 65

Irradiation with 14-MeV Cu ions in the temperature range of 300-475°C induced copious precipitation of CuBe platelets, even at very low damage doses. Postirradiation annealing studies proved that the continuous precipitate morphology was unstable in the absence of irradiation. Thermal aging studies showed that the precipitation process was very sluggish in the absence of irradiation, and that prolonged thermal aging produced a precipitate morphology quite different from that induced by irradiation. A solute-drag mechanism is the most likely explanation for precipitate growth during irradiation.

8. Damage Development and Hardening in 14-MeV Neutron Irradiation of Copper Alloys at 25°C (HEDL) 81

Copper and copper alloyed with five atom percent of either aluminum, nickel or manganese were irradiated at 25°C with 14-MeV neutrons to fluences up to 7.5 x 10^{17} n/cm^2 (0.003 dpa). The radiation-induced microstructure of these materials was characterized by the coupled use of electron microscopy and microhardness. The radiation-induced microhardness changes were found to be independent of alloy identity and the magnitude of the solute-induced hardening. It appears that at least 70% of the defect clusters are too small to be resolved by microscopy (~1 nm). The point defects at 25°C which survive recombination and aggregate in either visible or invisible clusters constitute at least 9-10% of those produced in the cascades.

CHAPTER 3: FUNDAMENTAL MECHANICAL BEHAVIOR 95

1. Crack Propagation Characteristics in Helium-Irradiated Type 316 Stainless Steel (U. of Va.) **97**

In relatively ductile type 316 stainless steel a crack propagates in a oscillatory manner with the crack angle, crack tip angle, and

Page

mean crack propagation direction varying widely as the crack lengthens. The effect of helim irradiation of sufficient dose to produce large (diameter 120 nm) bubbles is to reduce the magnitude of the oscillations, reduce the mean value of the crack angle, and increase the crack-tip angle as a result of significant grain boundary sliding.

2. The Role of Luders Strain in Determining Flow Properties in Steel From an Instrumented Hardness Test (UCSB) 105

From tests on a set of steels heat treated to exhibit a range of Liiders strain ε_L *when tested in tension* (ε_L = 0.88% to ε_L = 5.40%) *a quantitative correlation was determined between the Liiders strain and the geometry of the lip around a ball indentation. Interferometric techniques were found superior to profilometric techniques for lip characterization. In addition, it was found that hardness/microhardness data were best correlated to the homogeneous plastic flow portion of the tensile stress-stmin curve.*

CHAPTER 4: CORRELATION METHODOLOGY 115

1. Tensile Property Correlation for 20% Cold-Worked 316 Stainless Steel (HEDL) 117

Ultimate tensile strength data on 20% cold-worked 315 stainless steel irradiated in fast and thermal reactors and by 14 MEV neutrons we-e analyzed and a ten-parameter equation was developed to describe the ultimate tensile strength behavior for the temperature range $25 < T < 800°C$. *Uniform elongation was characterized in terms of yield and ultimate tensile strength. Total elongation was found to be insensitive to helium at temperatures below 500°C but sensitive to helium above 550°C.*

Page

2. Dose and Helium Injection Rate Dependence of Swelling on Dual-Ion Irradiated 316 Stainless Steel (ANL) 135

The dose and helium injection rate dependence of dislocation and cavity microstructure in 316 stainless steel was measured. Five and 15 appm He/dpa irradiations produced similar dislocation and cavity microstructures. Irradiation at 50 appm He/dpa produced higher densities of dislocations and cavities and greater swelling than did the lower injection rates.

3. The Influence of Preinjected Helium on Void Rucleation in Fe-17Cr-16.7Ni-2.5Mo During Irradiation at 550°C in ORR (HEDL) 144

preinjection of 40-appm helium leads to a suppression of swelling, although there is some concern that the preinjection may inhibit void growth and result in voids which are smaller than the resolution limit of TEM.

4. The Influence of Cold Work on Swelling of "Pure" AISI 316 Irradiated in ORR (HEDL) 148

Cold working causes an increase in the void density white the swelling is essentially unchanged.

5. Comparison of the Swelling and the Microstructural/Microchemical Evolution of AISI 316 Irradiated in EBR-II and HFIR (HEDL) 162

The microstructural and microchemical evolution has been compared for *one heat of cold-worked 316 stainless steel irradiated in both HFIR and EBR-11 at 500-620°C. The dislocation and cavity densities and the swelling at high fluence are remarkably insensitive to the over two orders of magnitude difference in helium/dpa ratios. Minor differences in microchemical evolution were observed, possibly arising from solid transmutants that form only in HFIR. The microchemical evolution is accompanied by the development of a swelling rate typical of steels irradiated in fast reactors.*

CONTENTS (Cont'd)

Page

6. The History Dependence of the Microchemical Evolution of Irradiated AISI 316 and 304L Steels (HEOL and ANL-West) 176

It appears that the effect of helim on cavity density in AISI 316 is primarily a transient phenomenon and that both the microchemical evolution and swelling behavior of austenitic stainless steels exhibit their primary sensitivity to other variables. The total nickel removal from the alloy matrix is a good index of the microchemical evolution,

7. The Effects of Solid Transmutation Products on Swelling in 316 Stainless Steel (HEDL) 190

The isotopic evolution of AISI 316 was calculated for two breeder reactors, two fusion devices and the High Flux Isotope Reactor (HFIR). The largest changes in composition arise in HFIR, where the manganese is strongly depleted and substantial vanadium is generated. Depletion of manganese in HFIR will lead to changes in the swelling behavior of 316 SS. It is anticipated also that the production of vanadium will alter the swelling behavior in a manner typical of other strong MC-carbide forming elements such as titanium.

8. The Inclusion of Transmutant Effects on Development of Fission-Fusion Correlations (HEDL) 205

The scope of a study is outlined that is designed to assess potential areas where differences in transmutation rates wilt impact analysis of data and the development of correlations. The study focuses on four problem areas: trace element effects, major element effects, consequences of radiation-induced segregation on local helim deposition rates, and recoil effects on precipitate stability.

FIGURES

Page

CHAPTER 1

2. Nuclear Data for Damage Studies and FMIT (HEDL)

FIGURE 1. Iron Transmission Experiment Neutron Spectrum at 0 Degrees. 9

FIGURE 2. Iron Transmission Experiment Neutron Spectrum at 90 Degrees. 10

FIGURE 3. Dose After Saturating Bombardment Time FMIT Prototype Beam on Thick Carbon 0.2A-2.5-MeV Protons Plus 15μA-5.0-MeV Deuterons. 11

FIGURE 4. Dose After Saturating Bombardment Time FMIT Tune-up Beam on Thick Carbon 4mA-17.5-MeV Protons Plus 0.3μA-35-MeV Deuterons. 12

CHAPTER 2

1. Fission Reactor Dosimetry (ANL)

FIGURE 1. Fluence Values are Shown for the ORR-MFE2 Irradiation as a Function of Vertical Height Above Midplane. 19

FIGURE 2. Total Fluence and DPA Values for 316 Stainless Steel as Shown for the ORR-MFE2 Irradiation. 19

FIGURE 3. Neutron Flux Spectrum Computed Using the STAYSL Computer Code for the HEDLI Experiment in Position 4-F of the Omega West Reactor. 23

4. Solid and Gas Transmutation Production Code Development (HEDL)

FIGURE 1. Transmutation of SS 316 in FMIT (10 x 10^{22} corresponds to ~200 dpa). 38

5. Computer Simulation of High Energy Recoils in fcc Metals: Cascade Shapes and Sizes (HEDL)

FIGURE la. A Comparison of 200-keV and 20-keV Cascades, Vacancies Only, After Recombination. 43

FIGURE lb. A 200-keV Cascade, With Both Vacancies (small boxes) and Interstitials (dots), After Recombination. 44

FIGURES (Cont'd)

Page

FIGURE 2. The Average Maximum Extent in Lattice Parameters of Simulated Cascades in Copper as a Function of PKA Energy, Measured on the Vacancy Distribution Only, After Recombination. 45

FIGURE 3. Density Map for Part of a 200-keV Cascade in Copper. 46

FIGURE 4. The Number of Subcascades and Lobes per PKA in Copper Cascades as a Function of PKA Energy. 47

FIGURE 5. The Average Lobe Separation in Lattice Parameters as a Function of PKA Energy. 48

6. The Effect of Irradiation on The Order/Disorder Transformation in CuPd (U. Wis.)

FIGURE 1. Typical Damage Structure, Shown in Two Magnifications, of Initially Ordered CuPd Irradiated With 14-MeV Copper Ions From 23 to 200°C to Doses Above 0.2 dpa. 54

FIGURE 2. A Bright Field Image of the Damage Structure of a Sample Irradiated at 23°C to 0.05 dpa at 1.4 x 10^{-3} dpa/sec is Shown in (a). 55

FIGURE 3. Bright Field (a) and Dark Field (b) Images of a CuPd Sample Irradiated at 23°C to 0.06 dpa at 2 x 10^{-4} dpa/sec. 56

FIGURE 4. Variation of Steady State Degree of Order in CuPd With Irradiation Temperature. 58

FIGURE 5. Phase Diagram of CuPd as Modified by Irradiation Described in Figure 4. 58

FIGURE 6. (a) and (b) Show the Fotmation of Ordered Grains in the Disordered Matrix After Postirradiation Annealing at 260°C for 90 Minutes. 59

FIGURE 7. Resistivity Increase in an Initially Ordered Sample (a) and an Initially Disordered Sample (b) During Irradiation With 14.8-MeV Neutrons. 61

FIGURE 8. Differential Isochronal Annealing Results of the Ordered (a) and Disordered (b) CuPd Samples After Fusion Neutron Irradiation. 62

FIGURES (Cont'd)

Page

7. Effects of Heavy-Ion Irradiation on the Phase Stability of a Cu-3.4 at% Be Alloy (U. Wis.)

FIGURE 1. Copper-Rich End of the Equilibrium Phase Diagram of the Cu-Be System, Showing the Temperatures at Which the Cu-3.4 at% Be Alloy was Irradiated. 67

FIGURE 2. Radiation-Induced Precipitation in Supersaturated Cu-3.4 at% Be Alloy. 69

FIGURE 3. Temperature Dependence of Mean Precipitate Size in Low Dose (0.5-1 dpa) and High Dose (5-10 dpa) Cu-3.4 at% Be Specimens. 70

FIGURE 4. The Dependence of Precipitate Number Density on Irradiation Temperature in Low Dose and High Dose Samples. 71

FIGURE 5. Temperature Dependence of the Unprecipitated Fraction of Be Solute Under Near Steady-State Irradiation Conditions. 72

FIGURE 6. Precipitation in Cu-3.4 at% Be Irradiated at 350°C With 7 x 10^{15} ions/cm^2. 73

FIGURE 7. Depth Dependence of the Mean Precipitate Size and Number Density in Cu-3.4 at% Be Alloy Irradiated With 14 MeV Cu Ion at 375°C, to a Fluence Level of 1.8 E16 ions/cm^2. 74

FIGURE 8. Dependence of Precipitate Size on dpa Level and dpa Rate. 75

FIGURE 9. Effect of Postirradiation Annealing at 400°C on Specimen Irradiated at 400°C. 76

FIGURE 10. Discontinuous Precipitation in Unirradiated, Thermally Aged Cu-3.4 at% Be Alloy. 77

8. Damage Development and Hardening in 14-MeV Neutron Irradiation of Copper Alloys at 25°C (HEDL)

FIGURE 1. Microhardness and Microstructure of Copper and Copper Alloys Irradiated in RTNS-II at 25°C with 14-MeV Neutrons. 84

FIGURE 2. The Size Distribution of Visible Defect Clusters Formed in the Copper and Copper Alloys. 86

Page

FIGURE 3. Comparison of Calculated Estimates of Yield Stress Changes With the Results of Earlier Tests Performed on Copper Specimens Irradiated in RTNS-I. 92

CHAPTER 3

1. Crack Propagation Characteristics in Helium Irradiated Type 316 Stainless Steel (U. of Va.)

FIGURE 1. Graph of Crack Length Data Produced by Two Cracks Versus Total Elongation for an Unirradiated Specimen Tested at Room Temperature. 99

FIGURE 2. Graphs of Crack Angle and Crack-Direction Angle Versus Crack Length for Unirradiated and He-irradiated 316 SS Tested at Room Temperature. 101

FIGURE 3. Graphs of Crack Length, Crack Angle and Crack-Tip Angle versus Total Elongation for Unirradiated 316 SS Tested at Room Temperature. 102

2. The Role of Luders Strain in Determining Flow Properties in Steel From an Instrumented Hardness Test (UCSB)

FIGURE 1. Geometric Features of an Indentation Profile. 110

FIGURE 2. Comparison of Hardness/Microhardness Derived Stress-Strain Data With the Uniaxial Tension Curve of Sample Type S8. 110

FIGURE 3. Relationship Between the Area Measured Under the Indentation Lip Profile and Luders Strain. 111

FIGURE 4. Profilometer Traces and Interferographs of Indentations Made at 9.07 kg for Specimen Types a) S2, b) S8 and c) s20. 111

CHAPTER 4

1. Tensile Property Correlation for 20% Cold Worked 316 Stainless Steel (HEDL)

FIGURES (Cont'd)

		Page
FIGURE 1.	Measured and Calculated Ultimate Tensile Strength for Heat 87210 versus dpa.	123
FIGURE 2.	Measured versus Calculated Ultimate Tensile Strength in 20% CW 316 Stainless Steel.	123
FIGURE 3.	True Uniform Elongation versus an Empirical Strength Function (T_{IRR} < 500°C).	124
FIGURE 4.	Uniform Elongation versus dpa for an Irradiation Temperature of 376°C.	126
FIGURE 5.	True Uniform Elongation versus an Empirical Strength Function ($T_{IRR} \geq$ 500°C).	127
FIGURE 6.	Sensitivity of Total Elongation in 20% CW 316 SS to Helium Content.	128
FIGURE 7.	Total Elongation versus dpa in 20% CW 316 Stainless Steel (T_{IRR} = 575°C).	130
FIGURE 8.	Total Elongation in 20% CW 316 Stainless Steel versus Total Helium Content (T_{IRR} = 575°C).	131

2. Dose and Helium Injection Rate Dependence of Swelling in Dual-Ion Irradiated 316 Stainless Steel (ANL)

FIGURE 1.	Dose Dependence of Dislocation Density in 316 SS.	138
FIGURE 2.	Dose Dependence of Cavity Size in 316 SS.	139
FIGURE 3.	Dose Dependence of Cavity Number Density in 316 SS.	140
FIGURE 4.	Dose Dependence of Swelling in 316 SS.	142

4. The Influence of Cold Work on Swelling of "Pure" AISI 316 Irradiated in ORR (HEDL)

FIGURE 1.	Typical Micrograph of P-7 Alloy in Annealed Condition After Irradiation to 3 dpa at 550°C.	151
FIGURE 2.	Typical Micrograph of P-7 Alloy in 20% Cold-Worked Condition After Irradiation to 5 dpa at 550°C.	152

FIGURES (Cont'd)

Page

FIGURE 3. Void Densities Observed in Cold-Worked AISI 316 (DO-Heat) Irradiated in HFIR and Roughly a Factor of Two Greater Than That Formed in Annealed Specimens. 154

FIGURE 4. Effect of Cold Work on Swelling of AISI 316 Stainless Steel at High Neutron Fluences. 155

FIGURE 5. Dependence of Neutron-Induced Swelling on Cold-Work Level in AISI 316 at 550°C. 155

FIGURE 6. Dependence of Neutron-Induced Swelling on Cold-Work Level in AISI 304 at 450°C. 156

FIGURE 7. Dependence of Swelling on Cold-Work Level in 1.4981 Wrapper Steel (Niobiun-Stabilized) After Irradiation by 46-MeV Ni^+ Ions at 575°C. 156

FIGURE 8. Swelling Curves Inferred from Step-Height Measurements on Annealed Type 316 and 20 Percent Cold-Rolled Type 316 Bombarded With 5-MeV Nickel Ions at 625°C. 157

FIGURE 9. Dependence of Swelling at 625-635°C in AISI 316 on Impurity Level as Revealed by Ion Irradiation at Two Laboratories. 157

FIGURE 10. Swelling of Fe-17Cr-14.4Ni-2.8Mo Irradiated in EBR-II. 158

5. Comparison of the Swelling and the Microstructural/Microchemical Evolution of AISI 316 Irradiated in EBR-II and HFIR (HEOL)

FIGURE 1. Concentration Profiles Observed Near M_6C Precipitates in 20% Cold-Worked DO-Heat at 500°C and 33 dpa. 165

FIGURE 2. Concentration Profiles Observed Near G-Phase Precipitate in 20% Cold-Worked DO-Heat at 510°C and 69 dpa. 166

FIGURE 3. Comparison of Cavity Densities Observed in 00-Heat Irradiated in EBR-II and HFIR. 171

FIGURE 4. Comparison of Cavity Volumes Observed in DO-Heat Irradiated in EBR-II and HFIR. 172

FIGURE 5. Comparison of Swelling Observed in Solution Annealed DO-Heat in HFIR With That of Cold-Worked DO. 172

FIGURES (Cont'd)

Page

6. The History Dependence of the Microchemical Evolution of Irradiated AISI 316 and 304L Steels (HEDL)

FIGURE 1. Nickel Content of Precipitates Extracted From Pressurized Tubes of Annealed or 20% Cold-Worked AISI 316 Irradiated at 550°C. 178

FIGURE 2. Nickel Content of Precipitates Extracted From Pressurized Tubes of Cold-Worked AISI 316 Irradiated at 400°C. 179

FIGURE 3. Data From Figure 2 on 10% Cold-Worked AISI 316 Only, Showing Amounts of Precipitate Associated With Each Concentration Measurement. 180

FIGURE 4. Total Nickel Removal Calculated From Data in Figure 3, Broken Down into Subsets, Each Representing Only Data Extracted From a Single Tube. 182

FIGURE 5. Schematic Representation of Helium Influence on Void Nucleation in AISI 316 Stainless Steel. 184

FIGURE 6. Comparison of Void Densities Observed in AISI 316 After Irradiation in HFIR and Two Breeder Reactors, Showing That Saturation Densities are Essentially Identical in Both Types of Reactors, but That the Transients are Longer in Breeder Reactors. 186

FIGURE 7. Comparison of Swelling of Annealed 304L Steel in Both the Isothermal and Annealed/Reirradiated Conditions. 187

7. The Effects of Solid Transmutation Products on Swelling in 316 Stainless Steel (HEDL)

FIGURE 1. Effects of Manganese Content on Swelling in Both Annealed and 20% Cold-Worked 316 at 400°C. 197

FIGURE 2. Effects of Manganese Content on Swelling in Both Annealed and 20% Cold-Worked 316 at 510 and 520°C. 197

FIGURE 3. Effects of Manganese Content on Swelling of Annealed 316 at Low Temperatures and Low Fluence. 198

FIGURE 4. Vanadium Concentration as a Function of Exposure for Various Reactors. 199

FIGURE 5. Change in Manganese as a Function of Exposure for Various Reactors. 200

FIGURES (Cont'd)

Page

8. The Inclusion of Transmutant Effects on Development of Fission-Fusion Correlations (HEDL)

FIGURE 1. Effect of Solute Content on Irradiation Creep of 20% Cold-Worked **AISI** 316 at 450°C, 4.6 x 10^{22} n/cm^2 (E > 0.1 MeV) and 172 MPa Hoop Stress. 207

FIGURE 2. Changes in Manganese Concentration in AISI 316 as a Function of Exposure for Various Reactors. 211

FIGURE 3. Vanadium Concentration in AISI 316 as a Function of Exposure for Various Reactors. 212

TABLES

Page

CHAPTER 2

1. Fission Reactor Dosimetry (ANL)

TABLE 1. Status of Reactor Experiments 18

TABLE 2. Average Fluences and Damage Parameters for Various Levels for ORR-MFE2 20

TABLE 3. Activation Rates for Omega West - HEDLl 22

TABLE 4. Flux and Fluence Values for Omega West - HEDLl 24

TABLE 5. Spectral-Averaged Damage Parameters for Omega West - HEDLl 25

TABLE 6. Dosimetry Results for the ORR-MFE4A Experiment 27

TABLE 7. Flux and Fluence Values for ORR-MFE4A 27

3. Calculation of Damage Parameters (HEDL)

TABLE 1. ENDF/B-V Materials Processed for Gas Production 34

5. Computer Simulation of High Energy Recoils in fcc Metals: Cascade Shapes and Sizes (HEDL)

TABLE 1. Averages of $R_{max}/\Delta Z$ and the Aspect Ratio 49

8. Damage Development and Hardening in 14 MeV Neutron Irradiation of Copper Alloys at 25°C (HEDL)

TABLE 1. Microscopy Data - RTNS-II Copper Binary Series 85

TABLE 2. Room Temperature Hardness of Unirradiated Alloys 90

CHAPTER 3

2. The Role of Luders Strain in Determining Flow Properties in Steel From an Instrumented Hardness Test (UCSB)

TABLE 1. Tensile Data Regression Parameters 108

Page

CHAPTER 4

1. Tensile Property Correlation for 20% Cold Worked 316 Stainless Steel (HEDL)

TABLE 1. Fitted Parameters for Equation (1) 121

2. Dose and Helium Injection Rate Dependence of Swelling in Dual-Ion Irradiated 316 Stainless Steel (ANL)

TABLE 1. Irradiation Conditions 137

4. The Influence of Cold Work on Swelling of "Pure" AISI 316 Irradiated in ORR (HEDL)

TABLE 1. Effects of Cold Work on Swelling of Pure Metals 158

5. Comparison of the Swelling and the Microstructural/Microchemical Evolution of AISI 316 Irradiated in EBR-II and HFIR (HEDL)

TABLE 1. Chemical Composition on DO-Heat and a Typical U.S. Breeder AISI 316 Stainless Steel 168

6. The History Dependence of the Microchemical Evolution of Irradiated AISI 316 and 304L Steels (HEDL)

TABLE 1. Amount of Nickel Removal into Precipitates at 400°C 181

7. The Effect of Solid Transmutation Products on Swelling in 316 Stainless Steel (HEDL)

TABLE 1. Fluxes and Cross Sections for Various Reactors 194

TABLE 2. Initial Concentration of Elements in AISI 316 195

TABLE 3. Percentage Changes in Composition Due to Transmutations 196

8. The Inclusion of Transmutant Effects on Development of Fission-Fusion Correlation (HEDL)

TABLE 1. Transmutation of Materials in the First Wall of a Fusion Reactor 208

CHAPTER 1

IRRADIATION TEST FACILITIES

RTNS-II IRRADIATIONS AND OPERATIONS

C. M. Logan and D. W. Heikkinen (Lawrence Livermore National Laboratory)

1.0 Objective

The objectives of this work are operation of OFE's RTNS-II (a 14-MeV neutron source facility), machine development, and support of the experimental program that utilizes this facility. Experimenter services include dosimetry, handling, scheduling, coordination, and reporting. RTNS-II is dedicated to materials research for the fusion power program. Its primary use is to aid in the development of models of high-energy neutron effects. Such models are needed in interpreting and projecting to the fusion environment engineering data obtained in other neutron spectra.

2.0 Summary

Irradiations were done on a total of six different experiments. No major unscheduled outages occurred.

3.0 Program

Title: RTNS-II Operations (WZJ-16)
Principal Investigator: C. M. Logan
Affiliation: Lawrence Livermore National Laboratory

4.0 Relevant DAFS Program Plan Task/Subtask

TASK II.A.2,3,4.
TASK II.B.3,4.
TASK II.C.1,2,6,11,18.

5.0 Accomplishments and Status

5.1 Irradiations - C. M. Logan, D. W. Heikkinen and M. W. Guinan (LLNL)

The intermediate irradiation for N. Panayotou (HEDL) using the HEDL dual temperature furnace was completed. Dosimetry results give a fluence of 5.9×10^{18} n/cm^2 at the front surface of the furnace. An irradiation of Nb, Ti and V was done for R. Bradley (PNL). The total fluence was 5.8×10^{17} n/cm^2. An additional increment of irradiation was begun on samples of superconducting wire of Nb_3Sn, V_3Ga and NbTi for C. Snead (BNL) and M. W. Guinan (LLNL). Further irradiations of thermocouple wire specimens for C. Logan and D. Heikkinen (LLNL) were done. An in-situ Nb creep experiment was completed for W. Barmore (LLNL). A short irradiation of electronic components was done for J. Srour (Northrop).

5.2 RTNS-II Status - C. M. Logan and D. W. Heikkinen (LLNL)

There were no major unscheduled outages during this quarter. The HEDL dual temperature furnace was removed after completion of the intermediate irradiation. The Remotely Operated Vehicle and Experiment Retriever (ROVER) has been completed. Tritium loading of two 50-cm diameter targets has been accomplished at Oak Ridge National Laboratory. The 1500 ℓ/s turbo pump in the high voltage terminal has been replaced with a 2800 ℓ/s turbo pump. This has resulted in better ion source performance.

6.0 Future Work

Irradiations are scheduled for C. Snead (BNL), M. W. Guinan (LLNL), R. Bradley (PNL), C. Logan and D. Heikkinen (LLNL), and S. Zinkle (U. of Wisc.) during the next quarter.

7.0 Publications

Development of Manufacturing Methods for 50-cm Diameter Neutron Source Targets for RTNS-II, C. M. Logan, J. W. Dini, W. D. Ludemann, B.J. Schumacher, E.N.C. Dalder, W. K. Kelley, G. A. Harter (UCRL 85429) to be presented at the Second Topical Meeting on Fusion Reactor Materials, Seattle, Washington, August (1981).

NUCLEAR DATA FOR DAMAGE STUDIES AND FMIT (AVC)

D. L. Johnson and F. M. Mann (Hanford Engineering Development Laboratory)

1.0 Objective

The objective of this work is to supply nuclear data needed for damage studies and in the design and operation of the Fusion Materials Irradiation Testing (FMIT) facility.

2.0 Summary

Calculations of the transmission spectra of FMIT-like neutrons through thick iron were completed and are in good agreement with revised experimental data.

An evaluation was completed of proton and deuteron-induced activation and neutron production from graphite beam stops for both the FMIT prototype and full energy accelerators.

3.0 Program

Title: Nuclear Data for Damage Studies and FMIT (WH025/EDK)
Principal Investigators: D. L. Johnson/F. M. Mann
Affiliation: Hanford Engineering Development Laboratory (HEDL)

4.0 Relevant DAFS Program Plan Task/Subtask

All tasks that are relevant to FMIT use, with emphasis upon:

SUBTASK II.A.2.3 Flux spectra definiti'on in FMIT
TASK II.A.4 Gas Generation Rates
SUBTASK II.A.5.1 Helium Accumulation Monitor Development
SUBTASK II.B.1.2 Acquisition of Nuclear Data

5.0 Accomplishments and Status

5.1 Neutron Transport Measurements and Calculations

D. L. Johnson, F. M. Mann, and L. L. Carter (HEDL), G. L. Woodruff (Univ. of Wash.), F. P. Brady, J. L. Romero, J. L. Ullmann, M. L. Johnson and C. M. Castaneda (Univ. of Calif. at Davis).

Measurements of the transmission of FMIT-like neutrons through thick iron and the radiation heating within the iron were outlined in the DAFS Quarterly Report for July-Sept. 1980[1]. The objective was to provide data to confirm neutron transport calculations which are used for predictions of radiation heating in the FMIT test cell walls. Furthermore, data were obtained for a situation that is nearly identical to that which will be experienced in the test assemblies within the FMIT test cell.

The neutrons were produced by a beam of 35 MeV deuterons (from the cyclotron at the University of California at Davis) which was stopped in a solid lithium target that was ∿ 2.5 cm in diameter by 2 cm thick. This target was placed close to the center of a nearly cubical block of solid iron which was about 60 cm on each side. Neutrons from the source had to penetrate at least 30 cm of iron in any direction in order to escape the iron block.

Measurements of the neutron spectra were made with detectors placed 10 cm outside the block at 0° and 90° with respect to the beam direction. Proton recoil proportional counters were used to measure the portion of the spectrum from about 10 keV to about 1.5 MeV where most of the transmitted neutrons are found. An NE213 liquid scintillator was used to measure the spectrum from about 1 MeV up to the maximum that might be observable (about 50 MeV).

Subsequent to obtaining the preliminary results given in ref. 1, calculations of the corresponding neutron spectra were performed using the Monte Carlo neutron transport code MCNP[2]. Pointwise cross sections were obtained from ENDF/B-IV below 20 MeV and appended from other sources for energies between 20 and 60 MeV[3]. Comparison of the experimental data to the calculations indicated a large discrepancy for neutron energies less than a few hundred

keV. The discrepancy was found to be from an incorrect representation of the data from proton recoil proportional counters and was subsequently corrected. The updated experimental data are compared to the calculations in Fiqs. 1 and 2.

There is now generally good agreement over the full energy range. For neutron energies greater than 1 MeV the ratio of calculational to experimental data tends to be about 0.6 - 0.7. Note that there are similar discrepancies between other experiments and calculations for the transmission of 14-MeV neutrons through iron of comparable thickness. For example, in Ref. 4, C/E ratios of about 0.4 are seen for leakage neutrons in the range of 1 to 5 MeV using ENDF/B-IV cross sections. Moreover, in Ref. 5, C/E ratios of about 0.77 are seen for leakage neutrons between 2 and 5 MeV using both ENDF/B-IV and -V cross sections and thinner iron. Some of the discrepancies may be due in part to poor statistics in the Monte Carlo calculations. This is especially true for the highest energy neutrons because of their low probability.

5.2 Evaluation of Residual Gamma Doses and Neutron Production from Graphite Beam Stops for the Prototype and FMIT Accelerators.
D. L. Johnson

Large beam currents will be incident upon beam stops for both the prototype and FMIT accelerators for use in tune-up. The tune-up beam for the prototype is nominally expected to consist of 100mA of 5-MeV $^{+}H_2$ ions (200mA of 2.5-MeV protons) plus about 15μA of 5 MeV deuterons. For the FMIT beam stop, a current of 2mA of 35-MeV $^{+}H_2$ ions (4mA of 17.5 MeV protons) plus about 0.3μA of 35-MeV deuterons is expected. The natural isotopic ratio of 1.5×10^{-4} is assumed for $^{t}D/^{t}H_2$ ions. Graphite is a leading candidate for the stopping material partly because of expected low activation and low neutron production. Evaluation of the activation and neutron production is needed for design.

The thick target rates for production of significant radionuclides by the incident protons or deuterons were evaluated using the data in Refs. 6, 7,

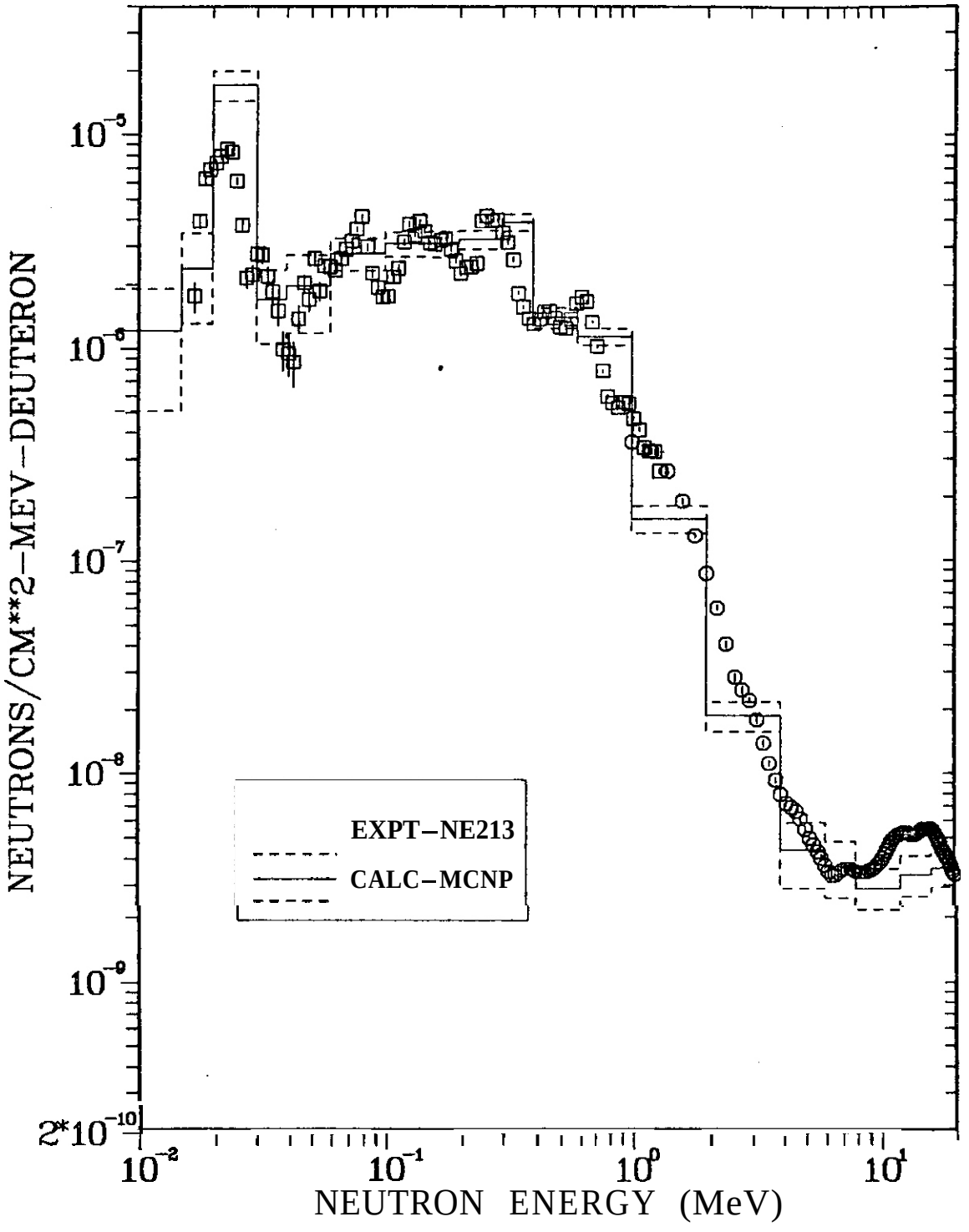

FIGURE 1. Iron Transmission Experiment Neutron Spectrum at 0 Degrees.

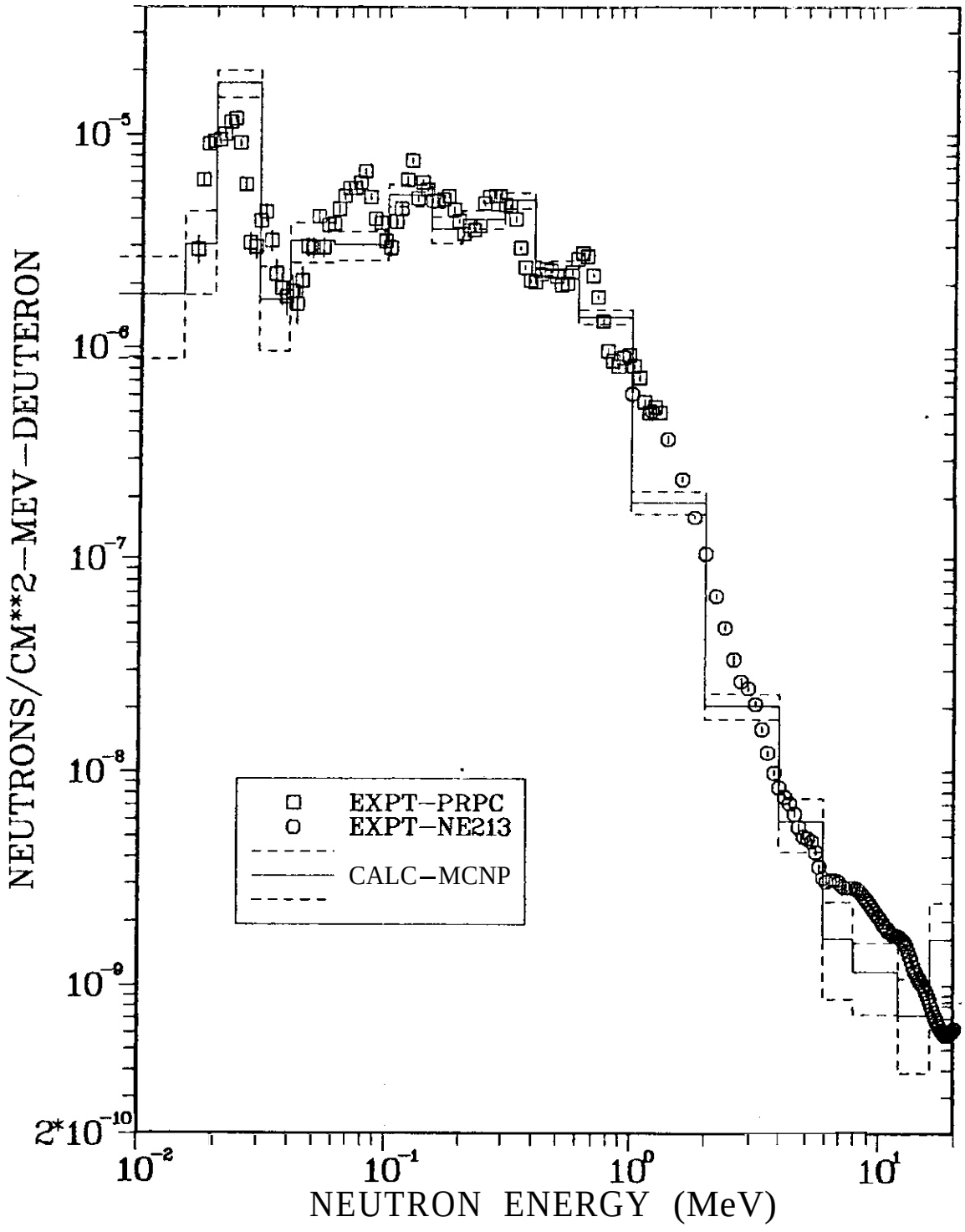

FIGURE 2. Iron Transmission Experiment Neutron Spectrum at 90 Degrees.

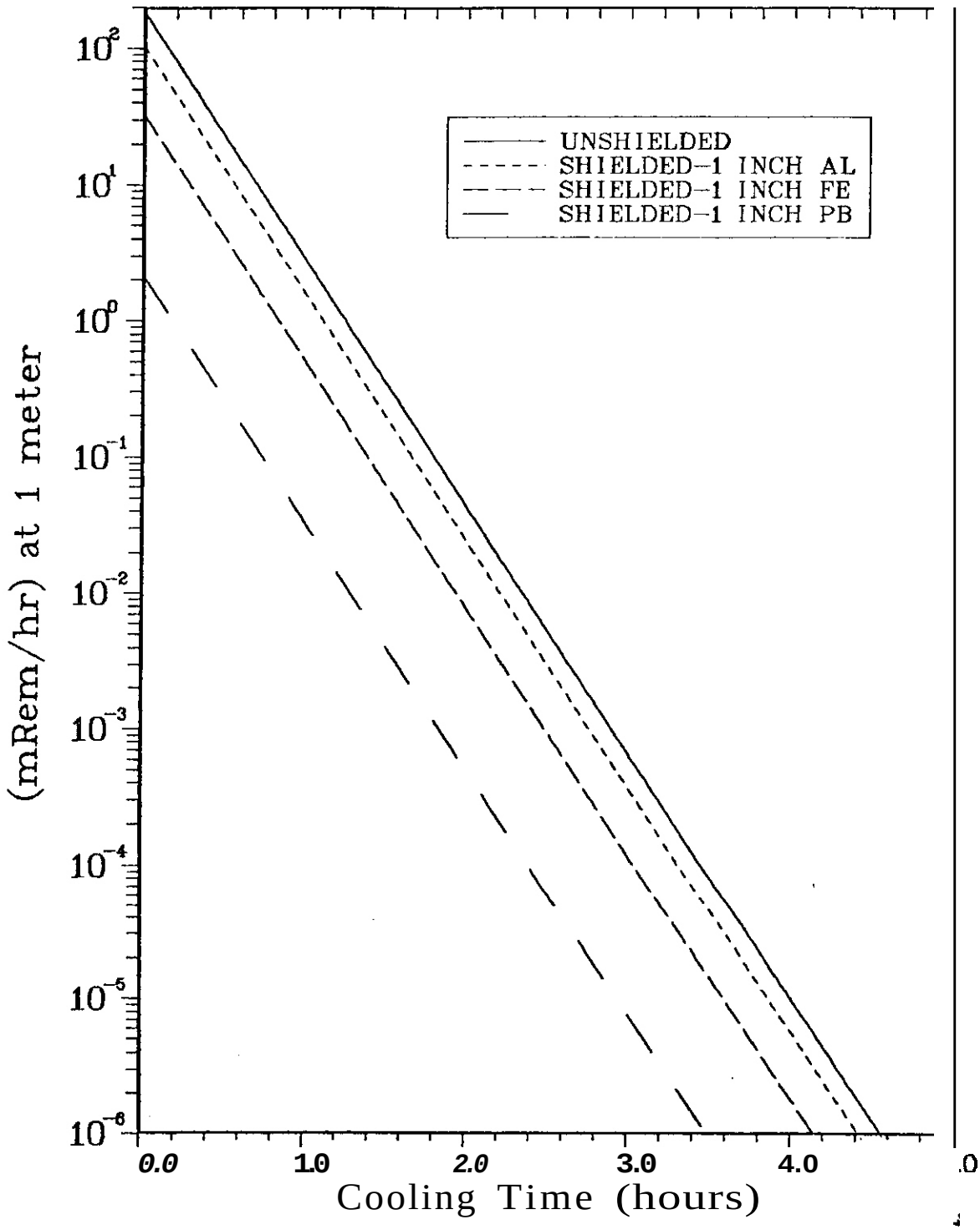

FIGURE 3. Dose After Saturating Bombardment Time FMIT Prototype Beam on Thick Carbon 0.2A to 2.5-MeV Protons Plus 15μA to 5.0-MeV Deuterons.

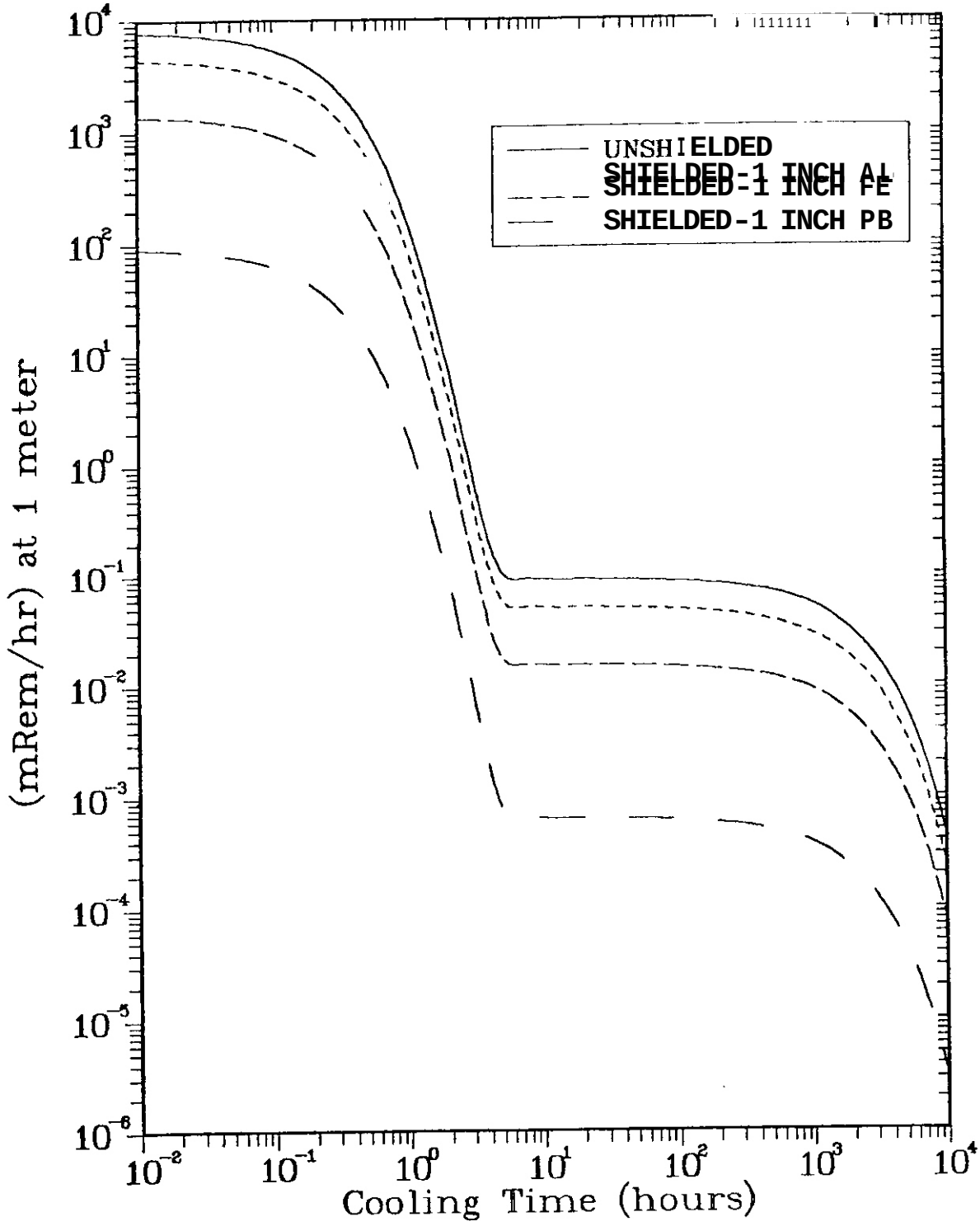

FIGURE 4. Dose After Saturating Bombardment Time FMIT Tune-up Beam on Thick Carbon 4mA to 17.5-MeV Protons Plus 0.3μA to 35-MeV Deuterons.

and 8. The residual dose from decay gamma rays was then evaluated following an irradiation time in which each radionuclide was saturated.

The maximum initial unshielded dose following bombardment of graphite by the prototype tune-up beam will be about 185 mRem/hr at 1 meter. This will decay away with a half-life of about 10 minutes that is characteristic of ^{13}N, the only radionuclide produced. The small deuteron component contributes about 74% of the dose. Fig. 3 shows the decay of the dose from the prototype beam stop for various shielding materials.

The maximum initial unshielded dose following bombardment of graphite by the FMIT tune-up beam will be about 8 Rem/hr at 1 meter. The leading contributors to this are ^{13}N and ^{11}C ($T_{\frac{1}{2}} \simeq 20$ min.) which will decay away in a few hours. The remaining dose of about 0.09 mRem/hr at 1 meter is from ^{7}Be which will decay away with a half-life of about 53 days. The small deuteron component contributes only about 1% to the dose at short cooling times but is responsible for all of the long-lived dose. Fig. 4' shows the decay of the dose from the FMIT full energy beam stop for various shielding materials.

The neutron production rate from the prototype beam on thick graphite will be about 1.6×10^{10} neutrons/sec. All of this rate is due to the small deuteron component.

The neutron production rate from the FMIT tune-up beam on thick graphite will be about 1.5×10^{12} neutrons/sec. Only about 4% of this rate is due to the deuteron comoonent.

Data used to obtain the neutron production rates were obtained in Refs. 9, 10, and 11.

6.0 References

1. D. L. Johnson and F. M. Mann, Damage Analysis and Fundamental Studies, Quarterly Progress Report, July-September 1980, DOE/ER-0046/3, Nov. 1980,

pgs. 6-13.

2. LASL Group X-6, "MCNP - A General Monte Carlo Code for Neutron and Photon Transport," LA-7396-M, Los Alamos Scientific Laboratory (revised Nov.1979).

L. L. Carter and E. D. Cashwell, "Particle Transport Simulation with the Monte Carlo Method," TID-26607, ERDA Critical Review Series, U.S. Energy Research and Development Administration, Technical Information Center, Oak Ridge, TN (1975).

3. L. L. Carter, R. J. Morford and A. D. Wilcox, "Nuclear Data Relevant to Shield Design of FMIT Facility," Proceedings of Symposium on Neutron Cross-Sections from 10 to 50 MeV, held at Brookhaven National Laboratory May 12-14, 1980. BNL-NCS-51245, July 1980, pgs. 431-458.

4. N. E. Hertel, R. H. Johnson, J. J. Dorning, and B. W. Wehring, "Measurements and Analyses of Neutron Transport Through Iron," Proceedings of the International Conference on Nuclear Cross Sections for Technology," Knoxville Tennessee, October 22-26, 1979. Ed. by J. L. Fowler et al., NBS Special Publication 594, pgs. 563-567, Sept. 1980.

5. Guy P. Estes and John S. Hendricks, "Integral Testing of Some ENDF/B-V Cross Sections," Trans. ANS 23 (1979) 679.

6. N. A. Roughton, M. R. Fritts, R. J. Peterson, C. S. Zaidins, and C. J. Hansen, "Thick Target Measurements and Astrophysical Thermonuclear Reaction Rates: Proton-induced Reactions," Atomic Data and Nuclear Data Tables 23 (1979) 177-194.

7 N. N. Krasnov, P. P. Dmitriev, Z. P. Dmitrieva, I. O. Konstantinov, and G. A. Molin, "^{13}N, ^{11}C, and ^{18}F Yields from Charged Particle Irradiation of Carbon and Oxygen." Soviet Atomic Energy 27 (1969) 832-835.

a. C. B. Fulmer and D. A. Goldberg, "Excitation Functions for ^{7}Be Production by Light-Ion Bombardment of ^{12}C." Physical Review C11 (1975) 50-53.

9. R. J. Jaszczak, R. L. Macklin, and J. H. Gibbons, "$^{12}C(d,n)^{13}N$ total Cross Section from 1.2 to 4.5 MeV," Physical Review 181 (1969) 1428-1430.

10. V. K. Daruga and E. S. Matusevich, "Neutron Yields from Thick Targets Bombarded with 11.5 and 23.5 MeV Protons," Soviet Atomic Energy 29 (1971) 1233.

11. J. P. Meulders et al., "Fast Neutron Yields and Spectra from Targets of Varying Atomic Number Bombarded with Deuterons from 16 to 50 MeV." Phys. Med. Biol. 20 (1975) 235-243.

CHAPTER 2

DOSIMETRY AND DAMAGE PARAMETERS

FISSION REACTOR DOSIMETRY

L. R. Greenwood (Argonne National Laboratory)

1.0 Objective

To establish the best practicable dosimetry for mixed-spectrum reactors and to provide dosimetry and damage analysis for OFE experiments.

2.0 Summary

Neutron fluence and damage parameters are reported for the ORR-MFE2 and Omega West-HEDL1 irradiations. Analysis is in progress for the EBRII-X287 and ORR-MFE4A experiments.

3.0 Program

Title: Dosimetry and Damage and Damage Analysis
Principal Investigator: L. R. Greenwood
Affiliation: Argonne National Laboratory

4.0 Relevant DAFS Program Plan Task/Subtask

Task II.A.1 Fission Reactor Dosimetry

5.0 Accomplishments and Status

The status of all fission reactor dosimetry is given in Table 1.

5.1 Recommended Fluence and Damage Parameters for the ORR-MFE2 Irradiation

Analysis has been completed for the ORR-MFE2 experiment in core position E7 of the Oak Ridge Research Reactor from September 1978 to March 1980 (10,972 MWD, average power 26.4 MW).

TABLE 1

STATUS OF REACTOR EXPERIMENTS

Facility/Experiment		Status and Comments
ORR	- MFE1	Analysis complete (12/79)
	- MFE2	Analysis complete (6/81)
	- MFE3	Delayed
	- MFE4A	Samples received (5/81)
	- MFE4B,C	Irradiation in progress
	- TBC07	Analysis complete (7/80)
	- TRIO	Planning in progress
HEIR	- CTR 32	Samples received (5/81)
	- CTR 30, 31	Irradiation in progress
	- T1,T2	Irradiation in progress
	- RB1	Planning in progress
Omega West	- Spectral Run	Analysis complete (10/80)
	- HEDLI	Analysis complete (5/81)
EBR II	- X287	Preliminary results (6/81)

The placement and types of dosimeters used were reported in our previous report (DOE/ER-0046/5). The fluence values given previously were at the location of the dosimetry wires at either the top or bottom of each of the four levels. Complete fluence and dpa gradients have now been measured, as shown in Figures 1 and 2. It is important to note that the gradient measurements were made with long wires located on the east side of the experimental assembly. The fast flux was about 8% higher at this position than at the sample locations; although, the thermal flux was the same at both locations. Horizontal gradients within the samples were less than 2% and have thus been neglected. The gradients were averaged over each of the four levels and recommended average fluence valves are given in Table 2.

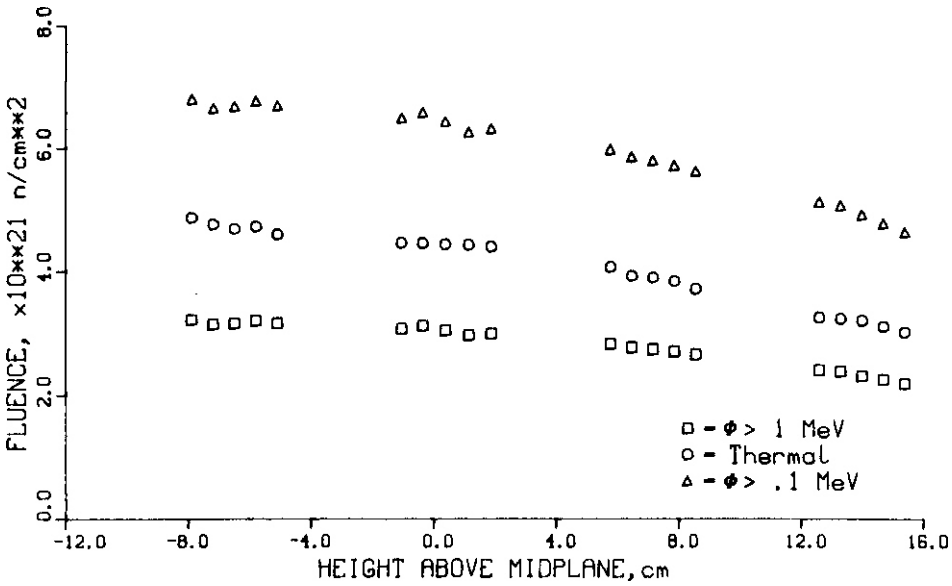

FIGURE 1. Fluence Values are Shown for the ORR-MFE2 Irradiation as a Function of Vertical Height Above Midplane. Level 4 Corresponds to the Points on the Left and Level 1 to Those on the Right.

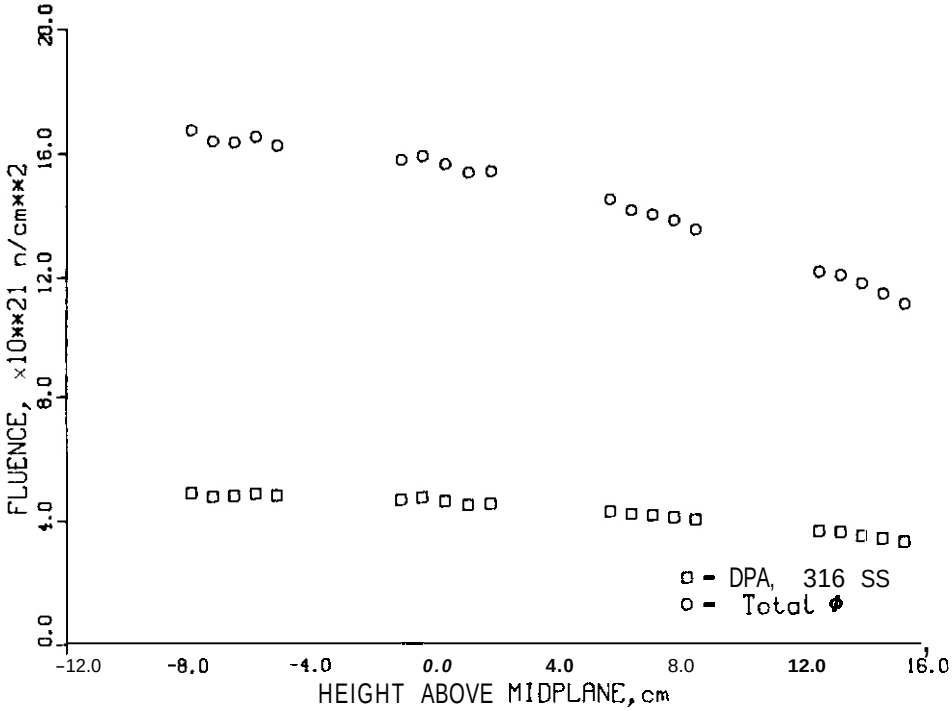

FIGURE 2. Total Fluence and dpa Values for 316 Stainless Steel as Shown for the ORR-MFE2 Irradiation. dpa Values Can Be Read Directly from the Scale on the Left.

TABLE 2

AVERAGE FLUENCES AND DAMAGE PARAMETERS
FOR VARIOUS LEVELS FOR ORR-MFE2

Gradients averaged at each level; cross sections from ENDF/B-V, (n,γ) included; helium in appm (±15%); OPA (±10%).

	LEVEL							
	1		2		3		4	
Height, cm:	11.4, 16.2		4.8, 9.5		-1.9, 2.8		-3.8, -9.5	
Fluence ($\times 10^{21}$ n/cm^2):								
Total:	12.04		14.40		15.97		16.93	
Thermal:	3.14		3.87		4.44		4.74	
>0.11 MeV:	4.89		5.78		6.41		6.78	
>1.0 MeV:	2.33		2.71		3.01		3.17	
Element:	dpa	He	dpa	He	dpa	He	dpa	He
Al	6.17	2.06	7.28	2.46	8.04	2.69	8.50	2.77
Ti	3.60	1.83	4.32	2.14	4.77	2.35	5.04	2.47
V	4.16	0.08	4.91	0.09	5.41	0.09	5.72	0.10
Cr	3.74	0.55	4.40	0.65	4.86	0.72	5.13	0.75
Mn	3.96	0.41	4.68	0.49	5.17	0.53	5.48	0.55
Fe	3.32	0.88	3.90	1.04	4.30	1.14	4.55	1.18
co	3.76	0.43	4.47	0.52	4.93	0.57	5.25	0.58
Ni[a]	3.53	153.	4.17	248.	4.58	325.	4.86	386.
cu	3.21	0.75	3.80	0.90	4.19	0.98	4.42	1.02
Zr	3.55	0.09	4.19	0.10	4.63	0.11	4.89	0.11
Nb	3.25	0.18	3.85	0.21	4.24	0.23	4.48	0.24
Mo	2.37	-	2.82	-	3.09	-	3.28	-
Ta	0.91	-	1.07	-	1.19	-	1.25	-
316 SS[b]	3.40	16.0	4.00	25.6	4.41	33.4	4.67	39.6

[a] Thermal helium production included.

[b] Composition assumed as: Cr(16), Mn(2), Fe(70), Ni(10), Mo(2).

Damage parameters were then computed and also averaged over the four levels. Recommended dpa and helium production values are also listed in Table 2. The damage calculations were performed using our recently revised damage cross sections based on ENDF/B-V. The (n,γ) reaction is also included; however, the contribution to the total damage is generally less than 2%, the exceptions being Co(13%) and Mn(5%). Caution should be used in these two cases since neutron self-shielding and burnup effects would drastically alter the results.

Helium cross sections were also taken from ENDF/B-V. The thermal process for nickel was computed using the equations in ORNL/TM-6361 (1979) with the total thermal flux below 0.5 eV. This procedure was found to agree with measured helium rates for the OFF-MFE1 experiment. Of course, H. Farrar IV and D. Kneff (Rockwell International) will report precise helium measurements for a variety of materials.

All of the fluence and damage parameter gradients can be well-described by a simple quadratic formula:

$$f(x) = N(1 + bx + cx^2)$$

where x is the height above midplane (cm), and the other variables are given in the following table.

Quantity	b	c	N
Fluence	-0.01101	-0.0004690	6.45 x 10^{21} n/cm^2
DPA (316 SS)	-0.01101	-0.0004690	4.47 DPA
He(Ni)	-0.03010	-0.0006364	330.1 appm

Additional dpa, PKA, and helium values are available (37 isotopes) on request.

5.2 Dosimetry Results for the Omega West Reactor

Dosimetry measurements have been completed for the HEDLI experiment (N. Panayotou) in the Omega West Reactor at Los Alamos Scientific Laboratory.

Samples were irradiated in the LLL-HEDL furnace in core position 4F from January 22, 1981 to February 10, 1981. The net exposure was 849.36 MWH with an up time of 106.25 hours at 8.0 MW.

Thin foils of Fe, Ni, Ti, Mn, and Co-A1 (wire) were included with the irradiated samples and at least four of each type of foil was gamma counted. Values were very consistent for each reaction measured indicating that gradients were less than 1% within the experimental capsule.

Seven reaction rates were determined, as listed in Table 3. These rates are compared to rates measured in October 1980, during a complete (30 reaction) spectral measurement (DOE/ER-0046/4, p. 15, 1981). As shown in Table 3, the fast reactions agree with the previous measurements within 5%; however, the two thermal reactions indicate about 10% more thermal flux in the present irradiation. This difference is most likely due to small changes in the fuel or reactor operating conditions.

TABLE 3

ACTIVATION RATES FOR OMEGA WEST - HEOLI

(Irradiation from 1-22-81 to 2-10-81)
(Exposure = 849.36 MWH; Average Power (live) = 8.0 MW)

Reaction	$\sigma\phi$ (atom/atom-s) Position 6	Position 10	Spectral Run[a]	Ratio
$^{59}Co(n,\gamma)^{60}Co$	2.43-9	2.43-9	2.15-9	1.130
$^{58}Fe(n,\gamma)^{59}Fe$	6.88- 11	6.75-11	6.29-11	1.083
$^{54}Fe(n,p)^{54}Mn$	2.91-12	2.91-12	3.07- 12	0.948
$^{58}Ni(n,p)^{58}Co$	3.73-12	3.73-12	3.78-12	0.987
$^{46}Ti(n,p)^{46}Sc$	3.94-13	3.94-13	3.99-13	0.987
$^{55}Mn(n,2n)^{54}Mn$	9.01-15	9.06-15	8.66-15	1.043
$^{54}Fe(n,\alpha)^{51}Cr$	3.00-14	-	2.89-14	1.038

[a] L. R. Greenwood, DOE/ER-0046/4, Volume 1, p. 15 (1981).

The flux spectrum, shown in Figure 3, was determined using the STAYSL computer code and the seven reaction rates in Table 3. The input spectrum was taken from our previous spectral measurement. The integral fluxes and fluence values are listed in Table 4. Damage parameters were then computed using the SPECTER computer code with our recently calculated, ENDF/B-V displacement cross sections and recommended values are listed in Table 5. The (n,γ) reaction is also included in the damage calculations; however, this effect is generally less than 2%.

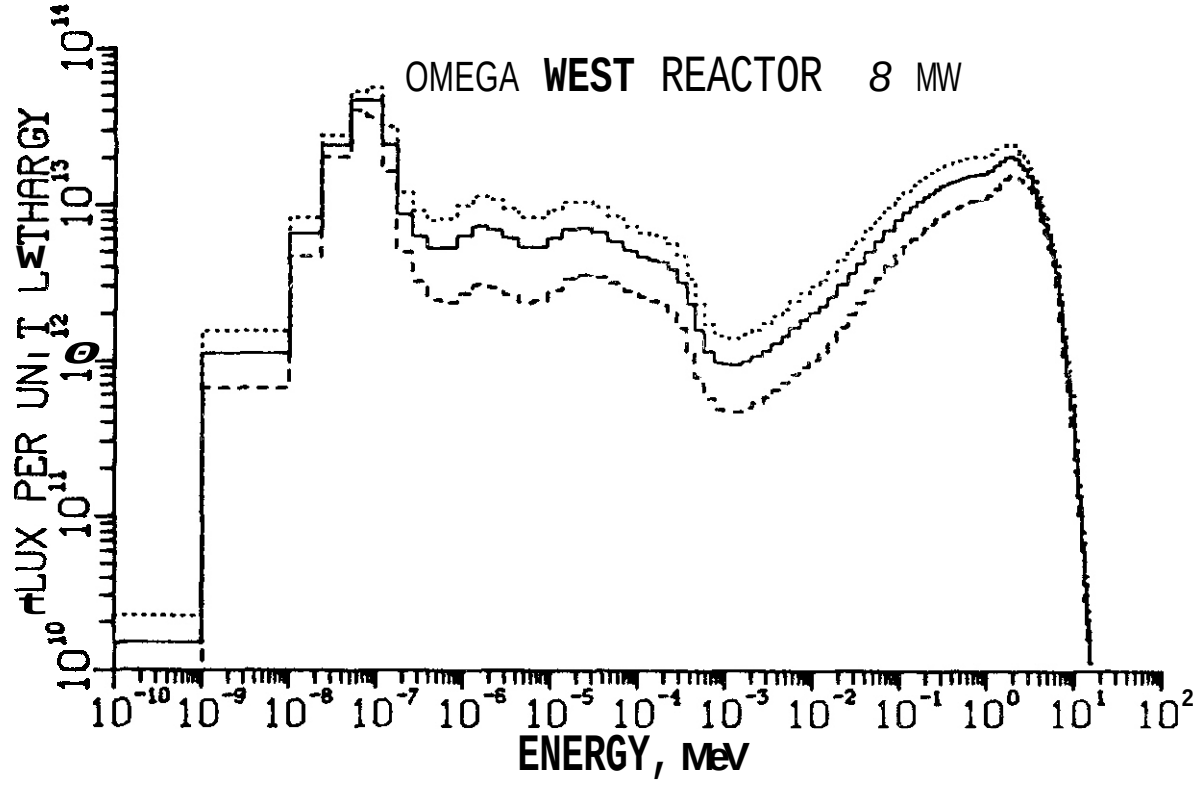

FIGURE 3. Neutron Flux Spectrum Computed Using the STAYSL Computer Code for the HEDL1 Experiment in Position 4-F of the Omega West Reactor. Seven Reactions Were Used to Adjust a Previously Measured Spectrum. The Dotted and Dashed Lines Represent One Standard Deviation. The Flux Per Unit Lethargy is Simply Energy Times Flux.

TABLE 4

FLUX AND FLUENCE VALUES FOR OMEGA WEST - HEDL1

(Fluxes normalized to 8.0 MW)

Energy Range, MeV	Flux ($\times 10^{13}$)	Fluence ($\times 10^{19}$)	Error, %
Total	19.03	7.27	10
Thermal	8.06	3.08	15
>0.11	5.74	2.19	15
>1.0	2.82	1.08	16
>5.0	0.20	0.076	14
>10.0	0.0047	0.0018	21

Helium calculations for nickel were performed using the total thermal flux (<.5 eV) and the equation recommended by T. Gabriel (ORNL/TM-6361, 1979). This procedure was found to work quite well in previous tests in ORR. It is important to note that for very short irradiations, this equation requires more exact parameters. More accurate values can actually be obtained at low fluence using the first order expansion:

$$He/M(^{58}Ni) = 1/2(\phi t)^2 \, \sigma_\gamma \sigma_\alpha$$

where ϕt is the thermal fluence, $\sigma_\gamma \sigma_\alpha$ the (n,γ) and (n,α) cross sections for ^{58}Ni and ^{59}Ni, respectively. Some helium measurements are now in progress for the OWR by D. Kneff and H. Farrar IV (Rockwell International) and more precise helium values will thus be reported later.

5.3 Analysis of the ORR-MFE4A Experiment

Dosimetry samples have been analyzed from the MFE4A irradiation in ORR. The experiment started on June 12, 1980 and ended on January 20, 1981 with a total exposure of 5471 MWD. Fe, Ni, Ti, and Co-V wires measuring about 6" in length were irradiated near the center of the assembly. Six reactions were measured

TABLE 5

SPECTRAL-AVERAGED DAMAGE PARAMETERS FOR OMEGA WEST - HEOLI

[Fluence = 7.3 x 10^{19} (2.2 x 10^{19} above 0.11 MeV)]
(Damage cross sections calculated using ENDF/B-V.)

Element	σ_D, keV-b	Damage Energy (eV/atom)	DPA	He (appb)
Al	26.0	1.9	0.028	9.5
Ti	22.7	1.6	0.016	8.5
V	25.8	1.8	0.019	0.31
Cr	23.3	1.7	0.017	2.5
Mn	23.9	1.7	0.017	1.9
Fe	20.8	1.5	0.015	4.1
co	20.9	1.5	0.015	2.0
Ni	21.7	1.6	0.016	66.0 (83.3)[a]
Cu	20.0	1.5	0.015	3.5
Zr	22.3	1.6	0.016	0.38
Nb	20.5	1.5	0.015	0.83
Mo	22.2	1.6	0.011	-[b]
316SS[c]	21.4	1.6	0.016	9.9 (11.6)[a]

[a] Thermal process included in parentheses.

[b] Helium cross section not known.

[c] Composition assumed to be Mn(2), Cr(16), Ni(10), Mo(2), Fe(70); minor elements neglected.

at five different locations along the length of the wire. The (n,p) reactions were gamma-counted from ^{54}Fe, ^{46}Ti, ^{58}Ni, and ^{60}Ni; however, the two nickel reactions cannot be used since about half of the ^{58}Co is converted to ^{60}Co in the high thermal flux. The thermal flux was determined by counting the (n,γ) reaction products from ^{58}Fe and ^{59}Co.

Fast gradients were found to vary by less than 5% along the length of the wires (6"). However, the thermal gradients were larger and showed a 10% change. The measured reaction rates near the center of the wire (about maximum flux) are listed in Table 6 and compared to those measured previously curing the ORR-MFE2 experiment. As can be seen, the $^{59}Co(n,\gamma)$ reaction is about 15% higher than the $^{58}Fe(n,\gamma)$ results, when compared to previous measurements. In fact, both thermal reactions usually agree in ORR and depend primarily only on the thermal flux. This difference may be due to an uncertainty in the cobalt concentration in the Co-V alloy (supplied by ORNL). Checks are now in progress to compare this alloy with a Co-A1 alloy (NBS standard) during a simultaneous neutron activation analysis.

Fluence values were obtained using the STAYSL computer code, the four reaction rates in Table 6, and a neutronics calculation by T. A. Gabriel (ORNL). The fluxes listed in Table 7 are normalized to a 30 MW power level. The fluxes are about 30% lower than the neutronics calculations. The reason for this difference is not known and is under investigation. The thermal flux values are also uncertain since the neutron temperature distribution is not correct. An ambient (20°C) distribution was assumed to agree with the neutronics calculations. Raising the temperature to the correct value (600°C) would raise the thermal flux considerably. However, this would not change average thermal reaction rates (e.g., helium production from nickel) since most thermal cross sections have the same 1/V energy dependence. Hence, care must be taken to use thermal fluxes properly at elevated temperatures. We are now attempting to obtain the proper temperature and will revise our thermal fluxes accordingly.

Preliminary estimates can be made for displacement damage and helium production. Using our recently revised (ENDF/B-V) cross sections, we estimate DPA values of 2.6(Ni), 2.4(Fe), and 2.5(316 SS). Helium rates are estimated to be 122 appm(Ni), 0.63 appm(Fe), and 12.7 appm(316 SS). The nickel values for helium assume a thermal fluence of 2.7 x 10^{21} n/cm^2 and the equations in ORNL/TM-6361 (1979). This procedure worked well for the MFEl experiment and agreed with helium measurements by Rockwell International. Some nickel samples from

TABLE 6

DOSIMETRY RESULTS FOR THE ORR-MFE4A EXPERIMENT

(Results normalized to 30 MW; accuracy ±2%)

Reaction	$\sigma\phi$(atom/atom-s)	Ratio to MFE2
$^{54}Fe(n,p)^{54}Mn$	1.02×10^{-11}	1.025
$^{46}Ti(n,p)^{46}Sc$	1.40×10^{-12}	1.022
$^{58}Fe(n,\gamma)^{59}Fe$	1.79×10^{-10}	1.053
$^{59}Co(n,\gamma)^{60}Co$[a]	7.17×10^{-9}	1.203[a]

[a] Burnup correction of 6% included; concentration of cobalt in Co-V alloy may be uncertain.

TABLE 7

FLUX AND FLUENCE VALUES FOR ORR-MFE4A

(5471 MWD, 222 days, normalized to 30 MW)

Reaction	Flux (30 MW) ($\times 10^{14}$ n/cm^2-s) ANL	ORNL[a]	Ratio	Fluence ($\times 10^{21}$ n/cm^2)	Error (%)
Total	(5.39)	7.85	(0.69)	(8.45)	10
Thermal[b] (<.5 eV)	(1.72)	2.51	(0.69)	(2.70)	15
0.5 eV-0.11 MeV	1.88	2.73	0.69	2.95	22
>0.11 MeV	1.79	2.61	0.69	2.81	15
>1 MeV	0.96	1.39	0.69	1.50	14
>2 MeV	0.51	0.75	0.68	0.80	12
>5 MeV	0.072	0.107	0.67	0.11	15

[a] T. G. Gabriel (ORNL).

[b] Thermal temperature distribution not correct (ambient assumed)

the present experiments are now being analyzed by D. Kneff and H. Farrar IV, so precise helium data, will be available for the MFE4A experiment.

6.0 References

None.

7.0 Future Work

Further measurements are planned to resolve the outstanding questions concerning the MFE4A experiment. Helium measurements are in progress at Rockwell International for both irradiations in ORR and the results will be integrated with the radiometric data to improve our knowledge of helium production for these experiments. More complete dosimetry sets are still being irradiated with the MFE4 samples. Hence, more precise fluence and damage measurements will be available for the final irradiated samples.

The samples from the **EBRII-X287** irradiation have been counted and analysis is in progress. Samples have been received from the HFIR-CTR32 experiment and they are now being gamma counted.

8.0 Publications

A paper entitled "Neutron Source Characterization for Fusion Materials Studies" has been submitted for the Second Topical Meeting on Fusion Reactor Materials, Seattle, August, 1981.

HELIUM GENERATION CROSS SECTIONS FOR FAST NEUTRONS

D. W. Kneff, B. M. Oliver, M. M. Nakata, and Harry Farrar IV (Rockwell International, Energy Systems Group)

1.0 Objective

The objectives of this work are to measure helium generation rates of materials for Magnetic Fusion Reactor applications in the various neutron environments used for fusion reactor materials testing, to characterize these neutron test environments, and to develop helium accumulation neutron dosimeters for neutron fluence and energy spectrum dosimetry in these test environments.

2.0 Summary

An initial three-dimensional neutron fluence map has been constructed for the high-flux region of the Rotating Target Neutron Source-I1 (RTNS-II) neutron field for the joint Rockwell International-Argonne National Laboratory (ANL)-Lawrence Livermore National Laboratory (LLNL) source characterization experiment. This map is based on the radiometric dosimetry foils from the irradiation capsule, and will next be correlated with the helium accumulation neutron dosimetry to produce a final map. Helium analyses are nearing completion for the RTNS-11-irradiated separated isotopes of Fe, Ni, and Cu.

3.0 Program

Title: Helium Generation in Fusion Reactor Materials
Principal Investigators: D. W. Kneff and Harry Farrar IV
Affiliation: Rockwell International, Energy Systems Group

4.0 Relevant DAFS Program Plan Task/Subtask

Subtask II.A.2.2 Flux-Spectral Definition in RTNS-II
Subtask **II.A.4.2** T(d,n) Helium Gas Production Data

5.0 Accomplishments and Status

An initial three-dimensional neutron fluence map has been constructed for the irradiation volume of the miniature sample assembly irradiated at RTNS-II for source characterization and helium generation cross section measurements. Details of the experiment, a joint irradiation with ANL and LLNL, have been described in a previous report.[1] This initial map is based on the ANL and LLNL counting results from the segmented radiometric foils irradiated in the sample assembly. A final neutron fluence map will be constructed from this map when it is correlated with the fluence gradient information from the more finely segmented helium accumulation dosimetry rings. The helium analyses for these ring segments were completed last quarter.

The radiometric map indicates a decrease in the axial neutron fluence (along the RTNS-II beam axis) of about a factor of 3 in the front 4 mm of the irradiation capsule, a gradient similar to that found for RTNS-I.[2] The axial fluence drop through the 8.5-mm thickness of the capsule was about a factor of 6. Both the RTNS-II and RTNS-I irradiation capsules were mounted as close as possible to the RTNS targets, with the RTNS-II capsule 0.8 mm (30 mils) from the front face of the rotating target assembly. The radial neutron fluence variation across the 16-mm-diameter radiometric foils was about a factor of 2 at the capsule front face and about a factor of 1.3 at the capsule back face. The capsule was offset from the neutron source axis by about 1.1 mm.

The helium analyses are nearing completion for the RTNS-11-irradiated separated isotopes of Fe, Ni, and Cu. These results, plus those recently completed for molybdenum and its separated isotopes, will be combined with the final RTNS-II fluence map to deduce 14.8-MeV T(d,n) total helium generation cross sections. The cross sections will be reported at the Second Topical Meeting on Fusion Reactor Materials in Seattle in August.

6.0 References

1. D. W. Kneff, B. M. Oliver, M. M. Nakata, and H. Farrar IV, "Characterization of the RTNS-II Neutron Field," in Damage Analysis and Fundamental Studies, Quarterly Progress Report July-September 1980, DOE/ER-0046/3, U.S. Department of Energy (1980).

2. D. W. Kneff. B. M. Oliver. M. M. Nakata. and H. Farrar IV, "Helium Generation Cross Sections-for Fast Neutrons," in Proc. Symp. on Neutron Cross-Sections from 10 to 50 MeV, M. R. Bhat and S. Pearlstein (Eds), BNL-NCS-51245, Brookhaven National Laboratory, N.Y. (1980), p. 289.

7.0 Future Work

The helium analyses of selected pure elements and separated isotopes irradiated in the RTNS-I, RTNS-II, and Be(d,n) neutron spectra will continue. The analyses of the RTNS-II- and Be(d,n)-irradiated separated isotopes of Fe, Ni, and Cu will be completed during the next quarter. The RTNS-II fluence mapping of the sample capsule irradiation volume will also be completed during this period.

8.0 Publications

None.

CALCULATION OF DAMAGE PARAMETERS (AKJ)

F. M. Mann (Hanford Engineering Development Laboratory)

1.0 Objectives

The objective of this work is to apply nuclear data to radiation damage studies.

2.0 Summary

The damage energy cross sections processed (E < 20 *MeV*) from ENDF/B-V *by* the DISCS and NJOY codes were found to have only slight differences.

CSEWG has established a charged particle format for ENDF/B which will also be used for neutron evaluations above 20 MeV.

Helium production cross sections from ENDF/B-V were processed.

3.0 Program

Title: Irradiation Effects Analysis (AKJ)
Principal Investigator: D.G. Doran
Affiliation: Hanford Engineering Development Laboratory

4.0 Relevant DAFS Program Plan Task/Subtask

II.B.1 Calculation of Defect Production Cross Sections

5.0 Accomplishments and Status

5.1 Introduction

Because so many different neutron environments are being used in the fusion

program to determine different material property changes, parameters such as fluence or even fluence above 0.1 MeV are not sufficient to characterize neutron exposure. Rather, the number of displacements per atom is increasingly being used as the relevant exposure parameter.

5.2 Code Comparison

Greenwood (ANL) has calculated damage energy cross sections from ENDF/B-V (see report this issue) using the code DISCS[1]. MacFarlane (LANL) has modified the NJOY code[2] to also calculate damage energy cross sections. The latest version of NJOY was run at HEDL using the same group structure and weighting function as those used by Greenwood for Fe.

The multigroup values were usually within 3% of each other. At low neutron energies (<20eV) where only capture is important, the codes produce different results (within ∿ 15%) because of different treatments of photon recoil. The values of DISCS lie between the available values calculated by the two different treatments in NJOY. As NJOY presently uses a material independent recoil threshold of 25eV, the values of the two codes differ near the accepted Fe threshold energy of 40eV used in the DISCS calculations. Isolated discrepancies remain in the resonance region and will be investigated. The simpler treatment of charged particle emission by NJOY does not produce significantly different results than DISCS.

5.3 Damage Cross Sections at High Energies

The Cross Section Evaluation Working Group (CSEWG) has approved a format for charged particle-induced cross sections. This format will also be used for neutron-induced evaluations above 20 MeV. Because recoil energies are included in the new format, damage energy cross sections can be more accurately calculated. Other improvements will provide a more complete description of the basic nuclear cross sections. The conversion of NJOY to handle this new format is continuing. First, however, the code is being modified to handle

the LANL Fe evaluation[3], which is not in the new format.

5.4 Gas Production Cross Sections

Hydrogen and helium production have been calculated for the materials shown in Table 1, in 55 groups using the ENDF/B-V General Purpose File[4]. These calculations support the HEDL studies of the correlation of material property changes with damage parameters.

Table 1

ENDF/B-V MATERIALS PROCESSED FOR GAS PRODUCTION

Material	Mat #	Evaluator (Lab)	Ref.
B-10	1305	G.Hale, L.Stewart, P.Young (LANL)	4
B-11	1160	C. Cowan (GE-BNL)	5
C	1306	C.Y.Fu, F.G.Perey (ORNL)	6
N-14	1275	P.Young, D.Foster Jr., G.Hale (LANL)	4
O-16	1276	P.Young, D.Foster Jr., G.Hale (LANL)	4
Mg	1312	D.C.Larson (ORNL)	5
Al	1313	P.G.Young, D.G.Foster Jr. (LANL)	4
Si	1314	Larson, Perey (ORNL), Drake (SAI), Young (LANL)	5
P	1315	R.Howerton (LLNL)	5
S	1316	M. Divadeenam (BNL)	5
Ti	1322	C.Phillis (BUR), A.Smith (ANL), R.Howerton (LLNL)	7
V	1323	A.Smith et al (ANL), R.Howerton (LLNL) F.M.Mann (HEDL)	8
Cr	1324	A.Prince and T.W.Burrows (BNL)	9
Fe	1326	C.Y.Fu, F.G.Perey (ORNL)	10
co	1327	S.F.Mughabghab (BNL)	5
Ni	1328	M.Divadeenam (BNL)	11
cu	1329	C.Y.Fu (ORNL), Drake, Fricke (SAI)	5

6.0 References

1. G.R.Odette and D.R.Doiron, "Neutron-Energy-Dependent Defect Production Cross Sections for Fission and Fusion Applications," Nuclear Technology 29 (1976) 346.

2. R.E.MacFarlane, R.J.Barrett, D.W.Muir, and R.M.Boicourt, "The NJOY Nuclear Data Processing System: User's Manual" LA-7584-M (ENDF-272), Los Alamos National Laboratory, 1978.

3. E.D.Arthur and P.G.Young, "Evaluated Neutron-induced Cross Section for $^{54,56}Fe$ to 40 MeV," LA-8626-MS (ENDF-304), Los Alamos National Laboratory, 1980.

4. R. Kinsey (compiler), "ENDF-201, ENDFB Sunnnary Documentation," BNL-NCS-17541 (ENDF-201), 3rd edition (ENDF/B-V), Brookhaven National Laboratory, 1979.

5. P.G.Young (compiler), "Summary Documentation of LASL Nuclear Data Evaluations for ENDF/B-V," LA-7663-MS, Los Alamos National Laboratory, 1979.

6. C.Y.Fu and F.G.Perey, "Neutron Scattering Cross Sections of Carbon below 2 MeV Recommended from R-Matrix Fits to Data," Atomic Data and Nuclear Data Tables 22 (1978) 249.

7. C.Phillis, R.Howerton, and A.B.Smith, "Titanium II: An €valuated Nuclear Data File," ANL/NDM-28, Argonne National Laboratory 1977.

8. P.Guenther, D.Havel, R.Howerton, F.Mann, D.Smith, A.Smith and J.Whalen, "Fast Neutron Cross Sections of Vanadium and an Evaluated Neutronic File," ANL/NDM-24, Argonne National Laboratory, 1977.

9. A.Prince and T.W.Burrows, "Evaluation of Natural Chromium Neutron Cross Sections for ENDF/B-V," BNL-NCS-51152 (ENDF-286) Brookhaven National Laboratory, 1979.

10 C.Y.Fu and F.G.Perey, "Evaluation of Neutron and Gamma Production for Natural Iron (ENDF/B-V Mat 1326)," Oak Ridge National Laboratory.

11. M.Divadeenam, "Nickel Elemental Neutron-induced Reaction Cross Section Evaluations," BNL-NCS-51346 (ENDF-294), Brookhaven National Laboratory, 1981.

SOLID AND GAS TRANSMUTATION PRODUCTION CODE DEVELOPMENT (AKJ)

F.M.Mann (Hanford Engineering Development Laboratory)

1.0 Objective

The objective of this work is to develop and maintain a computer code system to calculate the amounts of solid and gas transmutants at various facilities used by OFE experimentalists.

2.0 Summary

The computer code REAC with its associated libraries has been developed and successfully used.

3.0 Program

Title: Irradiation Effects Analysis (AKJ)
Principal Investigator: D.G.Doran
Affiliation: Hanford Engineering Development Laboratory

4.0 Relevant DAFS Program Plan Task/Subtask

II.A.4.5 Gas Generation Rates
II.C.4.1 Effects of Solid Transmutation Products on Microstructure

5.0 Accomplishments and Status

5.1 Introduction

When materials are placed in neutron environments, not only are atoms displaced from their sites, but transmutants are also produced. A code system called REAC has been developed to calculate transmutation for the various facilities that OFE uses.

5.2 Code Description

The code reads data from four libraries (flux, cross section, material, and decay data), collapses the appropriate multigroup flux and cross sections to generate reaction rates, calculates the transmutations caused by reactions and by decays, and finally sorts and prints the results.

5.3 Library Description

The flux library contains multigroup spectra for HFIR, ORR, ETR, EBR-II, FFTF, UWMAK-I, RTNS-2, and FMIT. The cross section library contains multigroup values from 10^{-5} eV to 50 MeV for all important reactions on C, N, Al, Si, P, Cr, Mn, Fe, Co, and Ni. Multigroup cross sections are based on ENDF/B-V[1] whenever possible with other sources used to fill in gaps. The material library has the compositions of 3 heats of 316 stainless steel, 304 steel, 600 steel, 625 steel, aluminum 6061 alloy, as well as other materials. The decay library which has 625 sets of decay data is based on ENDF/B-V[1] and the 1978 Table of Isotopes.[2]

5.4 Typical Results

Figure 1 shows the predicted transmutation of CN-13 lot of 316 stainless steel when irradiated in the highest flux region of FMIT. For a fluence of 1.0 x 10^{23} n/cm^2, Fe, Cr, and Si change by less than 5%, while V, Mn, and Co show significant increases. H and He are, of course, produced in large amounts.

Further results are discussed in the report "The Effects of Transmutation Products on Swelling in 316 Stainless Steel" by J. F. Bates, F. A. Garner, and F. M. Mann elsewhere in this issue.

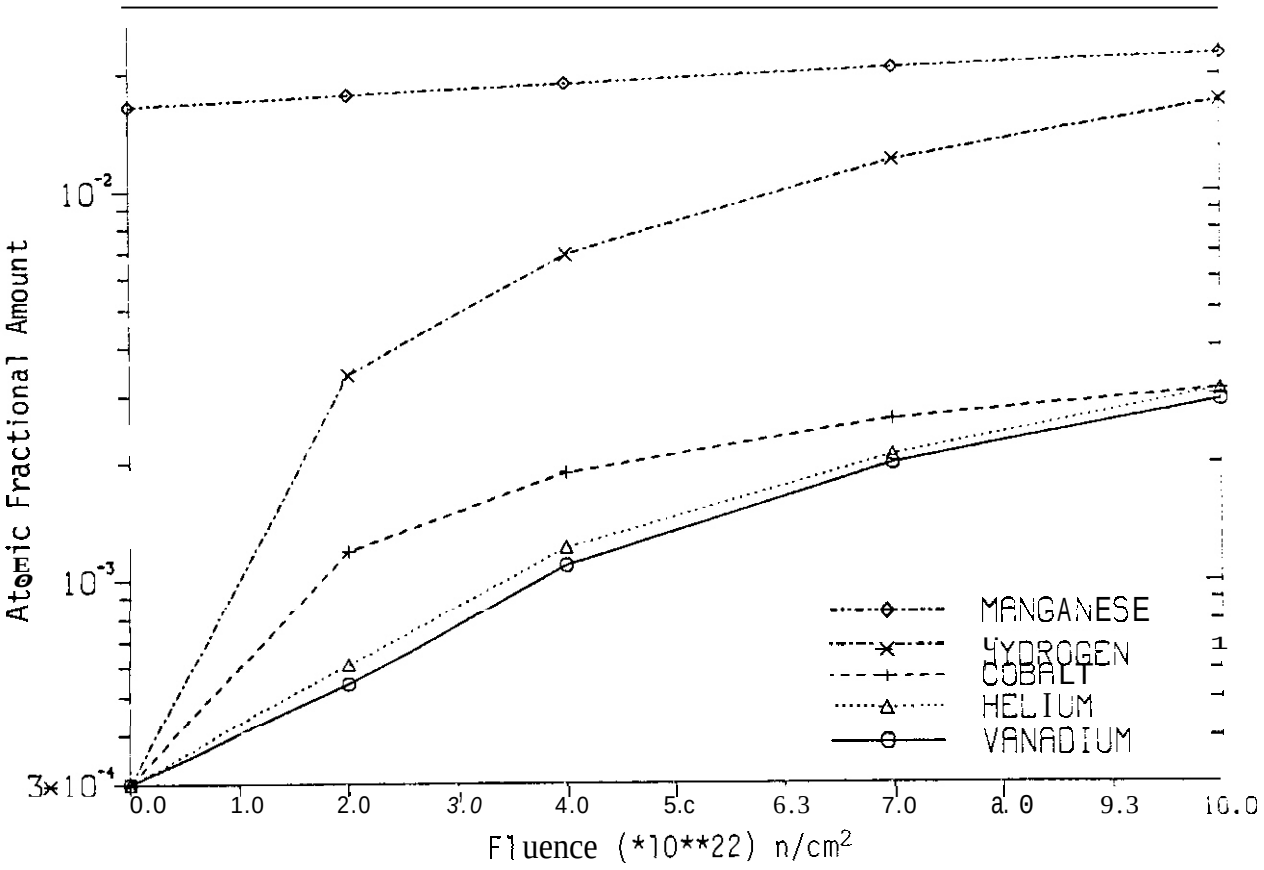

FIGURE 1. Transmutation of 316SS in FMIT (10 x 10^{22} corresponds to 7.200 dpa).

6.0 References

1. R. Kinsey (compiler), "ENDF-201, ENDF/B Summary Documentation," BNL-NCS-17541, 3rd edition (ENDF/B-V). Brookhaven National Laboratory, 1979.

2. C. M. Lederer and V. S. Shirley (editors), Table of Isotopes, 7th edition, John Wiley and Sons, New York, 1978.

7.0 Future Work

The cross section library will be expanded with initial work planned for Ti, V, and Mo. The code will be modified to include multi-step reactions.

COMPUTER SIMULATION OF HIGH ENERGY RECOILS IN fcc METALS: CASCADE SHAPES AND SIZES - H. L. Heinisch and J. D. Valett (Hanford Engineering Development Laboratory)

1.0 abjective

The objective of this work is to develop computer models for the simulation of high energy cascades which will be used to generate defect production functions for correlation analysis of radiation effects.

2.0 Summary

Displacement cascades in copper generated by primary knock-on atoms with energies from 1 keV to 500 keV were produced with the computer code MARLOWE. The sizes and other features of the point defect distributions were measured as a function of energy. In the energy range from 30 keV to 50 keV there is a transition from compact single damage regions to chains of generally closely spaced, but distinct multiple damage regions. The average spacing between multiple damage regions remains constant with energy. Only a small fraction of the recoils from fusion neutrons is expected to produce widely separated subcascades.

3.0 Program

Title: Irradiation Effects Analysis (AKJ)
Principal Investigator: D. G. Doran
Affiliation: Hanford Engineering Development Laboratory

4.0 Relevant DAFS Program Plan Task/Subtask

Subtask II.B.2.3 Cascade Production Methodology

5.0 Accomplishments and Status

5.1 Introduction

A knowledge of the initial damage state produced in metals by the various neutron spectra of fusion materials test facilities is an essential element for the development of correlation models. Computer simulations of the production of displacement damage by primary knock-on atoms (PKAs) provide detailed information on an atomistic scale not presently attainable by experimental methods. The work reported on here is a simulation of the displacement damage from the high energy PKAs (up to 500 keV in this study) which result from irradiation by fusion neutrons. The major emphasis of this report is on the description of the spatial distribution of the defects in these displacement cascades. The sizes and shapes of cascades will be examined as a function of energy. The tendency to produce subcascades, i.e., multiple, widely separated regions of damage from the same PKA, is also discussed.

5.2 Computations

Five hundred fifty cascades ranging in energy from 1 keV to 500 keV were generated in copper using the computer code MPRLOWE.[1] The binary collision approximation employed in the MARLOWE model should be a good approximation for the high energy collisions, which determine the gross features of high energy cascades. The binary collision approximation, as used in MARLOWE, is apparently a reasonable approximation for fairly low energy collisions as well. The MARLOWE parameter settings used in this work were those which have produced good agreement with many-body simulations of low energy events[2] (20-500 eV).

To achieve the appropriate lengths for focused collision sequences in low energy events, it is necessary to allow for collisions to occur in MARLOWE involving atoms which have as little as 5 eV of kinetic energy. Collisions for atoms with less energy are not followed.

At this low setting of the minimum energy for collisions, the number of atoms displaced from their perfect lattice sites becomes extremely large for cascades with energies of hundreds of keV. In order to handle cascades above 100 keV it was necessary to use a higher minimum energy for allowable collisions, namely 17 eV, which is about the minimum displacement threshold. It was found that the features of the defect distribution reported on here are independent of the values used for this minimum energy parameter.

To simulate the recombination which occurs as the highly energetic cascade region "quenches", i.e., comes to thermal equilibrium with the surrounding material, the closest point defect pairs are recombined until the remaining number of pairs is equal to a value extracted from resistivity measurements on copper irradiated at ~4K.[3]

The dimensions of the quenched (recombined) cascades were determined for the distributions of vacancies only. The maximum dimension of the vacancy distribution was determined, as well as the dimensions along and transverse to the original PKA direction. Information on other cascade features such as their shapes and the formation of subcascades was determined from three-dimensional graphic representations and two-dimensional defect density maps.

5.3 Results

It was reported previously for MPRLOWE cascades in copper[4] that the number of defect pairs remaining after quenching recombination was in good agreement with values extracted from resistivity measurements for PKA energies up to 100 keV, using a recombination volume which is independent of energy. It was also reported that simulated short-term annealing of isolated cascades was found consistent with Stage I resistivity recovery measurements. The higher energy cascades generated for the present work were similarly recombined and annealed. The results show the same consistency with experimental measurements as reported for the lower energy cascades. Thus, these simple models of cascade quenching and annealing have now been successfully applied to cascades of up to 500 keV.

Cascade modeling studies with MAQLOWE have also been performed recently for Cu_3Au.[5] The sizes of MPRLOWE defect distributions for Cu PKAs in ordered Cu_3Au compare favorably with the sizes of disordered regions measured from electron micrographs of ordered Cu_3Au irradiated with Cu^+ ions. (Agreement is obtained at energies above 50 keV only if the small foil thicknesses necessary for this type of microscopy is taken into account.) Thus, MPRLOWE cascades in copper have been compared favorably with several experimental measurements.

In general, the high energy cascades appear to be made up of collections of lower energy cascades, sometimes contiguous, sometimes widely separated. They could be described as chains made of different size links, each link oriented in a different direction. Figures la-b illustrate some defect distributions resulting from 200-keV cascades. Figure la compares a 200-keV cascade with a 20-keV cascade. The wide separation between major damage areas in the 200-keV cascade is not a rare event, but not typical of all 200-keV cascades. Figure lb illustrates a 200 keV cascade which has damage regions somewhat more typical, except that they appear to emanate from a central point in starlike fashion rather than the more usual chain configuration.

Because of their irregularity, it is difficult to describe the true lengths or volumes of the high energy cascades in quantitative terms. However attempts were made to obtain quantitative characterization of the cascades. The maximum extent of each cascade, R_{max}, which was taken as the distance between the two most widely separated vacancies, was determined. The maximum extent parallel to the PKA direction, ΔZ, and the corresponding transverse dimensions, ΔX and ΔY, were also determined. Figure 2 shows the average values of R_{max} as a function of PKA energy, E. The line is a best fit to the points and is described by the function $R_{max} = 3.25\ E'^{.78}$, with R_{max} in lattice parameters and E in keV.

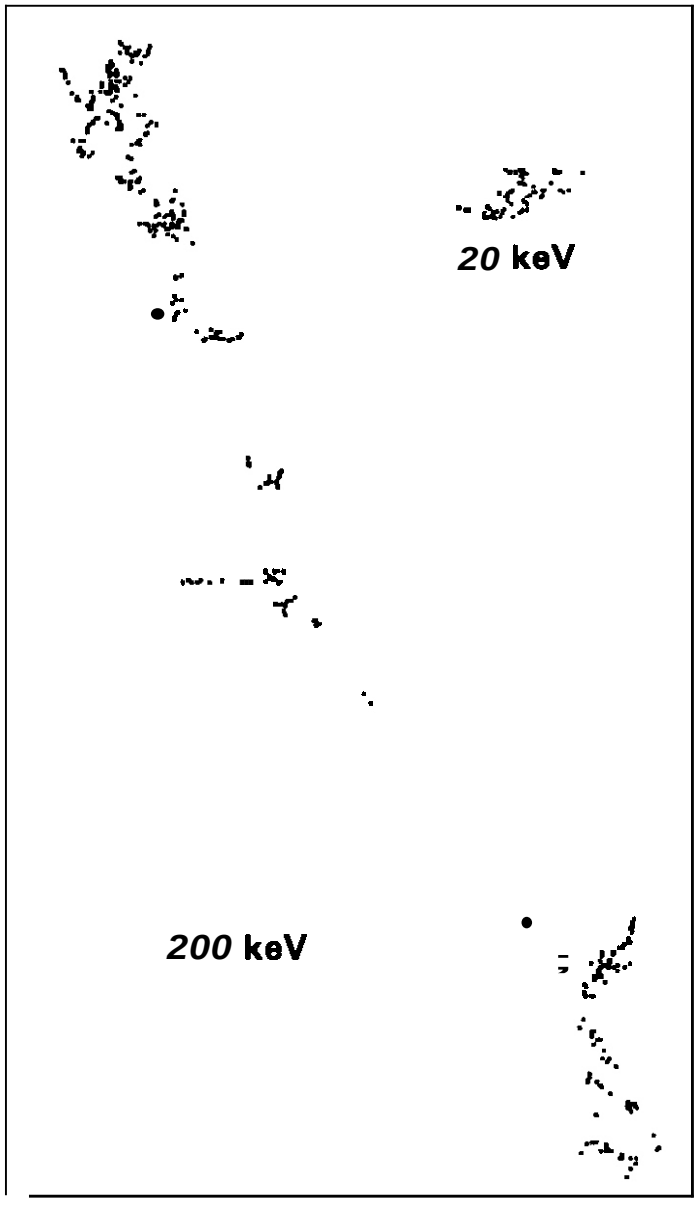

FIGURE 1a. A comparison of 200-keV and 20-keV cascades, vacancies only, after recombination. The 200-keV PKA began at the lower right in a direction approximately along which the vacancies now lie. The length of this cascade is 278 lattice parameters (100 nm).

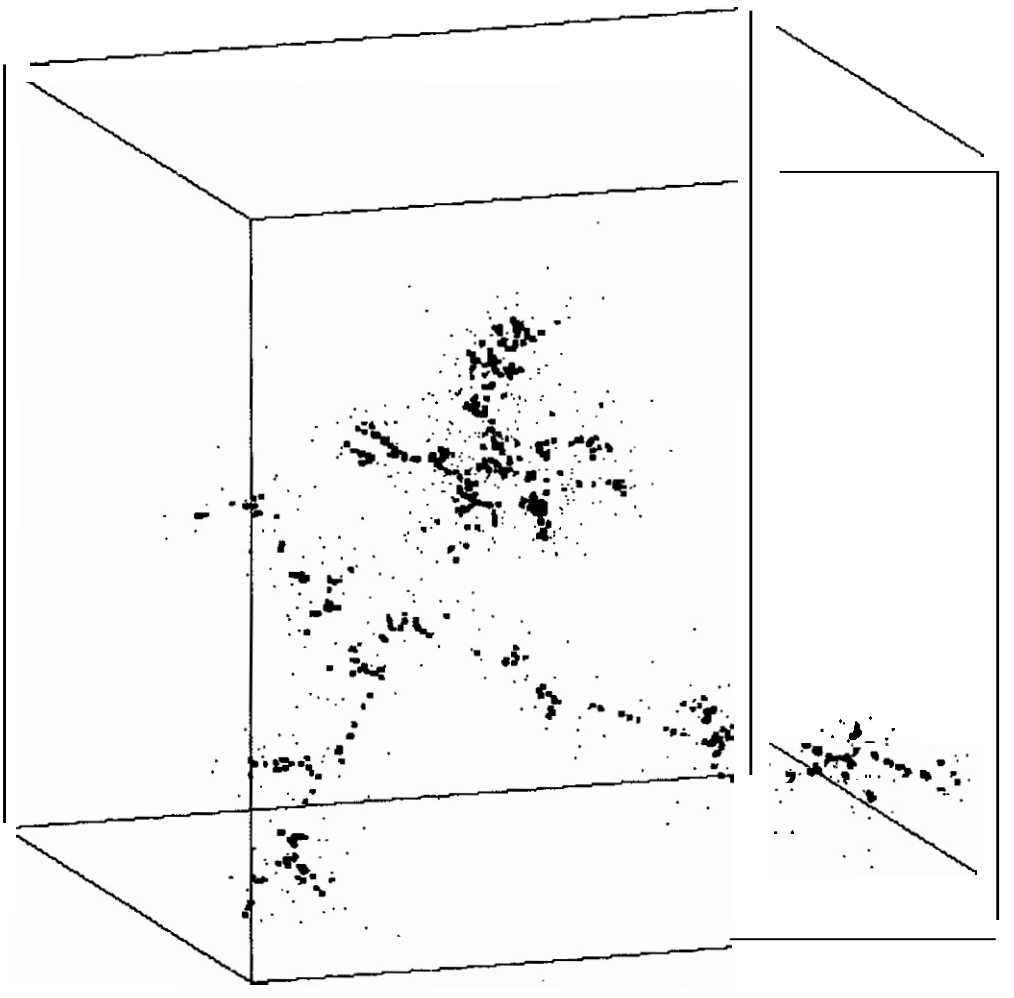

FIGURE 1b. A 200-keV cascade, with both vacancies (small boxes) and interstitials (dots), after recombination. The PKA began at the lower left. The cube side is 125 lattice parameters (45 nm).

Density maps of the defect distribution were plotted in two or three orthogonal views, and they were analyzed to obtain the average number and separations of the distinct segments of which the cascades are composed. In order to have the greatest possible densities of defects to define the cascade segments, the density maps included both vacancies and interstitials with no quenching recombination. A typical density map is shown in Figure 3.

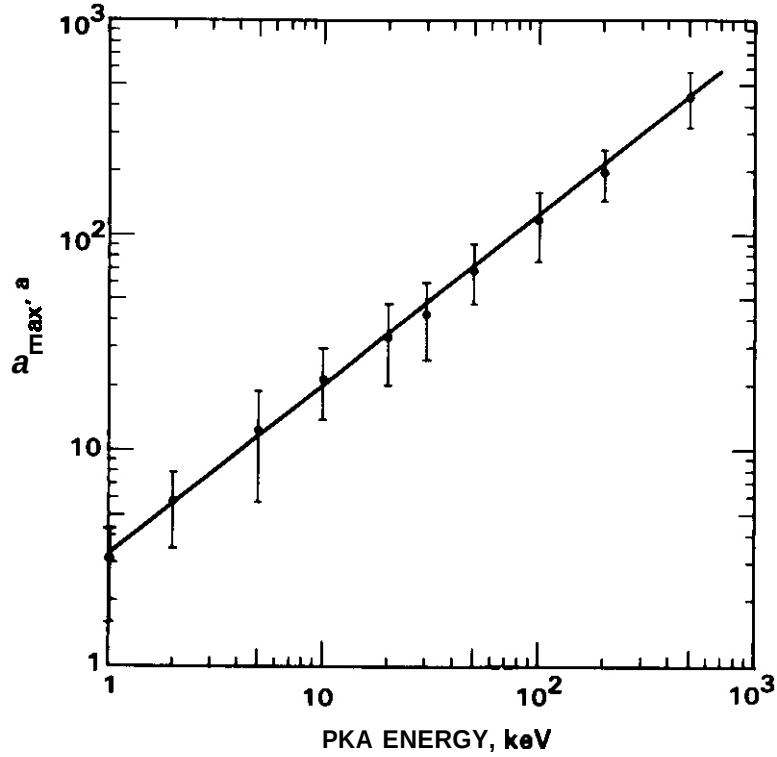

Figure 2. The average maximum extent in lattice parameters of simulated cascades in copper as a function of PKA energy, measured on the vacancy distribution only, after recombination. Error bars on all figures are one standard deviation.

Three categories of sub-regions of the cascades were identified: 1) widely-separated subcascades, for which the edge to edge separations are at least as large as the subcascade diameter, 2) close subcascades, for which the edge to edge separation is at least 6 lattice parameters (about the diameter of the average 2 keV cascade), and 3) lobes, which appear as contiguous but identifiably separate parts of the cascade. Distinct regions smaller than the average 2 to 3 keV cascade were not considered as separate lobes or subcascades. They were either associated with another lobe or ignored. Individual subcascades often have several lobes.

Figure 4 shows the average number of lobes and subcascades per cascade as a function of energy. The category "subcascade" includes both close and widely-separated subcascades. "Lobes" refers to the total number of lobes

Figure 3. Density map for part of a 200-keV cascade in copper. The PKA direction is into the page, and it began at a point about 22 lattice parameters down from the top of the picture. Each number represents the number of point defects (both vacancies and interstitials) which fall in a square of side 2 lattice parameters centered on the location of the number. Numbers greater than 9 are represented by small letters of the alphabet.

in each cascade regardless of the subcascade structure. The 20-keV cascades exhibit some lobe-like irregularities, therefore they were analyzed. However, the true multiple region cascade structure occurs at about 50 keV and above. Both lobes and subcascades per cascade increase approximately linearly with energy. The frequency of occurrence *of* widely separated subcascades is about 5% of the cascades at 50 keV, and the frequency increased linearly with energy to a level of 50% at 500 keV.

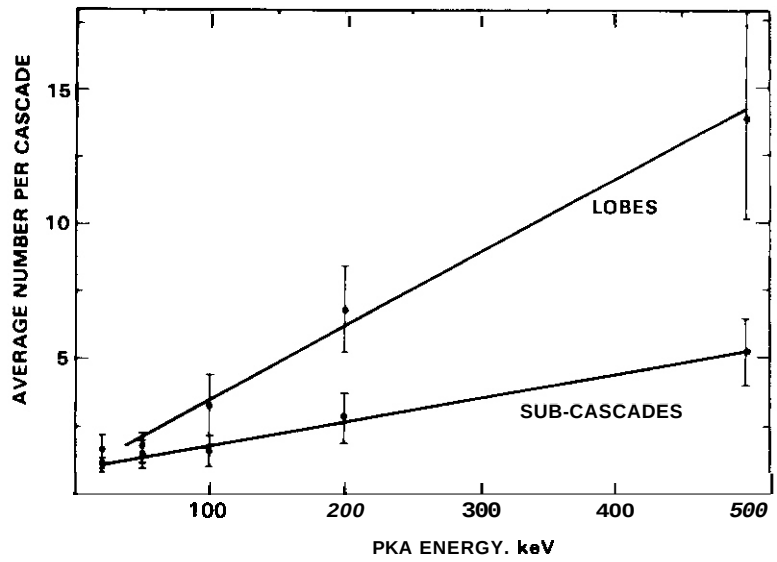

Figure 4. The number of subcascades and lobes per PKA in copper cascades as a function of PKA energy.

Figure 5 shows the average center to center separation of lobes as a function of energy. Measurements were made from lobe to lobe in the order they were produced. The average separation of lobes is constant for energies greater than 50 keV. The error bars indicate a large variation in separation lengths partly because of the smaller sample sizes of the higher energy cascades, and partly because, by the convention used in the analysis, some lobe separations include the large subcascade separations.

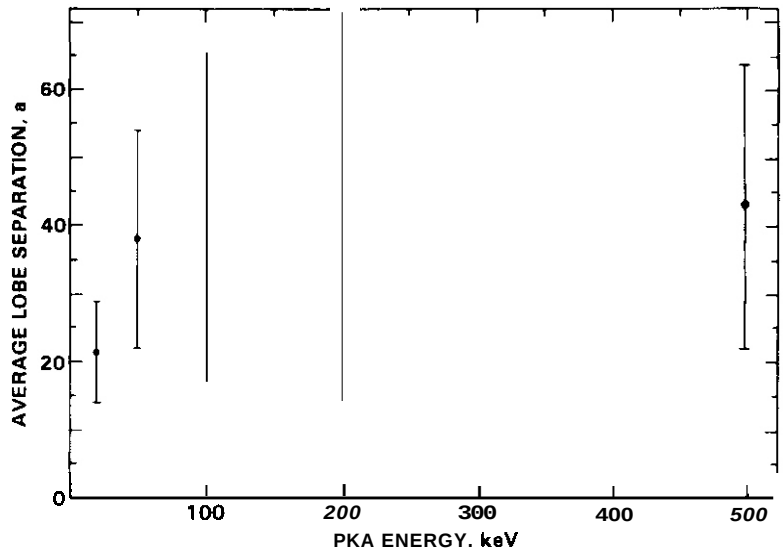

Figure 5. The average lobe separation in lattice parameters as a function of PKA energy.

5.4 Discussion

At energies greater than about 50 keV the cascade shapes become quite irregular. A quantitative determination of the shape and volume of the region of the crystal occupied by defects for each cascade can easily be done only in a rather crude way. The maximum dimensions along (ΔZ) and transverse to (ΔX and ΔY) the PKA direction were determined for each cascade.

In Table 1 this information is presented in the form of ratios. Neither the ratio of R_{max} to ΔZ nor the aspect ratio relative to the PKA direction give an indication of the drastic differences between configurations of the defects at low and high energies, as illustrated by Figure la. The dimensions AX, AY, and AZ define a rectangular parallelepiped which contains the cascade. At low energies this volume is occupied 'fairly densely by defects, whereas for the highly irregular high energy cascades a large fraction of this volume is free of defects. While this measure of cascade dimensions does not adequately reflect the change in nature of the cascade configuration with energy, it nevertheless provides an indication of the volume of

crystal under the influence of the cascade. Hence, it may be useful in estimating the amount of cascade overlap to be expected at a given fluence.

TABLE 1

AVERAGES OF R_{max}/Z AND THE ASPECT RATIO

$$\Delta Z / \left(\frac{\Delta X^2 + \Delta Y^2}{2} \right)^{1/2}$$

E (keV)	$R_{max}/\Delta Z$	Asoect Ratio
1	1.38	1.99
2	1.29	1.77
5	1.39	1.26
10	1.38	1.61
20	1.53	1.32
30	1.36	1.38
50	1.42	1.47
100	1.37	1.58
200	1.25	1.89
500	1.16	1.92

The cascade in Figure la exhibits widely separated subcascades, perhaps produced by the phenonemon of "quasi-channeling". Based on the present sample of cascades, widely spaced damage regions occur no more than 20% of the time for cascades of 200 keV or less, and only rarely below 50 keV. In only a few cases did the subcascade separation exceed 2 or 3 times the average R_{max} for cascades of that energy. Thus, for most of the PKAs produced in copper by 14-MeV neutrons, widely separated subcascades would be the exception.

Individual lobe sizes were not measured, but few lobes at any energy exceeded the dimensions of a 30 keV cascade. Thus, one might characterize the high energy cascades in copper as a series of mostly-connected 5 to 30 keV cascades separated by an average spacing (Figure 5) of ~43 lattice parameters (15.5 nm). Indeed, the average number of lobes in a cascade (Figure 4) is approximately equal to the PKA energy divided by 30 keV.

Concerning loop formation in cascades, the general configurations of these cascades, especially the segmented nature, would lead one to the conclusion that, if the vacancy distributions collapse to form loops during cascade quenching, then they should have an average size on the order of those that form from 30 keV PKAs. Also, the number of loops per cascade should increase with PKA energy. These conclusions are consistent with electron microscope observations of copper irradiated with self-ions[6] as well as with high energy neutrons from RTNS-II.[7] Interactions among defects from adjacent lobes could probably produce some larger loops, but apparently a very large loop from a single high energy cascade could be accomplished only through the diffusion of defects over distances *of* hundreds of lattice parameters.

6.0 References

1. Robinson, M. T. and Torrens, I. M., Phys Rev B, 9 (1974) p. 5008.

2. Robinson, M. T., DAFS Quarterly Progress Report, January-March 1980, DOE/ER-0046/1, U. S. Department of Energy (1980), p. 55.

3. Simons, R. L., DAFS Quarterly Progress Report, July-September 1980, DOE/ER-0046/3, U. S. Department of Energy (1980), p. 41.

4. Heinisch, H. L., Doran, D. G. and Schwartz, D. M., Effects of Radiation on Materials, ASTM Special Technical Publication 725 (1981), p. 191.

5. Heinisch, H. L. and Morford, M. P., DAFS Quarterly Progress Report, January-March 1981, DOE/ER-0046/5, U. S. Department of Energy (1980), p. 52.

6. Wilson, M. M., Phil Mag, 24 (1971) p. 1023.

7. Brager, H. R., Heinisch, H. L. and Panayotou, N. F., DAFS Quarterly Progress Report, January-March 1980, DOE/ER-0046/1, U.S. Department *of* Energy (1980), p. 76.

7.0 Future Work

Interactions of cascades during short term annealing will be investigated along with simple models of cascade quenching.

8.0 Publications

This paper will be presented at the Second Topical Meeting on Fusion Reactor Materials, Seattle, August, 1981.

THE EFFECT OF IRRADIATION ON THE ORDER/DISORDER TRANSFORMATION IN CuPd

G. L. Kulcinski, R. A. Dodd, and R. Zee (University of Wisconsin-Madison)

1.0 Objective

The objective is to study the disordering and reordering characteristics of the ordered CuPd system under 14-MeV copper and 14.8-MeV neutron irradiations using resistivity and transmission electron microscopy.

2.0 Summary

This report covers the investigation of damage structure of initially ordered CuPd under different irradiation conditions. Results of irradiation with 14-MeV copper ions show that the ordered structure disappears at temperatures below 200°C after 0.2 dpa when irradiated at a dose rate of 10^{-3} dpa/sec. Disordered zones are formed randomly throughout the entire material. Irradiation at high temperature (250 to 550°C) was not capable of disordering the same alloy system due to the high mobility of vacancies. Results of postirradiation annealing indicate that the reordering process is a classical nucleation and growth type.

Low temperature (4.1°K) 14.8-MeV neutron irradiation of ordered and disordered CuPd provides a replacement to displacement ratio of 70. Postirradiation an-anealing indicates that interstitial migration is responsible for some reordering. Vacancy migration, however, is stil1 the main mechanism for reordering.

3.0 Program

Title: Radiation Damage Studies for Fusion Reactors

Principal Investigators: G. L. Kulcinski, R. A. Dodd, (Experimental work performed by R. Zee)

Affiliation: University of Wisconsin-Madison

4.0 Relevant DAFS Program Task/Subtask

Subtask II.C.1.1 Phase Stability Mechanism Experiments

5.0 Accomplishments and Status

5.1 14-MeV Copper Irradiation

All the initially ordered CuPd samples are disordered when irradiated with 14 MeV copper ions at temperatures between 23°C and 200°C at doses as low as 0.2 dpa at a damage rate of 10^{-3} dpa/sec. Figure 1(a) and 1(b) show the damage structure representative of these disordered samples in two different magnifications. A diffraction pattern is included in the insert. The basic lattice parameter corresponds to that of a random fcc phase. The original order structure belongs to a CsCl bcc type (B2). Therefore, irradiation not only destroys the ordered structure but also transforms the basic lattice from bcc to fcc. This is because the free energy of the ordered B2 phase increases with decreasing order S. The increase in this case is large enough so that the free energy of the random fcc phase becomes lower, thus allowing the formation of this phase.[1,2]

Diffusion plays little or no role in the transformation since vacancies are imnobile up to 250°C as indicated by a separate annealing experiment of a quenched wire. The damage structure shown in Figure 1 consists mainly of microtwins and internal faults inside 0.1 micron diameter disordered clusters. The microtwins are formed in order to relieve the stress induced by the volumetric change accompanying the phase transformation.

A lower dose sample irradiated at 23°C to only 0.05 dpa shows the co-existence of ordered and disordered materials. This is shown in Figure 2 along with the diffraction pattern in the insert. The diffraction pattern has spots corresponding to both the (100) superlattice reflections (arrowed) as well as the disordered reflections. Figure 2(a) is a bright field and 2(b) and 2(c) are dark field images using a (100) superlattice reflection and a disordered reflection. The direct angular correlation between the (100) superlattice spots and the disordered pattern in the diffraction insert indicates that the orientation of the product and parent phases is related. This characteristic is typical of the formation of semi-coherent precipitates.

Figure 3(a) and 3(b) show a bright and a dark field image using (100) superlattice reflection from a sample irradiated at 23°C to 0.06 dpa but at a lower damage rate of 2 x 10^{-4} dpa/sec. This sample is still highly ordered. The dark field image in Figure 3(b) shows that the basic damage is microtwins which are probably created to relieve the induced stress discussed earlier.

At temperatures above 250°C, irradiation at a rate as high as 10^{-3} dpa/sec is unable to disorder the ordered structure. This is most likely because the vacancies are very mobile in this temperature range and reorder any disorder induced by irradiation. The high mobility of vacancies is confirmed by the high thermal reordering rate observed in the same temperature range.

Figure 4 is a plot of the variation of steady state degree of order with irradiation temperature at a displacement rate of 10^{-3} dpa/sec. The phase diagram modified by such irradiation is shown in Figure 5. At temperatures below 250°C, order structure is destroyed due to low reordering rate.

Result of post-irradiation annealing shows that reordering (recovery) does not occur until 260°C. At this temperature, small ordered nuclei of about 0.5 microns in diameter are formed in the disordered matrix. The order-disorder material forms a sharp boundary as shown in Figure 6(a) and 6(b). At 310°C, almost the entire matrix is transformed (ordered). Figure 6(c) shows the final grain structure of the transformed material. The recovery is typical of a classical nucleation and growth phenomena which is, of course, entirely different from the disordering process.

5.2 14.8-MeV Neutron Irradiation

Two CuPd foils, one ordered and one disordered were irradiated at RTNS-II up to a fluence ~ 1.6 x 10^{17} neutrons/cm^2. The irradiation temperature was maintained at 4.3°K. Figure 7(a) and 7(b) give the resistivities of these two samples as a function of neutron fluence. The increase in resistivity in the ordered sample is due to the simultaneous production of point defects and disordering whereas in the disordered sample, only the former effect needs to be

5.0 Accomplishments and Status

5.1 14-MeV Copper Irradiation

All the initially ordered CuPd samples are disordered when irradiated with 14 MeV copper ions at temperatures between 23°C and 200°C at doses as low as 0.2 dpa at a damage rate of 10^{-3} dpa/sec. Figure 1(a) and 1(b) show the damage structure representative of these disordered samples in two different magnifications. A diffraction pattern is included in the insert. The basic lattice parameter corresponds to that of a random fcc phase. The original order structure belongs to a CsCl bcc type (B2). Therefore, irradiation not only destroys the ordered structure but also transforms the basic lattice from bcc to fcc. This is because the free energy of the ordered B2 phase increases with decreasing order S. The increase in this case is large enough so that the free energy of the random fcc phase becomes lower, thus allowing the formation of this phase.[1,2]

Diffusion plays little or no role in the transformation since vacancies are imnobile up to 250°C as indicated by a separate annealing experiment of a quenched wire. The damage structure shown in Figure 1 consists mainly of microtwins and internal faults inside 0.1 micron diameter disordered clusters. The microtwins are formed in order to relieve the stress induced by the volumetric change accompanying the phase transformation.

A lower dose sample irradiated at 23°C to only 0.05 dpa shows the co-existence of ordered and disordered materials. This is shown in Figure 2 along with the diffraction pattern in the insert. The diffraction pattern has spots corresponding to both the (100) superlattice reflections (arrowed) as well as the disordered reflections. Figure 2(a) is a bright field and 2(b) and 2(c) are dark field images using a (100) superlattice reflection and a disordered reflection. The direct angular correlation between the (100) superlattice spots and the disordered pattern in the diffraction insert indicates that the orientation of the product and parent phases is related. This characteristic is typical of the formation of semi-coherent precipitates.

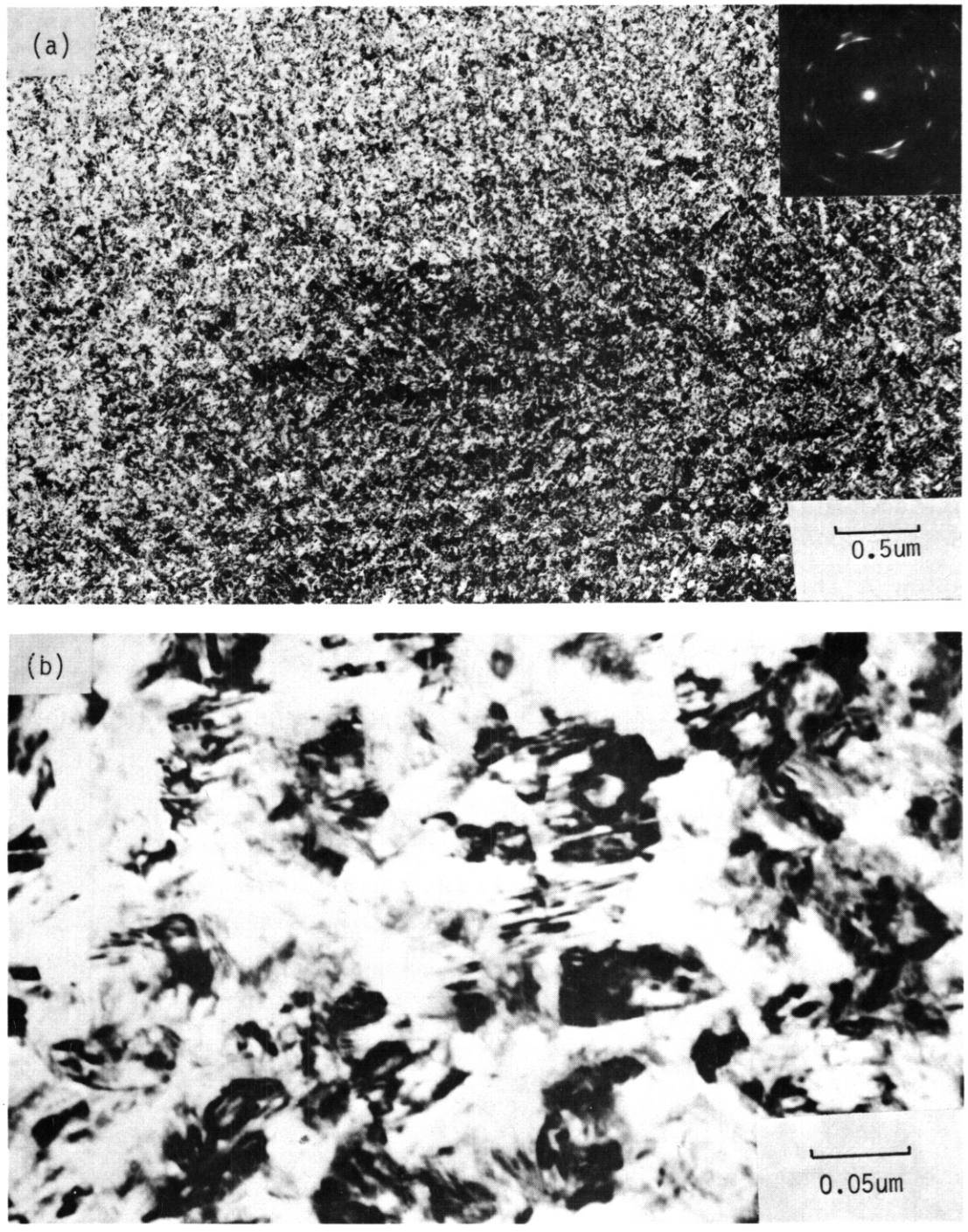

FIGURE 1. Typical Damage Structure, shown in two magnifications, of initially ordered CuPd irradiated with 14-MeV copper ions from 23°C to 200°C to Doses Above 0.2 dpa. Diffraction pattern is included.

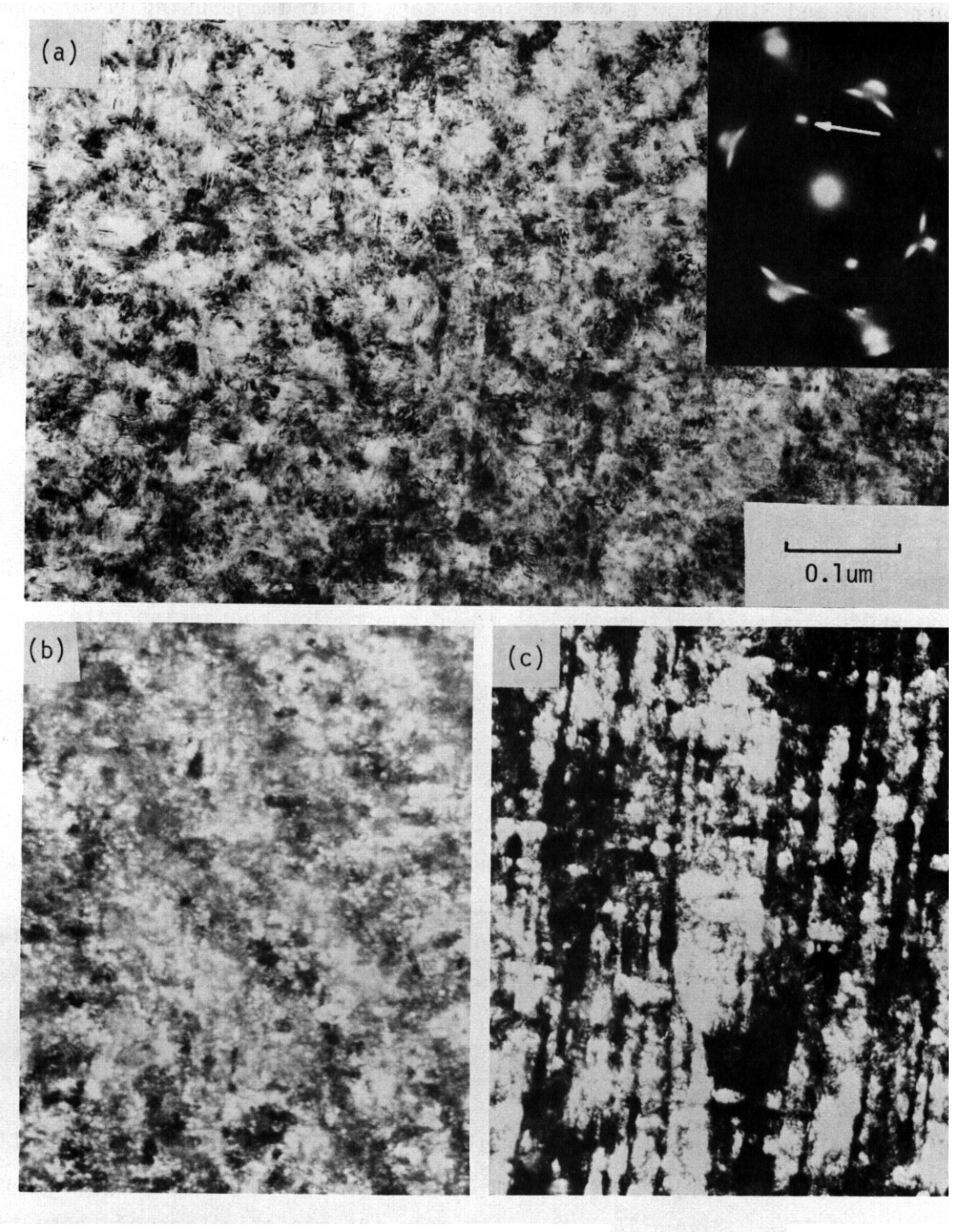

FIGURE 2. A Bright Field Image of the Damage Structure of a Sample Irradiated at 23 C to 0.05 dpa at 1.4 x 10^{-3} dpa/s is shown in (a). The corresponding dark field images using (100) superlattice spot (arrowed) and a disordered spot are shown in (b) and (c).

Figure 3(a) and 3(b) show a bright and a dark field image using (100) superlattice reflection from a sample irradiated at 23°C to 0.06 dpa but at a lower damage rate of 2 x 10^{-4} dpa/sec. This sample is still highly ordered. The dark field image in Figure 3(b) shows that the basic damage is microtwins which are probably created to relieve the induced stress discussed earlier.

At temperatures above 250°C, irradtation at a rate as high as 10^{-3} dpa/sec is unable to disorder the ordered structure. This is most likely because the vacancies are very mobile in this temperature range and reorder any disorder induced by irradiation. The high mobility of vacancies is confirmed by the high thermal reordering rate observed in the same temperature range.

Figure 4 is a plot of the variation of steady state degree of order with irradiation temperature at a displacement rate of 10^{-3} dpa/sec. The phase diagram modified by such irradiation is shown in Figure 5. At temperatures below 250°C, order structure is destroyed due to low reordering rate.

Result of post-irradiation annealing shows that reordering (recovery) does not occur until 260°C. At this temperature, small ordered nuclei of about 0.5 microns in diameter are formed in the disordered matrix. The order-disorder material forms a sharp boundary as shown in Figure 6(a) and 6(b). At 310°C, almost the entire matrix is transformed (ordered). Figure 6(c) shows the final grain structure of the transformed material. The recovery is typical of a classical nucleation and growth phenomena which is, of course, entirely different from the disordering process.

5.2 14.8-MeV Neutron Irradiation

Two CuPd foils, one ordered and one disordered were irradiated at RTNS-II up to a fluence ~ 1.6 x 10^{17} neutrons/cm^2. The irradiation temperature was maintained at 4.3°K. Figure 7(a) and 7(b) give the resistivities of these two samples as a function of neutron fluence. The increase in resistivity in the ordered sample is due to the simultaneous production of point defects and disordering whereas in the disordered sample, only the former effect needs to be

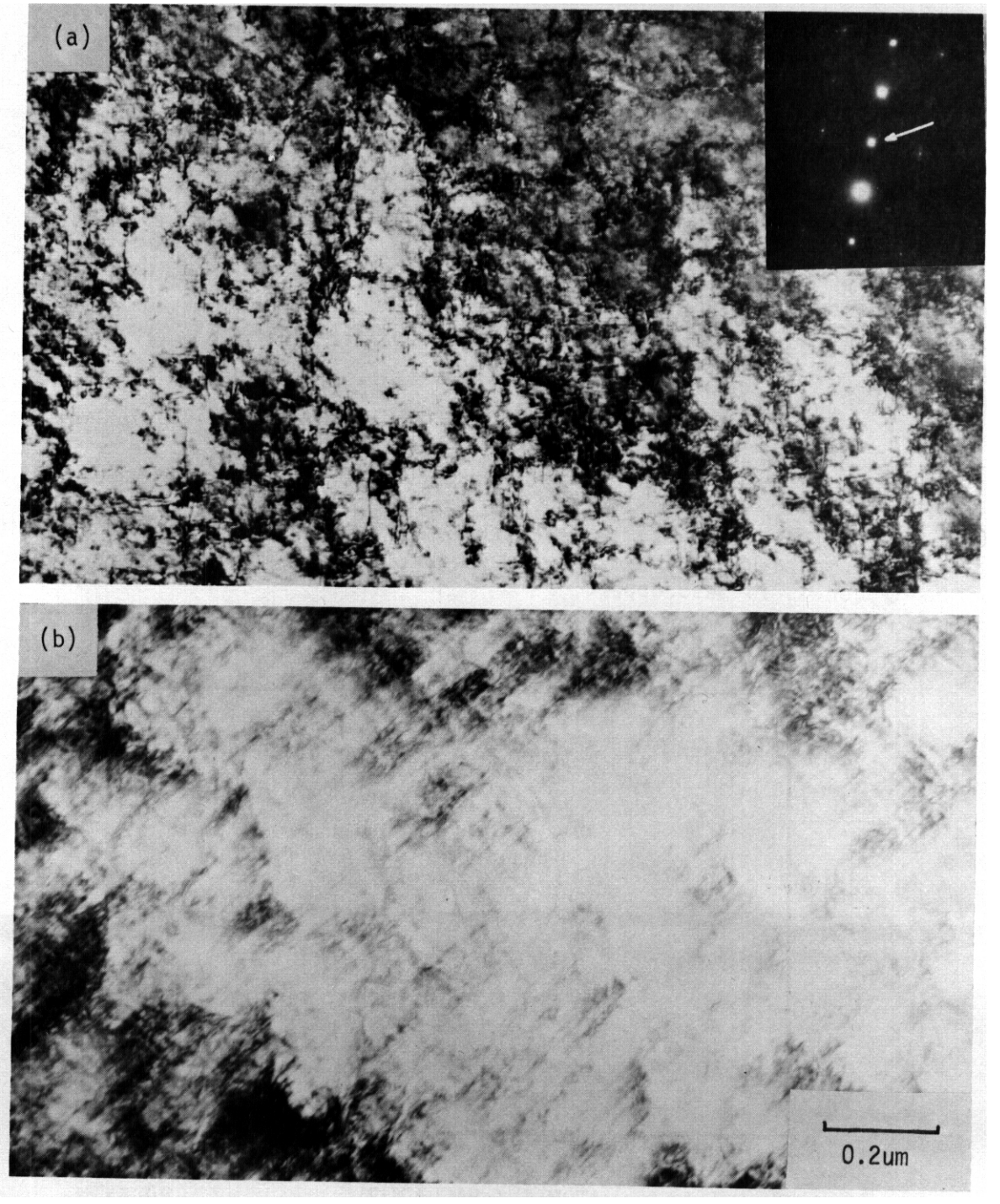

FIGURE 3. Bright Field (a) and Dark Field (b) Images of a CuPd Sample Irradiated at 23°C to 0.06 dpa at 2 x 10^{-4} dpa/s. The dark field image uses the (100) superlattice relfection (arrowed).

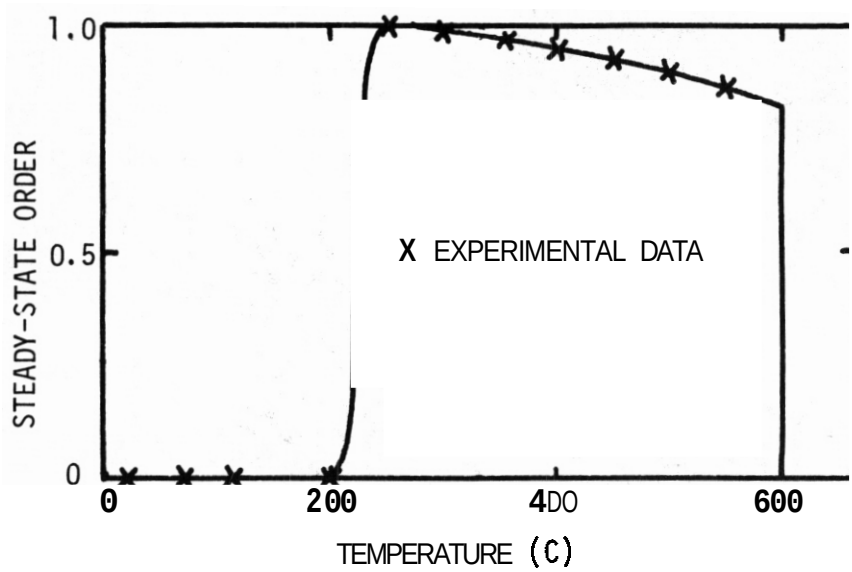

FIGURE 4. Variation of Steady-State Degree of Order in CuPd with Irradiation Temperature. The displacement rate is 10^{-3} dpa/s, and the Incident ion is 14-MeV copper.

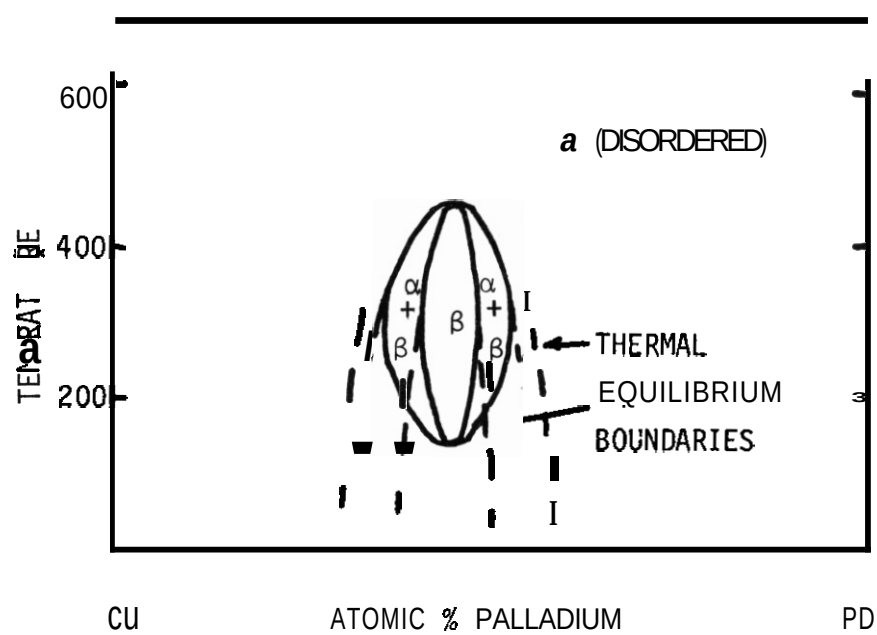

FIGURE 5. Phase Diagram of CuPd as Modified by Irradiation Described in Figure 4.

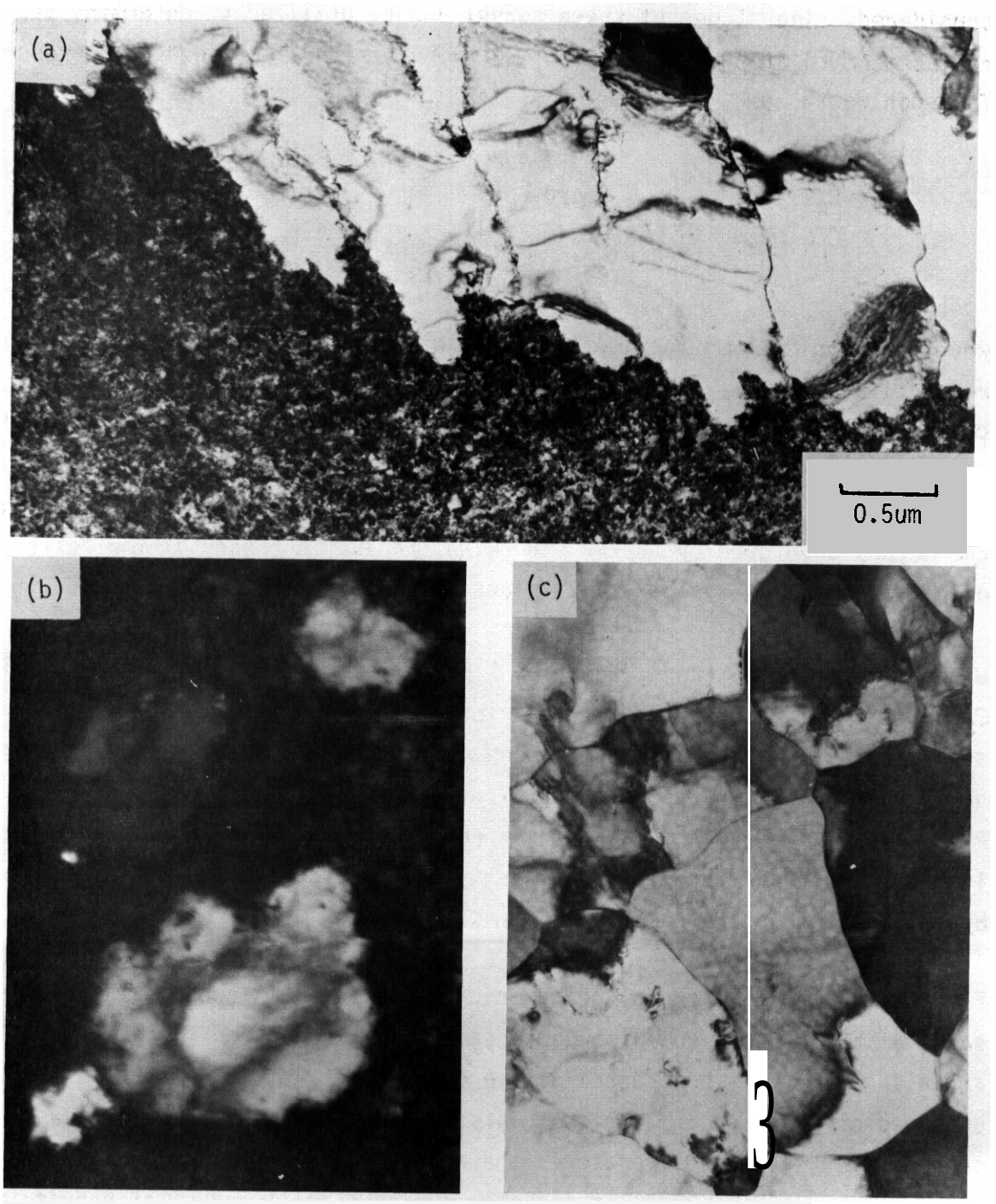

FIGURE 6. The Formation of Ordered Grains in the Disordered Matrix After Postirradiation Annealing at 260°C for 30 min is Shown in (a) and (b). The final-ordered grain structure is shown in (c).

considered. The slopes of these curves can be utilized to determine the replacement to displacment ratio (C_R/C_F). Becker[3] obtained an expression for such ratio as:

$$\frac{C_R}{C_F} = \frac{\Delta\rho_F}{\Delta\rho_R}\left[\frac{(d\Delta\rho/d\Phi t)^{ord}}{(d\Delta\rho/d\Phi t)^{dis}} - 1\right] \qquad \text{(Equation 1)}$$

wher $(d\Delta\rho/d\Phi t)^{ord}$ and $(d\Delta\rho/d\Phi t)^{dis}$ are the slopes of Figure 7(a) and 7(b) respectively, and $\Delta\rho_F$ is the resistivity per unit concentration of Frenkel pairs. The value $\Delta\rho_F = 2.5 \times 10^{-4}$ Ω-cm will be used. This is obtained from pure copper data which is a good approximation for CuPd. The resistivity increase per unit concentration of replacement, $\Delta\rho_R$, can be calculated using the method developed by Becker and using Landauer's theory[4] for resistivity of a two component system. This gives $\Delta\rho_R \approx 6 \times 10^{-6}$ a-cm.

With all these parameters, Equation 1 gives $C_R/C_F \approx 70$. This agrees well with $C_R/C_F = 80$ for fast neutron irradiation of Cu_3Au by Kirk and Blewitt[5] and suggests that, in term of replacement efficiency, fast and fusion neutrons are quite similar. Even though a 14-MeV neutron can transfer more energy to the PKAs than a 1 MeV-neutron, the extra energy from the 14 MeV-neutron is more likely to produce subcascades rather than a supercascade. This is confirmed by the TEM work of English and Jenkins.[6]

Figure 8(a) and 8(b) shows the numerical differential isochronal annealing results of the ordered and disordered samples after neutron irradiation. The annealing curve of the ordered sample shows a peak at 35°K which is probably due to close-pair recombination. This, of course, does not involve any reordering. At higher temperatures the annealing is rather gradual. The annealing from 35°K to 200°K is probably due to a small amount of reordering due to interstitial migration. A similar annealing result was found by Takamura and Okuda[7] in fast neutron irradiated CuZn and Cu_3Au. The amount of recovery they observed up to 200°K is 60% for CuZn and 7% for Cu_3Au as opposed to 12% in this study. This is attributed to a size effect on interstitial

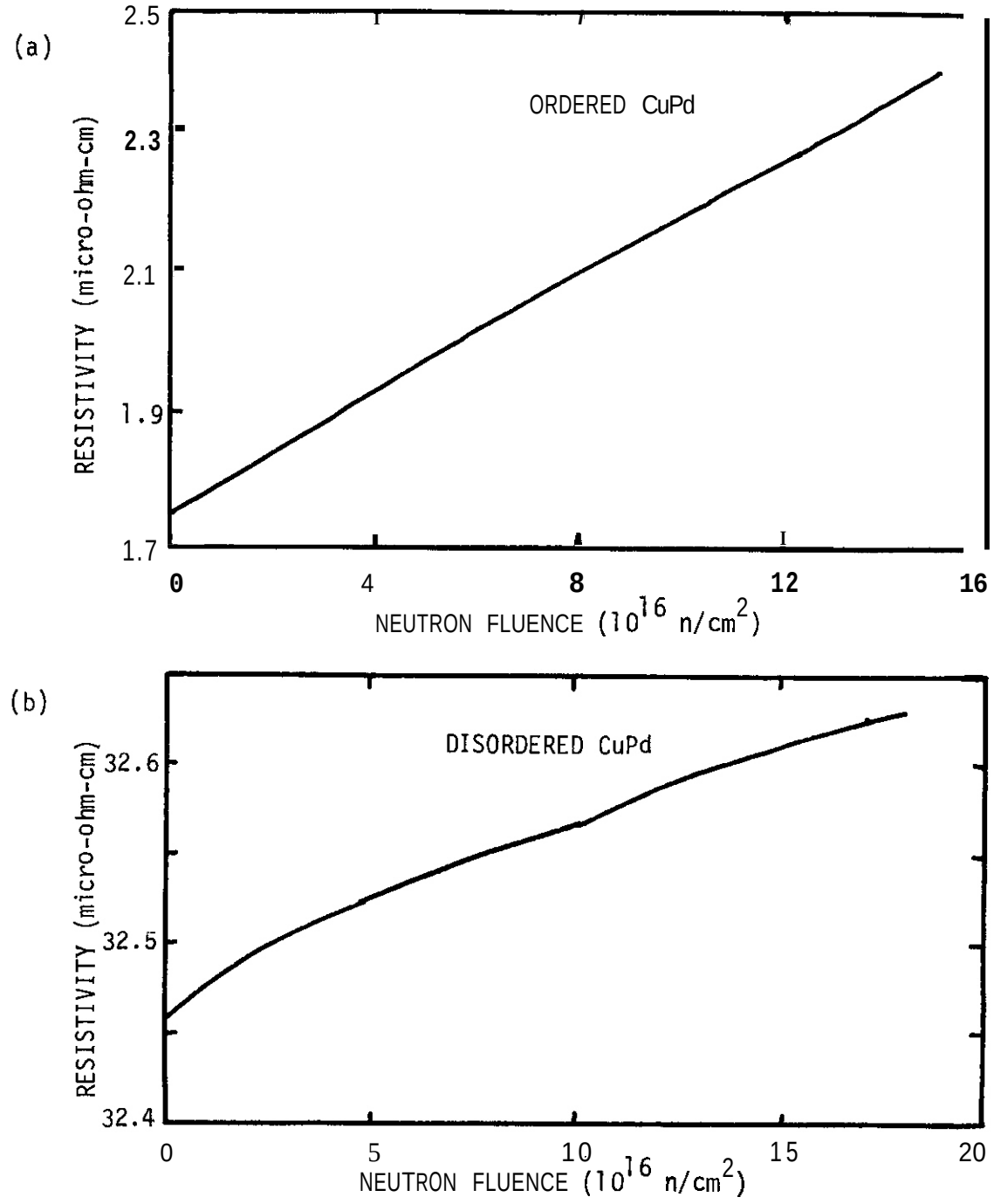

FIGURE 7. Resistivity Increase in an Initially Ordered Sample (a) and an Initially Disordered Sample (b) During Irradiation with 14.8-MeV Neutrons.

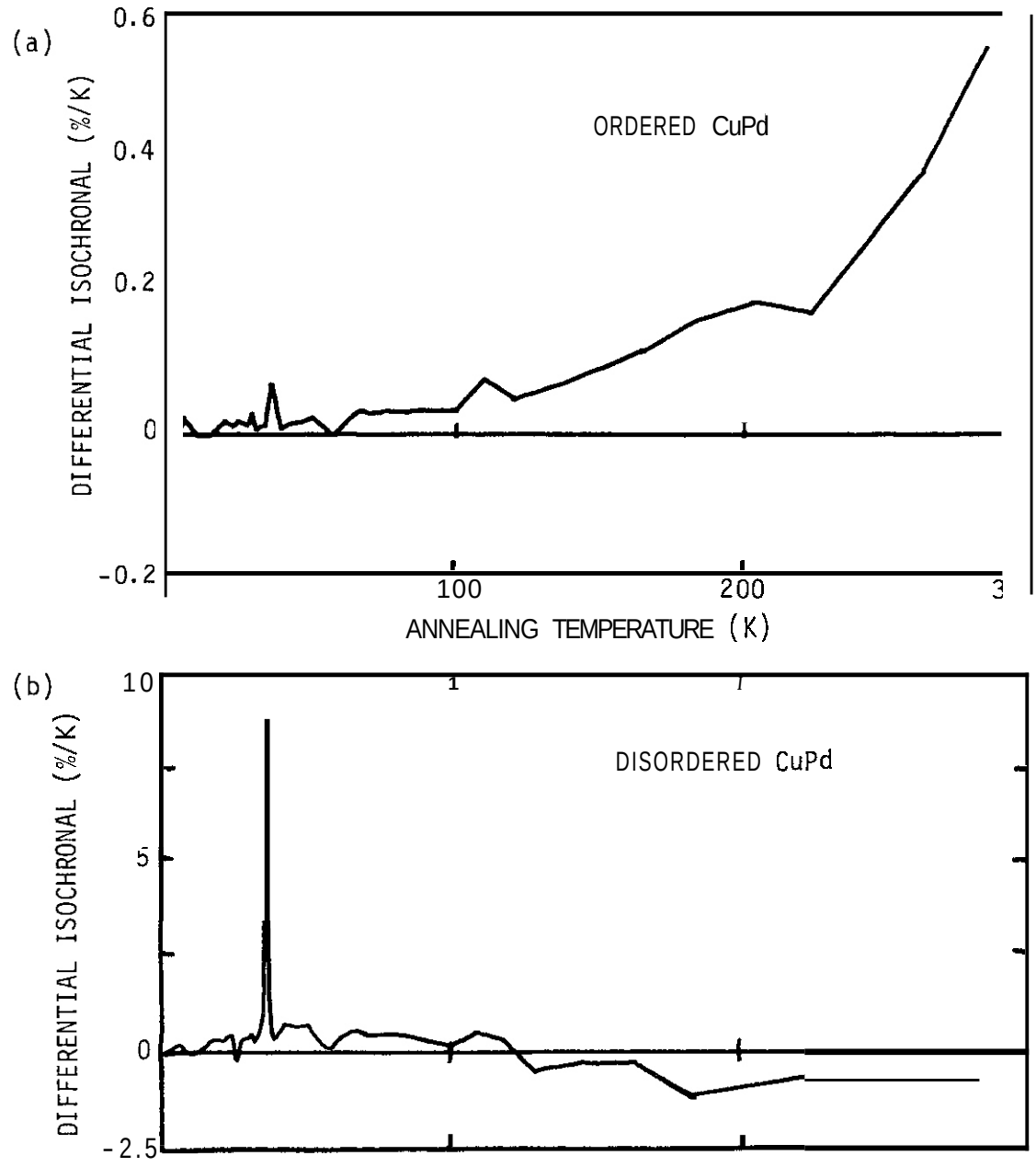

FIGURE 8. Differential Isochronal Annealing Results of the Ordered (a) and Disordered (b) CuPd Samples After Fusion Neutron Irradiation.

reordering. Interstitial migration is unlikely to produce reordering if the size difference between the components of the alloy is large. Since the size difference between copper and zinc is 17%, between copper and gold is 48% and between copper and palladium is 29%[8], it is reasonable that the recovery of CuPd is between CuZn and Cu_3Au.

The higher temperature (200°K to 300°K) annealing of the ordered sample is also quite smooth. The high temperature annealing behavior is probably due to vacancy reordering.

In the disordered sample, a similar low temperature peak at 35°K is observed. This can again be assigned to close-pair recombination but at temperatures above 120°K, the resistivity actually increases with annealing temperature. A possible explanation of this behavior is as follows. The ordered nuclei in the disordered matrix grow due to reordering. When these ordered nuclei reach an average size comparable to the wavelength of the conduction electrons (in copper this is about 0.5 nm), these clusters behave as extra scattering sites and the resistivity therefore increases.

6.0 References

1. K. Y. Liou and P. Wilkes, Journal of Nuclear Materials, 87, 317 (1979).
2. R. H. Zee and P. Wilkes, Proceeding of the Symposium on Irradiation Phase Stability for the Fall AIME Meeting, (1980).
3. D. Decker, F. Oworschak, C. Lehmann, K. T. Tie, H. Schuster, H. Wollenberger, and J. Wurm, Phys. Stat. Sol., 30, 219 (1968).
4. R. Landauer, J. Applied Physics, 23, 779 (1952).
5. M. A. Kirk and T. H. Blewitt, Met. Trans., 9A, 1728 (1978).
6. C. A. English and M. L. Jenkins, Harwell Report, AERE-R9695 (1980).
7. S. Takamura and S. Okuda, Rad. Eff., 17, 151 (1973).
8. H. W. King, Journal of Materials Science, 1, 78 (1976).

7.0 Future Work

This radiation induced order–disorder transformation study in CuPd is now completed.

EFFECTS OF HEAVY-ION IRRADIATION ON THE PHASE STABILITY OF A Cu-3.4 at% Be ALLOY

R.W. Knoll and G.L. Kulcinski (University of Wisconsin-Madison)

1.0 Objective

To develop a fundamental understanding of the formation of voids, loops, and precipitates in heavy ion and electron irradiated metals and alloys.

2.0 Summary

This paper reports on an investigation into radiation-induced precipitation in undersaturated and supersaturated Cu-3.4 at% Be solid solutions, during irradiation with 14 MeV Cu ions. Irradiation in the temperature range of 300"-475°C induced copious precipitation of CuBe platelets, even at very low damage doses. Using transmission electron microscopy (TEM), the precipitation was systematically characterized with respect to radiation parameters, and data regarding the effects of dose and dose rate were also obtained. By using a cross sectional TEM thinning technique, the precipitation was also characterized as a function of depth into the damaged region. Although the damage dose and dose rate varied strongly with depth within the region traversed by the heavy ions, the precipitate characteristics were not strongly depth dependent. Post-irradiation annealing studies proved that the continuous precipitate morphology was unstable in the absence of irradiation, even at an annealing temperature within the two-phase region on the equilibrium phase diagram. Thermal aging studies showed that the precipitation process was very sluggish in the absence of irradiation, and that prolonged thermal aging produced a precipitate morphology quite different than that induced by irradiation. The mechanism responsible for radiation-induced precipitation could not be conclusively determined, although the solute-drag mechanism provided the most likely explanation for precipitate growth during irradiation.

3.0 Program

Title: Radiation Effects to Reactor Materials
Principal Investigator: G. L. Kulcinski
Affiliation: University of Wisconsin

4.0 Relevant DAFS Program Plan Task/Subtask

Phase stability mechanism experiments (II.C. 1.1.)

5.0 Accomplishments and Status

5.1 Introduction

There is considerable experimental evidence that during irradiation, undersize solute elements in alloys can become redistributed or can precipitate out of solution due to interactions with irradiation-produced point-defects.[1-6] Several mechanisms have been postulated in the literature that can qualitatively or semiquantitatively account for these effects.[3,7-9] However, more experimental data is needed to fully understand the behavior of even simple binary alloys under irradiation. The aim of this study[10] was to characterize radiation-induced precipitation in the Cu-3.4 at% Be alloy, and to try to elucidate mechanisms responsible for the precipitation. This alloy was chosen because the lattice parameter of the Be solute is considerably smaller than that of Cu, and because the precipitation process in some Cu-Be alloys has been well characterized.[11] The irradiation temperature range that was chosen spanned the α phase boundary as shown in Fig.1, so both supersaturated and undersaturated solid solutions were studied.

5.2 Experimental Procedure

The Cu-3.4 at% Be (0.5 wt% Be) alloy was from stock material prepared by Wilkes.[12] Before irradiation, the alloy was solution annealed at 800°C and quenched into water. The specimens were mechanically polished and

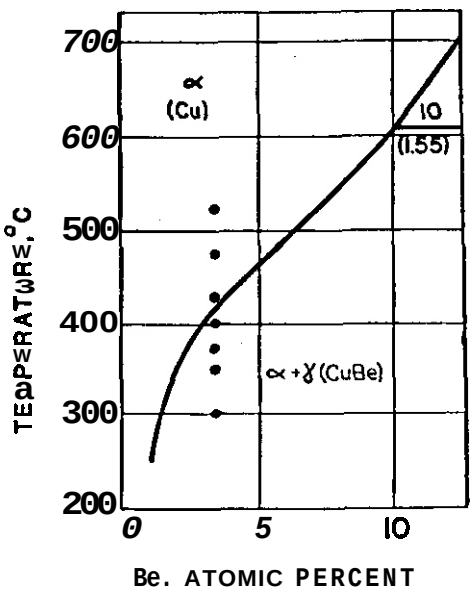

FIGURE 1. Copper-Rich End of the Equilibrium Phase Diagram of the Cu-Be System, Showing the Temperatures at which the Cu-3.4 at% Be Alloy was Irradiated.

electropolished to produce flat, clean surfaces. Depth dependent displacement damage was produced by irradiation with 14 MeV Cu ions, which have a maximum range of about 3 μm in the alloy. The displacement rate was about 10^{-3} dpa/sec and the damage dose ranged from 0.25 to 10 dpa at a depth of 1 μm into the damage zone. Two different methods of TEM specimen preparation were employed for post-irradiation analysis: some specimens were backthinned to a depth of about 1 μm from the original surface; other specimens were thinned in cross section to produce a thin-section lying in a plane parallel to the path of the incident ions, which allowed the entire damage zone to be imaged.

5.3 Results

5.3.1 Temperature Dependence

Irradiation of the Cu-3.4 at% Be alloy with 14–MeV Cu ions induced the formation of CuBe precipitate platelets, whose size, number density, and total volume fraction were strongly temperature dependent within the temperature range of 300°C to 475°C. In contrast, no precipitation of any kind was observed in unirradiated regions of the specimens (which experienced the same temperature history), indicating the precipitation kinetics are normally quite sluggish in this alloy. The TEM micrographs in Fig.2 show that precipitate size increases and number density decreases with increasing irradiation temperature in the supersaturated specimens. This same trend was followed in the undersaturated specimens at 430°C and 475°C, but at 525°C no precipitation formed during irradiation. The crystallographic structure and habit plane of the precipitates were the same as that reported for the mature γ' precipitate in heat treated Cu-13 at% Be alloys.(11) In Figs.3 and 4, respectively, the temperature dependence of the mean precipitate size and number density is plotted, for high dose (5-10 dpa) and for low dose (0.5-1 dpa) specimens (size is defined as the maximum precipitate dimension). The platelet thickness also increased with temperature, from 6 nm at 300°C to 35 nm at 430°C. From the size and density data, the temperature dependence near steady-state, of the atom fraction of Be remaining in solution (the unprecipitated solute), was computed as shown in Fig.5. The unprecipitated fraction of Be solute was lowest in the temperature range of 390°C ~430°C, in contrast to the equilibrium case, where almost all Be remains in solution at these temperatures.

5.3.2 Depth Dependence, and Effects of Dose and Dose Rate

The TEM micrograph of a cross sectioned specimen in Fig.6 illustrates the depth dependence of the CuBe precipitation within the region traversed by the high energy Cu ions. By dividing such micrographs into depth intervals, measurements of the depth dependence of precipitate size and number density were obtained, as plotted in Fig.7 for a specimen irradiated at 375°C. It is interesting that the precipitate size and number density vary with depth in a manner such that the precipitate volume fraction remains relatively constant with

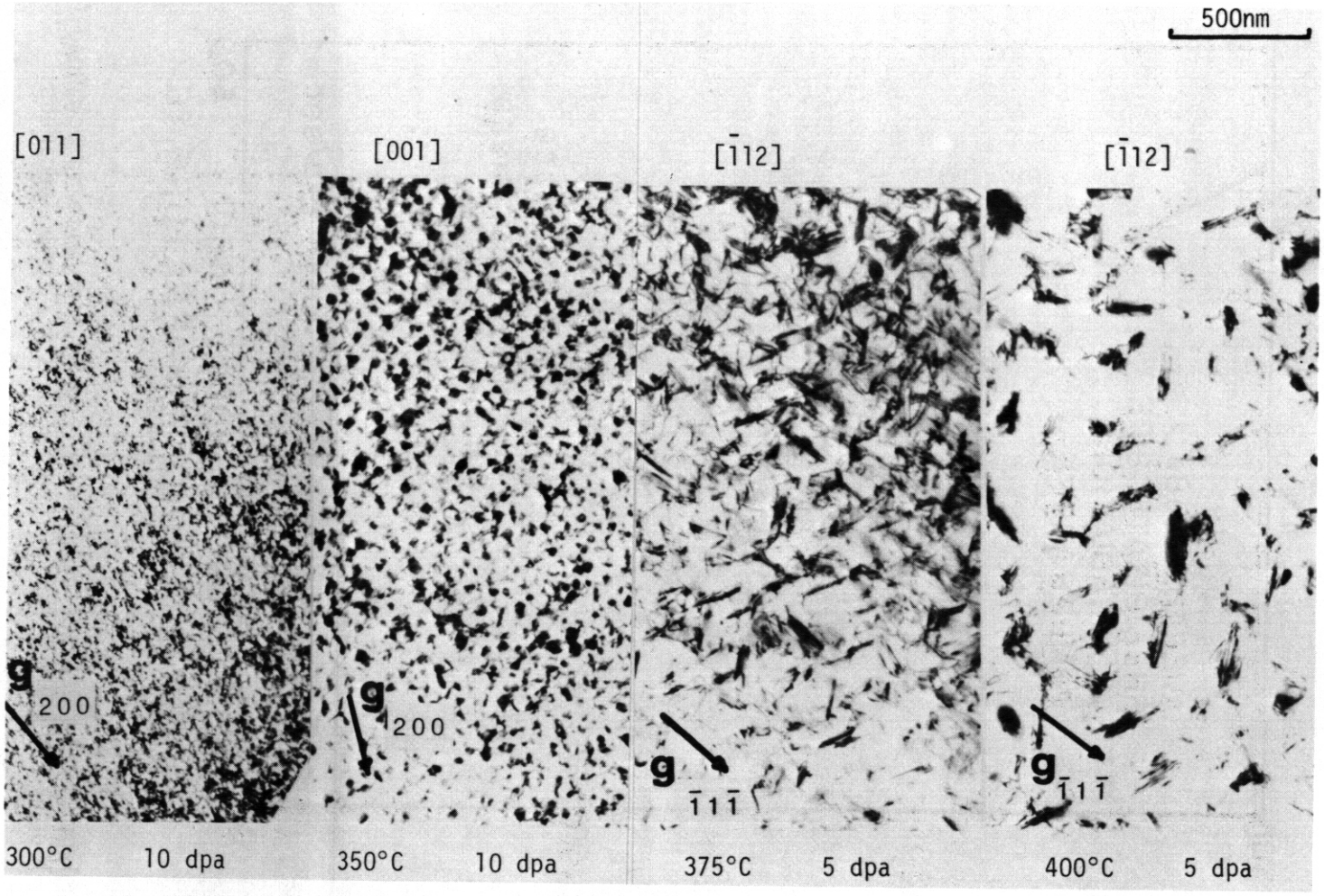

FIGURE 2 Radiation-Induced Precipitation in Supersaturated Cu-3 4 at% Be Alloy.

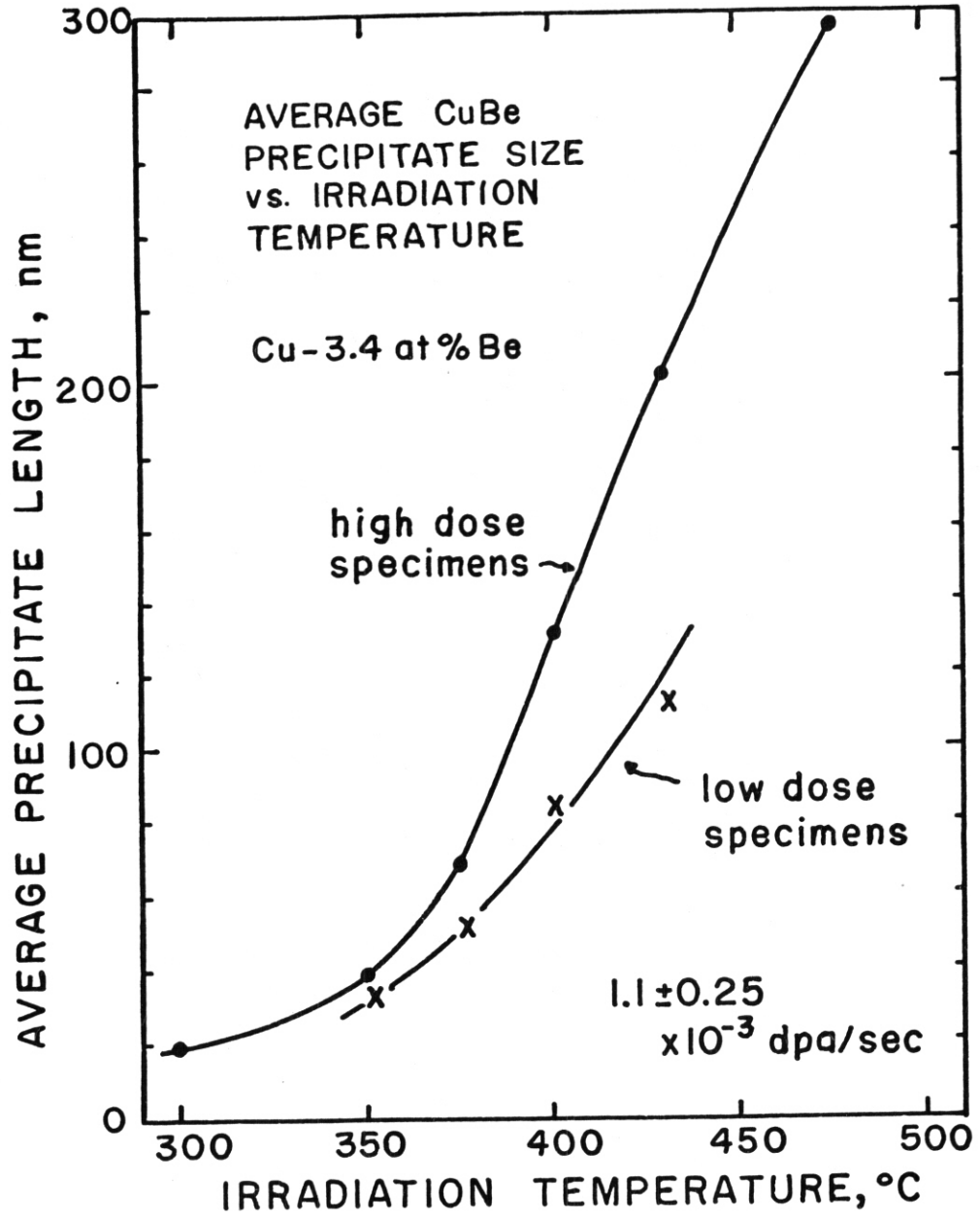

FIGURE 3. Temperature Dependence of Mean Precipitate Size in Low Dose (0.5-1 dpa) and High Dose (5-10 dpa) Cu-3.4 at% Be Specimens.

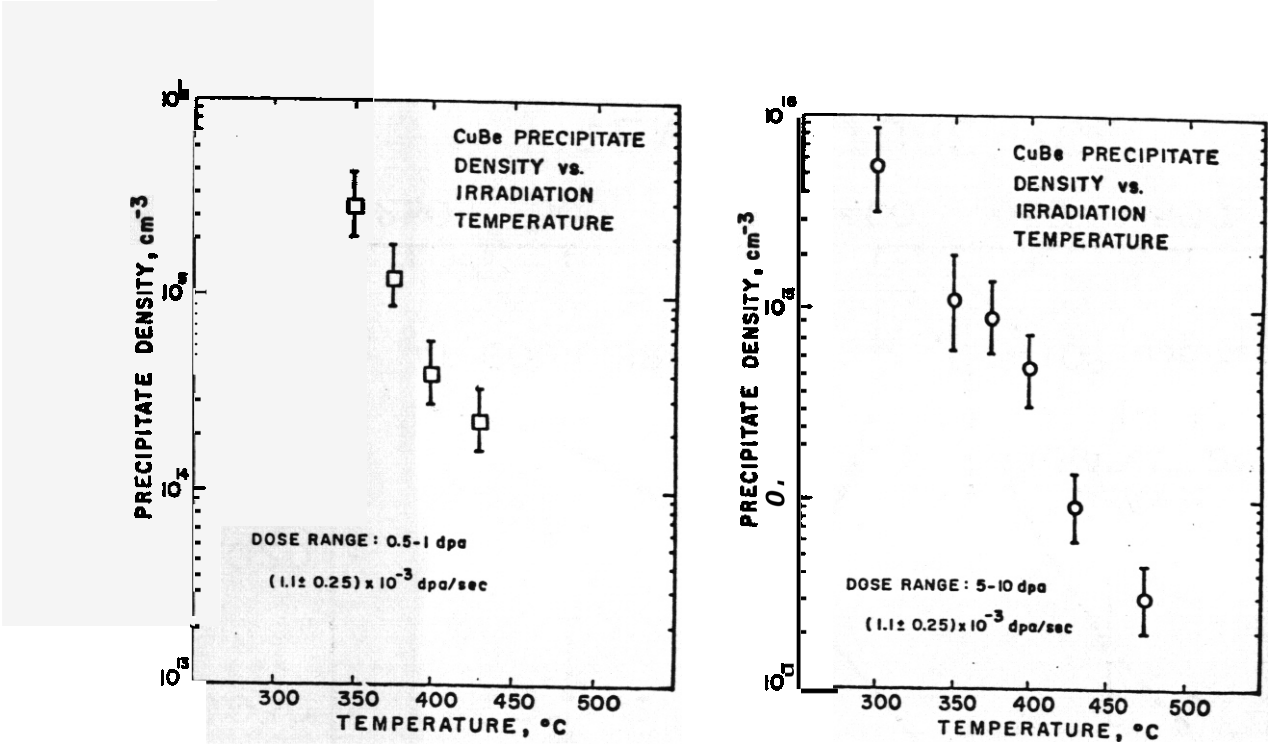

FIGURE 4 The Dependence of Precipitate Number Density on Irradiation Temperature in Low Dose and High Dose Samples.

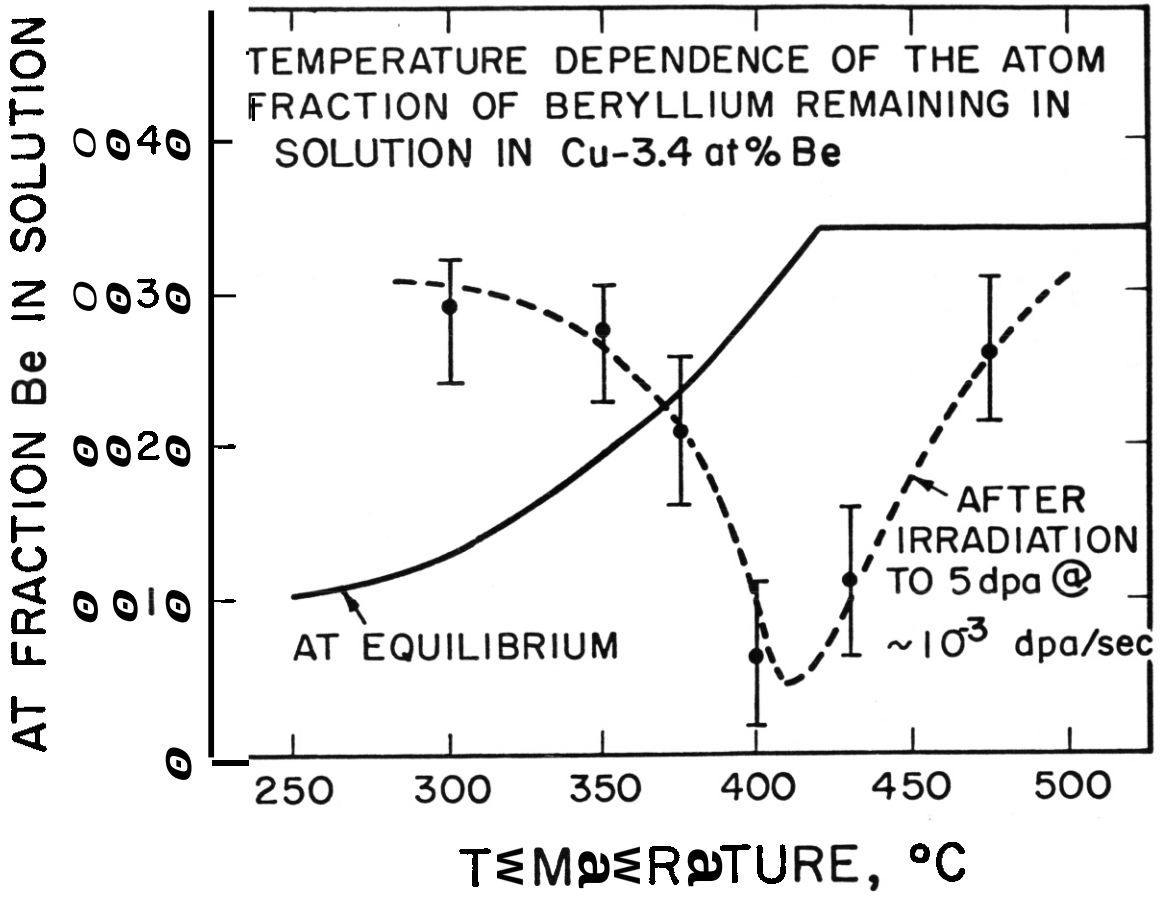

FIGURE 5 Temperature Dependence of the Unprecipitated Fraction of Be Solute Under Near Steady-State Irradiation Conditions.

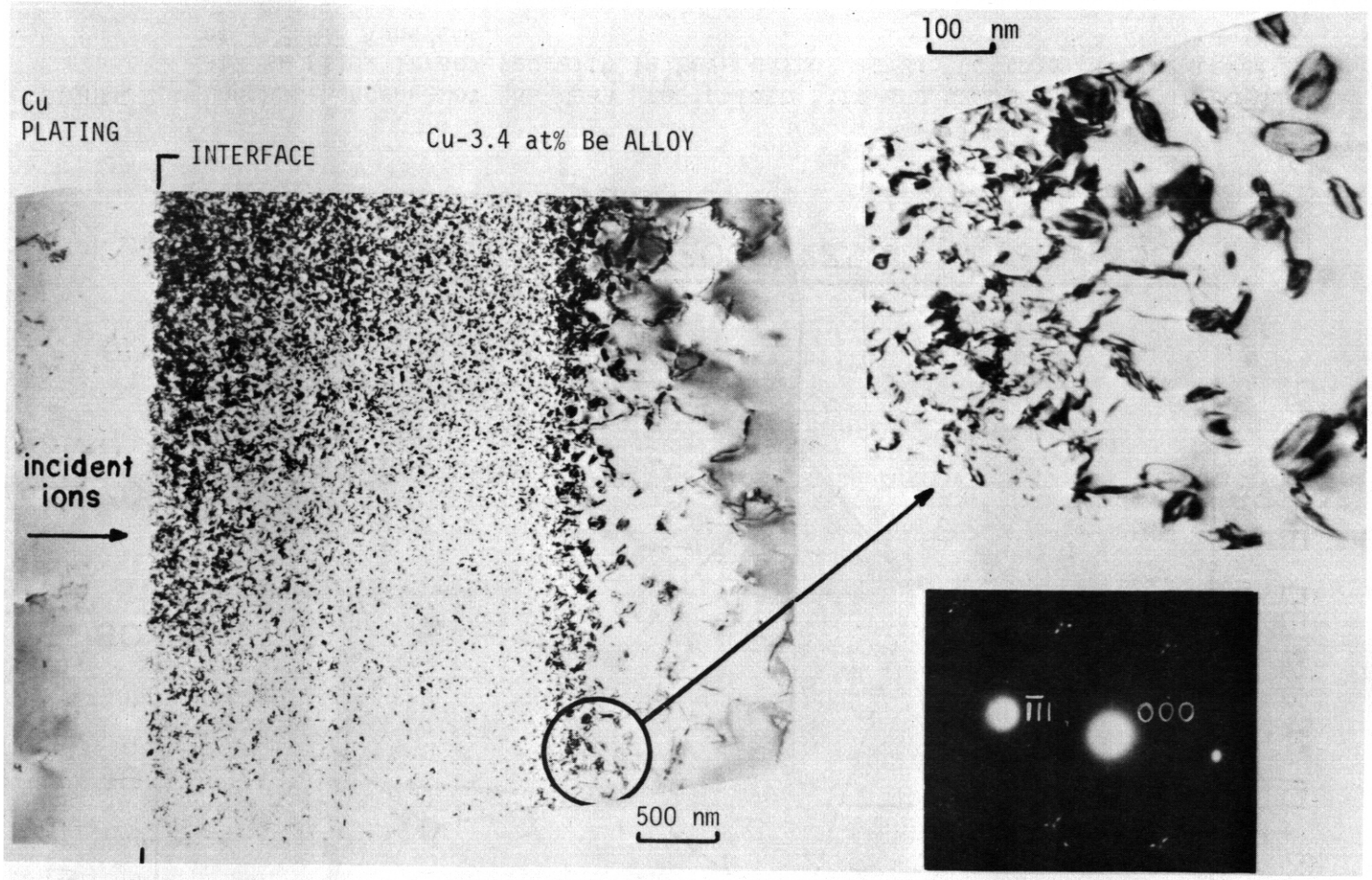

FIGURE 5 Precipitation in Cu-3.4 at% Be Irradiated at 350°C with 7×10^{15} ions/cm^2.

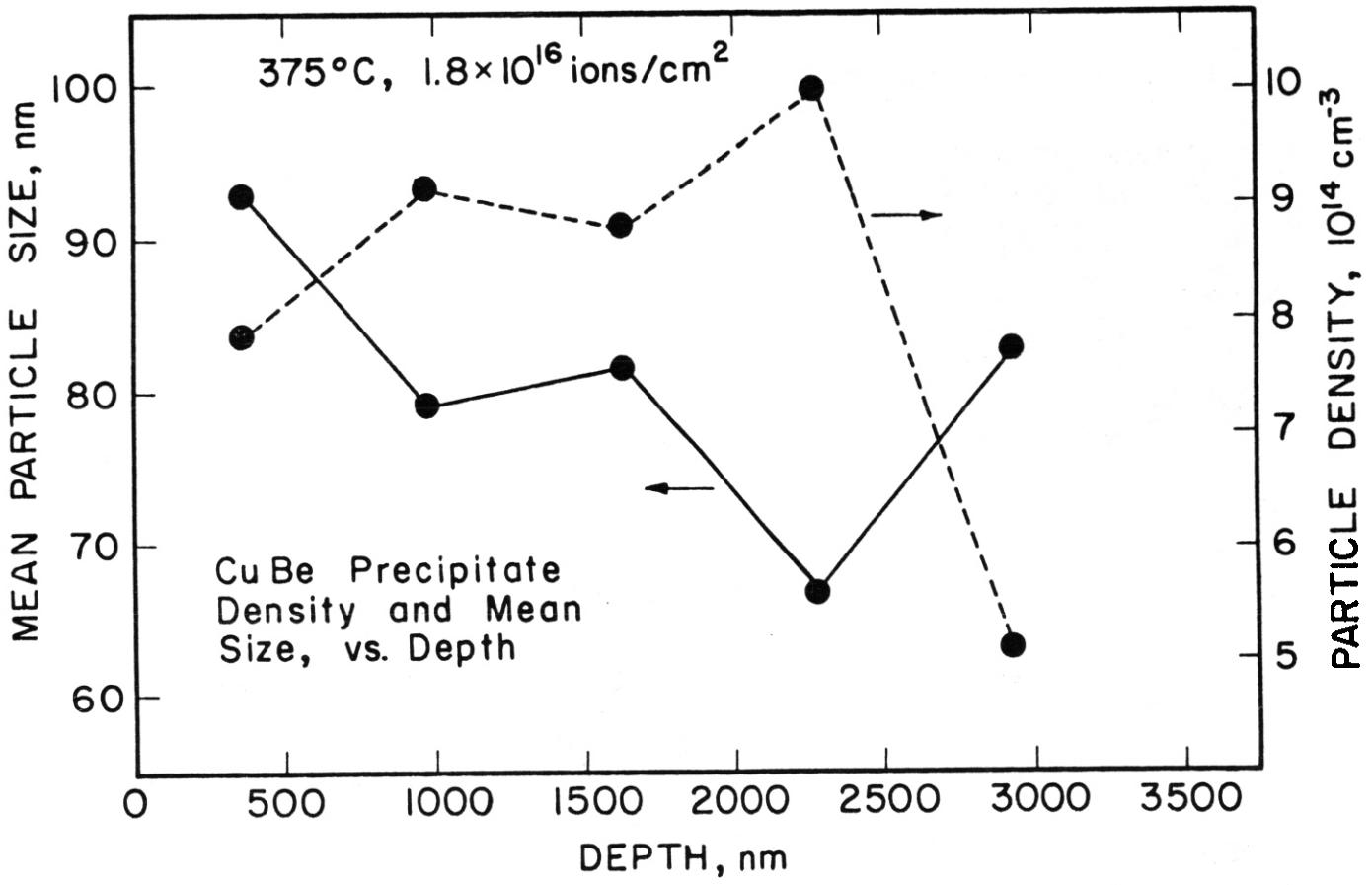

FIGURE 7. Depth Dependence of the Mean Precipitate Size and Number Density in Cu-3.4 at% Be Alloy Irradiated with 14 MeV Cu Ions at 375°C, to a Fluence Level of 1.8 E16 ions/cm^2.

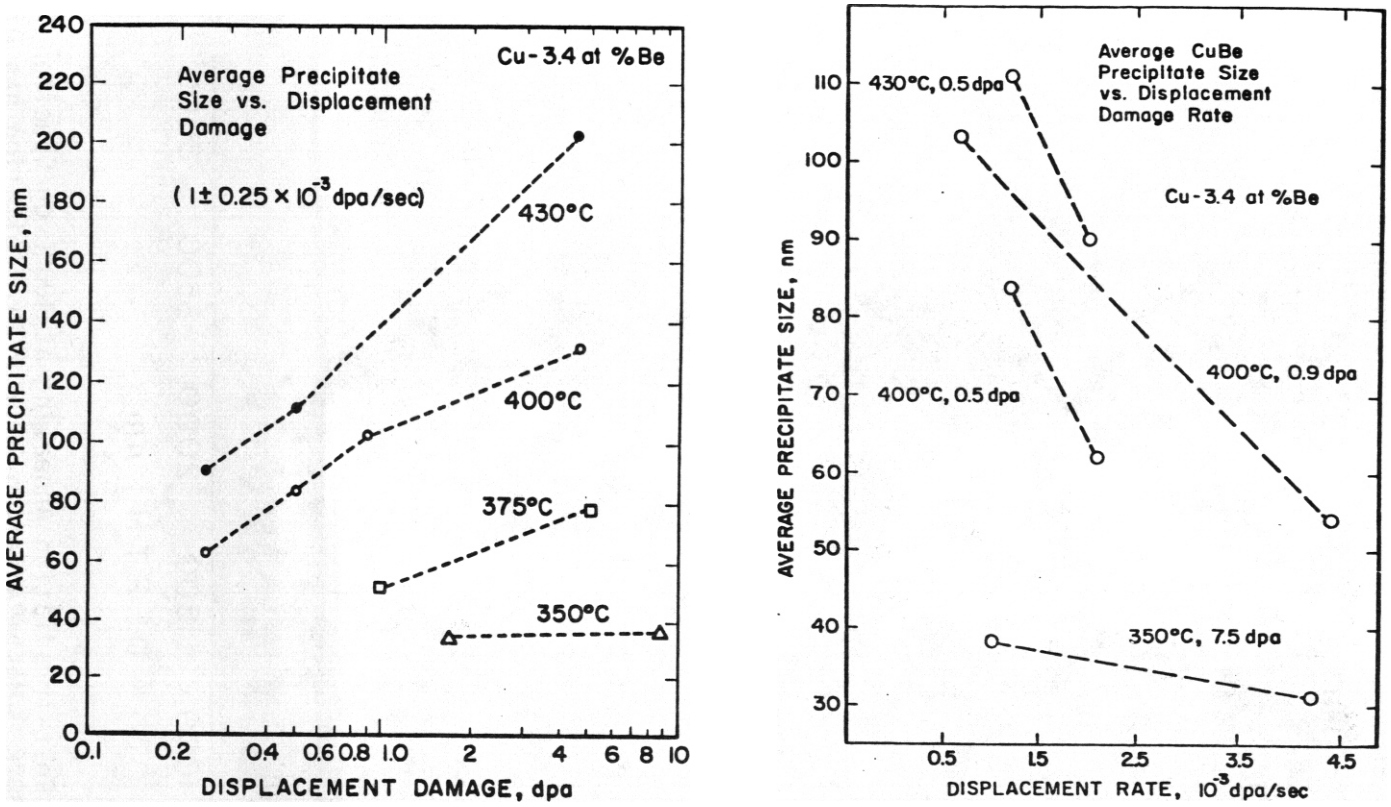

FIGURE 8. Dependence of Precipitate Size on dpa Level and dpa Rate

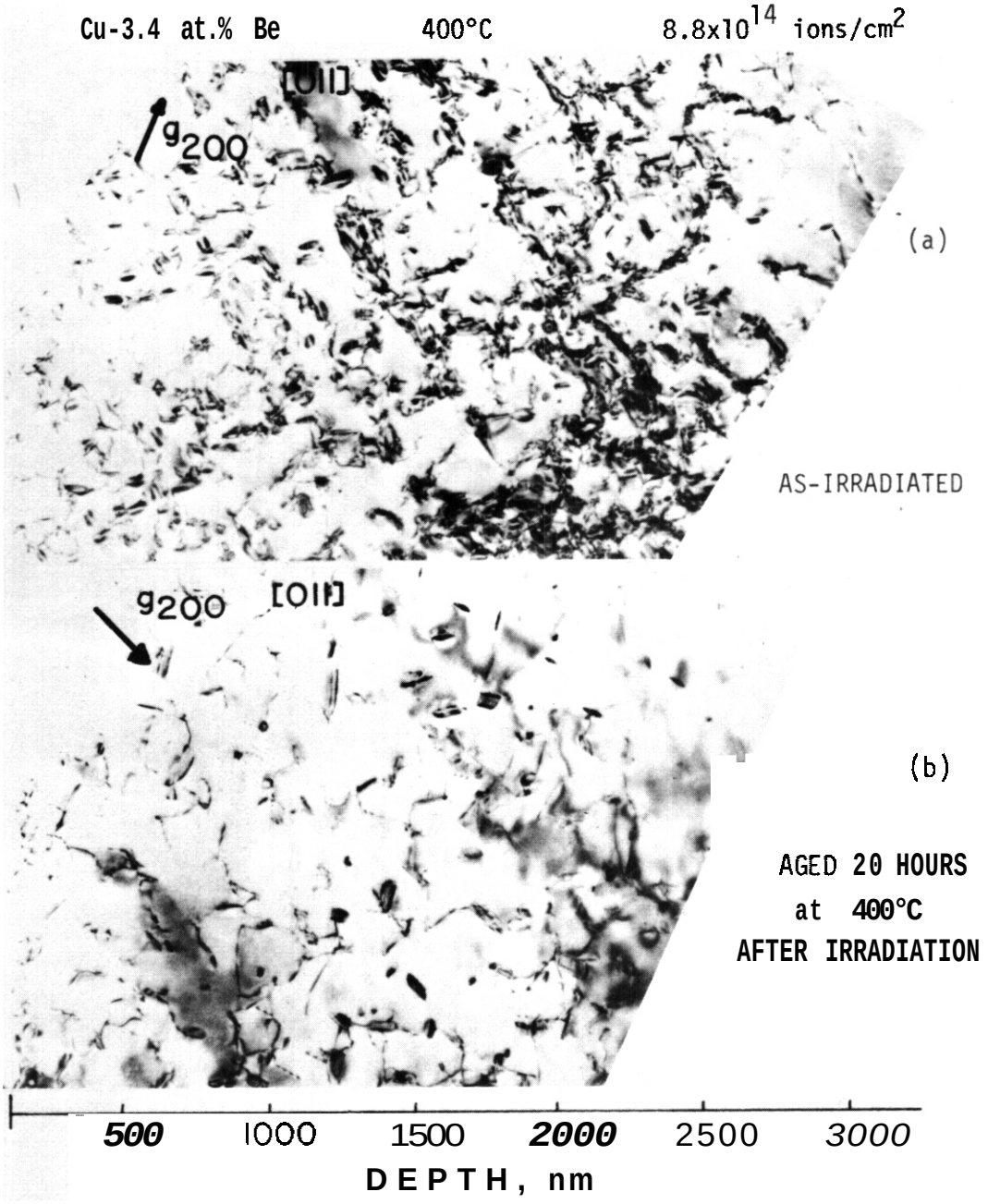

FIGURE 9. Effect of Post-Irradiation Annealing at 400°C on Specimen Irradiated at 400°C. Most Radiation-Induced Precipitation has Dissolved.

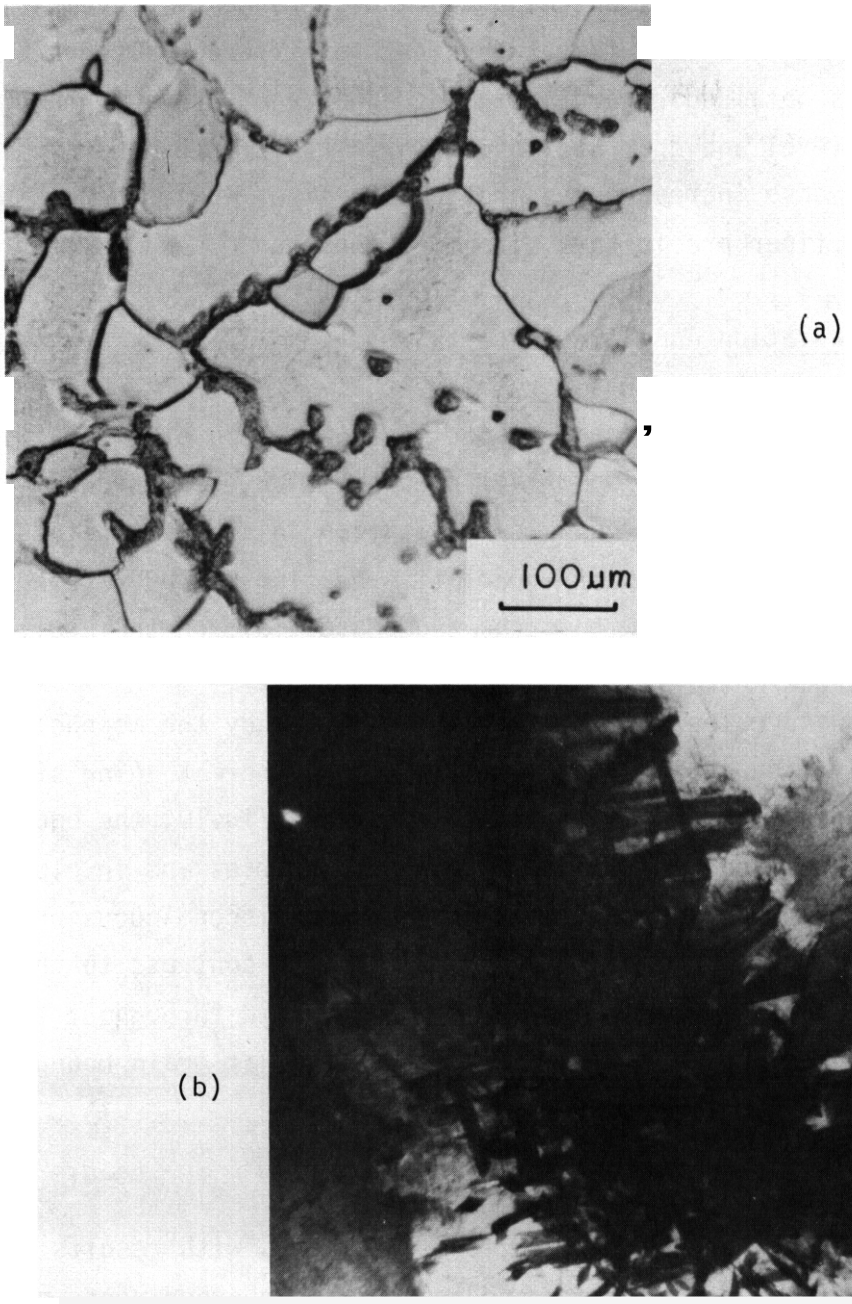

FIGURE 10. Discontinuous Precipitation in Unirradiated, Thermally Aged Cu-3.4 at% Be Alloy. (a) Optical Micrograph Showing CuBe Precipitation at Grain Boundaries. (b) TEM Micrograph of a Two-Phase Region Composed of Densely Clustered CuBe Platelets. Surrounding Matrix is Completely Free of Precipitates.

depth within the damage zone (except near the end-of-range). By comparing specimens irradiated at the same temperature but to different fluence levels, some information was obtained regarding the dependence of precipitate characteristics on dpa level and dpa rate, as shown in Fig.8. In general, increasing the damage dose increased the precipitate size, while increasing the dpa rate produced a finer precipitate size distribution.

5.3.3 Post-Irradiation.Annealing Effects

Continued heating of the undersaturated specimens (at 430°C or 475°C) with the ion beam off caused dissolution of all precipitation, as expected. However, it was found that the continuous precipitation in supersaturated solid solutions also dissolved during post-irradiation heating at 400°C (Fig.9), even though this temperature is within the two-phase field on the equilibrium phase diagram. Instead, the 400°C anneal produced some coarse discontinuous CuBe precipitation within the specimens. To further study the morphology of equilibrium precipitation in the Cu-3.4 at% Be alloy, thermal aging studies were conducted on unirradiated specimens. As shown in Fig.10, the equilibrium precipitation is discontinuous, forming at grain boundaries and in clusters within the grains. Generally, the matrix between the discontinuous precipitate clusters was completely free of precipitation, in contrast to the irradiated specimens, where continuous precipitation formed throughout the matrix, but no discontinuous precipitation was observed at grain boundaries.

5.4 Discussion

Comparison of the results of the irradiation experiments with results of the post-irradiation annealing experiments and thermal aging experiments proved that a nonequilibrium precipitate morphology was produced in the Cu-3.4 at% Be alloy by irradiation with heavy ions. Therefore, a radiation-induced mechanism was necessary for nucleation and growth of the continuous CuBe precipitation. Because the precipitates apparently nucleated quickly after the start-up of irradiation, and the nucleation stage ceased before doses of about 0.2

dpa were attained (at irradiation temperatures below about 430°C), it could not be determined whether the precipitates nucleated homogeneously in the matrix, or whether they nucleated on point-defect clusters. However, the growth of the precipitates can be satisfactorily explained by the solute-drag mechanism proposed by Okamoto, Lam and coworkers,[3,7] for the following reasons: a) The Be solute is undersize with respect to the matrix and interacts with interstitials, therefore Be is expected to be transported with the interstitial defect flux. If the periphery of a CuBe platelet acts as a point-defect sink, then Be atoms will be deposited at the precipitate/matrix interface and growth will be encouraged. b) From Fig.5, it appears that the precipitation (segregation) mechanism is most efficient near the temperature of 400°C, which is approximately one-half the melting temperature of the alloy (1/2 T_m). This agrees with a study by Rehn, et al.[1] (in a Ni-Si alloy) where the greatest degree of segregation occurred at about 1/2 T_m.

5.5 Conclusions

a) Irradiation with 14-MeV Cu ions at a dose rate of about 10^{-3} dpa/sec, and at temperatures in the range 300°C-475°C, caused the Cu-3.4 at% Be alloy to decompose into a mixture of α_{Cu} solution and CuBe platelets. The platelets were distributed uniformily throughout the matrix, and their size, number density, and volume fraction were strongly temperature dependent.
b) Post-irradiation annealing experiments proved that the continuous precipitate morphology was unstable in the absence of irradiation, hence the precipitation was radiation-induced rather than just radiation-enhanced.
c) The solute-drag mechanism provides a satisfactory explanation for growth of the CuBe precipitates during irradiation.

6.0 References

1. L.E. Rehn, P.R. Okamoto, D.I. Potter, and H. Wiedersich, J. Nuc. Mat. 74 242 (1978).

2. R.C. Piller and A.D. Marwick, J. Nuc. Mat. 71 309 (1978).

3. P.R.Okamoto and H. Wiedersich, J. Nuc. Mat. 53 336 (1974).

4. A. Barbu and A.J. Ardell, Scripta Met. 9 1233 (1975).

5. A. Barbu and G. Martin, Scripta Met. 11 771 (1977).

6. C. Kinoshita and T.E. Mitchell, 38th An. Proc. Electron Mic. Soc. *Am.* 148 (1980) and Elec. Microscopy 1980 4 236 (1980).

7. R.A. Johnson and N.Q. Lam, Phys.Rev. B15 1794 (1977).

8. G. Martin, Phil Mag A38 131 (1978).

9. R.Cauvin and G. Martin, J. Nuc. Mat. 83 67 (1979).

10. R.W. Knoll, "Effects of Heavy Ion Irradiation on the Phase Stability of Several Copper Base Alloys", Ph.D. Thesis, University of Wisconsin, Madison, 1981.

11. R.J. Rioja and O.E. Laughlin, Acta Met. 28 1301 (1980).

12. P. Wilkes, Acta Met. 16 153 (1968).

7.0 Future Work

Work on this phase of the project will be completed Summer of 1981.

DAMAGE DEVELOPMENT AND HARDENING IN 14-MeV NEUTRON IRRADIATION OF COPPER ALLOYS AT 25°C

H. R. Brager, F. A. Garner and N. F. Panayotou (Hanford Engineering Development Laboratory)

1.0 Objective

The purpose of this study is to determine the effect of 14-MeV neutron irradiation on the microstructural development of copper alloys, using the coupled techniques of electron microscopy and microhardness. The ultimate application of this effort is to correlate the microstructural development to macroscopic mechanical property changes in metals of interest to the Fusion Reactor Development program.

2.0 Summary

Copper and copper alloyed with five atom percent of either aluminum, nickel or manganese were irradiated at 25°C with 14-MeV neutrons to fluences up to 7.5×10^{17} n/cm^2 (0.003 dpa). The radiation-induced microstructure of these materials was characterized by the coupled use of electron microscopy and microhardness. The irradiation-induced microhardness changes were found to be independent of alloy identity and the magnitude of the solute-induced hardening. It appears that at least 70% of the defect clusters are smaller than resolvable by microscopy ($\sim$1 nm). The point defects at 25°C which survive recombination and aggregate in either visible or invisible clusters constitute at least 9-10% of those produced in the cascades.

3.0 Program

Title: Irradiation Effects Analysis (AKJ)
Principle Investigator: D. G. Doran
Affiliation: Hanford Engineering Development Laboratory

4.0 Relevant DAFS Program Plan Task/Subtask

Subtask II.B.3.2
Subtask II.C.6.3
Subtask II.C.11.4

5.0 Accomplishments and Status

5.1 Introduction

Application of the extensive fission reactor data base to design of fusion reactors requires an understanding of the differences in the displacive and transmutational characteristics of the two types of neutron spectra. One of the many kinds of experiments directed toward this goal involved comparison of the microstructures induced by irradiation in each environment. When seeking information on differences in atomic displacive behavior of neutrons, microstructural examinations must be conducted on specimens in which the damage level is relatively small. The important criterion here is that no significant alteration, overlap or erasure of the microstructural record occur due to interaction of damage regions arising from different neutrons. Since the characteristic dimension of the clusters resulting from the displacement and cascade events is small, the resolution limit of the experimental tools employed becomes a major consideration.

This paper describes the results of a microstructural characterization of a copper alloy series irradiated at 25°C to fluences up to 7.5 x 10^{17} n/cm^2 (E = 14 MeV) or 0.003 dpa. The resolution aspect of the characterization has been addressed by the coupled use of electron microscopy and microhardness measurements. The specific objectives of the examinations reported here were to determine the survivability and visibility of point defect clusters at 25°C, and also the influence on these parameters of both solute additions and increasing neutron fluence. Similar specimens from fission irradiations have not yet become available.

5.2 Experimental Details

The metals employed in this study were pure (99.99 + atom %) copper and copper alloyed with five atom percent of either aluminum, nickel or manganese. The specimens were in the form of 3 mm diameter microscopy disks of 0.25 mm thickness. The irradiations were conducted at 25°C using 14 MeV neutrons from the Rotating Target Neutron Source II (RTNS-II) at Lawrence Livermore Laboratory to fluences up to 7.5 x 10^{17} n/cm^2 (E = 14 MeV) or 0.003 dpa. After irradiation, the specimens were tested using a Vickers diamond pyramid indenter loaded to 50 grams in a TUKON microhardness machine. Five measurements were made on each specimen, carefully avoiding the edges of the disk which might have been deformed in specimen preparation.

Selected specimens were then prepared for examination in a JEOLCO 100 CX electron microscope. Electrolytic thinning was performed at 20°C and 12 volts DC, employing a solution of 5% isopropyl alcohol, 24% phosphoric acid, 24% ethyl alcohol and 47% water by volume.

5.3 Results

Figure 1 shows the neutron-induced changes in microhardness produced in the four copper alloys. The microhardness changes are essentially independent of alloy identity, linear with the square root of neutron fluence and extrapolate back to the origin.

Typical micrographs of each alloy examined are also shown in Figure 1, along with an arrow which identifies the fluence and associated hardness measurements of each specimen examined. The microstructural data extracted by transmission microscopy are tabulated in Table 1. Note that for all alloys except Cu + 5% Al that there are roughly two visible clusters per calculated PKA. In the copper aluminum alloy, there are four to five visible clusters per PKA. Figure 2 shows that the size distribution of defect clusters in each of the various alloys is not very different, even though the pure

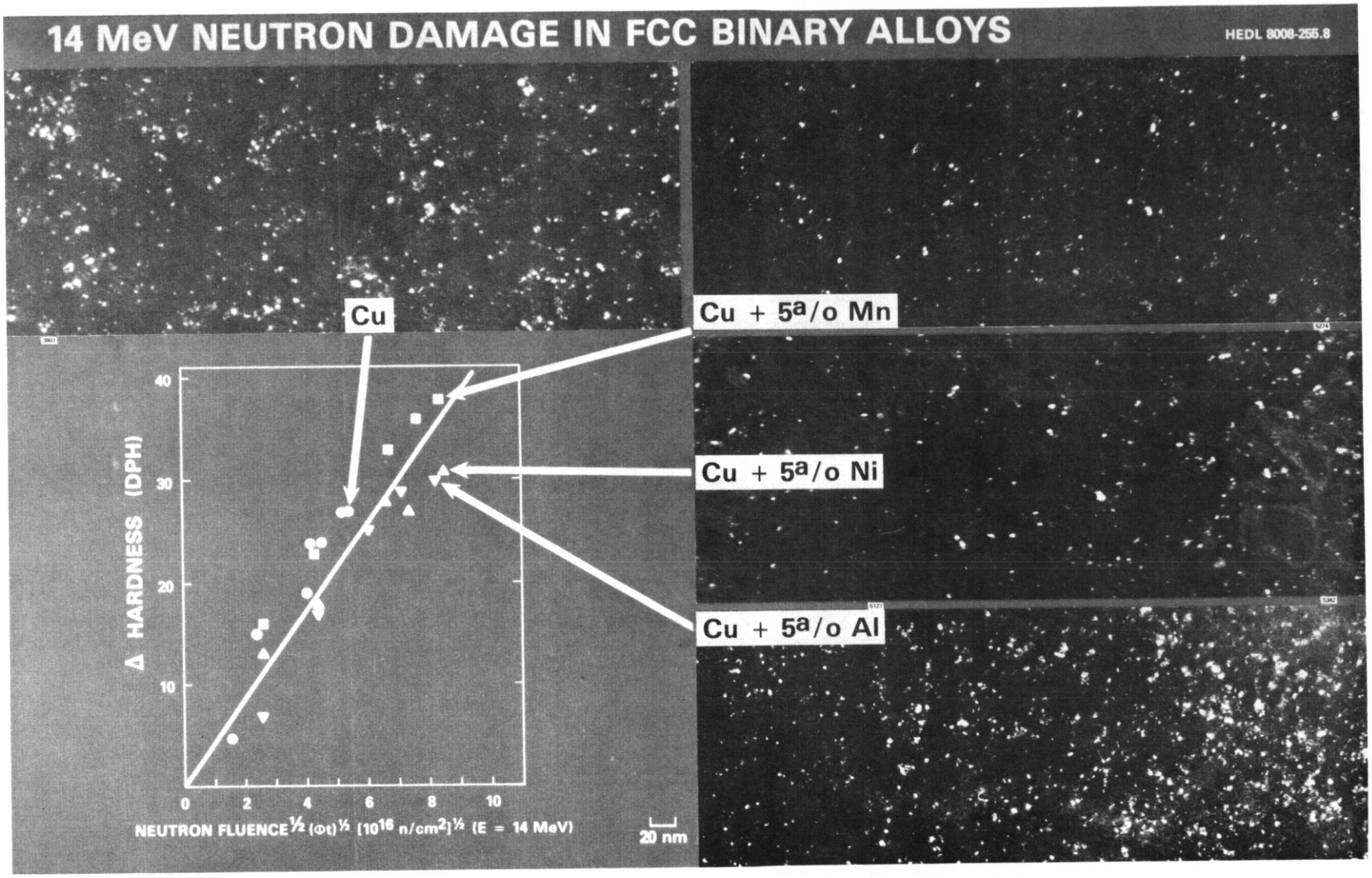

FIGURE 1. Microhardness and Microstructure of Copper and Copper Alloys Irradiated in RTNS-II at 25°C with 14-MeV neutrons. The thickness of the foils imaged here are comparable for the binary alloys, but are roughly twice that of the copper foil.

TABLE 1

MICROSCOPY DATA - RTNS-II COPPER BINARY SERIES

Alloy	Neutron Fluence (10^{17} n/cm^2)	$\bar{d}$ Cluster Diameter (nm)	ρ Cluster Conc./ (10^{17}/cm^3)	($\rho/\phi t$) Cluster Conc./ Unit ϕt	N Total Defect Density (10^{19} (defects/cm^3)*	($N/\phi t$) Defect Density/ Unit ϕt	PKA Conc. (10^{17}/cm^3)	ρ/PKA
Cu	0 [illegible]**	3.0	0.25	0.33	0.3	44	0.16	1.6
Cu	[illegible]	[illegible]	[illegible]	0 48	[illegible]	[illegible]	0 [illegible]	[illegible]
Cu +5% Mn	[illegible] 4	[illegible] 7	[illegible] 4	0 4[illegible]	[illegible]	50	[illegible]	[illegible]
Cu +5% Ni	[illegible]	[illegible]	[illegible]	0 47	[illegible] 5	4[illegible]	[illegible]	[illegible]
Cu +5% Al	7 [illegible]	[illegible] 0	[illegible]	[illegible] 08	5 [illegible]	8[illegible]	[illegible] 5[illegible]	5 [illegible]
Cu +5% Al	[illegible] 8	[illegible] 5	[illegible]	0 [illegible]	5 8	85	[illegible] 45	4 [illegible]

[illegible]his calcul[illegible]ion [illegible]ssum[illegible]s d[illegible]fect clu[illegible]ter[illegible] to [illegible]e circ[illegible]lar di[illegible]ks of eith[illegible]r vacancies [illegible]r inter[illegible]titials
* [illegible]he fluence [illegible]evel for [illegible]his specimen is [illegible]ncer[illegible]ain to within ±50% [illegible]f quot[illegible]d valu[illegible].

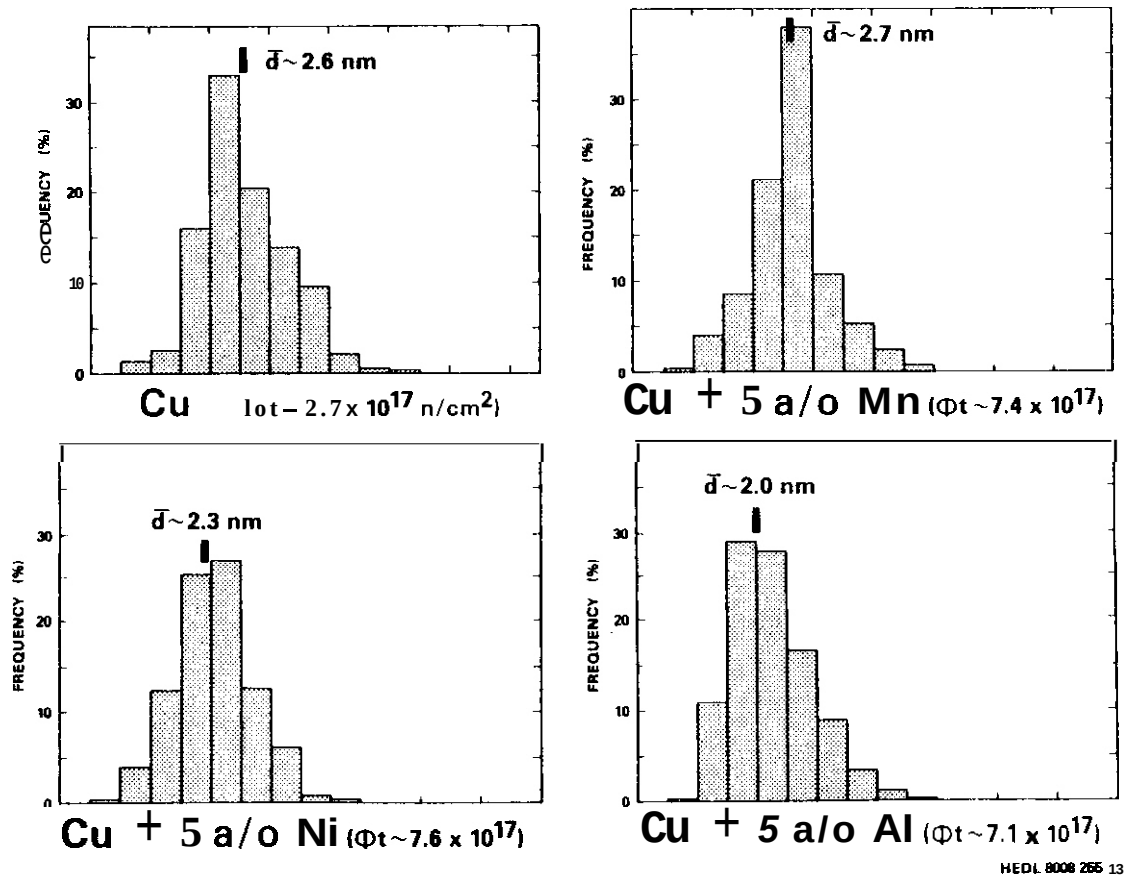

FIGURE 2. The size distribution of visible defect clusters formed in the copper and copper alloys. The mean size of the clusters is indicated.

copper specimen shown in Figures 1 and 2 was irradiated to a much lower fluence than were the other alloys. Another pure copper specimen at even lower fluence was also found to have roughly the same size distribution.

For a given diamical diffraction condition, the defect clusters produce black/white contrast images which are parallel to specific crystallographic directions. The defect clusters appear to be platelets with Burger's vectors of a/2 <111> and a/2 <110>. Preliminary analysis of the defects with the "2½D" technique") has identified both vacancy and interstitial clusters

5.4 Discussion

For fluences approaching 10^{18} n/cm^2 (0.004 dpa) at flux levels of $\leq 2 \times 10^{12}$ n/cm^2 at RTNS-II, the PKA-cascade damage events and their subsequent internal rearrangements can be considered to be essentially isolated events, both in space and time. The evidence supporting this conclusion is that the visible cluster density is linear with fluence, the mean size of these clusters is independent of fluence and, consistent with the expectations of most hardening theories, the hardness measurements vary linearly with the square root of the fluence with no measurable incubation period. This conclusion is significant in that no judgment concerning the magnitude of defect survivability can be made if a significant fraction of the point defects created by each cascade are erased by subsequent cascades.

There are several significant observations to be made concerning the size of the clusters. First, the clusters are significantly larger than indicated directly by current cascade/clustering models. Second, the hardness calculations indicate that the total hardening is independent of the alloy while the visible cluster density is significantly larger in the copper-aluminum alloy. This suggests that a substantial fraction of the defects are in clusters which are smaller than the resolution limit of the microscope.

A lower-bound estimate of the number of invisible clusters can be made using the following logic. If the copper and copper plus 5% aluminum alloys exhibit identical hardening, then the density per unit fluence ($\bar{\rho}$) and diameter (d) of the invisible (i) and visible (v) clusters should obey the following relationship:

Copper		Copper + 5% Aluminum

$$\bar{\rho}_v^{Cu}\, d_v^{Cu} + \bar{\rho}_i^{Cu}\, d_i^{Cu} = \bar{\rho}_v^{Al}\, d_v^{Al} + \bar{\rho}_i^{Al}\, d_i^{Al} \qquad (1)$$

Rearranging this expression leads to

$$1 + \frac{\bar{\rho}_i^{Cu}\, d_i^{Cu}}{\bar{\rho}_v^{cu}\, d_v^{cu}} \quad \frac{\bar{\rho}_v^{Al}\, d_v^{Al}}{\bar{\rho}_v^{cu}\, d_v^{cu}} \quad \frac{\bar{\rho}_i^{Al}\, d_i^{Al}}{\bar{\rho}_v^{cu}\, d_v^{cu}} \,. \tag{2}$$

where the first term on the right hand side is a known quantity and therefore

$$\frac{\bar{\rho}_i^{cu}\, d_i^{cu}}{\bar{\rho}_v^{Cu}\, d_v^{Cu}} = 0.79 + \frac{\bar{\rho}_i^{Al}\, d_i^{Al}}{\bar{\rho}_v^{cu}\, d_v^{cu}} \tag{3}$$

If one assumes that no clusters are invisible in the 5% aluminum alloy, the above expression defines the lower limit of the hardening due to the invisible cluster population in copper. The resolution limit of the microscope in these studies is ~1.0 nm and it is not unreasonable to assume that the mean size of the invisible clusters lies in the range $0.5 \leq d_i^{Cu} \leq 1.0$ nm since a typical atomic diameter is 0.25 nm. Since the mean visible cluster diameter is about 2.5 nm, then $d_i^{Cu}/d_v^{Cu} \sim 1/3$. Using this relationship and assuming that the clusters are circular loops, the following quantities can be calculated, using the values for copper at 2.7×10^{17} n/cm^2 and the average values for Cu + 5% Al.

Fraction of hardening due to invisible defect clusters:

$$\frac{\bar{\rho}_i^{cu}\, d_i^{cu}}{\bar{\rho}_v^{cu}\, d_v^{cu} + \bar{\rho}_i^{cu}\, d_i^{cu}} \gtrsim 44\% \tag{4}$$

Fraction of invisible defect clusters:

$$\frac{\bar{\rho}_i^{cu}}{\bar{\rho}_v^{cu} + \bar{\rho}_i^{cu}} \gtrsim 70\% \tag{5}$$

Fraction of defects in the form of invisible clusters:

$$\frac{\bar{\rho}_i^{Cu} (d_i^{Cu})^2}{\bar{\rho}_v^{Cu} (d_v^{cu})^2 + \bar{\rho}_i^{Cu} (d_i^{Cu})^2} \gtrsim 21\% \qquad (6)$$

The total defects in the visible clusters in a specimen irradiated to 7.5 x 10^{17} n/cm^2 is *3.6* x 10^{19} defects/cm^3, which means that the visible and invisible clusters can account for at least 4.6 x 10^{19} defects/cm^3.

Assuming 8.42 x 10^{22} atoms/cm^3, a displacement cross section of 3690 barns,(2) and two defects per displacement leads to the conclusion that 4.7 x 10^{20} defects/cm^3 were originally created. At least 9.7% now survive. (Remember that 9.7% is a lower bound estimate in that some clusters in the 5% aluminum alloy must also be invisible.)

It is important to notice that the above analysis assumes that the solute hardening and defect cluster hardening are directly additive and that the radiation hardening is insensitive to the magnitude of the solute hardening. As shown in Table 2, the differences in measured hardness of the alloys in the unirradiated condition are qualitatively consistent with that expected on the basis of an increase or a decrease in the lattice parameter. Note that the concentration of the solute atoms ($\sim$4 x 10^{21} atoms/cm^3) is about 100 times larger than that estimated for the defect clusters. Since the magnitude of solute hardening is comparable to or less than that of the defect cluster hardening, the hardening per solute atom is about two orders of magnitude smaller than that due to defect clusters and can be considered separable and additive.

The data presented in this report also appear to indicate that solutes such as nickel and manganese have no significant effect on the damage production and recombination process in copper. This is not surprising in that the atomic weights of the three elements are similar. The atomic weight is an

TABLE 2

ROOM TEMPERATURE HARDNESS OF UNIRRADIATED ALLOYS

Alloy	Hardness (DPH)	Solute Hardening (DPH)	Change in Lattice Parameter (%)
pure copper	56	0	0
copper + 5% nickel	58	2	-0.14
copper + 5% aluminum	66	10	+0.33
copper + 5% manganese	73	17	+0.47

important determinant of the amount of energy trahsferred from the neutron. The difference in atomic weight of solute and solvent atoms also affects atomic replacement sequences and energy propagation in the lattice. The magnitude and sign of the difference in lattice parameter does not appear to be a decisive factor either.

The aluminum atom has only 43% of the mass of the average copper atom however. This means that per collision the aluminum atoms will receive a greater share of the neutrons energy. There will also be a ~15% inefficiency of energy transfer between an energetic aluminum atom and the copper atoms which compose 95% of the alloy. These factors may have important consequences in the spatial distribution of damage in the cascade.

For the present, it appears that solutes such as aluminum lead to substantial differences in the in-cascade clustering of point defects and therefore affect the subsequent visibility of such clusters. It is also possible that interactions may exist between vacancies and elements such as aluminum. These interactions would also affect the defect clustering and recombination processes.

5.5 Comparison With Other Data

The copper data of this study can be compared to that of Mitchell[3], who irradiated two heats of copper in RTNS-I at 25°C. The postirradiation

microstructure of Mitchell's specimens was similar to that of this study. There was a difference, however, in the impurity solute level of his specimens, each containing about 500 appm vs. the <25 appm level of this study. In light of the conclusion of this study that up to five atomic percent of solute does not change the level of radiation-induced hardness, one would not expect the difference between 25 and 500 appm to be significant.

Mitchell measured the change in 0.2% offset yield strength rather than microhardness. However, using the relationship between indenter hardness and the true flow stress of a metal[4,5], one can estimate the change in 0.2% offset yield strength $\Delta\sigma_Y$ that would be expected for the specimens of this study.

$$\sigma \sim DPH/3, \text{ or, } \Delta\sigma_Y(MPa) = 3.27\ \Delta DPH(Kg/mm^2) \qquad (7)$$

Figure 3 shows that a good correlation is obtained between Mitchell's results and estimates of yield strength based on microhardness measurements, particularly at fluences where the hardening is significant.

5.6 Conclusions

At least 70% of the clusters produced by 14-MeV neutrons in pure copper and in 5%-nickel and 5%-manganese copper alloys are smaller than the resolution limit of the microscope (~1 nm). It also means that TEM, used alone, is an inadequate tool to study the survivability of point defect clusters.

Providing that assumptions can be made on the distributions of cluster size as a function of fluence, microhardness measurements are a very good method to assess the relative amounts of defects, both visible and invisible. A better approach is the coupled use of TEM and microhardness measurements.

A minimum of 9-10% of the calculated displacements survive the original defect cascade event.

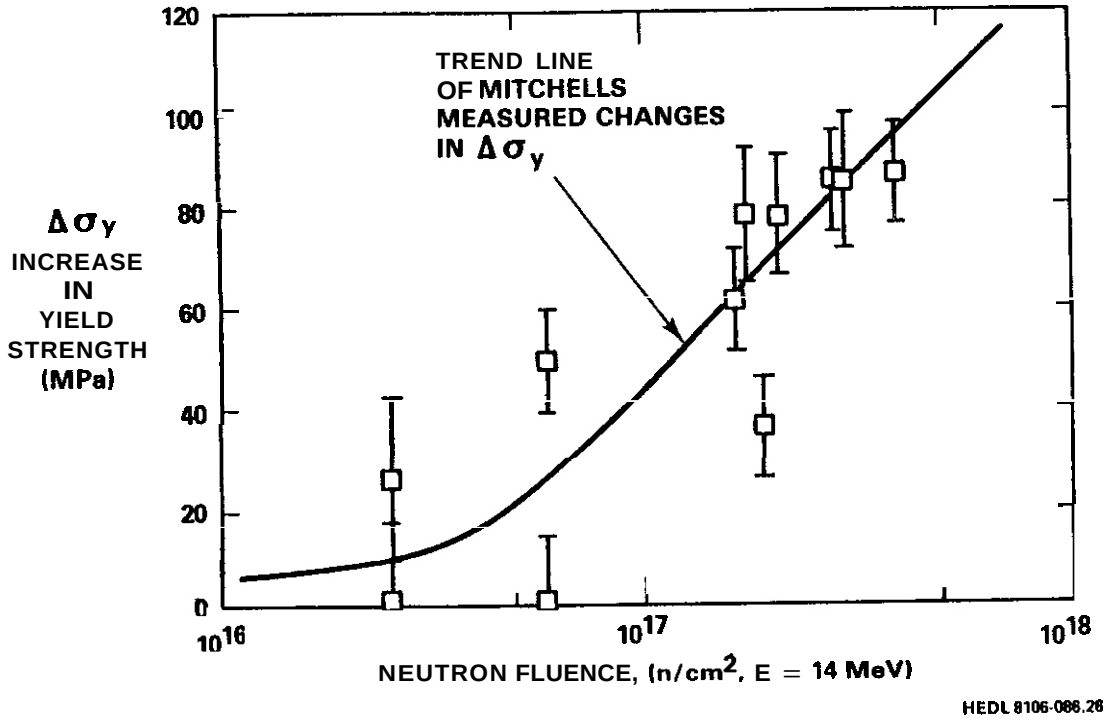

FIGURE 3. Comparison of calculated estimates of yield stress changes (based on microhardness measurements of o per irradiated in RTNS-II) with the results of earlier testsF35 performed on copper specimens irradiated in RTNS-I.

Additions of Ni or Mn have no observable effect on the damage production and recombination process in copper. The addition of Al has a strong effect on measurements of defect size distributions and possible defect survivability. None of these elements affect the radiation-induced change in microhardness.

6.0 References

1. J. B. Mitchell, Acta Met., 24, (1976) pp. 147-152.

2. D. G. Doran and N. J. Graves, "Displacement Cross Sections and PKA Spectra: Tables and Applications", USEROA Report HEDL-TME 76-70 (December 1976).

3. J. B. Mitchell, R. A. Van Konynenburg, C. J. Echer and D. M. Parkin, "DT Fusion Neutron Radiation Strengthening of Copper and Niobium, UCRL Preprint UCRL-77357, Rev. 1.

4. F. A. McClintock and A. S. Argon, "Mechanical Behavior of Materials", Addison-Wesley, Reading, Massachusetts, pp. 443-465.

5. G. E. Dieter, Mechanical Metallurgy, 2nd Edition McGraw-Hill, New York, pp. 389-402.

7.0 Future Work

Analysis and documentation will be completed on the nickel-alloy series irradiated in RTNS-II.

8.0 Publications

This paper will be published in the Proceedings of the Second Topical Meeting on Fusion Reactor Materials, August 9-12, 1981, in Seattle, WA.

CHAPTER 3

FUNDAMENTAL MECHANICAL BEHAVIOR

CRACK PROPAGATION CHARACTERISTICS IN HELIUM IRRADIATED TYPE 316 STAINLESS STEEL

R. D. Gerke, T. Hanamura, and W. A. Jesser (University of Virginia)

1.0 Objective

fhe purpose of this work is to investigate the nature of crack propagation in irradiated materials containing voids or bubbles by in-situ tensile testing in an HVEM, and to relate some proposed parameters to specimen ductility.

2.0 Summary

From continuous observations of the dynamic behavior of cracks during tensile tests in an HVEM, it was found that in relatively ductile type 316 stainless steel a crack propagates in a oscillatory manner with the crack angle and crack tip angle varying widely as the crack lengthens. The mean crack propagation oirection also varies widely during propagation. The effect of helium irradiation of sufficient dose to produce large (diameter 120 nm) bubbles is to reduce the indgnitude of the oscillations, reduce the mean value of the crack angle, anu increase the crack-tip angle as a result of significant grain boundary sliding.

3.0 Program

Title: Simulating the CTR Environment in the HVEM
Principal Investigators: W. A. Jesser and R. A. Johnson
Affiliation: University of Virginia

4.0 Relevant DAFS Program Plan Task/Subtask

Task II.C.13 Effects of Helium and Displacements on Crack Initiation and Propagation

5.0 Accomplishments and Status

5.1 Introduction

There are several microstructural parameters typically used as measures of ductility. Crack-tip angles and plastic zone widths are widely used.[1,2] It has previously been shown that cracks propagating in unirradiated solution annealed samples of 316 stainless steel tested at room temperature typically exhibit angles of about 10°.[3] However, further investigation of the crack angles has shown that as ductility increases the crack propagation characteristics become more complex and suggest that more detail is needed to understand the crack propagation characteristics in non-brittle materials. Several parameters have been proposed and investigated in this study.

5.2 Experimental Results

5.2.1 Experimental Procedure

In this study all unirradiated and helium irradiated specimens (Flux: 1.4×10^{15} ions $\cdot$ cm^{-2} $\cdot$ sec^{-1}, Dose: 4.2×10^{17} ions $\cdot$ cm^{-2}) were type 316 stainless steel solution annealed at 1000° C for one hour, and electropolished to electron transparency for 400 kV electrons. Then the samples were tensile tested to failure at room temperature in an HVEM. During the crack propagation, data was obtained from still micrographs and video tape. Also quantitative elongation data was obtained by using a tensile rod equipped with a linear transducer. From these sources crack angle, @, crack-tip angle, e, crack length, L, and crack directional angle against the tensile axis, α, was obtained as a function of total specimen elongation (crosshead displacement).

5.2.2 Correlation Between Crack Length and Total Elongation

Still micrographs were obtained from the HVEM during tensile testing of unirradiated specimens. The crack length L was measured directly from these micrographs and plotted in Figure 1 against the specimen elongation, which was ob-

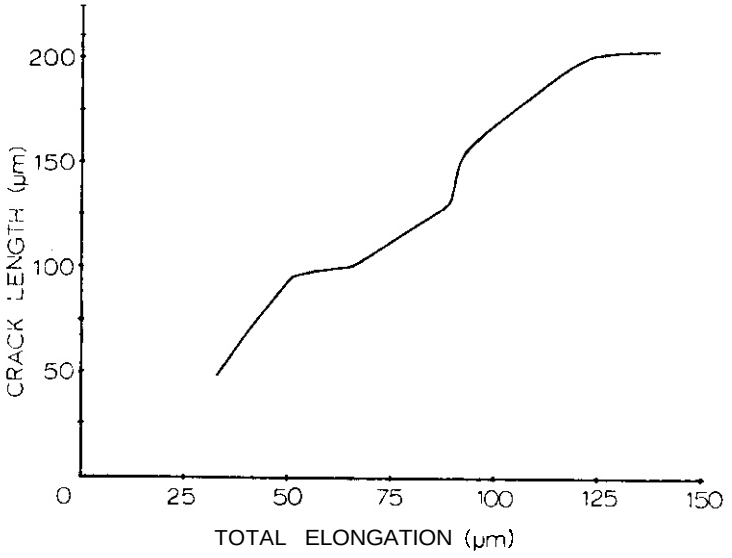

FIGURE 1: Graph of Crack Length Data Produced by Two Cracks versus Total Elongation for an Unirradiated Specimen Tested at Room Temperature.

tained from a strip-chart recording of the output of the elongation transducer. From this graph it appears that L follows a step-like relationship to elongation, the latter being smooth and continuous with time. In the specimen from which this data was obtained, two cracks, lying along the same line but pointing in opposite directions, propagated in opposite directions and exhibited the same L versus elongation graphs. Observations of both crack-tip positions showed that both cracks propagated and stopped propagating together. They were synchronized in their propagation behavior. Figure 1 is a graph which sums the data from both cracks.

5.2.3 Relationship Between Crack Angle and Crack Length

In this study crack angle Θ and crack-tip angle θ were considered separately. Crack-tip angles were measured at the crack tip, while crack angles were measured from the crack flanks approximately 10-15 μm behind the crack tip. The angle, a, is the angle between the tensile axis and the mean crack propagation direction.

All three crack angles were measured as a function of crack length for irradiated and unirradiated specimens. However, it was found that the crack-tip angle was very sensitive to the presence of grain boundary sliding, while the crack angle was insensitive to grain boundary sliding. For this reason the crack angle, Θ, rather than the crack-tip angle, θ, was plotted against L. The crack direction, *a*, was also plotted. These graphs were constructed for unirradiated and helium irradiated specimens pulled under similar conditions and are shown in Figure 2. It is clear from these graphs that large oscillations of the variables occur during crack propagation. There is a thickness gradient in the specimen, and the electrothinned section with its perforation acts as the initiation site for the cracks. As a result of this condition the cracks propagate from thin regions ($\sim$ 0.1 μm) to thick regions ($>$ 1 μm) and hence the crack lengths beyond two hundred microns represent the thick regions. From Figure 2 it is seen that the variation of crack angle in the unirradiated specimen is smaller in the thin region than it is in the thick region. In the helium irradiated specimen the variation of the crack angle in the thin region is smaller than that of the unirradiated sample in the same region. In the thicker region of the helium irradiated sample, the amplitude of oscillation of crack angle increases and approaches that of the unirradiated sample. This result agrees with previous reports[4] from this facility and shows that the helium affected region is limited to the thin sections of the specimen.

Also seen in Figure 2 is the variation of crack direction angle, *a*, during crack propagation, which seems to differ in unirradiated and helium irradiated specimens. The parameter, *a*, changes value more frequently and oscillates with a greater amplitude in the unirradiated specimen than in the irradiated one. Significant grain boudary sliding was observed in the irradiated specimen and can account for the reduced frequency of change in *a* versus crack length.

5.2.4 Composite Relation Between Crack Angle, Crack-tip Angle, Crack Length and Total Elongation

The characteristics of crack propagation during tensile testing are complex but correlations can be expected between the lengthening steps of a crack and its

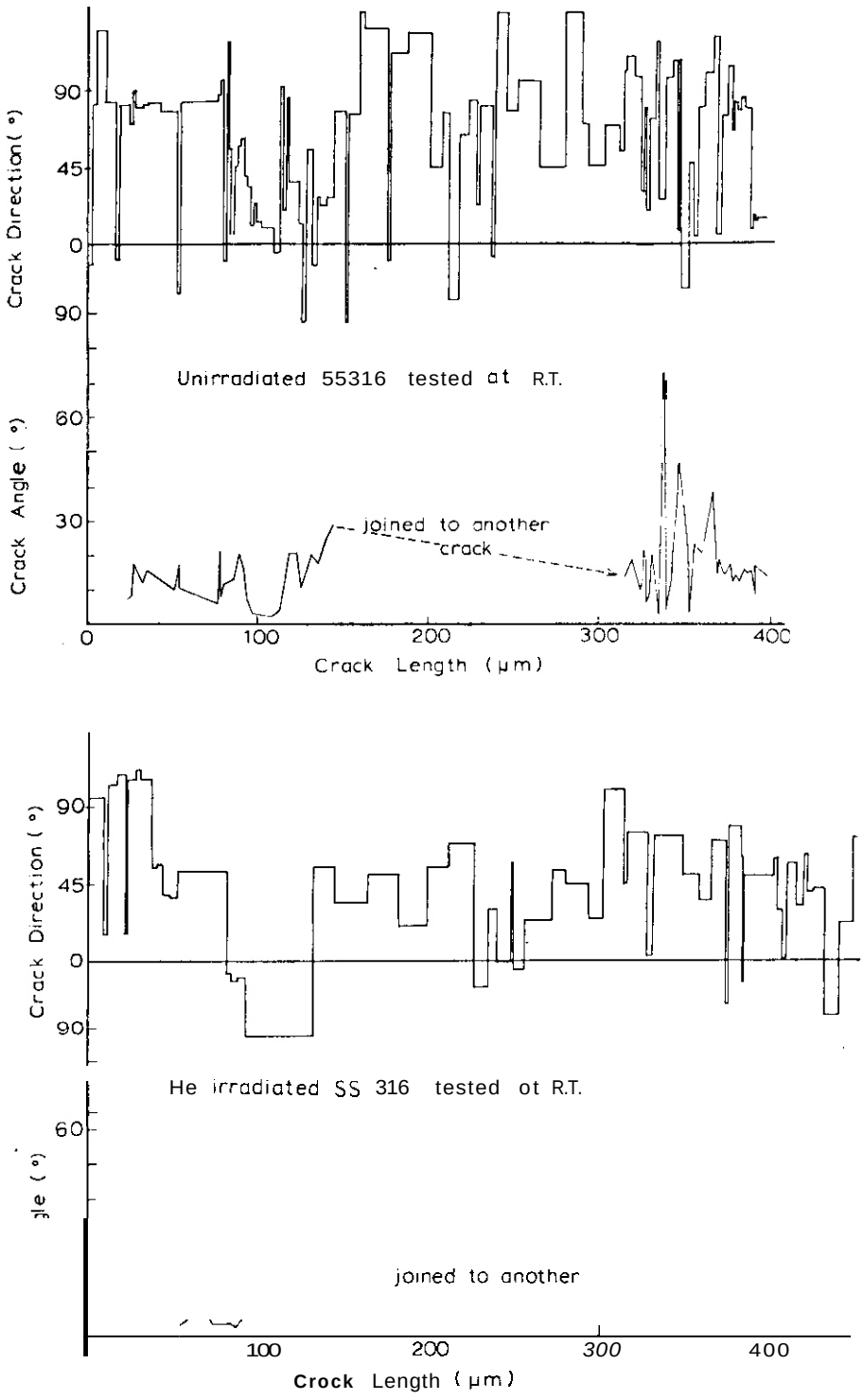

FIGURE 2: Graphs of Crack Angle and Crack-Direction Angle versus Crack Length for Unirradiated and He-Irradiated 316 SS Tested at Room Temperature.

angular oscillations. Any correlations would be revealed in a plot of crack length as well as crack angle and crack-tip angle versus elongation. Such a graph is shown in Figure 3 which applies to an unirradiated specimen. The following crack propagation features are suggested to a limited extent by this figure. Steady increases in crack length seem to occur when crack angle and crack-tip angle are both smoothly varying during propagation. Crack-tip blunting (increased e) is associated with a slowly propagating crack. Sharp crack-tip angles might be associated with rapid increases in crack length. Finally, rapid oscillations in crack-tip angle are not accompanied by rapid oscillations of crack angle.

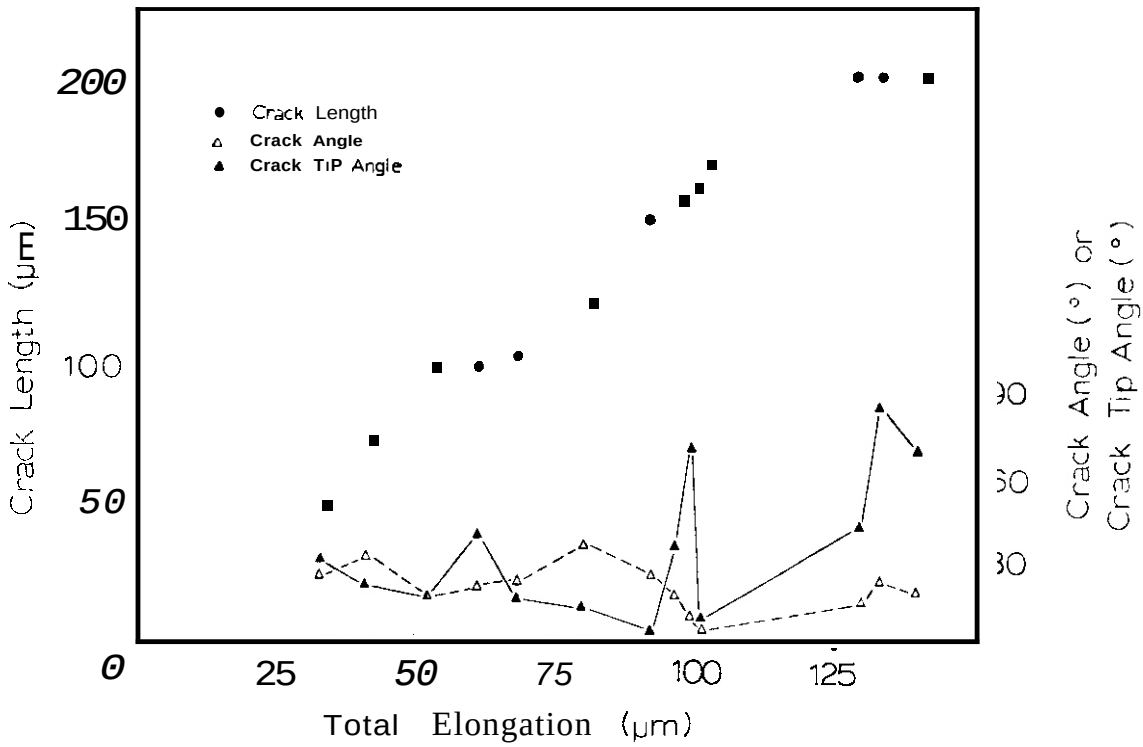

FIGURE 3: Graphs of Crack Length, Crack Angle and Crack-Tip Angle versus Total Elongation for Unirradiated 316 SS Tested at Room Temperature.

5.3 Discussion

The oscillations observed in the characteristic crack parameters,@, θ, a, and

L show that cracks propagate in a "jerky, breathing" manner which is associated with large changes in direction and crack-tip angle. This manner of crack propagation is not the result of an intersection of the crack with grain boundaries because rapid oscillations occur when the crack is propagating within one grain. It is possible that the oscillations in crack-tip angle are caused by the build-up and release of localized strain energy. During the crack blunting stage where e is increasing and L is only slowly increasing, an increase in strain energy may occur. Once a critical strain energy density is reached the crack may suddenly propagate as a crack with a sharp tip, thereby converting the stored strain energy density into energy absorbing plastic deformation processes. The variations in α reflect the inhomogeneity of the plastic deformation process. This type of oscillatory behavior during crack propagation would be expected to occur in relatively ductile material and not during brittle crack propagation.

The details of the plastic deformation mechanisms associated with crack propagation can provide an understanding of flow localization. The crystallography of the grain and the morphology of the crack and its relation to the tensile axis should allow one to predict the subsequent crack behavior when the strain energy density variations near the crack are known. The relation of this approach to that of microvoid coalescense, crack coalescence and the initiation of grain boundary sliding and twinning is not clear at this time;' however, data being collected suggests that these relations can be established.

5.3 Conclusions

In type 316 stainless steel microspecimens tensile tested at room temperature in an HVEM, the following conclusions were found for unirradiated and helium irradiated specimens containing large (diameter 120 nm) bubbles, i.e. for relatively ductile material.

Crack length versus total elongation exhibits a step-like relationship. Large oscillations are found in crack-tip angle and mean crack propagation direction. Significant oscillations in crack angle also occur. The effect of helium irradiation when large bubbles are present is to decrease the

amplitude of the angular oscillations, to decrease the mean crack angle, and possibly to promote grain boundary sliding.

The effect of decreasing specimen thickness is to decrease the amplitude of the angular oscillations.

6.0 References

1. J. I. Bennetch and W. A. Jesser, "Room Temperature Helium Embrittlement in 316 Type Stainless Steel," DAFS Quarterly Progress Report, DOE/ER-0046/3 (1980) 113.

2. D. S. Gelles, L. E. Thomas. and R. W. Powell. HVEM In Situ Deformation of Neutron Irradiated Fe-0.3 Cu, 109th AIME Annual Meeting, Las Vegas, Ne. (Feb. 24-28, 1980).

3. J. A. Horton and W. A. Jesser, Effects of Radiation on Materials (ASTM Proceedings) ASTM STP725, D. Kramer, H. R. Brager, J. S. Perrin (eds.) (1981) 642.

4. J. A. Horton, Ph.D. thesis, Materials Science Department, Univ. of Va. (Jan. 1980).

7.0 Future Work

The effect of temperature on crack propagation characteristics will be investigated in an effort to understand the mechanisms of flow localization which results from helium and displacement damage.

THE ROLE OF LUDERS STRAIN IN DETERMINING FLOW PROPERTIES IN STEEL FROM AN INSTRUMENTED HARDNESS TEST

G.E. Lucas and F. Haggag (University of California, Santa Barbara)

1.0 Objective

The purpose of this aspect of the program is to develop test techniques to extract mechanical property information from small volume specimens either being used or planned for use in high energy neutron irradiation experiments.

2.0 Summary

From tests on a set of steels heat treated to exhibit a range of Liiders strains ε_L when tested in tension (ε_L = 0.88% to ε_L = 5.40%) a quantitative correlation was determined between the LUders strain and the geometry of the lip around a ball indentation. Interferometric techniques were found superior to profilometric techniques for lip characterization. In addition, it was found that hardness/microhardness data were best correlated to the homogeneous plastic flow portion of the tensile stress-strain curve.

3.0 Program

Title: Damage Analysis and Fundamental Studies for Fusion Reactor Materials Development

Principal Investigators: G.R. Odette and G.E. Lucas

Affiliation: University of California, Santa Barbara

4.0 Relevant DAFS Program Plan Task/Subtask

Subtask B Fundamental Mechanical Properties

Subtask C Correlation Methodology

5.0 Accomplishments and Status

5.1 Introduction

One test technique of interest in extracting mechanical property information from the small volume specimens used in high energy neutron irradiation experiments is the microhardness test. Consequently, some effort has been undertaken at the University of California, Santa Barbara to develop the microhardness test for this application. The instrumented hardness test and the related ball-microhardness test described previously[1,2] are results of this effort.

In correlating hardness/microhardness data with uniaxial stress-strain data it was found[1] that in steels exhibiting relatively large Luders strains the correlation was uncertain. Consequently, a study was undertaken to 1) develop a technique for predicting the magnitude of Luders strains in steel specimens from a characterization of the geometry of a spherical indentation and 2) determine a methodology for predicting flow properties in steels exhibiting Liiders strain from hardness/microhardness data.

5.2 Materials

Tensile samples were cut from cold-rolled SAE No. 1015 steel sheet. The samples in groups of 4 were subjected to a range of elevated temperature, 20 minute anneals to obtain steels which exhibited a variety of Luders strains when tested in uniaxial tension. Anneal temperatures ranged from 121°C to 621°C.

5.3 Experimental Procedure

Following heat treatment, the samples were pulled in uniaxial tension at room temperature in an Instron mechanical testing machine. All tests were conducted at a crosshead speed of .021 mm/sec. Data from these tests were used to construct true-stress, true-plastic-strain curves for each set of heat treated steels. And these data were regressed to obtain values of the Luders

strain, the lower yield strength, $\sigma_{\ell y}$, and the strain hardening exponent n and coefficient K for homogeneous plastic flow.

The undeformed end tabs of the tensile samples were then subjected to ball hardness and microhardness tests, again at room temperature. These techniques have been described previously.[1,2] The hardness tests were conducted on an Instron® testing machine with a .159 mm diameter ball indenter; maximum loads were in the range .90 kg to 18.2 kg; all indentations were made at a cross head speed of 8.47×10^{-5} cm/sec. The microhardness tests were conducted on a Tukon® microhardness tester with both a .159mm and a .025mm diameter ball. Loads were applied in the range 2009 to 1000g. These data were then correlated to the uniaxial tensile data.

Selected indentations were characterized by both profilometric and interferometric techniques. The most systematic study was done on indentations made on each of the heat treated steels at a load of 18.2 kg. Profiles of each indentation were obtained with a Bendix® RCC-4 profilometer; and the geometric features, d, W, h_ℓ and h_P, as defined in Figure 1, were measured from the profile traces. In addition, the area A between the "Reference Surface" and the indentation lip boundary was measured with a planimeter for each trace. Empirical correlations between these features and ε_L were then investigated.

Optical interferographs were also obtained for selected indentations. Interferographs were made at 20x on a Unitron series N metallograph using an interference objective and a Xe light source and cadmium filter to obtain monochromatic light of wavelength A = 644 nm. These data were compared with the profilometric data, and correlations between interferographic features and ε_L were investigated.

5.4 Results

The tensile data regression parameters ε_L, σ_{QY}, K, and n are given in Table 1. As can be seen, steel samples were obtained which exhibited Luders strain in

uniaxial tension from 0.88% (as received) to 5.04% (aged 20 minutes at 621°C). However, other flow characteristics changed with heat treatment as well. In particular, the lower yield strength, the strain hardening exponent, and the strain hardening coefficient varied with ε_L as

$$\ell n \frac{K}{\sigma_{QY}} = \varepsilon_L - n \ell n \varepsilon_L \qquad (1)$$

in agreement with the observations of Morrison[3]

TABLE 1
TENSILE DATA REGRESSION PARAMETERS

Specimen Type	ε_L (5%)	σ_{1Y} (Mpa)	K (Mpa)	n
S2	.88	245	473	.138
S4	1.74	257	478	.150
S6	2.16	272	495	.154
S8	2.76	281	484	.147
S10	3.25	290	533	.175
S11	3.86	293	534	.182
S15	4.70	301	597	.221
S18	4.80	281	615	.256
S20	5.40	296	605	.244

Several approaches to correlating the hardness/microhardness data with uniaxial tensile data were tried. The best approach of those tried was found to be a correlation between the hardness data and the homogeneous flow portion of the uniaxial stress-strain curve, back-extrapolated to zero plastic strain. This correlation is given by

$$\varepsilon_P = .19\ d/D$$

$$\sigma = \frac{4W}{\pi d^2}\frac{1}{\Psi}$$

$$\Psi = \begin{cases} 1.07 & \phi \leq 1 \\ 1.07 + .76\ \ell n\ \phi & 1 < \phi < 24 \\ 3.48 & \phi \geq 24 \end{cases} \qquad (2)$$

$$\phi = \frac{\varepsilon_p E}{.43\ \sigma}$$

where σ = true stress at a true plastic strain ε_P
W = applied (maximum) load in the hardness test
D = indenter ball diameter
E = elastic modulus of the specimen

Although the form of Eqn. (2) is identical to the correlation reported earlier, "") the coefficients .76 and 3.48 are somewhat larger. This appears to be the result of a strain rate effect, as the hardness tests were conducted at a larger effective strain rate than the tesile tests[4]. For the less strain rate sensitive material investigated earlier,[1] this effect wa5 not apparent.

Equation (2) fit all of the hardness/microhardness data to the corresponding tensile data, i.e. the homogeneous flow portion of the tensile stress strain curve. A representative fit is given in Figure 2. Note that the hardness data fits the back-extrapolated line of the homogeneous flow part of the tensile curve as well. Consequently, the entire tensile curve can only be predicted from hardness data with such a correlation if the value of ε_L can be determined from the hardness test; then a horizontal line drawn on the u-E_P plot, intersecting the homogeneous flow curve at ε_L, would correspond to the

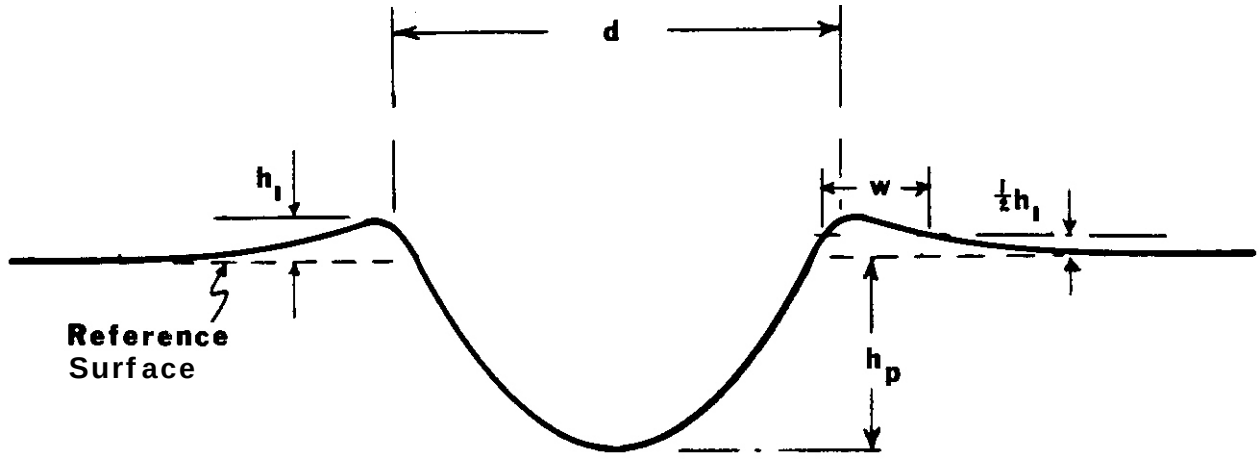

FIGURE 1. Geometric Features of an Indentation Profile

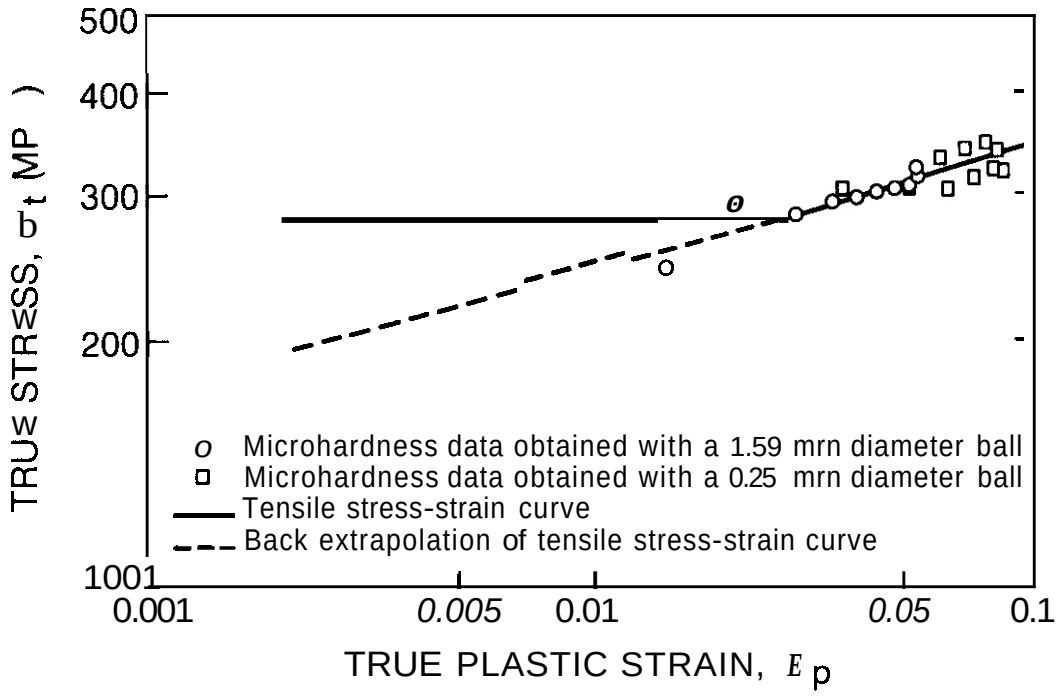

FIGURE 2. Comparison of Hardness/Microhardness Derived Stress-Strain Data with the Uniaxial Tension Curve of Sample Type S8.

Liiders plateau. To this end, some correlation between the indentation geometry and ε_L was sought.

The best correlation between features of the indentation obtained with the profilometer and ε_L was found to be for A, the area between the "Reference Surface" and the indentation lip boundary. The empirical correlation is shown in Figure 3. Note that there is a considerable amount of uncertainty associated with each data point as well as scatter from point to point. The reasons for this will be discussed shortly. For now, though, it is important to note that despite the data scatter a general trend was observed; the area under the lip increased with ε_L.

A much better characterization of the lip geometry was obtained with interferometric techniques. Representative results are shown in Figure 4 where the interferographs and corresponding profilometer traces are shown for indentations made on three different steels at 9.07 kg. In the interferographs each fringe corresponds to a displacement of $\lambda/2 = 322nm$ between the objective reference plane and the sample surface. Hence, the relatively few fringes indicate a small lip height around the indentation in Figure 4a and the larger number of fringes indicates a steeper and higher lip in Figure 4c. It is evident that as the material exhibits a larger ε_L, it also piles up around a ball indenter to a greater extent during penetration. Such behavior is consistent with the relationship between ε_L, n and the piling up phenomenon.

It should be noted that a set of nested fringes appears at the top of the lip in Figure 4. This is important for two reasons. First, this indicates that the edge of the lip is crown-like in appearance. This explains much of the data scatter in Figure 3, as the profilometer trace gives no indication of whether the profilometer stylus traced over a peak or a valley at the edge of the lip. Second, the crown-like appearance of the lip appears to be characteristic of steels exhibiting Luders strains and not of other materials exhibiting strictly homogeneous flow.[5] Consequently, such features may be useful in detecting the onset of other inhomogeneous plastic flow phenomena

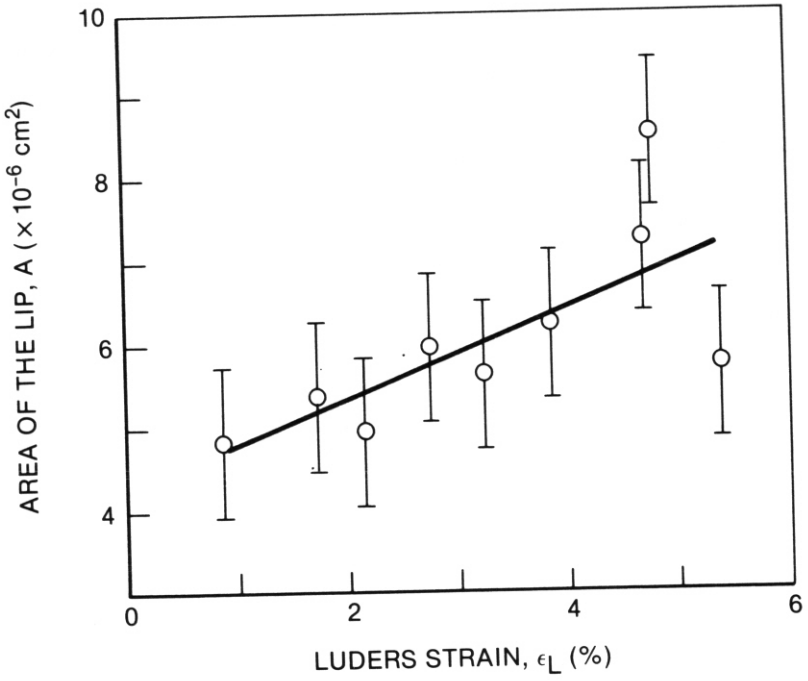

FIGURE 3 Relationship Between the Area Measured Under the Indentation Lip Profile and Lüders Strain.

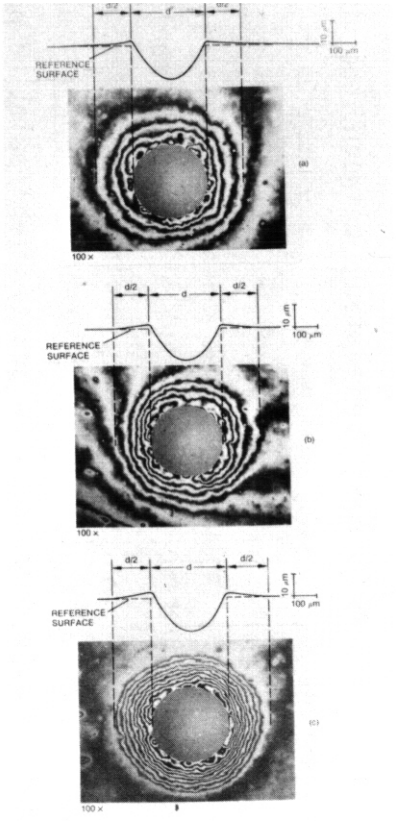

FIGURE 4. Profilometer Traces and Interferographs of Indentations Made at 9.07 kg for Specimen Types a) S2, b) S8 and c) S20.

such as localized plastic flow in irradiated metals. This is currently under further investigation.

5.5 Conclusions

It appears that the flow properties of steels exhibiting Lüders strains can be determined from ball hardness and/or ball microhardness data. Hardness data can be correlated to the homogeneous flow portion of the tensile stress-strain curve, and the geometry of the lip can be analyzed to determine the magnitude of the Liiders strain exhibited by the specimen.

The best technique found for examining indentation lip geometry was optical interferometry. This permits a three-dimensional representation of the indentation to be recorded and it should be compatible with microhardness test techniques. Moreover, some features of the indentation obtained in such a fashion may permit detection of localized flow phenomena other than Luders strain.

6.0 References

1. G.E. Lucas, et al., "Development of Instrumented Hardness Techniques," DAFS Quarterly Progress Report, DOE/ET-0065/5 (1979) 199.

2. G.E. Lucas, et al., "Small Specimen Test Development," DAFS Quarterly Progress Report, DOE/ER-0046/4 (1981) 45.

3. W.B. Morrison, "Plastic Instability During Lüders Deformation in Ultrafine-Grained Low-Carbon Ferritic Steel," Amer. Soc. Metals, 2nd Int. Conf. on Strength of Metals and Alloys (1970) 879.

4. C.H. Mok, "The Dependence of Yield Stress on Strain Rate as Determined from Ball-Indentation Tests," Exp. Mech., 6, 2 (1966) 87.

5. J.H. Underwood, "Residual Stress Measurement Using Surface Displacements Around an Indentation,' Proc. Soc. Exp. Stress Analysis, 30, 2 (1973) 1.

7.0 Future Work

A Tukon® microhardness tester is being modified to incorporate the techniques learned in this study. Load capacity is being increased from 1 kg to 10 kg, optical interferometry equipment is being added, and the output is being digitized for use in computerized data analysis. This should significantly enhance data acquisition and analysis for the ball-microhardness technique.

8.0 Publications

1. G.E. Lucas and N.F. Panayotou, "Microhardness Tests for High Energy Neutron Source Experiments," to be presented at the Second Topical Meeting on Fusion Reactor Materials, Seattle, August 8-12, 1981.

2. F. Haggag and G.E. Lucas, "Determination of Flow Properties of Steel From an Instrumente'd Hardness Test," to be presented at the ANS Winter Meeting, San Francisco, Nov. 29 - Dec. 4, 1981.

CHAPTER 4

CORRELATION METHODOLOGY

TENSILE PROPERTY CORRELATION FOR 20% COLD WORKED 316 STAINLESS STEEL

R. L. Simons (Hanford Engineering Development Laboratory)

1.0 Objectives

The objective of this work is to develop correlation methods for irradiation effects on tensile properties of materials important to magnetic fusion energy devices.

2.0 Summary

Ultimate tensile strength data on 20% cold-worked 316 stainless steel irradiated in fast and thermal reactors and by 14 MeV neutrons were analyzed and a ten-parameter equation was developed to describe the ultimate tensile strength behavior for the temperature range $25 < T < 800°C$. The equation includes the irradiation parameters: displaced atoms, helium content, and irradiation temperature. It is applicable to strain rates $< 5 \times 10^{-4}$/second and test temperatures approximately equal to the irradiation temperature. Uniform elongation data were characterized in terms of yield and ultimate tensile strength data. The total elongation was found to be insensitive to helium at temperatures below 500°C but sensitive to helium above 550°C.

3.0 Program

Title: Irradiation Effects Analysis (AKJ)
Principal Investigator: D. G. Doran
Affiliation: Hanford Engineering Development Laboratory

4.0 Relevant DAFS Program Plan Task/Subtask

Subtask II.C.2.2 Fast spectrum/mixed-spectrum correlations
Subtask II.C.16.1 Correlation model development

5.0 Accomplishments and Status

5.1 Introduction

Degradation of first wall or structural materials due to irradiation is a major consideration in fusion reactor design. A candidate alloy for first wall application in near term fusion devices (such as the Fusion Engineering Device) is 20% cold-worked (CW) 316 stainless steel. Development of correlation equations for irradiation effects in this material will be needed for design of near term fusion devices. There are a number of variables which affect the mechanical behavior of the stainless steel including test and irradiation temperature, product form, material heat (or chemistry), strain rate, irradiation spectrum, etc.

In the development of correlation equations for the tensile properties of 20% CW 316 stainless steel, the primary parameters treated were the effect of irradiation temperature and neutron spectrum. Neutron spectrum effects were characterized by the relative amounts of displacement damage and helium accumulation. Although other transmutation products may have a detrimental effect on the material, their effect was assumed to be negligible in this analysis. Only data from tensile tests performed at low strain rates (5×10^{-4}/second) were used and the test temperatures were required to be near the irradiation temperatures. This report addresses the irradiation behavior of ultimate tensile strength, uniform elongation and total elongation. The irradiation behavior of yield strength was reported previously.[1]

There were two primary sources of data used in this work -- N-lot and T-lot of heat 87210 used for Fast Flux Test Facility (FFTF) cladding[2-3] and D0 heat used in irradiation experiments by Oak Ridge National Laboratory (ORNL).[4-5]

The DO heat contains about twice as much silicon as heat 87210. Other differences between the data sets are differences in the irradiation environment (i.e., fast and thermal reactors) and product form. The DO heat was in the form of round stock tensile specimens while the N and T lots were in the form of tubes.

5.1.1 Data Compilation

The exposure parameter used by Fish et al.[2] in reporting tensile data from irradiations in Experimental Breeder Reactor-I1 (EBR-II) was fluence >0.1 MeV. For application to fusion environments the dose parameter was converted to displaced atoms per atom (dpa). The basis for determining the dpa values were the fluxes and spectrum-averaged displacement cross sections calculated from results obtained from the EBR-II run 50H and run 75D dosimetry tests. The 50H dosimetry was used for the irradiations performed prior to the blanket change (run 56) and the 75D dosimetry was used for the post-blanket change irradiations. For High Flux Isotope Reactor (HFIR) tensile data, the reported dpa values were used except for those from Reference 4. They were high by a factor of two, relative to the other values, because they are based on an earlier conversion of damage energy to displacements. Helium concentrations (hpa) are reported for the HFIR data and are based on a semi-empirical equation for helium production in HFIR.[8] Values for the EBR-II data were determined from the measurement made in EBR-II by McElroy and Farrar.[9]

There were a total of 104 data points used in this analysis. The data were grouped by irradiation temperature. Each group is identified by the mean temperature of the group. The maximum deviation from the mean of any group was 10°C. Since not all of the data were from the same heat or same specimen geometry, the unirradiated property levels were not the same.

Since the largest fraction of the data was from N and T lots of heat 87210, the correlation was tailored to this data set by giving it a weight of 1.0 and the other sets a weight of 0.5 or less. Most of the HFIR data were

given a weight of 0.5. A lower value was assigned to the data from Reference 4 because reported tensile properties deviated substantially from those expected, presumably due to a higher level of mechanical working.[5] The unequal weighting allows the behavior of the 00 heat data to influence the correlation equation while not allowing a large effect due to initial material differences. Furthermore, it is expected that the two materials will behave the same after extended neutron exposure.

5.1.2 Correlation Equation Development

The correlation equation developed assumed that the ultimate tensile strength like the yield strength") was equal to the initial value plus or minus an incremental change in ultimate tensile strength which depends on damage parameter and irradiation temperature. This analysis method is most appropriate for a single heat of material. Below 500°C, an irradiation hardening mechanism(s) was evident which shows a tendency to saturate with exposure. Saturation is definitely evident at low temperatures (<300°C) in CW 304 and M316 stainless steels.[10-11] The form of the yield strength and ultimate tensile strength equations used for the temperature range 25 < T < 800°C is

$$Y = Y_0 + Y_1 (1 - e^{-\beta x}) e^{-\alpha \sqrt{x z}} - Y_2 (1 - e^{-\gamma x}) \qquad (1)$$

where

$$Y_1 = A \quad T - B, \qquad T < T_1 = 773°K$$

$$Y_1 = A \quad T_1 - B, \qquad T \geq T_1 = 773°K$$

$$\beta = \exp (+ C/T)/D,$$

$$\alpha = E \exp (-F/T)$$

$$Y_2 = G (T - T_0) \exp \left\{-H(T - T_0)\right\}, \quad T > T_0$$

$$Y_2 = 0 \qquad , T \leq T_0$$

where A, B, C, D, E, F, G, H, T_0 and γ are fitted constants. The temperature T, is in units of degrees Kelvin, x is the number of displaced atoms per atom, z is the number of helium atoms per atom in units of appm, and

Y_0 is the measured unirradiated strength in MPa. In equation (1), δ dominates at low temperatures giving a saturation effect, while α dominates at high temperatures, resulting in essentially no hardening. In the intermediate temperature range (300–500°C) the ultimate tensile strength shows an initial increase due to irradiation hardening followed by a decrease at high exposures.

5.2 Results and Discussion

5.2.1 Strength Properties

The primary emphasis of this analysis was placed on heat 87210 (N and T lots) with lower emphasis on the DO heat. Table I summarizes the parameters for yield and ultimate tensile strength which minimize the weighted sum of the squares of the residuals for equation (1). The weighted 2σ uncertainty with these parameters is ±70 MPa for yield strength and for ultimate tensile strength. The values for yield strength are slightly different from those previously reported[11]) but they yield a comparable fit to the data. The changes are due to using lower weights on the reference 4 data.

TABLE I

Fitted Parameters for Equation (1)

Parameter	Yield Strength	Ultimate Tensile Strength	Units
A	.9997	1.000	MPa/°K
B	186.8	229.7	MPa
C	4713.0	4194.0	(°K)
D	11750.0	9252.0	$(dpa)^{-1}$
E	576.5	592.3	$(hpa\ dpa)^{-1/2}$
F	7035.0	6959.0	(°K)
G	5.053	7.897	MPa/°K
H	0.01137	0.01467	$(°K)^{-1}$
T_0	726.3	730.3	(°K)
γ	0.3350	0.3830	$(dpa)^{-1}$

Figure 1 shows the ultimate tensile strength data for heat 87210 and the curves for each temperature group. The curves correspond to an EBR-II core center spectrum. For the most part the curves fit the data reasonably well. At 840°C, the equation (1) is about 50% higher than the measured data. Although this is within the 95% confidence level of uncertainty, the application of equation (1) is limited to <800°C.

Figure 2 shows the measured heat 87210 and DO heat ultimate tensile strength data (except ref. 4 data) plotted versus calculated ultimate tensile strength. The dashed lines show the weighted 95% confidence bounds for the data. Most of the DO heat data falls within or near the 95% confidence bounds.

5.2.2 Ductility Properties

The tensile ductility properties uniform and total elongation were not as easily analyzed as the strength properties due to an apparently more complex irradiation temperature dependence. Odette[12] has proposed a simple relationship between the uniform elongation and the ratio of yield strength and ultimate tensile strength of the form

$$\sigma_u = C_1 \left(1 - \frac{\sigma_y}{\sigma_u}\right) \qquad (2)$$

where C_1 = 0.5 for annealed 316 and is a function of the work hardening coefficient. He found that this relationship was valid for annealed 316 stainless steel for temperatures <500°C. The a_Y values were based on a yield stress model and the σ_u values were based on an empirical model. Above 500°C, the ε_u function overpredicted the measured values of uniform elongation. This was attributed to the effect of helium on grain boundaries.

It would be convenient to represent the uniform elongation in terms of the yield and ultimate tensile strength. Figure 3 shows measured true uniform strain versus one minus the ratio of measured true stresses for T_I <500°C.

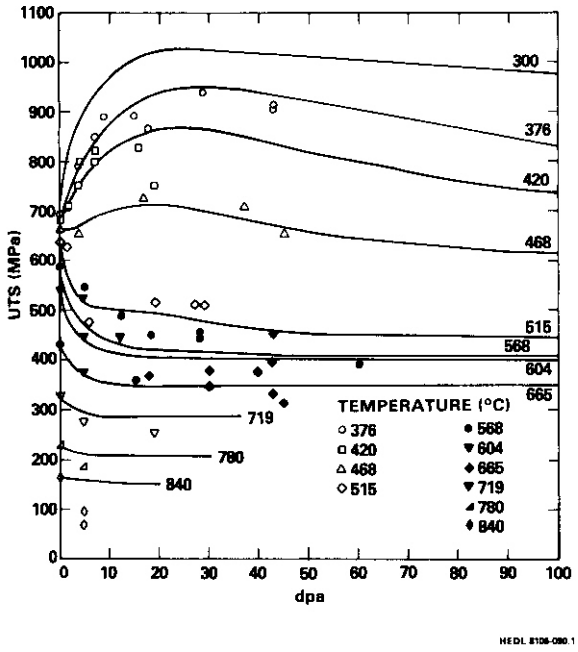

FIGURE 1 Measured and Calculated Ultimate Tensile Strength for Heat 87210 versus dpa.

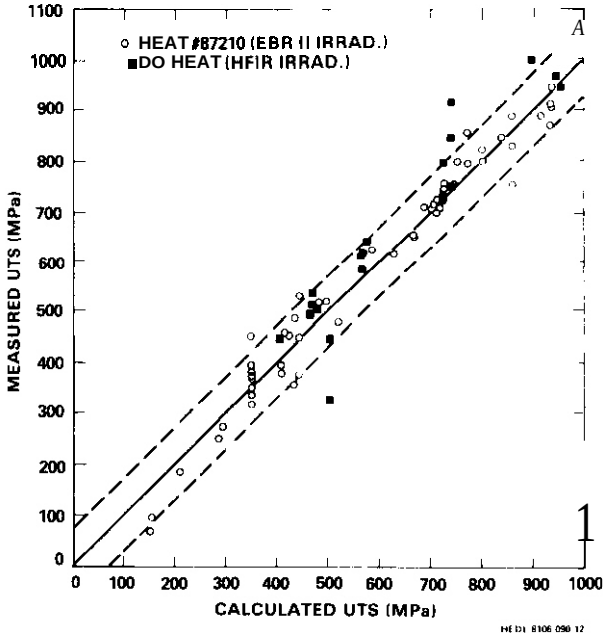

FIGURE 2. Measured versus Calculated Ultimate Tensile Strength in 20% CW 316 SS.

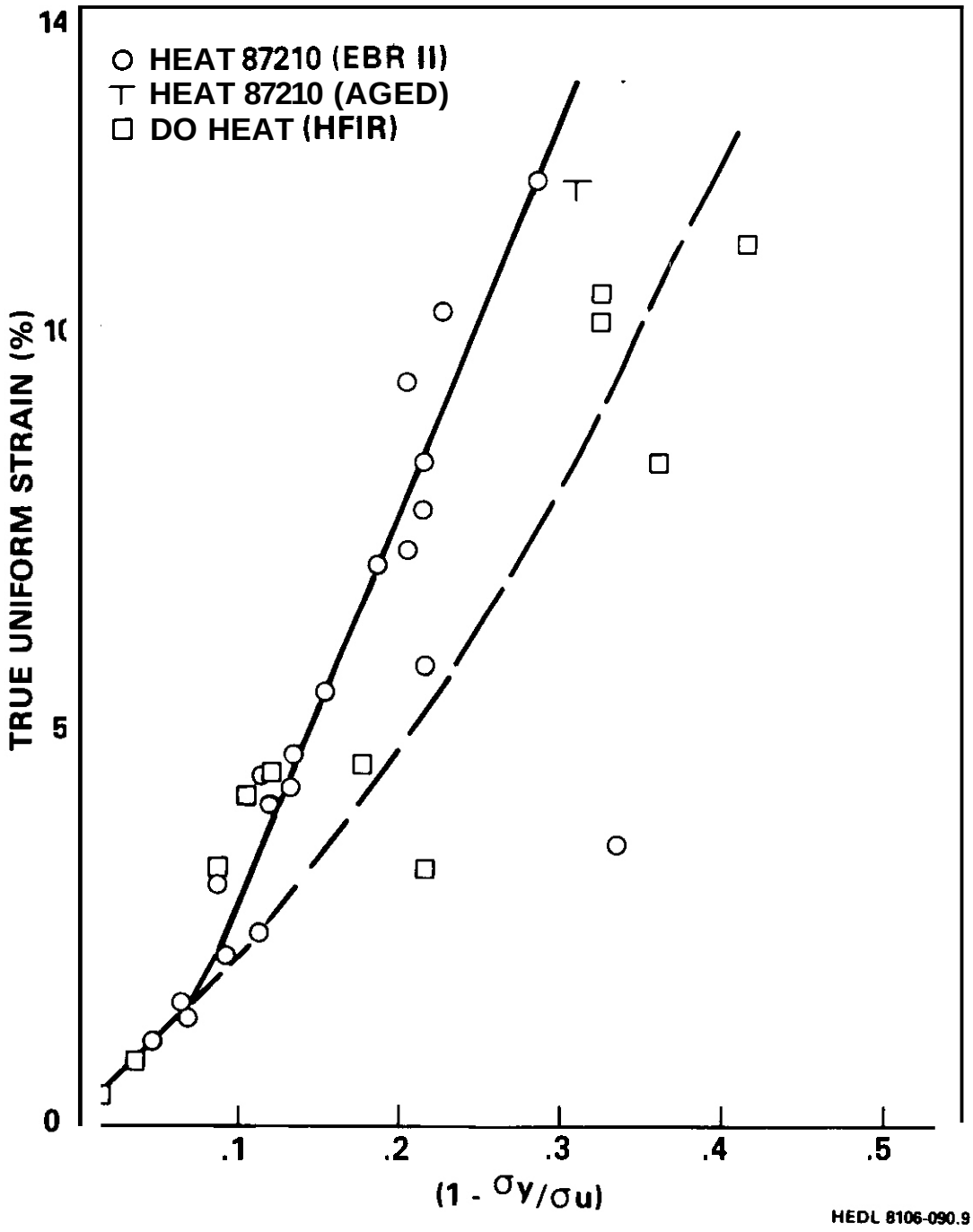

FIGURE 3. True Uniform Elongation Versus an Empirical Strength Function (T_{IRR} < 500°C).

The dpa values range from 1-40 and helium concentrations range from 1-1000 appm. The heat 87210 data show a single function of the strength ratio. The DO heat does not clearly fit this same curve. Some points agree and others disagree with the heat 87210 at 4-5% true strain (375°C). There appears to be no effect of excess helium at 375°C where both EBR-II and HFIR data correlate well with dpa in spite of the order of magnitude difference in helium content. At about 10% strain, the DO heat data (475°C) shows a definite deviation from heat 87210. However, this difference is not evident when comparing uniform elongation versus dpa (Figure 4). It is generally accepted that helium is not affecting ductility at these temperatures. Any differences between the HFIR and EBR-II aata is probably due to difference in material heat or product form.

Figure 5 shows the uniform elongation data for T_I >500°C. The 87210 heat is shifted to the right relative to the lower temperature data of Figure 4. The aging data shown in Figure 5 are in good agreement with the irradiation effects data which indicate recovery is the dominant mechanism. The DO heat irradiated in HFIR shows a pronounced shift to the right of heat 87210. Since the strengths for the two heats were in relative good agreement at these temperatures, the HFIR data suggest that the pronounced drop in ductility is possibly due to helium. However, if one considers the two steels to have distinct ε_u dependence on strengths at low temperatures as shown in Figure 4, both steels show comparable shifts between Figure 4 and 5. Thus, the shift in Figure 5 could reflect both a heat to heat variation and a helium effect. In order to arrive at the correct interpretation, the two heats need to be irradiated side by side in HFIR.

Figure 6 shows total elongation data versus dpa from stainless steel irradiated in EBR-II and HFIR at 376 ±10°C. The correlation of fast and mixed spectrum data is insensitive to the helium content. Plotting the data versus helium content or a combined function of dpa and helium increases the scatter.

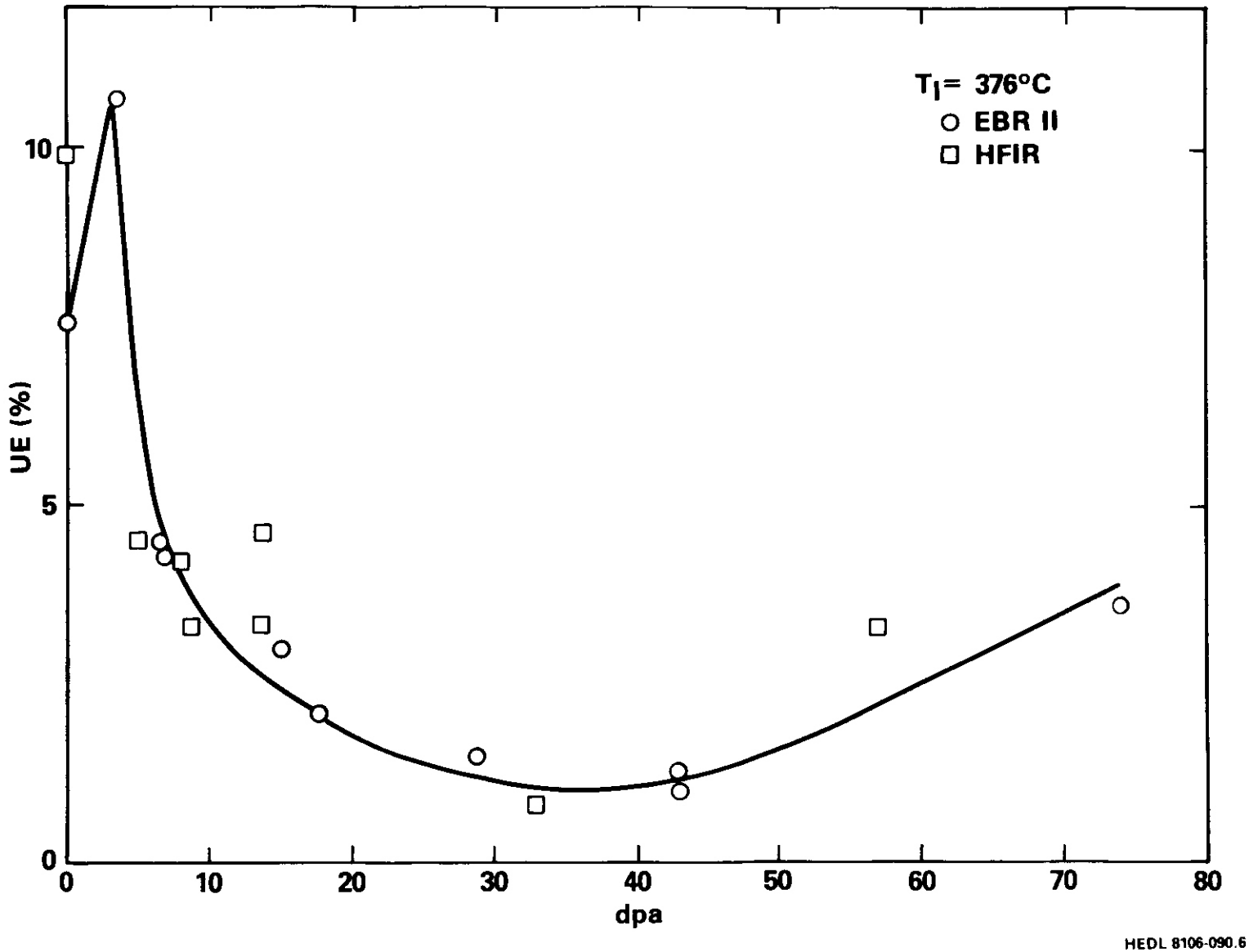

FIGURE 4. Uniform Elongation Versus dpa for an Irradiation Temperature of 376°C.

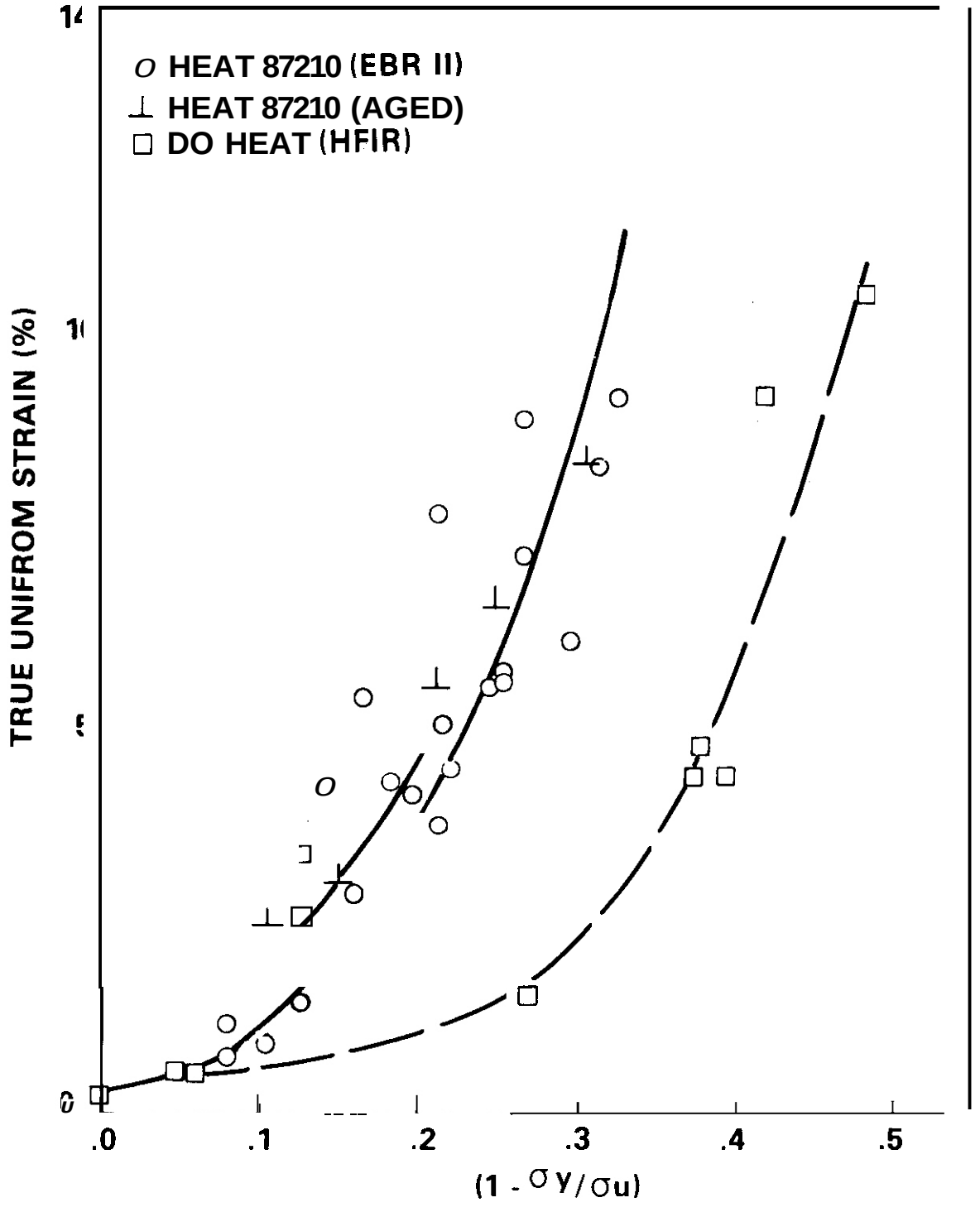

FIGURE 5. True Uniform Elongation versus an Empirical Strength Function ($T_{IRR} \geq 500°C$)

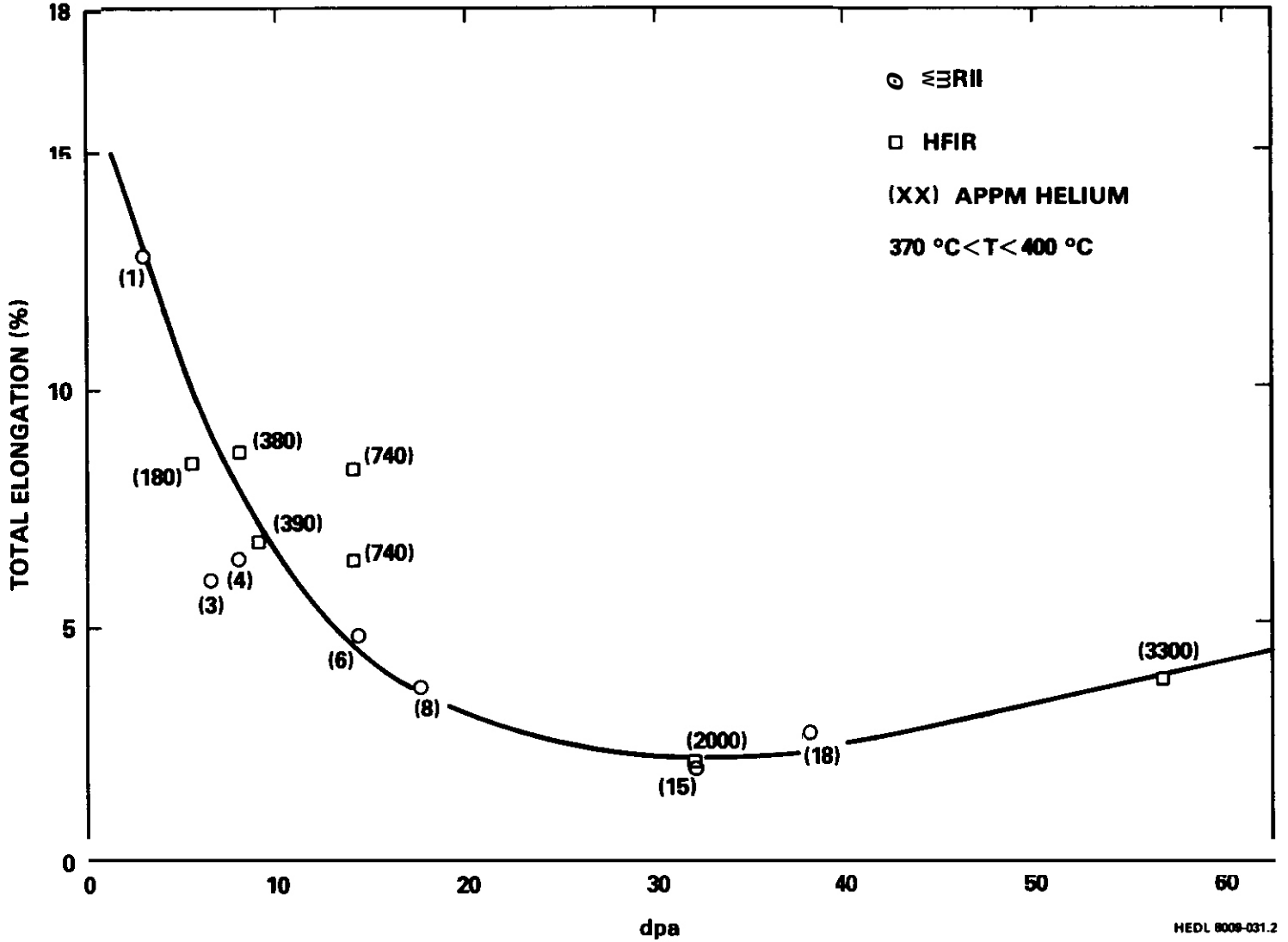

FIGURE 6. Sensitivity of Total Elongation in 20% CW 316 SS to Helium Content.

Figure 7 shows the total elongation data versus dpa for an irradiation temperature of 575 ±25°C. The HFIR irradiation data show a more rapid drop and ultimately a lower level of total elongation than the data from EBR-II irradiations. Grossbeck and Maziasz[5] showed that both cold worked and annealed material reached the same level of total elongation by 10-15 dpa in HFIR and they felt that the eventual level of total elongation would be the same as that measured by Bloom and Wiffen[4] at >30 dpa. This was expected to occur in spite of the fact that the earlier work initially showed lower total elongation. The best correlation and subsequent extension to a fusion environment would involve a merging of the data sets from the two reactor irradiations. Since helium is known to reduce ductility at or above half the melting temperature, this merging of data might be accomplished by a plot of total elongation versus helium (Figure 8). However, Figure 8 does not provide the desired correlation of the data. This appears to be in part due to the differences in unirradiated total elongation levels for the different heats or lots of material. These differences are expected to disappear after extended irradiation as pointed out by Grossbeck.[5] Blackburn[13] compiled a number of data points from the literature which show that the data for annealed 316 converges to a residual total elongation range of 10-16% after accumulating 25 appm helium. This is consistent with the range presented by the DO heat and 87210 heat data out to the 25 appm helium level. With the tensile properties from Reference 4 in question, it appears that additional data from mixed spectrum irradiations are needed for the helium concentration level of 1-100 appm. This will provide a better comparison with EBR-II data and establish the low exposure behavior in a high helium generation rate neutron environment.

5.3 Summary and Conclusions

The conclusions from this analysis are of two kinds: one concerns the behavior of stainless steel in a fusion type environment where both high helium and dpa exposure are expected, and the other is recommendations to fill the gaps in the data base for irradiation effects on stainless steel.

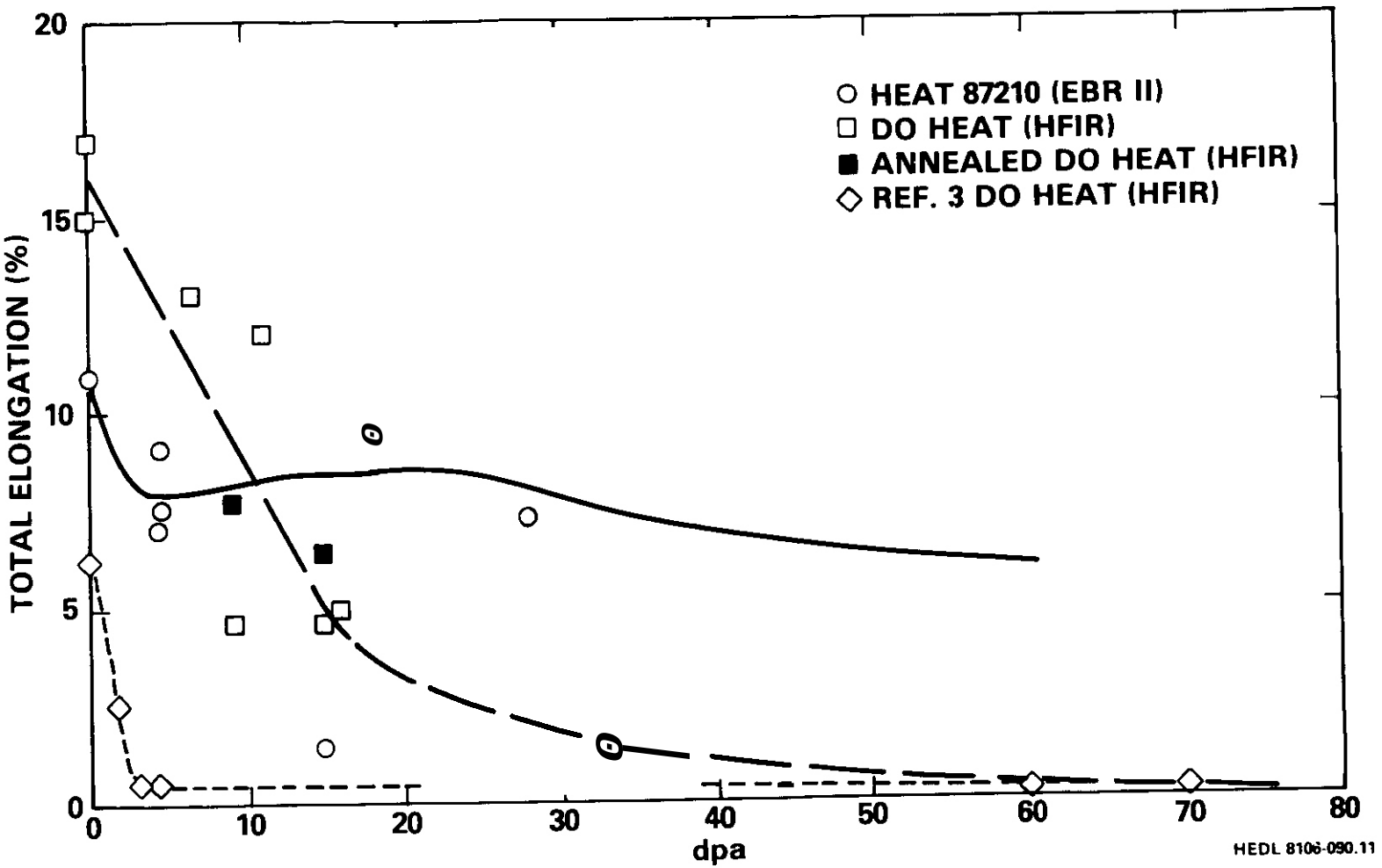

FIGURE [illegible] Total Elongation versus dpa in 20% CW 316 Stainless Steel (T_{IRR} = 575°C.)

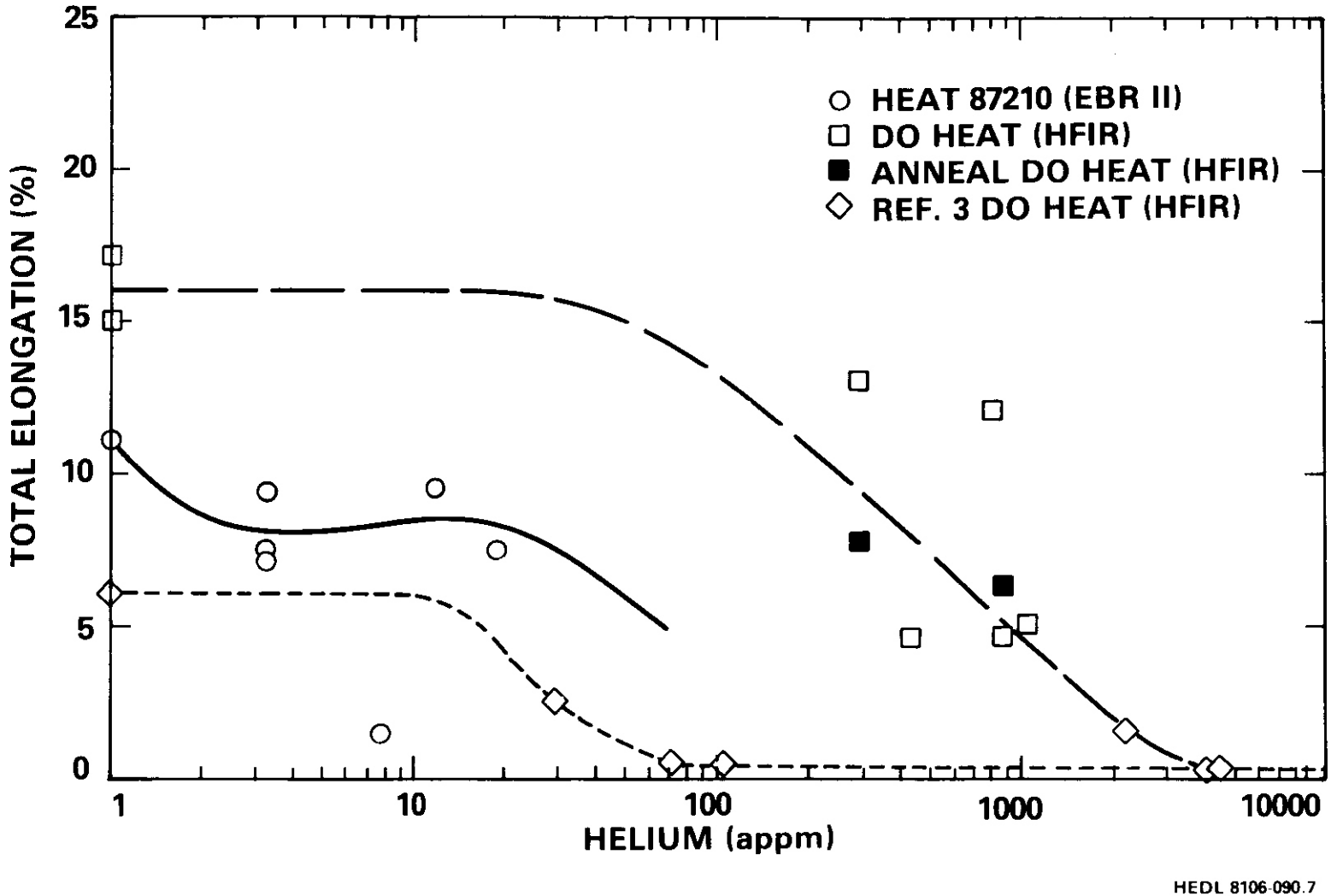

FIGURE 8. Total Elongation in 20% CW 316 Stainless Steel versus Total Helium Content (T_{IRR} = 575°C).

Empirical correlations for yield strength and ultimate tensile strength have been developed which are functions of dpa, helium concentration, and irradiation temperature. They apply for test temperatures equal to or near the irradiation temperature. The applicable strain rates are $<5 \times 10^{-4}$/second. The correlations are applicable to irradiation temperatures in the range of $25 < T < 800°C$. The correlations below 500°C are characterized as initially showing irradiation hardening which appears to saturate. At higher exposures, the strength tends to decrease. The decrease occurs predominently in the 300-500°C temperature range and can be correlated with the exposure parameter $\sqrt{dpa \cdot hpa}$. Above 500°C, the strength is diminished by recovery of the dislocation structure and is independent of helium concentration.

The ductility parameters are insensitive to helium below 500°C. Heat to heat variation may affect uniform elongation in this temperature range. Above 500°C, the uniform elongation is reduced by recovery in EBR-II irradiations. The DO heat shows either further loss in uniform elongation due to helium or a significant heat to heat variation. Residual total elongation behaves similarly. There is no apparent effect of helium below 500°C, but above 500°C helium reduces the total elongation at a faster rate in HFIR than in EBR-II on a per dpa basis.

Present experiments in the fusion materials research program are duplicating dpa and hpa values expected in fusion devices. However, both cannot be duplicated simultaneously in present test environments. Therefore, it is necessary to obtain the best possible correlation of all available data from both fast and mixed spectrum test facilities. In order to obtain a reliable correlation, it will be necessary to duplicate in a mixed spectrum the low helium concentration (<50 appm) accumulated in EBR-II. This will provide the best possible means of synthesizing a valid fission-fusion correlation.

The present data base does not include irradiation of a given heat of material in both fast and mixed spectrum environments for the full temperature range. It is important to accomplish this in order to eliminate the heat to heat variable which can cause misinterpretation of data.

6.0 References

1 R. L. Simons, "Yield Strength Correlation for 20% CW 316 Stainless Steel", DAFS Quarterly Progress Report, DOE/ER-0046/4, February 1981.

2. R. L. Fish, N. S. Cannon, and G. L. Wire, "Tensile Property Correlations for Highly Irradiated 20% Cold Worked Type 316 Stainless Steel," ASTM STP 683, 1979, pp. 450-465.

3. R. J. Puigh and N. F. Panayotou, "Tensile Properties Data on 316 SS Irradiated at RNTS-II," DAFS Quarterly Progress Report, DOE/ER-0046/3, November 1980.

4. E. E. Bloom and F. W. Wiffen, "The Effects of Large Concentrations of Helium on the Mechanical Properties of Neutron-Irradiated Stainless Steel," J. Nucl. Mat., 58, (1975), p. 171.

5. M. L. Grossbeck and P. J. Maziasz, "Tensile Properties of Type 316 Stainless Steel Irradiated in a Simulated Fusion Reactor Environment,' J. Nucl. Mat., 85 and 86, (1979), pp. 883-887.

6. F. W. Wiffen, "The Effects of Irradiation at About 55°C on Type 316 Stainless Steel," ADIP Quarterly Progress Report, DOE-ET-0058/1, January-March 1978.

7. C. L. Long, et al., "EBR-II Spectral Parameters Run 75D," HEDL-TME-78-84, March 1979.

8. F. W. Wiffen, et al., "The Production Rate of Helium During Irradiation of Nickel in Thermal Spectrum Fission Reactors," J. Nucl. Mat. 85 and 86, (1979).

9. W. N. McElroy and H. Farrar, IV, in Proceedings of Conference on Radiation Induced Voids on Metals, CDNF-710601, April 1972, p. 187.

10. K. Q. Bagley, J. W. Branaby, and A. S. Fraser, "Irradiation Embrittlement of Austenitic Stainless Steels," from British Nuclear Energy Society Conference Irradiation Embrittlement and Creep in Fuel Cladding and Core Components, November 9-12, 1980.

11. J. E. Irvin and A. L. Bement, "Nature of Radiation Damage to Engineering Properties of Various Stainless Steel Alloys," ASTM STP 426, (1967).

12. G. R. Odette and D. Frey, "Mechanical Properties and Mechanical Modeling," DOE/RT-0065/5, May 1979.

13. L. D. Blackburn, D. L. Greenslade, and A. L. Ward, "Mechanical Properties of Type 316 Stainless Steel Materials After Irradiation at 515 and 585°C," HEDL-TME-81-4, April 1981.

7.0 Future Work

Development of correlation equations for the ductility properties will continue.

8.0 Publications

R. L. Simons "Tensile Property Correlations for 20% CW 316 Stainless Steel," in Second Topical Meeting on Fusion Reactor Materials.

DOSE AND HELIUM INJECTION RATE DEPENDENCE OF SWELLING IN DUAL-ION IRRADIATED 316 STAINLESS STEEL

G. Ayrault, and H. A. Hoff (Argonne National laboratory)

1.0 Objective

The objective of this work is to determine the microstructural evolution, during irradiation, of first wall materials with special emphasis on the effects of helium production, displacement damage and rates, and temperature.

2.0 Summary

The dose and helium injection rate dependence of dislocation and cavity microstructure in 316 stainless steel irradiated simultaneously with Ni^+ and He^+ ions at 625°C has been studied with TEM. Bimodal cavity size distributions were found at all three helium injection rates investigated (5, 15, and 50 appm He/dpa). The 5 and 15 He/dpa irradiations produced similar dislocation and cavity microstructures, and swelling (1.2% at 28 dpa). In 50 appm He/dpa samples, the dislocation densities were generally higher, and higher cavity number densities produced greater swelling (~ 1.5% at 20 dpa) despite smaller mean cavity sizes.

3.0 Program

Title: Effects of Irradiation on Fusion Reactor Materials
Principal Investigator: A. P. L. Turner
Affiliation: Argonne National laboratory

4.0 Relevant DAFS Program Plan Task/Subtask

Subtask II.2.C.1 Mobility, Distribution, and Bubble Nucleation

5.0 Accomplishments and Status

5.1 Introduction

A major question in the irradiation response of candidate fusion reactor structural materials is the influence of concurrent displacement damage and helium production. Dual-ion irradiation, using heavy-ions for damage production and helium ions to simulate gas production by transmutation events provides a means of investigating such effects in the absence of a high energy neutron source.

This report presents the results on the dose and helium injection rate dependence of irradiation microstructures in dual-ion irradiated 316 stainless steel.

5.2 Irradiation Conditions

Type 316 stainless steel from the MFE heat was 50% cold-worked, then solution annealed at 1050°C for one hour and aged at 800°C for ten hours. Samples were irradiated with 3.0 MeV Ni^+ and simultaneously injected with degraded 0.87 MeV $^3He^+$.

Three helium injection rates were used: 5, 15 and 50 appm He/dpa. The nominal irradiation temperature was 625°C, and the nominal doses for each helium injection rate were 3, 6, 12 and 25 dpa. The displacement damage rate was 3×10^{-3} dpa s^{-1}. After irradiation the samples were electrochemically sectioned to a depth of 450 nm (peak damage was at 550 nm) and backthinned for TEM inspection. At-depth damage doses were computed for each sample. Irradiation temperatures of individual samples were measured with an infrared pyrometer. They are listed in Table 1 with the at-depth doses and He/dpa ratios.

TABLE 1

IRRADIATION CONDITIONS

He/dpa	Dose/ Temperature (dpa/°C)			
5	2.91610	7.01620	14.5/620	27.91615
15	2.8/645	7.6/620	12.0/635 13.21640	27.31610
50	2.61580	6.21610 6.9/585	11.8/645 13.01605	20.4/630

5.3 Dislocation and Cavity Microstructure

Quantitative TEM data was extracted from three or more regions in each of fifteen irradiated samples; cavity data from absorption contrast micrographs, and dislocation data from micrographs recorded in (200) two beam conditions. Considerable scatter was found, both between regions within the same sample (represented by the error bars in Figs. 1-4) and between different samples. The sample-to-sample differences were undoubtedly influenced to some extent by the differences in irradiation temperature, listed in Table 1. However, we do not believe that this was the major cause. The largest sample-to-sample differences between nominally "duplicate" samples were for the case of 12 dpa, 15 appm He/dpa where the temperature difference was only 5°C. Moreover, the region-to-region variations within samples were usually similar in magnitude to differences between nominally duplicate samples.

The dislocation density, Fig. 1, was fairly insensitive to both dose and helium injection rate; measured mean values for different conditions varied by less than a factor of three and region-to-region variations within samples were almost as large as the differences between samples. Nevertheless consistent trends are clear: 5 and 15 appm He/dpa irradiations produced very similar dislocation densities, which increased with dose. In 50 appm He/dpa samples the densities were higher up to ~ 12 dpa and decreased at the highest dose to a level similar to that in the 5 and 15 appm He/dpa samples.

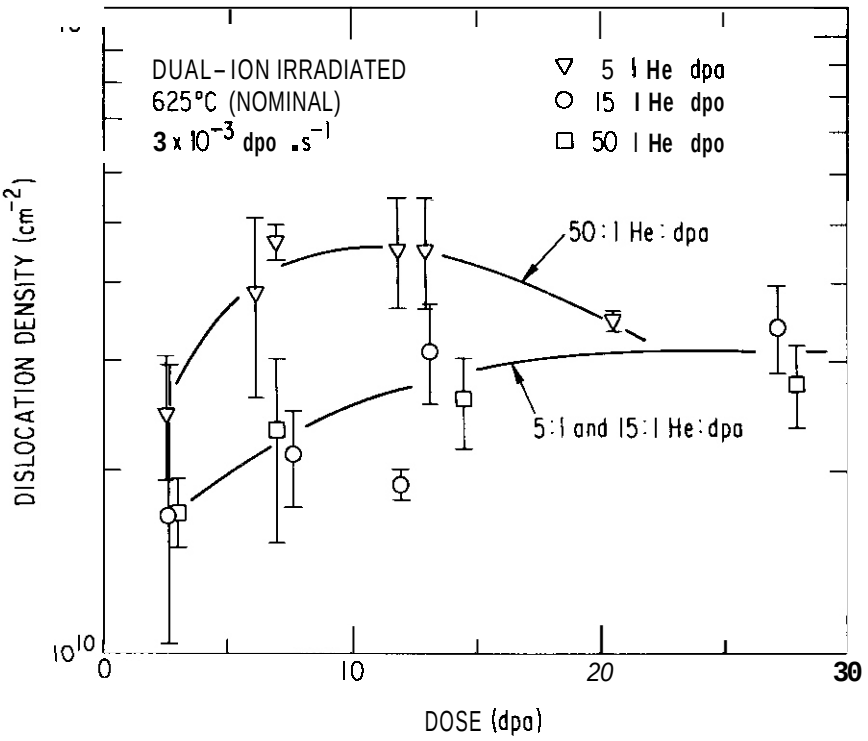

Figure 1. **Dose** dependence of dislocation density in **316** *ss.*

At the lowest dose level, the dislocations were almost exclusively Frank loops for all three helium injection rates. At the highest doses the structure was primarily a network of lines, and few loops remained. However, the rate of change from loops to lines depended upon the helium injection rate. **The** 5 and 15 appm He/dpa samples were similar in this respect, but the development in 50 appm He/dpa samples was more rapid; at ~ 6 dpa with 50 appm He/dpa a significant network dislocation component was already present, whereas in 5 and 15 appm He/dpa samples at similar doses the dislocations were still primarily in the form of loops.

Cavity size distributions in the highest dose samples for all three helium injection rates were bimodal, with high number densities of small-cavities and lower number densities of large-cavities. Both large- and small-cavities were preferentially associated with acicular precipitates lying along <100> directions. %all-cavities were also preferentially associated with dislocations and loops.

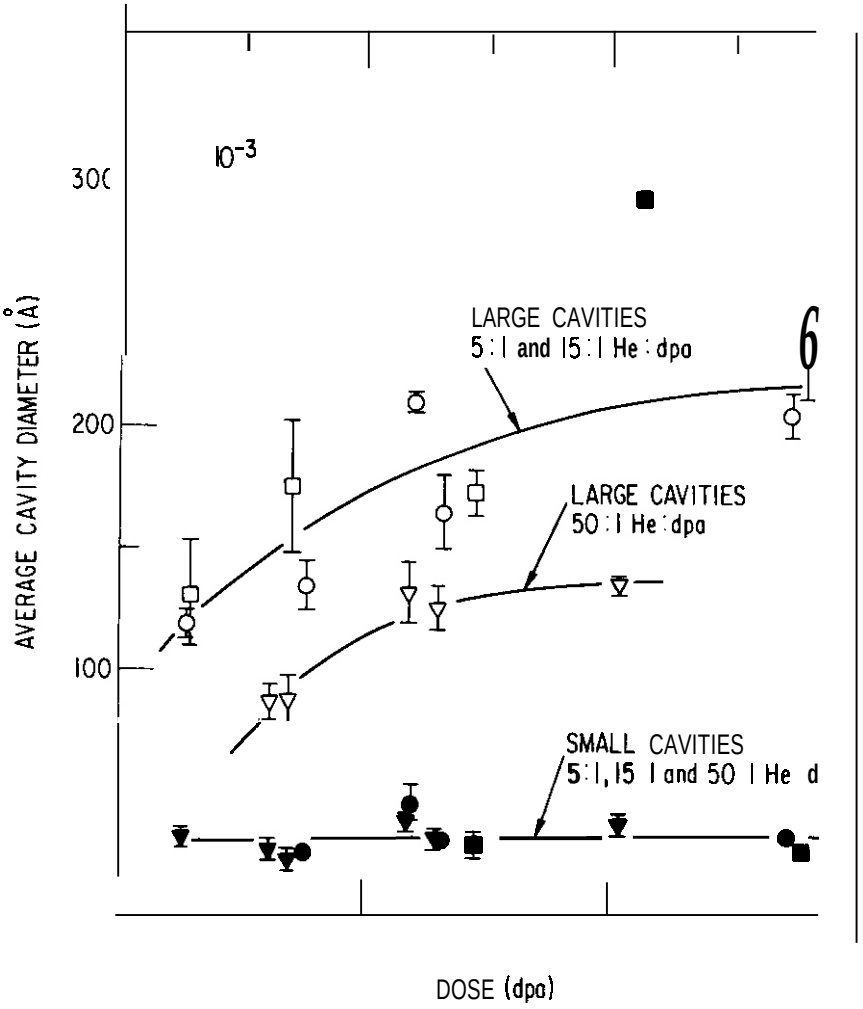

Figure 2. Dose dependence of cavity size in 316 SS; large-cavity and small-cavity components of the bimodal size distributions are plotted separately.

The large-cavity components in the bimodal distributions produced most of the swelling, but small-cavities usually dominated number density and cavity size statistics. For this reason the small and large cavity distributions were analyzed separately, and the mean sizes and number densities are plotted separately in Ngs. 2 and 3. The small-cavities were first visible at ~ 3, 6 and 12 dpa in 50, 15 and 5 appm He/dpa samples, respectively. The measured mean diameter of small-cavities in Fig. 2 was quite insensitive to both dose and helium injection rate. However, here we must make a distinction between actual and measured values. The measured mean cavity sizes, typically ~ 3 nm,

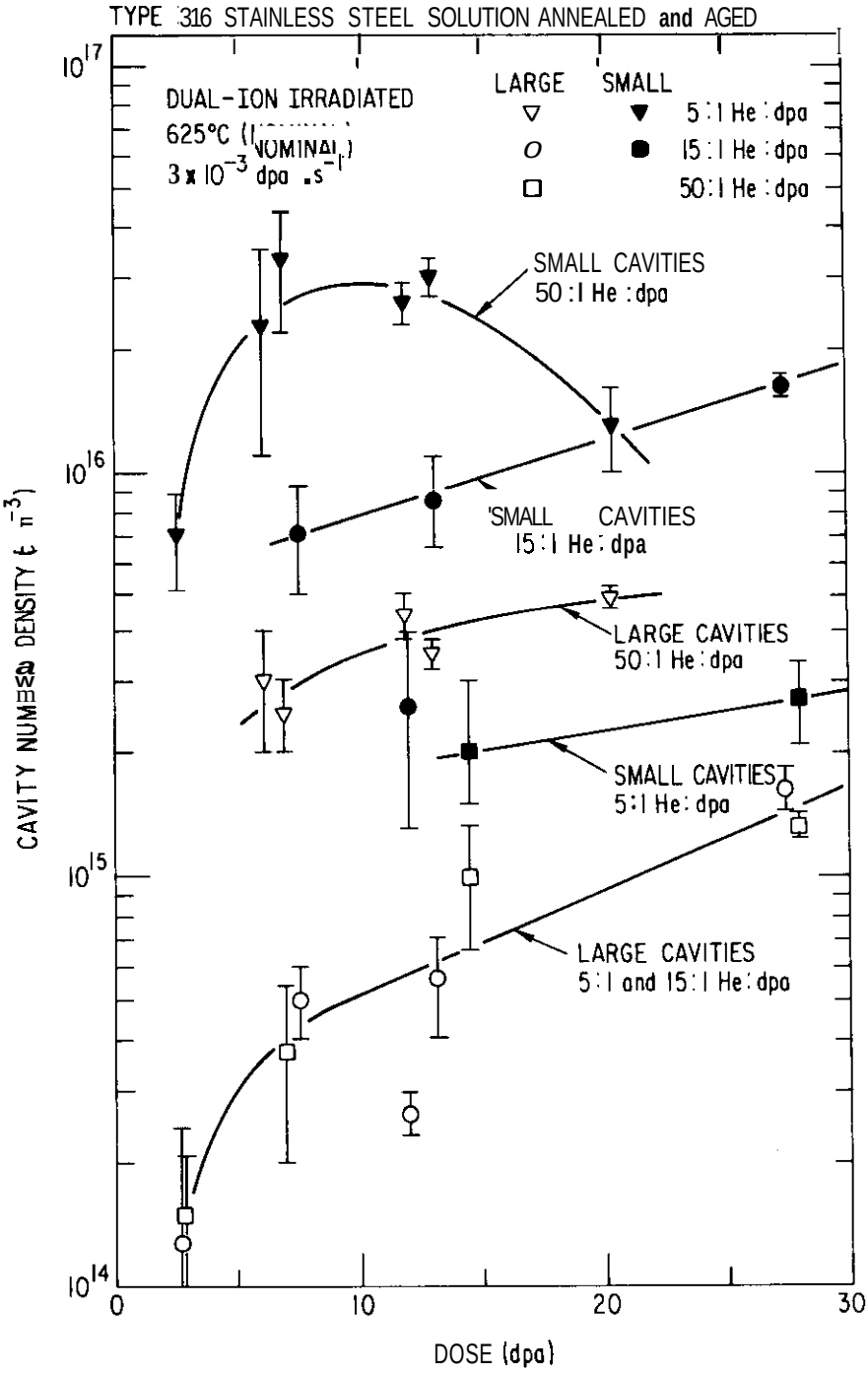

Figure 3. Dose dependence of cavity number density in 316 SS; large-cavity and small-cavity components of the bimodal size distributions are plotted separately.

were not much larger than the practical cavity resolution limit of the micrographs analyzed (usually ~ 2.0 to 2.5 nm depending on image quality). Moreover the small-cavity size distributions were usually peaked at the smallest visible size, i.e. the smallest cavities dominated the cavity-size statistics. Therefore growth of small-cavities with dose was likely to appear as an increase in number density (due to growth into the visible range) instead of as a significant increase in mean size. Thus the observed increases in small-cavity number density in Fig. 3 do not necessarily reflect continued cavity nucleation beyond the lowest dose, and may be largely due to growth of small-cavities. On the other hand, the decrease in number density between 12 and 20 dpa in 50 appm He/dpa samples appears to be genuine. In this connection we note an interesting parallel in 50 appm He/dpa samples between small-cavity number density and dislocation density. Both populations increased rapidly from 3-6 dpa, remained sensibly constant between 6 and 12 dpa, and decreased between 12 and 20 dpa. The growth and subsequent coarsening of the two distributions appear to be interrelated, and the relationship is likely to be through the preferential association of small-cavities with dislocations. In 5 and 15 appm He/dpa samples the dislocation densities and cavity number densities both increased with dose, but a direct correlation is not obvious.

Iarge-cavity sizes and number densities increased steadily with dose at all three helium injection rates. *The* combined effects were the swelling increases in Fig. *4*. The increases in mean cavity-size were due to cavity growth. Increases in large-cavity number density are likely to be due to growth of small-cavities into a size range where rapid growth could occur. For the 5 and 15 appm He/dpa samples the large-cavity sizes and number densities, and swelling, were essentially similar at each dose level, as was the dislocation density; thus the only obvious differences between 5 and 15 appm He/dpa samples were higher small-cavity number densities at 15 appm He/dpa. In 50 appm He/dpa samples the mean sizes of large-cavities were smaller, but swelling was higher at each dose level because of higher number densities.

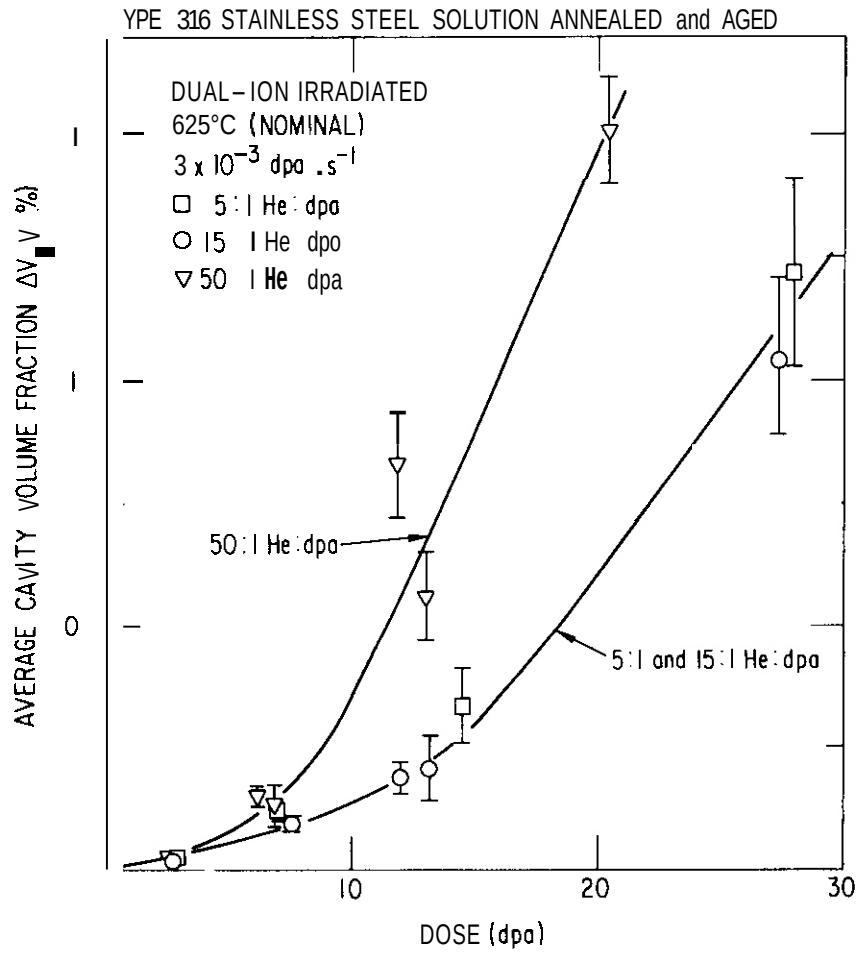

Figure 4. Dose dependence of swelling in 316 SS.

The increases in cavity number density with increasing helium injection rate were presumably due to helium-assisted cavity nucleation and growth. These increases were anticipated based on previous results in a high purity austenitic ternary alloy Fe-20 Ni-15 Cr irradiated at 700°C (1). However, the increased swelling at high helium injection rate was unexpected. In Fe-20 Ni-15 Cr, a high helium injection rate (55 appm He/dpa) caused a swelling reduction relative to lower (5 and 16 appm He/dpa) helium injection rates. This contrast between 316 SS and Fe-20 Ni-15 Cr is quite dramatic because, at low helium injection rates, the swelling in Fe-20 Ni-15 Cr was greater than in 316 SS (e.g. ~ 7% at 25 dpa and 5 appm He/dpa), but swelling in high helium Fe-20 Ni-15 Cr (~ 0.5% at 19 dpa and 55 appm He/dpa) was well below that of

high-helium 316 SS (~ 1.5% at ~ 20 dpa and 50 appm He/dpa). This is an anomaly which we find difficult to rationalize.

6.0 References

1. Agarwal, S. C., Ayrault, G., Potter, D. I., Taylor, A. and Nolfi, F. V., Jr., "Microstructure of single and dual-ion irradiated Fe-20Ni-15Cr and Ti-6Al-4V alloys", J. Nucl. Mater. 85 & 86 (1979) 653-657.

7.0 Publications

None.

THE INFLUENCE OF PREINJECTED HELIUM ON VOID NUCLEATION IN FE-17CR-16.7NI-2.5MO DURING IRRADIATION AT 550°C IN ORR - H. R. Brager, F. A. Garner and R. L. Gaines (Hanford Engineering Development Laboratory)

1.0 Objective

The objective of this effort is to define the mechanisms by which helium affects the microstructural evolution of alloys during irradiation.

2.0 Summary

The results of the MFE-II experiment on the role of heliun preinjection in the P-7 alloy (Fe-17Cr-16.7Ni-2.5Mo) are consistent with earlier ion bombardment studies on the same alloy. Preinjection of 40 appm helium leads to a suppression of swelling, although there is some concern that the preinjection may inhibit void growth and result in voids which are smaller than the resolution limit of TEM.

3.0 Program

Title: Irradiation Effects Analysis
Principal Investigator: D. G. Doran
Affiliation: Hanford Engineering Development Laboratory

4.0 Relevant DAFS Program Plan Task/Subtask

Task II.C.2 Effects of Helium on Microstructure
Task II.C.17 Microstructural Characterization

5.0 Accomplishments and Status

5.1 Introduction

It is now recognized that the schedule (e.g., preimplantation of helim vs.

simultaneous inspection) and helium implantation temperature can have a strong effect on the early microstructural evolution of irradiated metals.[1] One experiment directed toward the understanding of this phenomenon is the DAFS MFE-2 Test[2] which has recently been removed from the Oak Ridge Research Reactor (ORR).

One of the several alloys irradiated in this experiment is the Fe-17Cr-16.7Ni-2.5Mo quaternary alloy designated as P-7 or "pure 316." This alloy was irradiated at several temperatures in each of the following conditions: annealed, 20% cold worked, annealed plus He implanted, 20% cold worked plus He implanted, and various annealed and aged plus implanted conditions.[2] The implanted specimens contained a range of helium concentrations injected at ambient temperature. All the specimens chosen for examination were irradiated to 3 to 5 dpa.

This report is concerned with He implanted specimens irradiated at 550°C. Conventional immersion density measurements, specimen preparation and microscopy techniques were employed.

5.2 Results

The immersion density measurements showed neither significant swelling nor discernible influence from any preirradiation treatment. The mean density changes for the (1) 20% CW, (2) annealed, (3) annealed plus 40 appm He and (4) annealed plus 40 appm He plus 750°C aged were -0.22%, -0.15%, -0.12% and -0.25% respectively with a total deviation of $\sim\pm$0.10%.

The unimplanted specimens irradiated at 550°C are discussed in more detail in another report.[3] Low levels of visible void volume (0.03 to 0.08%) were found at 550°C. Cold working the alloy was found to increase the void number density.[3]

In the implanted specimens, electron microscopy revealed no voids in the annealed, cold worked, or annealed plus aged conditions. Apparently the

preinjection of 40 appm He either completely suppressed the small level of void volume seen in the unimplanted specimens or distributed the voidage so finely as to render it unresolvable by electron microscopy ($\lesssim$3 nm).

5.3 Discussion

At the low dose and potential swelling levels obtained in this experiment, it is impossible to tell whether swelling has been suppressed or merely rendered invisible. Irradiation to larger displacement levels is needed. However, postirradiation aging at a range of temperatures to determine coarsening kinetics may provide some interim answers.

The suppression of swelling by preinjection with 40 appm He is consistent with ion bombardment studies of similar materials. Swelling of ternary alloy specimens preinjected with 15 appm He at ambient temperature and bombarded with 3 MeV nickel ions at 625°C to 25 dpa was delayed about 10 dpa relative to that of specimens dual-ion bombarded at He/dpa ratios of 5 to 15. Bombardment at an He/dpa ratio of 55 induced large cavity nucleation but little void volune.[4] Neutron irradiated ternary alloys swelled with shorter incubation periods than did preinjected speicmens that were ion bombarded.[5]

In another study, specimens of alloy P-7 were irradiated with 4 MeV Ni^+ ions at 900°K (629°C) to 1, 10 and 70 dpa. Helium was either preinjected to 1400 appm at room temperature or at 900°K or introduced simultaneously at a helium-to-dpa ratio of 20. For reference, specimens were irradiated without the addition of heliun. At high fluence levels (10 and 70 dpa), swelling was decreased by the addition of helium; the largest effect was for room temperature preinjection. At 1 dpa, the cavity volume was small ($\sim$0.15%) in the uninjected state and was approximately halved by room temperature preinjection.

5.4 Conclusions

The first results of the MFE-II experiment on the role of helium preinjection in the P-7 alloys are consistent with earlier ion bombardment studies on the

same alloy. Preinjection of 40 appm helium leads to a suppression of swelling, although there is some concern that preinjection may have rendered the swelling less visible instead of decreasing its actual volune.

6.0 References

1. N. H. Packan and K. Farrell, J. Nucl. Mat., 85 and 86, (1979) p. 677-681.

2. G. R. Odette, R. W. Powell and F. Nolfi, "DAFS Experiment in the ORR MFE-2 Test," DAFS Quarterly Report DOE/ET-0065, May 1979, p. 5.

3. H. R. Brager and F. A. Garner, "The Influence of Cold-Work on the Swelling of "Pure" AISI 316 Irradiated in ORR," this report.

4. S. C. Agarwal et al., "Microstructure of Single and Dual-Ion Irradiated Fe-20Ni-15Cr and Ti-6Al-4V Alloys," Reference 1, p. 653-657.

5. F. A. Garner et al., "Simulation of High Fluence Swelling Behavior in Technological Materials," Radiation Effects in Breeder Reactor Structural Materials, M. L. Bleiberg and J. W. Bennett (Eds.), AIME 1977, p. 543.

7.0 Future Work

Four solution annealed specimens preinjected with about 35 appm He and aged at 700°C will be heat treated at a range of high temperatures to determine if small cavities exist or if swelling has been suppressed.

THE INFLUENCE OF COLD WORK ON SWELLING OF "PURE" AISI 316 IRRADIATED IN ORR

H. R. Brager and F. A. Garner (Hanford Engineering Development Laboratory)

1.0 Objective

The object of this effort is to determine the individual roles of the various microstructural and microchemical participants in the iradiation-induced evolution of AISI 316 and to apply the insight gained toward the development of fission-fusion correlations.

2.0 Summary

Solution-annealed and cold worked specimens of a Fe-17Cr-16.7Ni-2.5Mo alloy were irradiated in ORR and Examined by immersion density and transmission electron microscopy. The results were then compared with those of other studies.

The irradiation of this "pure" alloy containing no significant amount of minor solutes such as silicon, carbon, phosphorous, nitrogen, etc., leads to early swelling. Cold working causes an increase in the void density while the swelling is essentially unchanged. The addition of minor solutes extends the transient regime of swelling in this and other alloys while cold working of alloys with such solutes generally leads to a further extension and thereby less swelling.

3.0 Program

Title: Irradiation Effects Analysis (AKJ)
Principal Investigator: D. G. Doran
Affiliation: Hanford Engineering Development Laboratory

4.0 Relevant OAFS Program Plan Task/Subtask

Task II.C.1 Effects of Material Parameters on Microstructure

Task II.C.2 Effects of Helium on Microstructure
Task II.C.17 Microstructural Characterization

5.0 Accomplishments and Status

5.1 Introduction

In two previous reports,[1-2] it was proposed that the primary role of cold-work on the swelling of AISI 316 is to distribute the element carbon throughout the alloy matrix and thereby increase the apparent solubility of carbon by binding it in the strain-field of the dislocation core. The resultant decrease in supersaturation and activity of carbon then leads to a decrease in the rate of phase formation that preceeds swelling. It was also shown that all carbon in 20% cold worked AISI 316 of nominal alloying element concentrations would be in bound-solution at all relevant fusion and breeder reactor irradiation temperatures.[2]

The irradiation of pure metals tends to confirm this conclusion, since the effect of cold work on swelling is essentially independent of cold-work level as long as the stored energy does not induce recrystallization and as long as the influence of free surfaces is absent. Unfortunately, however, there have been few side-by-side irradiations of both annealed and cold-worked alloys and none of pure Fe-Ni-Cr ternaries or pure Fe-Cr-Ni-Mo quaternaries. Based on the proposed model, one would not expect that void formation would be depressed by cold work if solutes such as carbon are absent.

An alternate model ignores solute effects and considers only the interaction between point defects and microstructural features. These interactions are assumed to not be a strong function of the matrix composition. Based on this model, one would expect that void nucleation would be depressed by cold working.

One method of testing the validity of these two models is to irradiate a steel which contains no significant amount of solutes in the annealed and cold worked conditions. The best comparison would involve side-by-side irradiations over a

fluence range spanning the void incubation period of the steel in both conditions.

Specimens of annealed and 20% CW quaternary alloy (Fe-17Cr-16.7Ni-2.5Mo), designated as P-7 or "pure 316," were irradiated in the MFE-2 experiment in the Oak Ridge Research Reactor (ORR). This alloy lies toward the high nickel end of the composition range typical of AISI 316. Specimens in either the 20% cold-worked or annealed condition were irradiated in liquid-metal-filled capsules to doses in the range of 3 to 5 dpa at temperatures of about 350, 550 or 650°C.

These specimens were analyzed using conventional immersion density and transmission electron microscopy techniques.

5.2 Results

The immersion density results (within the accuracy of the technique) did not indicate any swelling or densification.

At 350°C and 3 dpa, no obvious voids were observed in either the annealed or 20% cold-worked specimens. In addition to the radiation-induced Frank loops, there were small clusters in both the annealed and cold-worked specimens, sane of which might be small ($\lesssim$3 nm) voids, however.

At 500°C, the solution-annealed specimen was found to contain 5.7 x 10^{14} voids/cm^3 with a mean size of 15 nm (Figure 1). The swelling in the area analyzed was 0.08% and appeared to be relatively uniform in other adjacent areas. The network dislocation density was approximately 3 x 10^9 cm/cm^3 and a low density of large Frank loops were found: $\sim$4 x $10^{12}/cm^3$ with a mean diameter of 100 nm.

The 20% cold-worked specimen contained roughly twice as many voids (1.2 x 10^{15}/cm^3) at an average diameter of 8 nm (Figure 2). The void volume was found to be 0.03%, the dislocation density was 2.2 x 10^{10} cm/cm^3 with no visible Frank 1oops.

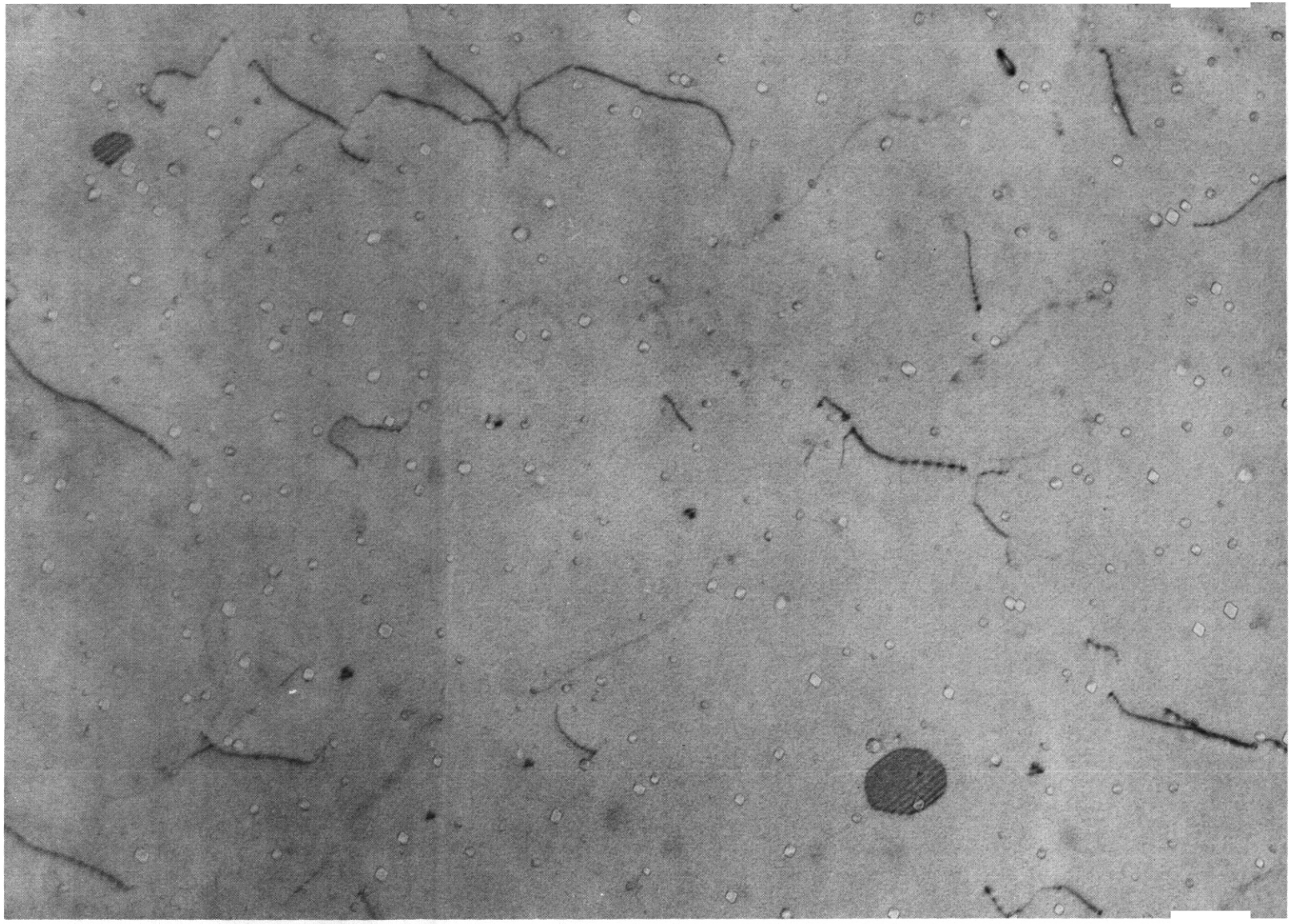

FIGURE 1. Typical Micrograph of P-7 Alloy in Annealed Condition After Irradiation to 3 dpa at 550°C.

FIGURE 2. Typical Micrograph of P-7 Alloy in 20% Cold-Worked Condition After Irradiation to 5 dpa at 550°C.

5.3 Discussion of Experimental Behavior

The swelling behavior normally observed in conventional AISI 316 containing various solute elements (and irradiated in breeder reactors) is different from that observed here in the P-7 quaternary alloy without solute. Whereas low fluence irradiation would lead to some swelling in annealed steel, complete or near-total suppression of both void density and volume is expected in the cold-worked steel. It is therefore significant that the cold-worked P-7 specimen has twice the void density of the annealed specimen and a swelling value which, while smaller, is not appreciably different from that of the annealed steel. Since the mean size of the voids in the cold-worked specimen is smaller and nearer the resolution limit of the microscope, it may be that a fraction of the swelling is in unresolvable voids.

It appears that the transients in microstructural evolution are not quite over at this fluence and temperature since the network dislocation density of the annealed specimen is less than and approaching that of the cold-worked specimen. As has been observed many times before, the saturation dislocation density of network dislocations in 316 is independent of cold work level and appears to be in the mid-10" cm/cm^3 range.[3] The absence of Frank loops in the cold-worked specimen is also consistent with the higher initial dislocation density of that specimen compared to that of the annealed specimen.[4]

The higher void density in the cold-worked specimen is also consistent with the behavior of a commercial heat of AISI 316 steel designated DO-heat and irradiated in HFIR,[5-6] as shown in Figure 3. (Both HFIR and ORR generate high levels of helium per displacement.) It is proposed that the role of pre-existing dislocations may be to collect the helium atoms into clusters on which voids nucleate. The higher average dislocation density of cold-worked alloys during the transient regime then leads to higher void densities.

5.4 Discussion of Other Data

It was shown earlier that the reduction of swelling by cold-working of AISI 316 could not be explained by the time-dependent microstructural development of

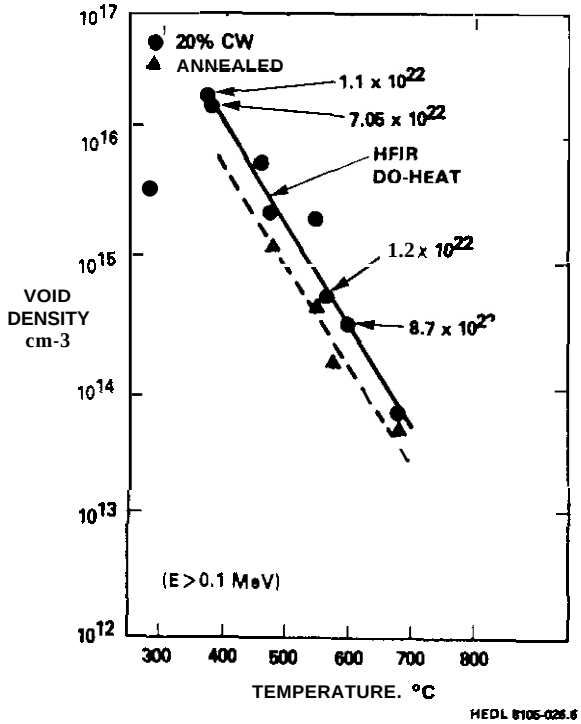

FIGURE 3. Void Densities Observed in Cold-Worked AISI 316 (DO-Heat) Irradiated in HFIR and Roughly a Factor of Two Greater Than That Formed in Annealed Specimens. (5-6)

Frank. loops and dislocations. [1,3,7] It was shown, however, that cold-working has a large effect on the phase evolution which precedes swelling in this alloy. [7] As shown in Figure 4, the typical behavior of swelling versus cold work level is a continuous decline in swelling at a given displacement level and temperature, with no significant reduction beyond about 30% cold-work. [8] Analysis of other data sets shows that the primary effect of cold-work on complex alloys [9-12] is to extend the transient regime of swelling, as shown in Figures 5-8.

The duration of the transient regime in annealed, cold-worked or aged AISI 316 steel as earlier shown to be determined by the details of the evolution of second phase precipitates. [7] This evolution is not only dependent on the pre-irradiation thermal-mechanical treatment but also on the amount of minor solutes. When such solutes are absent, the transient regime is reduced substantially as shown in Figures 9 and 10. The duration of the transient regime in alloys without minor solutes appears to depend only on the time required to reach saturation levels *of* the microstructure.

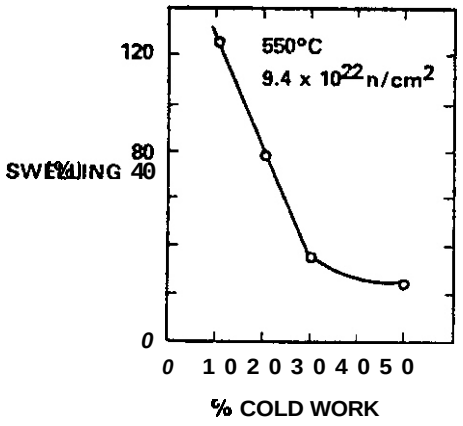

FIGURE 4. Effect of Cold Work on Swelling of AISI 316 Stainless Steel at High Neutron Fluences. (8)

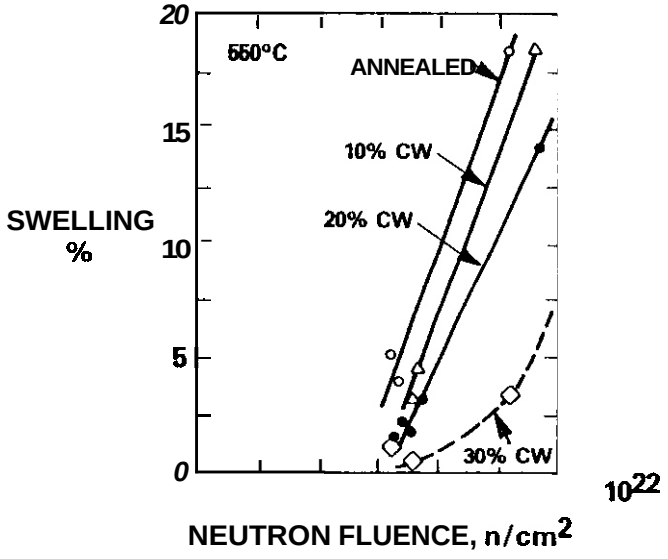

FIGURE 5. Dependence of Neutron-Induced Swelling on Cold-Work Level in AISI 316 at 550°C.(9)

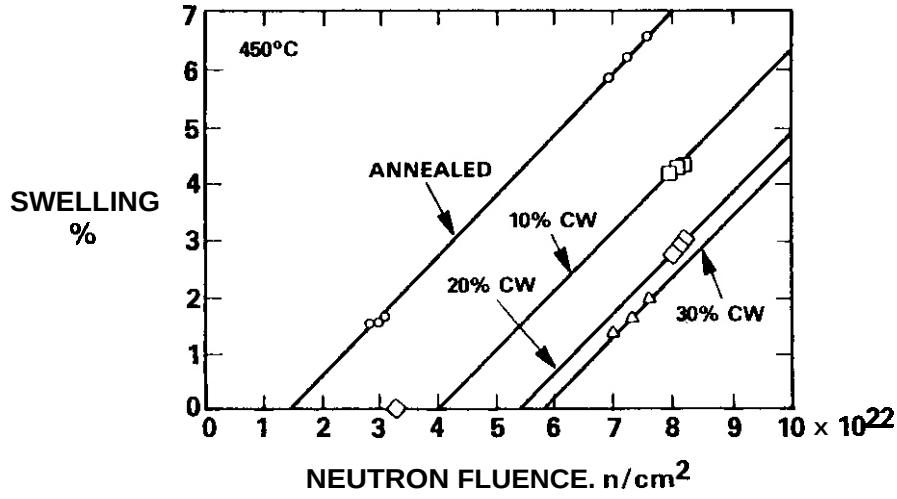

FIGURE 6. Dependence of Neutron-Induced Swelling on Cold-Work Level in AISI **304** at 450°C. (10)

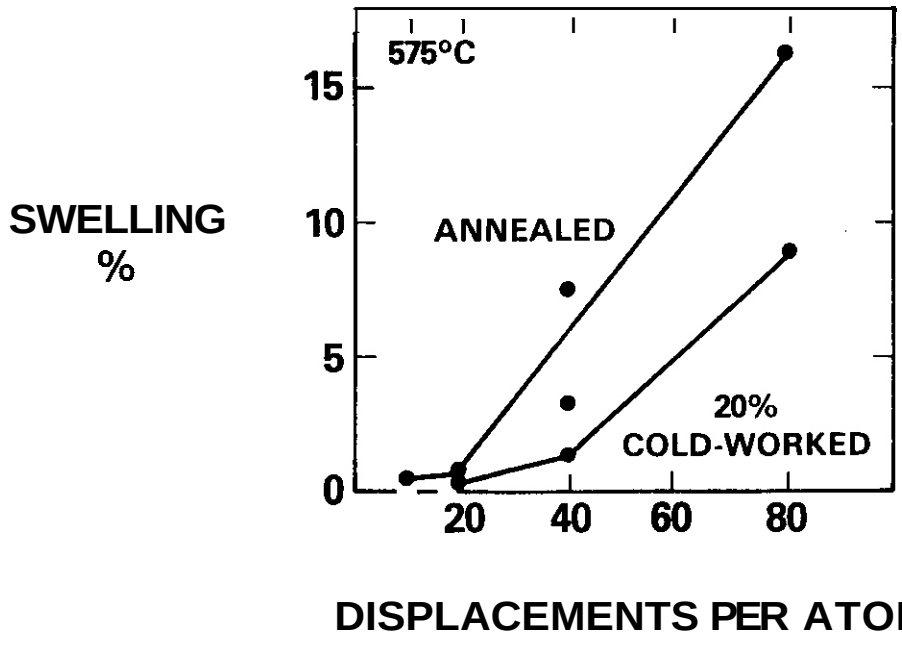

FIGURE 7. Dependence of Swelling on Cold-Work Level in 1.4981 Wrapper Steel (Niobium-Stabilized) After Irradiation by 46-MeV Ni^+ Ions at 575°C.(11)

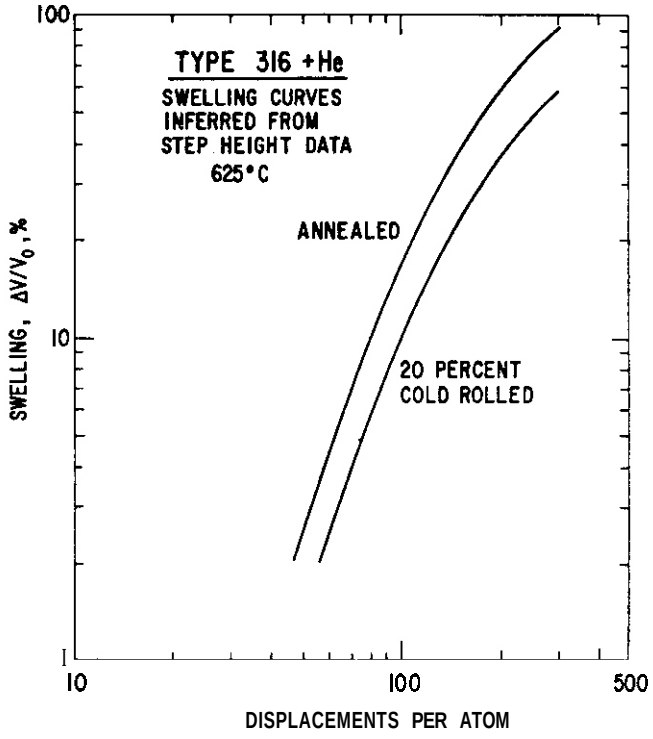

FIGURE 8. Swelling Curves Inferred from Step-Height Measurements on Annealed Type 316 and 20 Percent Cold-Rolled Type 316 Bombarded With 5-MeV Nickel Ions at 625°C.(12)

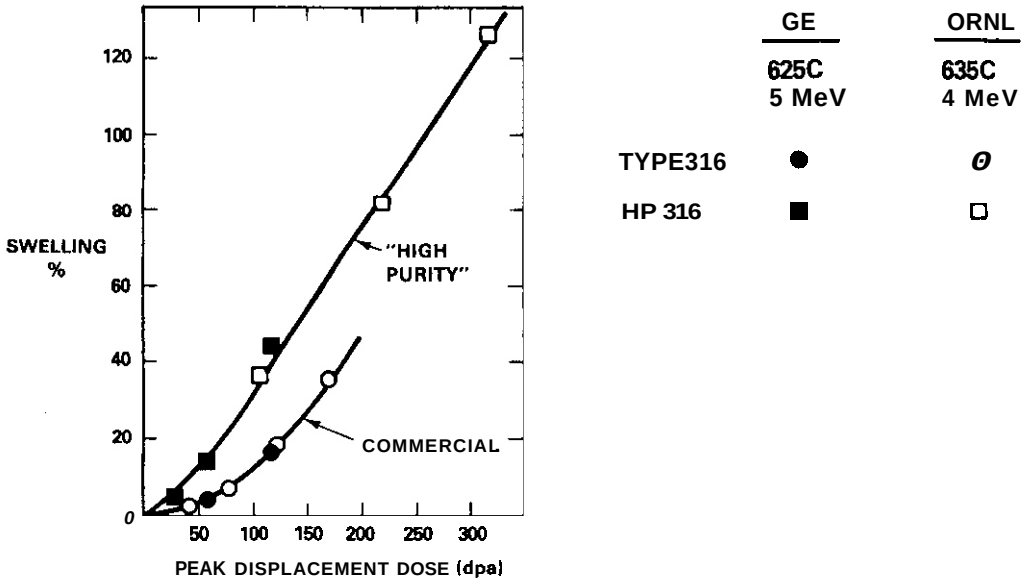

FIGURE 9. Dependence of Swelling at 625-635°C in AISI 316 on Impurity Level as Revealed by Ion Irradiation at Two Laboratories. (15)

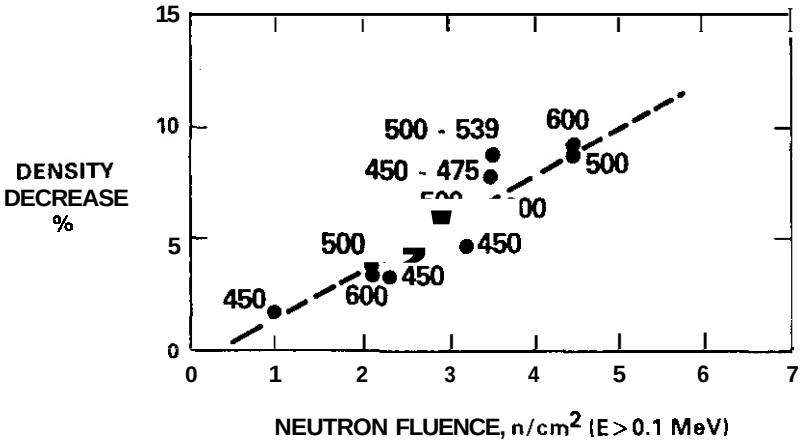

FIGURE 10. Swelling of Fe-17Cr-14.4Ni-2.8Mo Irradiated in EBR-II. *(9)* This alloy is one of several "pure 316 alloys" but has a lower nickel content that the P-7 alloy discussed in this report and also Reference 20.

One test of the proposed relative and interactive roles of dislocations and solutes lies in the examination of pure metals. Neutron irradiation data are rather sparce, but cold-working of Al, Mg, Cu and Ni leads either to small increases in swelling or no change, as shown in Table 1.[16] Vanadium seems to be an exception, however, in that cold-work reduces swelling.

TABLE 1

EFFECT OF COLD WORK ON SWELLING OF PURE METALS (16)

Metal	Impurity content, ppM	Temperature, °C	ΔV/V, % Annealed	Slightly cold worked	As rolled
Al*	60	55	0.064		0.35
Mg†	1	55	0.46	0.46	0.46
	100	55	0.16	0.18	0.20
Cu*	100	250	u.17	0.31	0.14
Ni*	500	335	0.5	0.65	1.0
V*	5000	435	0.25	0.08	<0.01

*~5 x 10^{20} neutrons/cm² (E > 0.1 MeV).
†~1.5 x 10^{20} neutrons/cm² (E > 0.1 MeV).

It also appears that at low doses the void density is higher in cold-worked cu [17] and Al [18] than in the annealed metal, although there appears to be some dislocation density beyond which the void density and swelling decrease again. [18] From other studies using charged particle irradiation, it appears that the subsequent reduction in swelling with cold-work is related to recrystallization induced by the energy stored by the dislocations. The recrystallization is assisted by the proximity of free surfaces, especially in charged particle irradiations. [19] In general, the effects of cold-work on swelling in ion or electron-irradiated specimens has yielded rather ambiguous results and probably reflects the difficulty in establishing or maintaining high near-surface dislocation densities.

5.5 Conclusions

The irradiation of a "pure" Fe-Cr-Ni-Mo quaternary alloy, having no significant levels of such solutes as silicon, carbon, phosphorous, nitrogen, etc., leads to early swelling. Cold-working of this alloy does not suppress void formation but rather induces a higher void density. Void volume is either decreased slightly or essentially unchanged.

6.0 References

1. F. A. Garner, "The Microchemical Evolution of Irradiated Stainless Steels," DAFS Quarterly Report DOE/ER-0046/5, May 1981, p. 151.

2. F. A. Garner and W. G. Wolfer, "The Influence of Dislocation Density and Radiation on Carbon Activity and Phase Development in AISI 316," DAFS Quarterly Report DOE/ER-0046/4, February 1981, p. 88.

3. H. R. Brager, F. A. Garner, E. R. Gilbert, J. E. Flinn and W. G. Wolfer, in Radiation Effects in Breeder Reactor Structural Materials, M. L. Bleiberg and J. W. Bennett (Eds.), the Metallurgical Society of the American Institute of Mining, Metallurgical and Petroleum-Engineers, 1977, pp. 727-755.

4. H. R. Brager, F. A. Garner and G. L. Guthrie, J. Nucl. Mat., 66, 1977. p. 301.

5. F. A. Garner and D. L. Porter, "The History Dependence of the Microchemical Evolution of Irradiated AISI 316 and 304L Steel," this report.

6. P. J. Maziasz and M. L. Grossbeck, "Swelling and Microstructure of HFIR - Irradiated 20% Cold-Worked Type 316 Stainless Steel and 316 +0.23 wt.% Ti," ADIP Quarterly Report DOE/ER-0045/5, p. 43.

7. H. R. Brager and F. A. Garner, "Dependence of Void Formation on Phase Stability in Neutron-Irradiated Type 316 Stainless Steel," Effect of Radiation on Structural Materials, ASTM STP 683, J. A. Sprague and D. Kramer (Eds.), ASTM 1979, pp. 207-232.

8. K. Uematsu, T. Kodama, U. Ishida, K. Suzuki and M. Koyama, "Swelling Behavior of Cold-Worked Type 316 Stainless Steel," Reference 3, p. 571.

9. W. K. Appleby, E. E. Bloom, J. E. Flinn and F. A. Garner, "Swelling in Neutron-Irradiated 300 Series Stainless Steels," Reference 3, p. 509.

10. H. J. Busboom, G. C. McClellan, W. L. Bell and W. K. Appleby, "Swelling of Type 304 and 316 Stainless Steel Irradiated to 8 x 10^{22} n/cm^2," General Electric Report GEAP-14062, July 1975.

11. K. Ehrlich, R. Gross and W. Schneider, "Void Formation in Stabilized Austenitic Stainless Steel," Reference 3, p. 529.

12. W. G. Johnston, J. H. Rosolowski, A. M. Tukalo and T. Lauritzen, "Nickel Ion Bombardment of Annealed and Cold-Worked Type 316 Stainless Steel," General Electric Report 73CRD217, 1973.

13. H. R. Brager and F. A. Garner, "Radiation-Induced Evolution of the Austenite Matrix in Silicon-Modified AISI 316 Alloys," Proc. AIME Symposium on Irradiation Phase Stability? October 5-9, 1980, Pittsburgh, PA (in press).

14. J. F. Bates, R. W. Powell and E. R. Gilbert, "Reduction of Irradiation-Induced Creep and Swelling by Compositional Modifications," Effects of Radiation on Materials, ASTM STP 725, D. Kramer, H. R. Brager and J. S. Perrin (Eds.), ASTM, 1981.

15. W. G. Johnston, T. Lauritzen, J. H. Rosolowski and A. M. Turkalo, "The Effect of Metallurgical Variables on Void Swelling," General Electric Report 76CRD019, January 1976; also J. M. Leitnaker, E. E. Bloom and J. O. Stiegler, J. Nucl. Mat., 49, p. 57, 1973.

16. Y. Adda, "Report of the CEA Program on Investigations of Radiation-Induced Cavities in Metals: Presentations of Some Results," Proc. Symposium on Radiation-Induced Voids in Metals, June 9-11, Albany, NY, p. 31.

17. M. Labbe and J. P. Poirier, J. Nucl. Mat., 46, 1973, pp. 86-98.

18. A. Risbet and V. Levy, J. Nucl. Mat., 46, 1973, pp. 341-352.

19. T. Leffers and B. N. Singh, "The Effect of Cold-Work on Void Formation and Growth in Copper During High Voltage Electron Microscopy Irradiation," (paper D-16), Proc. International Conference on Irradiation Behavior of Metallic Materials for Fast Reactor Components, Ajaccio, Corsica, June 5-8, 1979.

20. H. R. Brager and F. A. Garner, "The Influence of Preinjected Helium on Void Nucleation in Fe-17Cr-16.7Ni-2.5Mo During Irradiation at 550°C in HFIR," this report.

7.0 Future Work

Some additional microscopy will be performed on these specimens.

COMPARISON OF THE SWELLING AND THE MICROSTRUCTURAL/MICROCHEMICAL EVOLUTION OF AISI 316 IRRADIATED IN EBR-II AND HFIR

H. R. Brager and F. A. Garner (Hanford Engineering Development Laboratory)

1.0 Objective

The objective of this effort is to determine the influence of spectral differences on the evolution of AISI 316 during irradiation in HFIR and EBR-II and to extrapolate the insight gained to predict the alloy's behavior in proposed fusion devices.

2.0 Summary

The microstructural and microchemical evolution has been compared for one heat of cold-worked 316 stainless steel irradiated in both HFIR and EBR-II at 500-620°C. The dislocation andcavity densitiesand the swelling at high fluence are remarkably insensitive to the over two orders of magnitude difference in helium/dpa ratios. While the microchemical evolution is also largely unaffected, minor differences were observed possibly arising from solid transmutants that form only in HFIR. The reported absence of γ' phase in specimens irradiated in HFIR at these temperatures reflects its sluggish formation in both reactors. The microchemical evolution is accompanied by the development of a swelling rate typical of steels irradiated in fast reactors. The magnitude of this swelling rate is corroborated by HFIR data on this same heat in the solution annealed condition.

3.0 Program

Title: Irradiation Effects Analysis (AKJ)
Principal Investigator: D. G. Doran
Affiliation: Hanford Engineering Development Laboratory

4.0 Relevant DAFS Program Plan Task/Subtask

Task II.C.1 Effects of Material Parameters on Microstructure
Task II.C.2 Effects of Helium on Microstructure
Task II.C.4 Effects of Solid Transmutation Products on Microstructure
Task II.C.17 Microstructural Characterization

5.0 Accomplishments and Status

5.1 Introduction

The radiation-induced evolution of microstructure and microchemistry of AISI 316 in fast reactors has been found to be sensitive to many material and environmental variables.[1-4] It is reasonable to expect that this sensitivity will be maintained and possibly altered in fusion environments, in response to large changes in the helium/displacement ratio.

The accumulated fast reactor data on this steel shows that valid studies of environmental sensitivity can only be made in controlled, single-variable experiments utilizing specimens made from the same heat of steel and given identical thermal-mechanical treatments.[3] The published data allow only one comparison at reactor-relevant displacement rates directed toward the influence of helium/displacement ratio on the microstructural and microchemical evolution. These data were derived from HFIR and EBR-II irradiations[5-12] of "DO-heat," a commercial quality heat of steel. This paper presents data on the behavior of this steel irradiated in EBR-II. Presently, no other heat of this steel has been irradiated to large neutron exposures (>50 dpa) at both low and high helium/displacement ratios.

Comparison of the microstructures produced in DO-heat specimens in EBR-II and HFIR will not yield a straight forward single-variable determination of the role of helium. The analysis is complicated by differences in flux and temperature history and by other factors such as the changes in composition produced by transmutations in HFIR but not EBR-II.[13] There are also uncertainties

in the irradiation temperature in both reactors, with the largest in HFIR. The EBR-II data are for only two temperatures, while the HFIR data cover a larger range. The microstructures reported for the HFIR specimens [5-9] are possibly different from those produced by irradiation, since they were derived from tensile specimens tested at temperatures about 25°C less than the calculated irradiation temperature.[10] The heterogeneity of swelling in cold-worked AISI 316 is also reflected in the substantial disparities in some of the swelling estimates based on microscopy and density measurements.

The new data presented here were derived from specimens of 20% cold-worked DO-heat irradiated in EBR-II to 33 dpa at 500 and 600°C; portions of these specimens were then reirradiated to a total exposure of either 69 dpa at 510°C or 75 dpa at 620°C. Conventional immersion density, electron microscopy and energy dispersive X-ray analysis techniques were employed. Precipitates were analyzed in thin foil and in carbon extraction replicas prepared using 10% HCl in methanol.

5.2 Summary of the Microstructural Data

5.2.1 500°C, 6.6 x 10^{22} n/cm^2 (E > 0.1 MeV) (33 dpa), 13 appm Helium

Essentially no Frank loops were observed ($\lesssim 10^{11}$ cm^3) while the network dislocation density was $\sim 2 \times 10^{10}$ cm^{-2}. The cavities comprised two distinct populations, one at $\sim 10^{12}$ cm^{-3} averaging 50 nm in diameter and another at 1×10^{14} cm^{-3} averaging 5 nm in diameter. The cavity volume was less than 0.01% with the precipitate formation resulting in a net bulk densification of 0.1%. The composition of extracted precipitates fell primarily into two major categories with narrow compositional ranges. There were diamond cubic M_6C (39 wt.% Cr, 30 wt.% Ni, 15 wt.% Mo, 8 wt.% Fe and 8 wt.% Si) with a lattice parameter of 1.07 nm and another category with slightly lower nickel levels. The γ' (Ni_3Si) phase, not extracted by this technique, was not observed in thin foil specimens. Commensurate with previous studies, the low cavity volume was accompanied by evidence that the microchemical evolution was far from complete.[1-4] Gradients in nickel concentration extended over 150 nm from the M_6C precipitates (Figure 1) and the matrix nickel levels were at 12-15% vs. 13% initially.

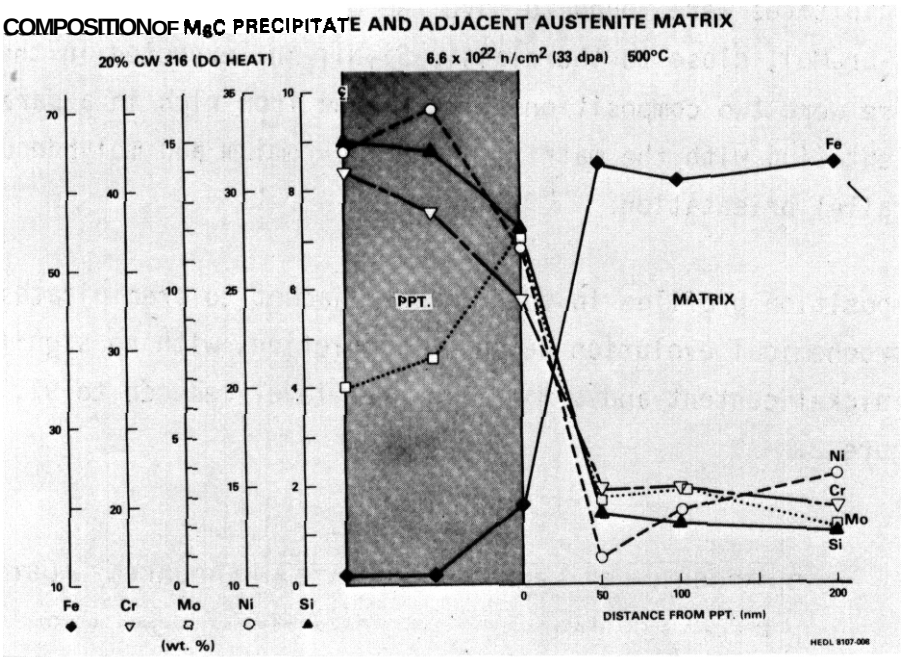

FIGURE 1. Concentration Profiles Observed Near M_6C Precipitates in 20% Cold-Worked DO-Heat at 500°C and 33 dpa.

5.2.2 510°C, 13.8 x 10^{22} n/cm^2 (69 dpa), 28 appm Helium

No Frank loops were found and the dislocation density was 3.2 x 10^{10} cm^{-2}. Void densities ranged from 1.3 to 1.7 x 10^{14} cm^{-3}, indicating that no net change in number density had occured since 33 dpa. The voids were larger, averaging 90 nm and accounting for 6.9 volume change in the areas examined. The bulk density underwent a change of 9.9% which indicates that on the average the steel had experienced 11% swelling.

The high swelling level was accompanied by evidence of the near-completion of the microchemical evolution. The precipitate density had increased substantially, with γ' the dominant phase, at 2 to 3 x 10^{14} cm^{-3} and sizes averaging 35 nm in diameter. Three other phases were found; M_6C, $M_{23}C_6$ and G-phase, totaling another 1 x 10^{14} cm^{-3} with sizes in the 50-100 nm range. Analysis of extracted precipitates indicated very narrow and consistent ranges of composition for each type of precipitate. The G-phase

precipitates were found to have the nominal composition of $Si_7(Ni_{15}Fe)(Mn_3Cr_2Mo)$, close to the classic $Si_7Ni_{16}Mn_6$ expected in the ideal phase. There were two compositions of M_6C, one iron-rich in a parallel (cube/cube) orientation with the matrix, and one chromium and molybdenum-rich in a non-parallel orientation.

Composition profiles in the region adjacent to precipitates showed that the microchemical evolution was near completion, with no significant gradients in nickel content and a matrix nickel level reduced to 9%, as shown in Figure 2.

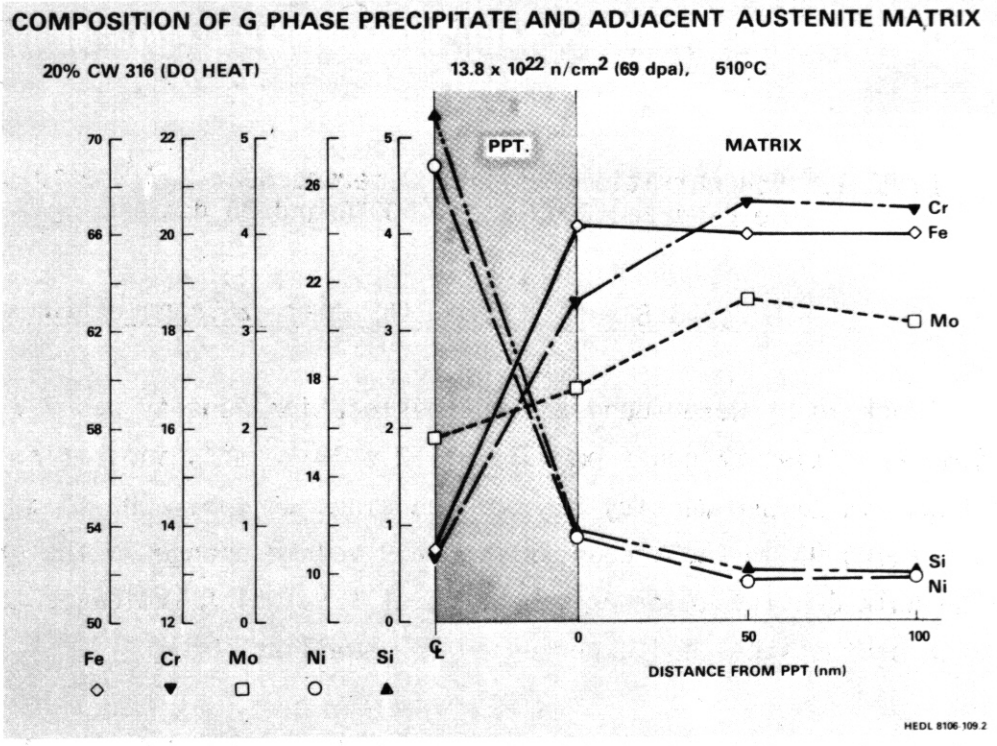

FIGURE 2. Concentration Profiles Observed Near G-Phase Precipitate in 20% Cold-Worked DO-Heat at 510°C and 69 dpa.

5.2.3 600°C, 6.6 x 10^{22} n/cm^2 (33 dpa), 13 appm Helium

No Frank loops were observed and the dislocation density was about 1.2 x 10^{10} cm^{-2}. The cavity population was again bimodal, with 1.5 x 10^{13} cm^{-3} of ~70 nm diameter and 1 x 10^{14} cm^{-3} of 5 nm diameter. The cavity volume was ~0.2% in fair agreement with a bulk density change of 0.3%. The predominant precipitate phases were Laves with nickel content averaging ~10%, and chrome-rich $M_{23}C_6$. Matrix nickel levels ranged from 10 to 15%with compositional gradients observed near precipitates.

5.2.4 620°C, 15.0 x 10^{22} n/cm^2 (75 dpa), 30 appm Helium

The network dislocation density was about 2.1 x 10^{10} cm^{-2} with no Frank loops. The void density had decreased slightly, ranging from 4 to 7 x 10^{13} cm^{-3} with mean diameters of 115 nm. The measured cavity volume ranged from 5.9 to 7.0% in agreement with a bulk density change of 6.4%.

The precipitates formed were primarily Laves, rich in nickel and silicon, and $M_{23}C_6$ which was not enriched in either element. The $M_{23}C_6$ precipitates appeared to be similar to thermally-induced chrome carbides and did not appear to be participating in the "infiltration-exhange" process observed for the Laves phase.(2-3) No precipitates of the γ', M_6C or G-phase were observed. There were no gradients in composition in matrix regions near precipitates. The matrix nickel level was reduced to ~9%.

5.3 Discussion

The microstructures developed in DO-heat at 500-620°C in EBR-II can be compared to those of other heats irradiated in fast reactors and to those of DO-heat irradiated in HFIR. It should be noted, however, that this heat has a somewhat atypical composition compared to the range employed in the U.S. Breeder Reactor Program, see Table 1. DO-heat contains 0.8 wt.% (vs. 0.5% typically in breeder steels) of silicon, an element which has a pronounced effect on void swelling and precipitate evolution. The comparison is also complicated by the temperature uncertainties, particularly those associated with HFIR. It is reported that most quoted temperatures may be low by at least 50-75°C.(9-10)

TABLE 1

CHEMICAL COMPOSITION OF DO-HEAT AND A TYPICAL U.S. BREEDER AISI 316 STAINLESS STEEL (weight percent)

	DO	CN-13		00	CN-13
C	0.05	0.054	P	0.013	0.005
Cr	18.0	17.3	S	0.016	0.004
Ni	13.0	13.6	V	<0.01	<0.01
Mo	2.6	2.3	Zr	0.05	<0.001
Mn	1.9	1.7	Co	0.03	0.01
Si	0.8	0.56	cu	0.10	0.01
Ti	0.05	<0.01	W	0.01	0.02
N	0.05	0.005	Sn	0.02	<0.005

The dislocation densities of DO-heat at 500-620°C were observed in this study to increase slightly with fluence but to remain on the lower side of the $6 \pm 3 \times 10^{10}$ cm^{-2} range observed in the U.S. Type 316 breeder steels.[14] Earlier irradiations of this steel in EBR-II showed that a density of 3×10^{10} cm^{-2} was developed at 500 and 625°C at 8.4 dpa and was not to be affected by the preinjection of 110 appm of helium.[9] In contrast to U.S. Type 316 breeder steels[14] Frank loops were not observed in any cold-worked specimens examined in this or previous studies to doses less than 15 dpa,[6,9-10] although they were observed in annealed material at $\leq$ 10 dpa.[11] It is presumed that the slightly lower dislocation density relative to other steels and the unexpected absence of Frank loops at 500°C results from differences in composition. Reported dislocation densities for DO-heat irradiated at lower fluences in HFIR are lower ($\leq 6 \times 10^9$ cm^{-2}, 475-620°C, $\leq$16 dpa) but many of these values were determined from tensile specimens tested at temperatures near those of the irradiation temperatures.[10] The dislocation density may have relaxed under these conditions.

It was earlier shown that the identity and predominance of precipitates that develop in AISI 316 can be quite variable from point-to-point and grain-to-grain, as well as sensitive to many environmental and material variables.[4] It is, therefore, risky to draw conclusions on phase development on the basis of limited data. It appears, however, that the precipitates that form

during EBR-II irradiation at 500-620°C are quite similar to those that form in HFIR, with several significant but explainable exceptions. In both reactors, $M_{23}C_6$ and M_6C precipitates form. The latter predominates at 500°C in both aged and irradiated conditions,[7,9] possibly as a consequence of the higher silicon level of the DO-heat. This phase, referred to as η in other studies,[5-9] is the only phase rich in both silicon and nickel that is reported to form in the absence of irradiation. Both this and previous studies[4-5] have shown more than one variant in orientation. The variants possess differences in composition, and both are rich in nickel and silicon.

There appears to be two types of $M_{23}C_6$ precipitates, those that form at low temperatures and are rich in nickel and silicon, and those that form as classical chrome carbides at higher temperatures (including 600°C) and which resist the infiltration-exchange process. Laves is observed to form in both reactors in the range 500-620°C, although this and other studies[2-3] have shown that Laves becomes progressively richer in nickel and silicon as the irradiation proceeds. Sigma and Chi phases have not been observed in this or other[9] EBR-II studies in the 500-620°C range, but they have been observed in HFIR studied at 620°C. This discrepancy is thought to be a consequence of the fact that the actual temperature is closer to 700°C than 600°C.

It is significant to note that the radiation-stable phases[4] γ' and G-phase are not reported for HFIR irradiated 00-heat in the range 500-620°C while this study found both precipitates at 69 dpa but neither at 33 dpa. If the absence of both phases in HFIR irradiated steel is permanent rather than temporary, it could signal a real dependence of microstructure on neutron spectra. However, the Mn-rich G-phase is not a major phase and may easily have been missed. Another possibility is that this late forming manganese-rich phase is precluded by the burn-out of manganese by transmutation in HFIR. The effect of transmutation in HFIR is also demonstrated by the vanadium enrichment in Laves in 20% cold-worked steel at 600°C and annealed steel at 550°C.[5-9] Vanadium, nominally <0.01%, is not produced in measurable quantities in EBR-II but forms in HFIR to levels approaching 0.82%.[12]

While the γ' phase was reported to form at low dose in HFIR at 385°C and then to be replaced by the M_6C phase, no γ' was observed in HFIR in the sparse data base covering the range 475-565°C for doses below 50 dpa. The present data show, however, that at 500°C γ' has not formed in EBR-II at 33 dpa but is present after 69 dpa. This suggests that its formation is as sluggish in the silicon-rich DO-heat as it is in several other heats irradiated in EBR-II.[14] At doses less than about 50 dpa, it appears that γ' does not form in the DO-heat in either reactor.

The swelling in AISI 316 has been shown to accelerate concurrently with the acceleration of the microchemical evolution.[1-3,14] The microchemical evolution is unfinished at 33 dpa, as evidenced by the low swelling, the near-precipitate gradients in elemental composition, the absence of γ' at 500°C *and the* similarity of matrix nickel at both 500 and 600°C to that of unirradiated steel. The evolution is nearing completion at about 70 dpa as evidenced by the absence of gradients, low matrix nickel concentrations and large swelling values.

Figure 3 shows that the void densities found in the HFIR and high fluence EBR-II specimens are approximately equivalent at 620°C and differ by a factor of about ten at 510°C. The difference at 510°C partially reflects coalescence events at the larger swelling level (11%) in the EBR-II specimen. It is significant to note that over two orders of magnitude difference in helium/dpa ratio has had a remarkably small effect on the void density. In another paper, it is shown that differences in helium/dpa ratios in typical reactor irradiation influence primarily the rate of approach to a saturation void density, but do not strongly influence its final value.[16] Given the uncertainties in irradiation temperature for HFIR and the large disparities in some of the HFIR density and microscopy measurements (16.8 vs. 8.0% at 680°C, 0.0 vs. 1.43% at 550°C, 0.8 vs. 2.0% at 460°C),[10,17] it is difficult to make a completely conclusive comparison between the HFIR and EBR-II swelling data. If we compare only microscopy determinations of cavity volume produced in the two reactors, a restriction that has no

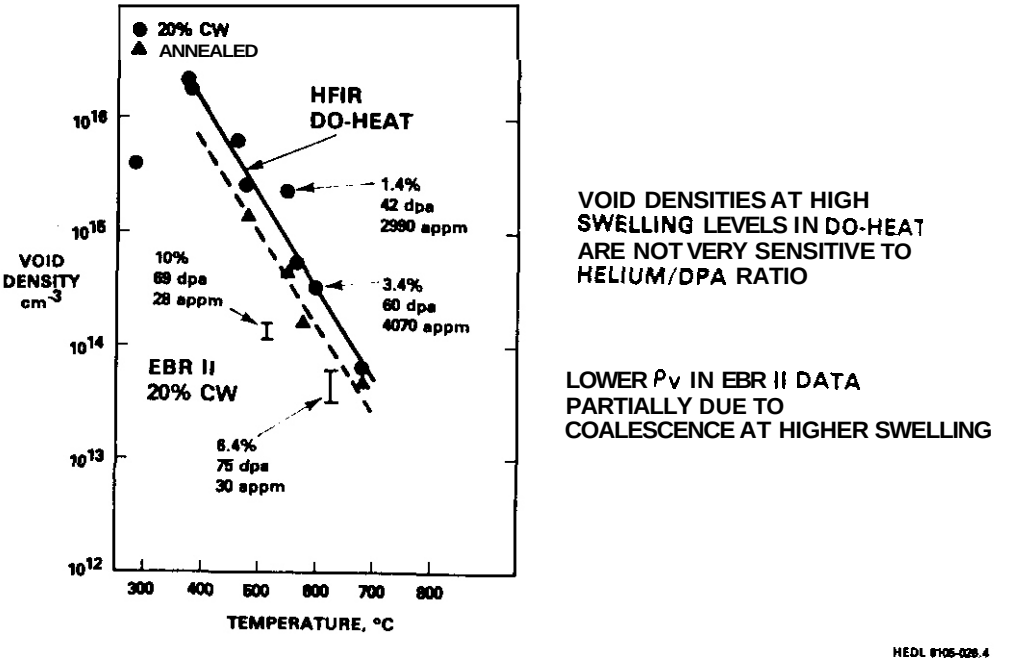

FIGURE 3. Comparison of Cavity Densities Observed in DO-Heat Irradiated in EBR-II and HFIR.

material influence on the conclusions drawn in this report, it can be seen in Figure 4 that all data lie within a narrow band, independent of both helium level and temperature. The relative insensitivity of swelling at high fluence to irradiation temperature has been observed earlier in AISI 316.[10,18]

While the HFIR data do not extend to as high a dose as do the EBR-II data, an estimate of the eventual swelling data in HFIR can be made. This assessment is based on data of solution annealed steel[10,11,17] and the observation that the steady-state swelling rate of AISI 316 is relatively independent of cold work level.[3,14,19] The available HFIR data on annealed steel, Figure 5, indeed corroborate the high swelling rate of Figure 4.

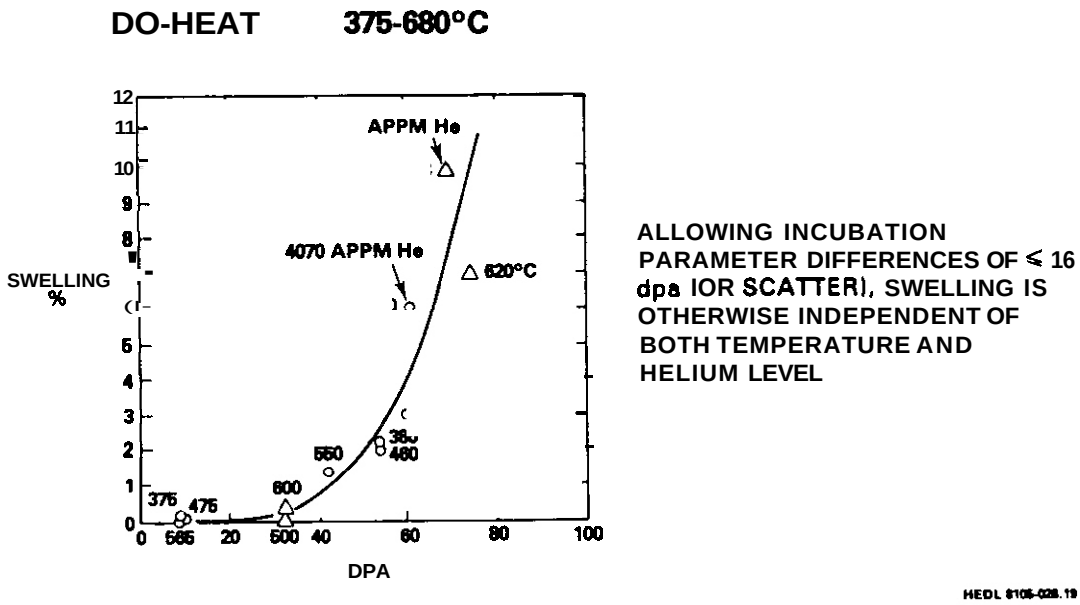

FIGURE 4. Comparison of Cavity Volumes Observed in DO-Heat Irradiated in EBR-II and HFIR.

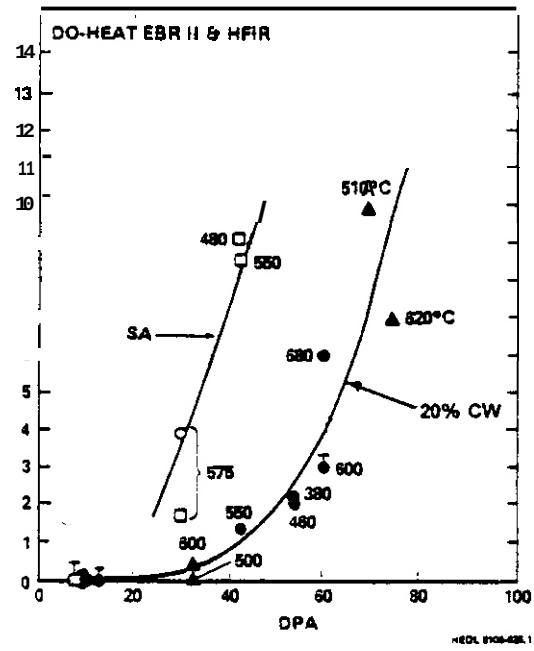

FIGURE 5. Comparison of Swelling Observed in Solution Annealed DO-Heat in HFIR (□density, omicroscopy) With That of Cold Worked DO (● HFIR, ▲EBR-II).

The apparent insensitivity of swelling to helium level at high fluence in the temperature range of 500 to 610°C is in contrast to conclusions drawn earlier from HFIR irradiations that swelling is accelerated by high helium/dpa ratios.[20,21] While the cavity density develops more quickly in HFIR, the swelling does not respond as dramatically.[16] It was observed, however, that due to the higher helium generation, the HFIR irradiation will produce at high temperatures an additional component of swelling at grain boundaries(") that will not occur in EBR-II.

Since projected fusion devices will exhibit helium/dpa ratios intermediate to that of EBR-II and HFIR, it is expected that the void density and associated swelling in fusion devices will not be too different at 500-620°C from that observed in EBR-II.

5.4 Conclusions

The microstructural and microchemical evolution of AISI 316 is not very sensitive to the more than two orders of magnitude difference in helium generation rates found in HFIR and EBR-II. The few differences observed in the microstructural evolution generated in HFIR and EBR-II can be explained in terms of differences in solid transmutation rates and neutron fluence levels.

6.0 References

1. H. R. Brager and F. A. Garner, "Dependence of Void Formation on Phase Stability in Neutron Irradiated Type 316 Stainless Steel," Effects of Radiation on Structural Materials, ASTM-STP-683, J. A. Sprague and D. Kramer (Eds.), 1979, pp. 207-232.

2. H. R. Brager and F. A. Garner, "Microchemical Evolution of Neutron-Irradiated Stainless Steels," Effects of Radiation on Materials, ASTM-STP-725, D. Kramer, H. R. Brager and J. S. Perrin (Eds.), 1981, pp. 470-483.

3. F. A. Garner, "The Microchemical Evolution of Irradiated Stainless Steels," Proceedings Symposium on Irradiation-Phase Stability, October 5-9, 1980, Pittsburgh, PA, (in press).

4. W. J. S. Yang, H. R. Brager and F. A. Garner, "Radiation-Induced Phase Development in AISI 316," ibid.

5. P. J. Maziasz, "Precipitation Response of Austenitic Stainless Steels to Simulated Fusion Irradiation," The Metal Science of Stainless Steels, E. W. Collings and H. W. King (Eds.), AIME, 1978, pp. 160-180.

6. P. J. Maziasz, J. Nucl. Mat., 85 and 86, (1979), pp. 713-717.

7. P. J. Maziasz, Scripta Met., 13, (1979), pp. 621-626.

8. P. J. Maziasz, Scripta Met., 14, (1980), pp. 1251-1256.

9. P. J. Maziasz, J. A. Horak and B. L. Cox, "The Influence of Both Helium and Neutron Irradiation on Precipitation in 20% Cold-Worked Austenitic Stainless Steel," (in Ref. 3).

10. P. J. Maziasz, F. W. Wiffen and E. E. Bloom, "Swelling and Microstructural Chanaes in Type 316 Stainless Steel Irradiated Under Simulated CTR Conditions," Proceedings of Conference on Radiation Effects and Tritium Technology for Fusion Reactors, CONF-750989 (1976), Vol. I, pp. 259-287.

11. E. E. Bloom and J. O. Stiegler, "Effect of Irradiation on the Microstructure and Creep-Rupture Properties of Type 316 Stainless Steels," Effects of Radiatibn on Substructure and Mechanical Properties of Metals and Alloys, ASTM-STP-529, ASTM, 1971, pp. 360-387.

12. F. W. Wiffen and E. E. Bloom, Nucl. Tech., 25, 1975, pp. 113-123.

13. J. F. Bates, F. A. Garner and F. M. Mann, "The Effects of Transmutation Products on Swelling in 316 Stainless Steel," this conference.

14. H. R. Brager, F. A. Garner, E. R. Gilbert, J. E. Flinn and W. G. Wolfer, in Radiation-Effects in Breeder Reactor Structural Materials, M. L. Bleiberg and J. W. Bennett (Eds.), AIME (1977), pp. 727-755.

15. H. R. Brager and F. A. Garner, J. Nucl. Mat., 73, (1978), p. 9.

16. B. B. Glasgow, A. Si-Ahmed, W. G. Wolfer and F. A. Garner, "Helium Bubble Formation and Swelling in Metals," this conference.

17. F. A. Garner, P. J. Maziasz and W. G. Wolfer, "Development of a Swelling Equation for 20% CW 316 for a Fusion Device," DAFS Quarterly Report, DOE/ER-0046/3, p. 159.

18. J. F. Bates and M. K. Korenko, Nucl. Tech., 48, (1980), p. 303.

19. W. K. Appleby, E. E. Bloom, J. E. Flinn and F. A. Garner, "Swelling in Nuetron-Irradiated 300-Series Stainless Steels," Reference 14.

20. E. E. Bloom, F. W. Wiffen, P. J. Maziasz and Stiegler, Nucl. Tech., 31, (1976), pp. 115-121.

21. J. A. Spitznagel, F. W. Wiffen and F. V. Nolfi, J. Nucl. Mat., 85 and 86, (1979), pp. 629-646.

7.0 Future Work

Analysis of microchemical data on DO-heat irradiated in EBR-II will proceed. Specimens irradiated in HFIR will also be examined.

8.0 Publications

This report will be published in the proceedings of the Second Topical Meeting on Fusion Reactor Materials, August 9-12, 1981 in Seattle, WA.

THE HISTORY DEPENDENCE OF THE MICROCHEMICAL EVOLUTION OF IRRADIATED AISI 316 AND 304L STEELS - F. A. Garner (Hanford Engineering Development Laboratory) and D. L. Porter (Argonne National Laboratory - West)

1.0 Objective

To determine the dependence of the radiation-induced microchemical evolution of stainless steels on variables such as thermal-mechanical starting condition, temperature, stress, helium-to-displacement ratio, neutron flux and fluence.

2.0 Summary

It appears that the effect of helium on cavity density in AISI 316 is primarily a transient phenomenon and that both the microchemical evolution and swelling behavior of austenitic stainless steels exhibit their primary sensitivity to other variables. The total nickel removal from the alloy matrix is a good index of the microchemical evolution, and exhibits a strong dependence on a large variety of environmental and material variables.

3.0 Program

Title: Irradiation Effects Analysis (AKJ)
Principal Investigator: D. G. Doran
Affiliation: Hanford Engineering Development Laboratory

4.0 Relevant DAFS Program Plan Task/Subtask

Task II.C.1 Effects of Material Parameters on Microstructure
Task II.C.17 Microstructural Characterization

5.0 Accomplishments and Status

5.1 Introduction

In a previous report is was shown that extraction and analysis of precipitates that develop in AISI 316 irradiated in EBR-II leadsto the conclusion that the microchemical evolution at a given temperature is sensitive to some variables but not others.[1] It was found that there is an acceleration with applied stress of the radiation-induced nickel removal process by precipitation at 550°C but not at 400°C, an observation which is in agreement with the results of other studies.[2] The relative swelling behavior of specimens with different heat treatments could also be correlated with the amount of nickel removed from the alloy matrix. At 400°C there appeared to be a sensitivity of the level of precipitation to neutron flux and/or time in reactor. At 400°C the microchemical evolution was found to be very sluggish and still in progress at 14×10^{22} n/cm^2 (E >0.1 MeV). At 550°C the evolution was less sluggish and still in progress at 7×10^{22} n/cm^2.

This analysis has now been extended to include additional data and also to group the data into smaller subsets. The analysis of the subsets confirms the original conclusions and yields additional insight on the nature of the microchemical evolution and its dependence on irradiation history.

5.2 Microchemical Evolution: Impact of Newer Data and Additional Analysis

Figure 1 shows that at 550°C both solution-annealed and 20%-cold worked steels continue during irradiation to develop precipitates which are progressively richer in nickel content. As expected from the relative swelling behavior, the nickel content of precipitates in the annealed steel is somewhat ahead of that in the 20% cold-worked steel. The annealed curve may represent material which was not stressed at the nominal 207 MPa level however. Although this tube started at a hoop stress of 207 MPa, it leaked at some unknown time and rate during irradiation and had only 24.4 MPa at the end of the experiment. If the stress was reduced prior to the end of the swelling incubation period, then the nickel removal and swelling levels might be larger (than shown in Figure 1) for conditions of constant stress.

The newest data point at $\sim 7 \times 10^{22}$ n/cm^2 for 20% cold worked AISI 316 confirms

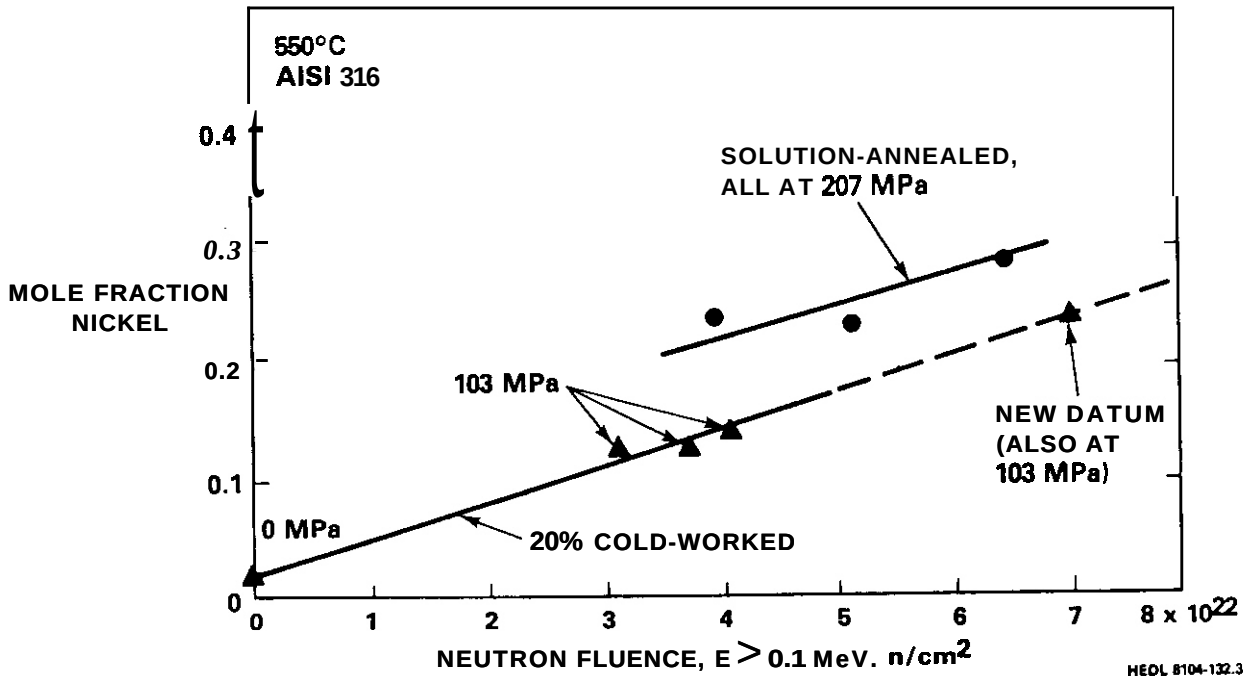

FIGURE 1. Nickel Content of Precipitates Extracted From Pressurized Tubes of Annealed or 20% Cold-Worked AISI 316 Irradiated at 550°C.

the earlier conclusion that there is indeed a separation between the annealed and cold worked curves.

Figure 2 shows the mole fraction of nickel in 10 and 20% cold-worked AISI 316 during irradiation at 400°C. Note that the latest datum confirms both the stress-insensitivity of these data and their independence of cold-work level at 400°C. (Some of the precipitates that form at 500°C and higher temperatures have been found to be sensitive to stress level, however [2-3].)

It is significant that the evolution at 400°C is still in progress at 14 x 10^{22} n/cm^2 (E >0.1 MeV). This demonstrates that the evolution is very sluggish at

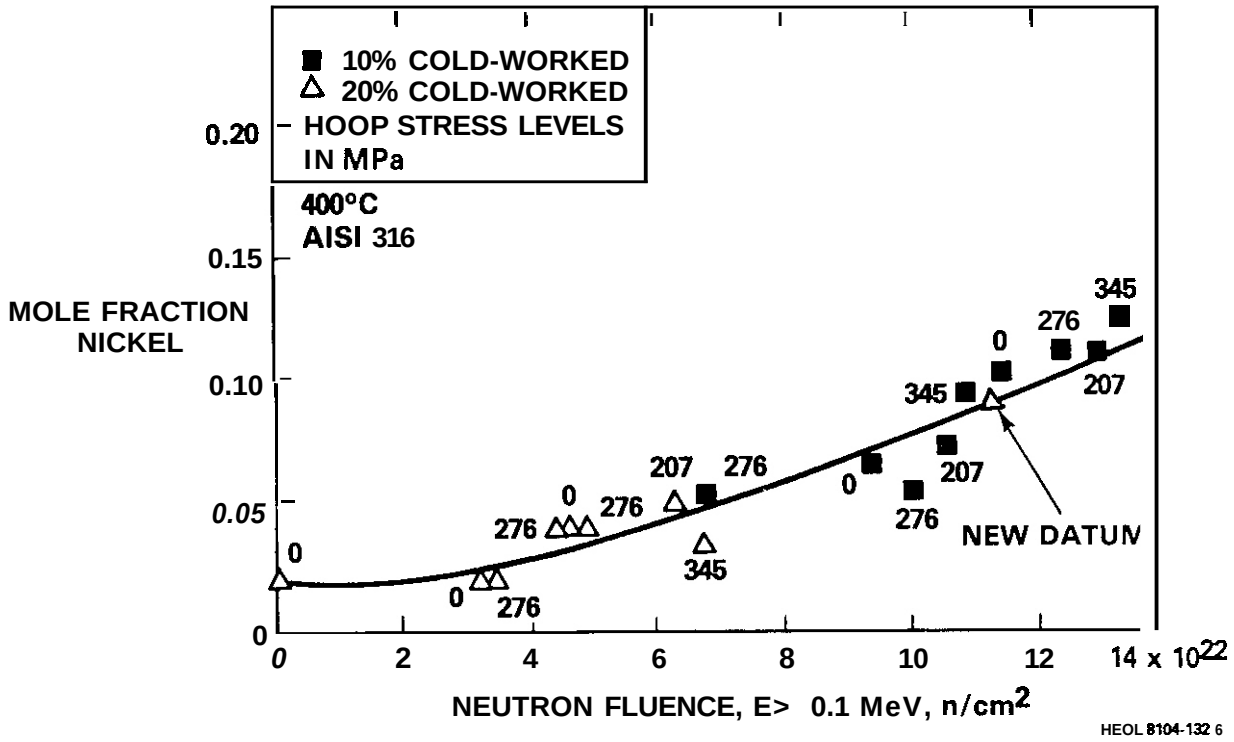

FIGURE 2. Nickel Content of Precipitates Extracted From Pressurized Tubes of Cold-Worked AISI 316 Irradiated at 400°C.

400°C and is proceeding toward yet a higher level of nickel removal. It is this potentially higher level of nickel removal, which can be reached in not quite so sluggish a fashion for certain temperature histories, and which can lead to substantially higher levels of swelling. (4-5)

In order *to* fully substantiate the conclusion that the microchemical evolution at 400°C continues till at least 14 x 10^{22} n/cm^2 and probably beyond, it would be best to plot the total nickel removal from the matrix rather than just the nickel concentration of the precipitates. In the previous report this was not done because the amount of precipitates produced in each specimen did not appear to follow as well-defined a trend with fluence as did the nickel level of the precipitates. The total nickel removal is of course the product of the amount of precipitates and their nickel content.

Figure 3 shows the precipitate levels for the 10%cold-work data, reproduced from Reference 1. The apparent lack of a clear trend of precipitate amount as a function of fluence was at first thought to be an experimental problem.

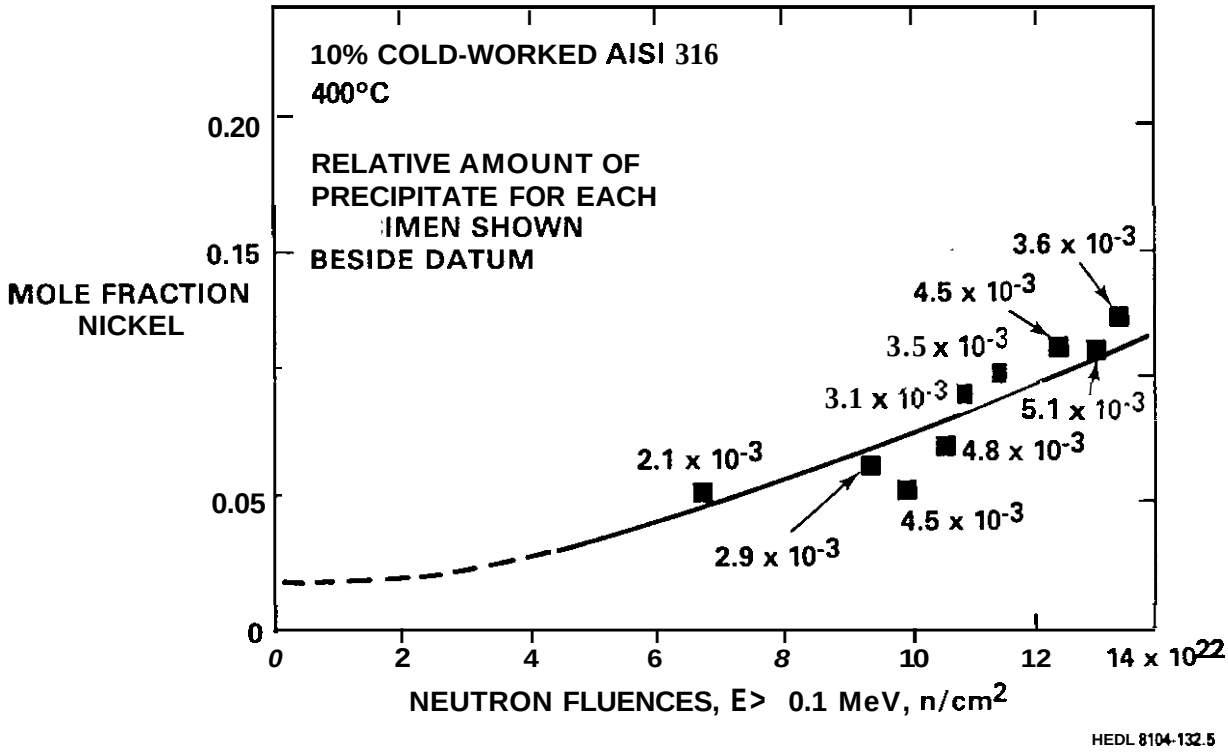

FIGURE 3. Data From Figure 2 on 10% Cold-Worked AISI 316 Only, Showing Amounts of Precipitate Associated With Each Concentration Measurement.

Precipitate extractions were done by dissolving tube sections (∿1 inch) electrolytically in a mixture of hydrochloric acid and dimethlformamide. The extracted precipitates are then dissolved by adding perchloric acid. After boiling the solution dry, hydrochloric acid is again added and the solution examined by atomic absorption. The data are produced as weights of Cr, Fe, Mo and Ni in the solution. From these data, relative concentrations of these elements can be obtained very accurately, and, with less confidence, a measure of the degree of precipitation can be obtained by dividing the sum of these elemental weights by the original weight of the tubing sample. The latter number carries more experimental error since it is difficult to insure that all the originally extracted precipitate remains in the final solution.

It now appears, however, that the lack of a clear trend is an artifact of the assumptions underlying the analysis. In plotting all the data on a single

curve it is implicitly assumed that there is no influence of tube-to-tube variations or history effects of time, flux, spectrum, etc. In an earlier report, however, some limited data were presented for 20% cold-worked AISI 316 irradiated at 400°C which showed that the largest amount of precipitates was formed for the lowest flux/longer residence time irradiations.[1] Therefore the available data were re-examined to see if more consistent trends could be found in subsets with comparable histories.

In the nine data points for 10% cold-worked steel at 400°C were found four subsets of two data each, derived from the same tube. Thus each partner in a given subset possessed a common preirradiation material history and residence time in reactor, but was irradiated at a different flux level to a different fluence. Note in Table 1 that in each subset the precipitate amount has either stabilized or increased during the fluence increment separating the two data points. The nickel levels of the precipitates have all increased during the fluence increment.

TABLE 1

AMOUNT OF NICKEL REMOVAL INTO PRECIPITATES AT 400°C

Tube Designation	Fluence 10^{22} n/cm^2 ($E > 0.1$ MeV)	Precipitate Amount/10^{-3}	Nickel Content	Product/10^{-3}	$\frac{\Delta V}{V_0}$ %
EA-85	9.4	2.9	.066	0.19	.69
	11.5	3.5	.101	0.35	1.09
EA-93	10.9	3.1	.093	0.29	1.66
	13.4	3.6	.123	0.44	2.47
EA-40	10.1	4.5	.055	0.25	1.52
	12.5	4.5	.110	0.49	1.73
EA-43	10.6	4.a	.073	0.35	1.41
	13.05	5.1	.110	0.56	1.89
EA-44	6.8	2.1	.054	0.11	0.53

Figure 4 shows the total nickel removal for the four subsets and the one datum for which there was no companion in the subset. It is clear from this figure that the microchemical evolution (as expressed in the removal of nickel from the matrix) is still proceeding at a fluence around 14 x 10^{22} n/cm^2.

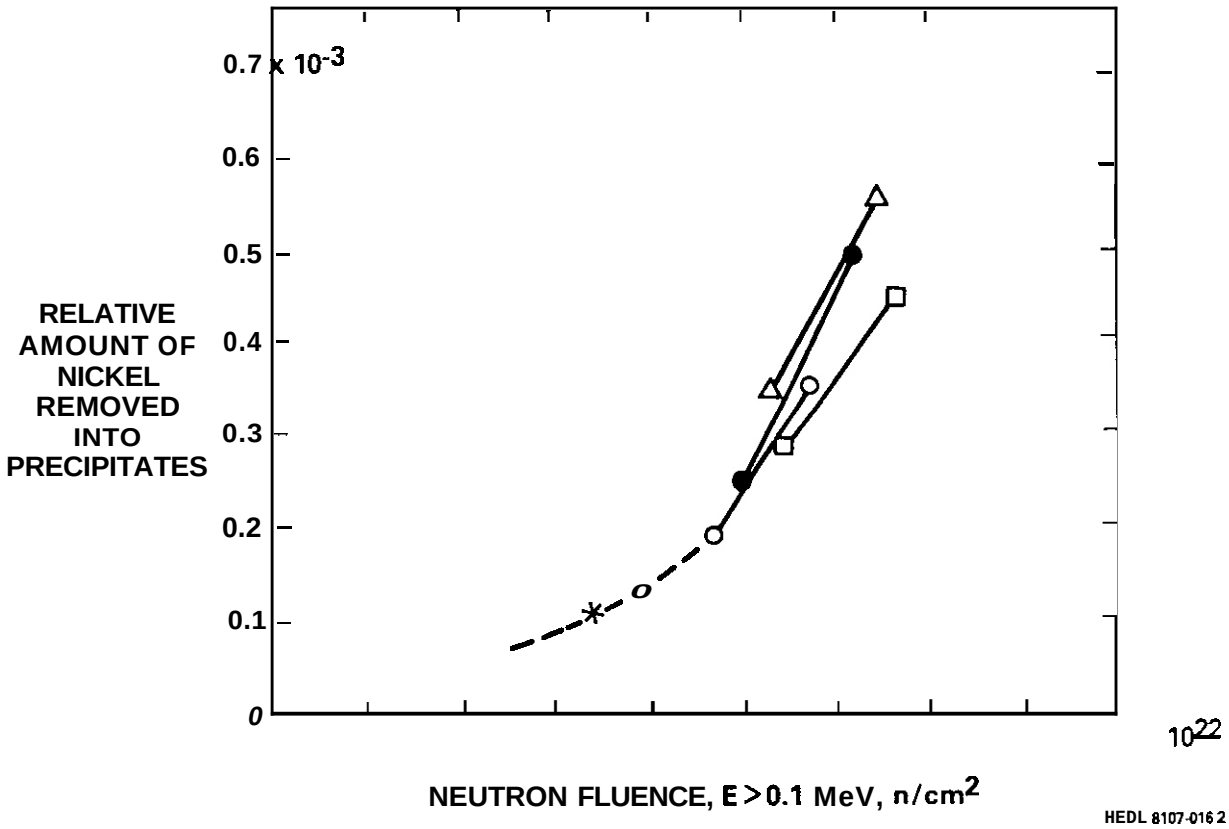

FIGURE 4. Total Nickel Removal Calculated From Data in Figure 3, Broken Down into Subsets, Each Representing Only Data Extracted From a Single Tube. (Refer to Table 1 for details).

The exact nature of the history difference between the various tubes in not yet clear. The tubes experienced not only various stress levels but also different flux levels. Additional analysis is proceeding in an attempt to identify the difference in history effects in the data set.

5.3 Relative Role of Microchemical Evolution and Helium Generation Rates

It appears that earlier conclusions [1,6] drawn about the importance

of the microchemical evolution of irradiated stainless steel, and its history dependence, are again partially confirmed. It was also shown earlier that this path-dependent evolution can be linked directly to the swelling and creep behavior of AISI 316 stainles steel,[1-6] and that the changes in nickel content of the matrix are an excellent index of the progress of this evolution.

One area of current interest is the relative importance of the microchemical evolution and the accelerated cavity development characteristic of irradiations in neutron spectra producing high helium-to-displacement ratios. This question is being addressed in a variety of ways.

One of the most direct ways is to study the relative behavior of a single heat of steel in two spectra, which hopefully differ only in the helium-to-dpa generation rate. As reported in Reference 7, an examination of the DO-heat of AISI 316 irradiated in HFIR and EBR-II does not show significant differences in microstructural and microchemical evolution in the two reactors. The primary difference is that the void density evolves at a somewhat slower rate in EBR-II at 500°C but not at 600°C. There is also some evidence that the phase evolution of AISI 316 in HFIR is perturbed somewhat by the burn-out of manganese.[8] It is also anticipated that there will be consequences of the large vanadium buildup that occurs in HFIR,[8] and that the transmutational changes in HFIR irradiated steels will complicate and possibly obstruct the successful determination of the relative roles of helium generation and the nickel removal process.

Another method of addressing this question is to analyze the microstructural data sets derived from irradiations of different heats of steel in reactors having large differences in helium generation rate. A comprehensive study is nearing completion and portions of that study are presented here.

5.4 Partial Summary of Available Data on Development of Void Densities in AISI 316

The time-dependent void density that develops in neutron-irradiated AISI 316 has

been found to be dependent on a number of variables. In general the evolution in number density for isothermal irradiation can be described in terms of two major regimes, transient and saturation (Figure 5), and one regime *of* apparently minor importance (coalescence at large swelling levels). The transient regime is where the majority of variables exert their strongest influence. These variables are temperature, displacement rate, cold work level, preirradiation thermal history, helium/dpa ratio, applied stress, etc. The cold-work level and helium/dpa ratio are perhaps the dominant determinants of the duration of the transient regime.

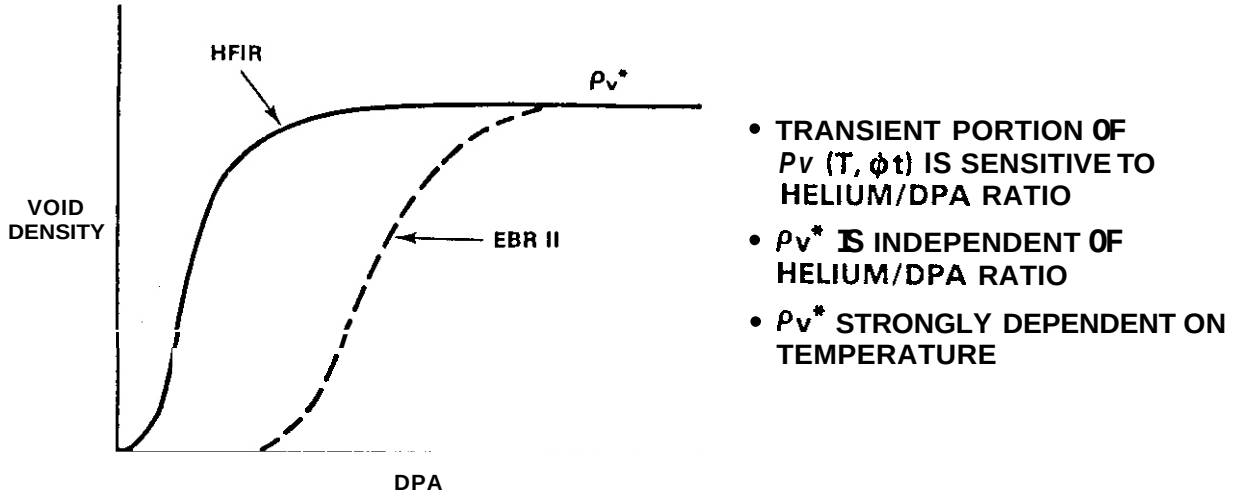

FIGURE 5. Schematic Representation of Helium Influence on Void Nucleation in AISI 316 Stainless Steel.

The steady-state or saturation regime has been found to be much less sensitive *to* these variables than originally anticipated, with the exception of temperature and displacement rate. The action of these two variables on void density is coupled, which requires that careful comparisons be made between data from various fission reactors to obtain comparable flux/temperature comparisons. For instance, the very high γ-heating rates in HFIR usually require that the highest test temperature occur at the position of peak displacement rate, while

in EBR-II fuel cladding the highest and lowest test temperatures are obtained at the ends of the core where the displacement rate is lowest. (In experimental test assemblies any flux-temperature combination is possible).

Figure 6a shows the void densities developed in HFIR irradiation of one heat of AISI 316.[9] (The displacement rate at 380°C is roughly one-third of that at 680°C). Note that at the two temperatures where comparisons can be made at different fluence, the void density has not increased beyond that observed at 1×10^{22} n/cm^2 (E >0.1 MeV). This means that void nucleation is over before ~300 appm of helium has accumulated. Hence the increase in He/dpa ratio in HFIR after 1×10^{22} n/cm^2 is of little consequence for void nucleation.

Figure 6b shows that the void densities of breeder fuel pin cladding in DFR [10] are comparable to that obtained in HFIR, particularly when data sets are chosen to avoid comparisons at substantially different swelling and/or flux levels.

Figure 6c shows that the void number densities are reproducible in comparable irradiations of one heat of steel, and that the approach to saturation at low helium/dpa ratios is slowest at higher temperatures.[10]

Figure 6d shows that the buildup of void density toward saturation in EBR-II at 500°C for one heat of steel is slower than that of another heat in HFIR and is also sensitive to stress. The void densities in each fluence subset of data increase with increasing stress level.

It therefore appears that the void densities that develop in AISI 316 during neutron irradiation are sensitive to helium only in the transient regime, and are remarkably insensitive at saturation to differences in helium generation rates which vary over two orders of magnitude.

Another data set which offers insight on the relative roles of cavity density and microchemical evolution has recently been published by Porter, McVay and Walters.[13] They studied the swelling and microstructural evolution of annealed 304L at 415°C in EBR-II after prior irradiation to 5.1 x 10^{22} n/cm^2 (E >0.1 Mev) and ex-reactor

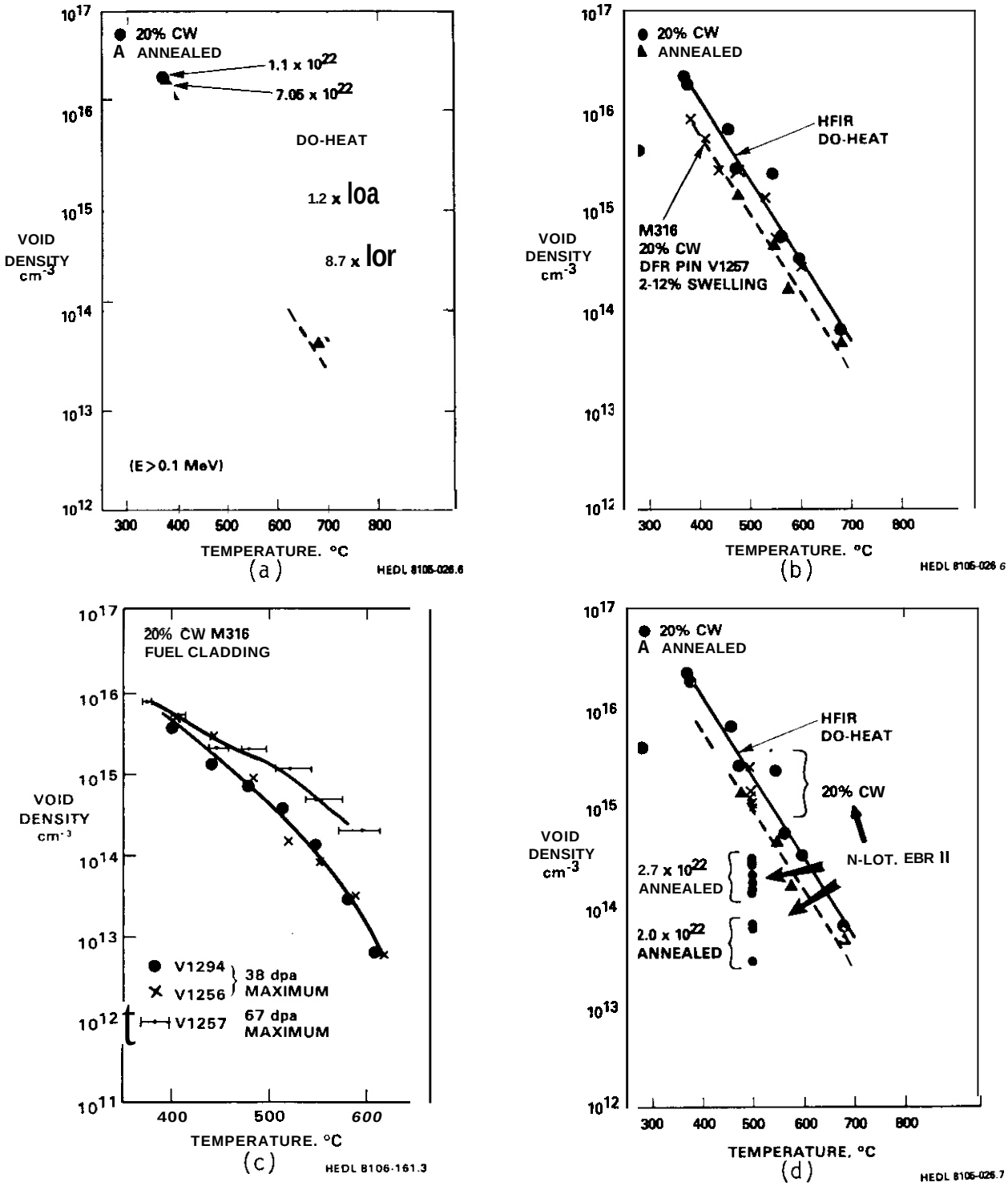

FIGURE 6. Comparison of Void Densities Observed in AISI 316 After Irradiation in HFIR and Two Breeder Reactors, Showing That Saturation Densities are Essentially Identical in Both Types of Reactors, but That the Transients are Longer in Breeder Reactors.

annealing at 700°C for one hour. As shown in Figure 7 the specimens had developed 3% swelling prior to the annealing. The void density is known to saturate quickly at lower fluence in 304L in the annealed condition. After annealing the void distribution was found to be unchanged but the dislocation density had been greatly reduced and the authors calculated that substantial redistribution of segregated elements had occured.

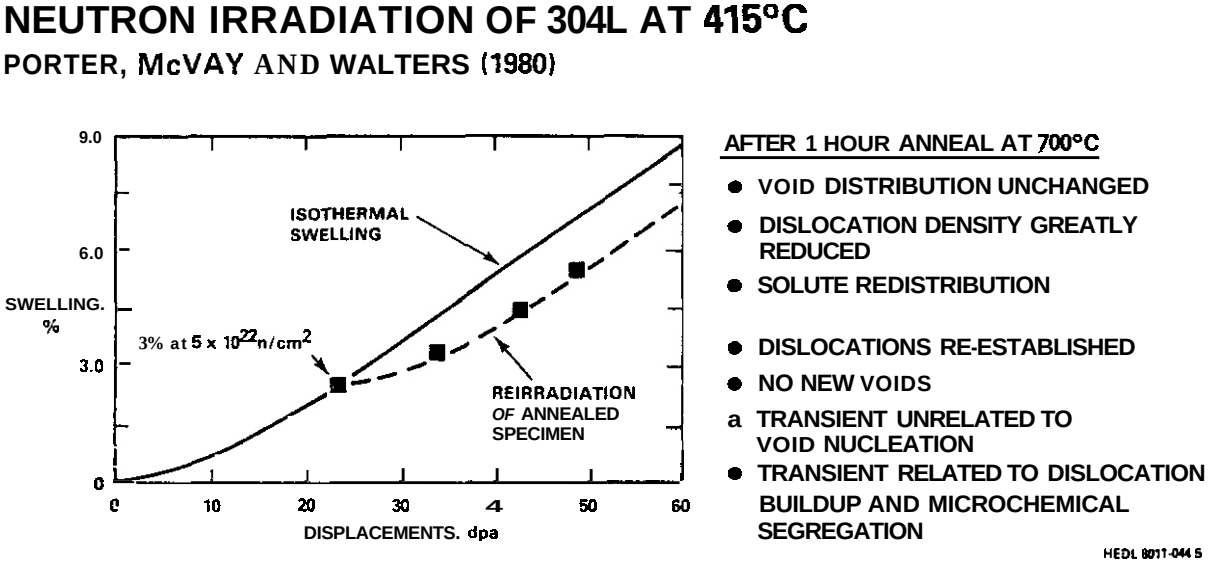

FIGURE 7. Comparison of Swelling of Annealed 304L Steel in Both the Isothermal and Annealed/Reirradiated Conditions. (13)

Upon subsequent reirradiation the dislocation density was quickly re-established and no new voids were observed. The most important conclusion drawn by the authors was that the transient was a duplicate of the original transient, even though there were $\sim 10^{16}$ voids/cm^3 present at the onset of the second irradiation. The steady-state swelling rate was also identical to that of the unannealed material. The authors concluded that the transient was unrelated to void nucleation but depended only on the dynamics of dislocation buildup and microchemical segregation.

5.5 Conclusions

It appears that the effect of helium on cavity density in AISI 316 is primarily

a transient phenomenon and that both the microchemical evolution and swelling behavior of austenitic stainless steels exhibit their primary sensitivity to other variables. The total nickel removal from the alloy matrix is a good index of the microchemical evolution, and exhibits a strong dependence on a large variety of environmental and material variables.

6.0 References

1. D. L. Porter and F. A. Garner, "The Influence of Microchemical Evolution on the Swelling of AISI 316 and Its Dependence on Stress, Temperature and Heat Treatment," DAFS Quarterly Report DOE/ER-0046/5, pp. 141-150.

2. F. A. Garner, "Extrapolation of Stress-Affected Swelling Models Into Compressive and Cyclic Stress States," DAFS Quarterly Report DOE/ER-0046/5, pp. 198-218.

3. F. A. Garner, E. R. Gilbert, and D. L. Porter, "Stress Enhanced Swelling of Metals During Irradiation," DAFS Quarterly Report DOE/ER-0046/4, p. 103.

4. F. A. Garner. E. R. Gilbert, D. S. Gelles. and J. P. Foster. "Effect of Temperature Changes on Swelling and Creep'of AISI 316," Effect of Radiation on Materials, Tenth Conference, ASTM STP 725, D. Kramer, H. R. Brager and J. S. Perrin (Eds.) ASTM (1981).

5. H. R. Braaer and F. A. Garner. "Dependence of Void Formation on Phase Stability-in Neutron Irradiated Type 316 Stainless Steel," ASTM STP 683, Proc. ASTM Ninth Internation Symposium on Effect of Radiation on Structural Materials, Richland, WA, July 10, 1978, p. 207.

6. F. A. Garner, "The Microchemical Evolution of Irradiated Stainless Steels," DAFS Quarterly Report DOE/ER-0046/5, pp. 151-186.

7. H. R. Brager and F. A. Garner, "Influence of the Helium Level on the Swelling and the Microstructural/Microchemical Evolution of AISI 316 Irradiated in HFIR and EBR-II," this report.

8. J. F. Bates, F. A. Garner, and F. M. Mann, "The Effect of Solid Transmutation Products on Swelling in AISI 316 Stainless Steel," this report.

9. P. J. Maziasz and M. L. Grossbeck, "Swelling and Microstructure of HFIR Irradiated 20% Cold Worked Type 316 Stainless Steel and 316 + 0.23 wt.% Ti," ADIP Quarterly Report DOE/ER-0045/4, p. 43.

10. C. Brown, J. K. Butler, and E. J. Fulton, "Void Swelling Studies of Austenitic Fuel Pin Cladding Material Irradiated in the Dounreay Fast Reactor," Proc. of Symposiun on Irradiation Behavior of Metallic Materials for Fast Reactor Core Components," June 5-14, 1979, Ajaccio, Corsica.

11. H. R. Brager, F. A. Garner, and G. L. Guthrie, J. Nucl. Mat., 66, (1977) pp. 301-321.

12. H. R. Brager, F. A. Garner, E. R. Gilbert, J. E. Flinn, and W. G. Wolfer, "Stress-Affected Microstructural Development and the Creep-Swelling Relationships," Proc. International Conference on Radiation Effects in Breeder Reactor Structural Materials, June 19-23, 1979, Scottsdale, AZ, p. 727.

13. D. L. Porter, G. L. McVay, and L. C. Walters, "Resoonse to Annealina and Reirradiation of AISI 304L Stainless Steel Following Initial High-Dose Neutron Irradiation in EBR-II," Effects of Radiation on Materials, ASTM STP 725, D. Kramer, H. R. Braqer, and J. S. Perrin (Eds.), American Society for Testing and Materials, 1981, pp. 500-511.

7.0 Future Work

This work will continue as more data become available.

THE EFFECTS OF SOLID TRANSMUTATION PRODUCTS ON SWELLING IN 316 STAINLESS STEEL

J. F. Bates, F. A. Garner and F. M. Mann (Hanford Engineering Development Laboratory)

1.0 Objective

The objective of this effort is to assess the amount of solid transmutants that develop in AISI 316 during irradition in fast, thermal or fusion reactors and by comparison with the compositional sensitivity of swelling observed in breeder reactors determine the potential swelling behavior of this steel in thermal and fusion reactors.

2.0 Summary

Application of the extensive data base developed in fission reactors to the design of fusion reactors requires an understanding of the differences in the characteristics of the two neutron spectra. Whereas the effects of gaseous transmutants have been previously recognized as potentially important, the amount and role of solid transmutants have been assumed to be inconsequential Although this assumption has been found to be correct for irradiations conducted in fast breeder reactors, it is not correct for fusion and thermal reactor irradiation.

This paper presents the results of a study in which the isotopic evolution of AISI 316 was calculated for two breeder reactors, two fus-ion devices and the High Flux Isotope Reactor (HFIR). The largest changes in composition arise in HFIR, where the manganese is strongly depleted and substantial vanadium is generated. Both of these elements increase in fusion reactors but much more slowly.

Data on the swelling of AISI 316 is presented to show that depletion of manganese in HFIR on the time-frdme of typical irradiations will lead to changes in the swelling behavior. While no swelling data for vanadium-modified steels are available it is anticipated that the swelling behavior will be altered in a

manner typical of other strong MC-carbide forming elements such as titanium.

3.0 Program

Title: Irradiation Effects Analysis (AKJ)
Principal Investigator: D. G. Doran
Affiliation: Hanford Engineering Development Laboratory

4.0 Relevant DAFS Program Plan Task/Subtask

Task II.C.4 Effects of Solid Transmutants on Microstructure
Task II.C.10 Effects of Solid Transmutation Products on Fracture Behavior

5.0 Accomplishments and Status

5.1 Introduction

The confident design of structural components for fusion devices requires not only a relevant materials data base but also some guidance on how to extrapolate the property correlations derived from that data into the untested fusion environment. The overwhelming majority of the relevant data have been developed from irradiations conducted in fast neutron breeder reactors, with smaller amounts of data derived in mixed spectrum (thermal) reactors and 14 MeV neutron sources at low flux. The major extrapolation effort has therefore centered on describing the impact of differences between breeder and fusion devices, primarily concentrating on differences in displacement characteristics and gaseous transmutation products. Transmutations which produce helium have long been recognized as having a large impact on the evolution and dimensional stability of irradiated steels.

However, the lifetime of the first wall of a fusion reactor is sufficient to product significant solid canpositional transmutations in 316 stainless steel. Some of the most significant of these transmutations can affect the manganese and vanadium levels in 316 stainless steel. These changes in the elemental

concentrations may result in substantial changes in void swelling of the first wall. In addition, the changes induced in mixed spectrum reactors such as the High Flux Isotope Reactor (HFIR) are larger than projections for fusion devices they are used to simulate.

The different swelling behavior of various, nominally similar, heats of 316 has been shown to arise from the variations in trace elements,[1] some below the manufacturer's ability to reproduce in commercial practice. Thus minor changes in trace elements due to transmutations may affect the swelling. In addition, the radiation-induced microstructural evolution of stainless steel involves a complex distribution of various solute and solvent atoms between a number of different phases. Differences in generation and segregation rates of solid transmutation products will also probably influence the nature of this "micro-chemical" evolution.

The dimensional stability of 316 as affected by compositional transmutations was evaluated previously [2] utilizing data from low fluence (2 to 4 x 10^{22} n/cm^2, E >0.1 MeV) irradiations in the Second Experimental Breeder Reactor (EBR-II). The studies indicated no detrimental changes in lattice dilation, yield strength, recrystallization temperature or void swelling. Swelling was reduced as the manganese level was increased from zero to around one weight percent and then remained fairly constant out to about four percent. However, higher fluence EBR-II data now reveal that the swelling does not remain constant but increases at the higher Mn levels. Increased or decreased manganese resulting from transmutations can thus produce swelling two to three times that which would occur in an alloy with a standard manganese level.

In this paper we address only solid transmutants. The generation of helium and hydrogen has been treated elsewhere.[3] Also addressed are differences in generation rates of those solid transmutants thought to be important in the chemical evolution of AISI 316 stainless steel for a variety of irradiation facilities. The levels of elemental variations are then compared to recent swelling data to assess the impact of the transmutations on fusion reactor component performance.

5.2 Experimental and Calculational Details

The recent swelling data were determined from pre- and postirradiation density measurements of specimens irradiated in sodium-filled subcapsules in row two of EBR-II. The specimens were solid right cylinders, approximately 0.2" diameter by 0.375" long. Irradiations were conducted at 620°C to a fluence (E >0.1 MeV) of 12.3 x 10^{22} n/cm^2 (61.5 dpa) and at 400 and 510°C to a fluence of 9.1 x 10^{22} n/cm^2 (45.5 dpa). Specimens were irradiated in both the solution annealed and 20% cold worked conditions.

The transmutation calculations were performed with the REAC computer system. This system allows the rapid calculation of transmutations of many isotopes in a material irradiated in nuclear facilities having different spectra. The system consists of a driver program and four libraries: flux, material, cross section, and decay data. The driver program reads information from the libraries, collapses the multigroup fluxes and cross sections to form the needed reaction rates, calculates transmutation and activation rates, and finally sorts the results for output.

The flux library contains 63 group representations of spectra for important Magnetic Fusion Energy facilities. Fluxes for EBR-II [4] and HFIR [5] are from the unfolding of dosimetry reactions, while fluxes for the Fast Flux Test Facility (FFTF), the University of Wisconsin Tokumak conceptual reactor (UWMAK-1),[6] and the Fusion Materials Irradiation Test facility (FMIT) [7] are from diffusion or transport calculations. The multigroup cross sections are based upon ENDF/B-V[8] whenever possible. The ACTL file,[9] special evaluations,[10] and THRESH [11] systematics were used to fill in gaps in cross section evaluations. All important reactions for neutron energies to 40 MeV were included for C, N, Al, Si, P, Cr, Mn, Fe, Co, and Ni. Values for the decay library come from ENDF/B-V or from the 1978 Table of Isotopes.[12] Total fluxes and displacement cross sections for the various reactors and associated displacements are given in Table 1. All calculations were based on the assumption of continuous irradiations but include the time-dependent decay to other isotopes.

TABLE 1

FLUXES AND CROSS SECTIONS FOR VARIOUS REACTORS

Reactor	Position	Total Flux (n/cm^2 sec)	Displacement Cross Section (barns)**
HFIR	HT5	5.60×10^{15}	152
HFIR	A-2	5.90×10^{15}	175
HFIR	PTP	5.84×10^{15}	200
FFTF	Row 1*	6.99×10^{15}	283
EBR-II	Row 2*	2.10×10^{15}	436
UWMAK	First Wall	4.76×10^{14}	856
FMIT	[0,0,0]	3.09×10^{15}	2000

* Midplane position
** Evaluated for AISI 316

The starting concentrations of each element are indicated in Table 2. The composition of the steel utilized in this study is that of CN-13, a 20% cold worked AISI 316 lot of FFTF cladding.

5.3 Results

The results of the swelling evaluations for manganese-modifications of AISI 316 are shown in Figures 1 and 2 for the 400°C and higher temperature data sets, respectively. A minimum in swelling, most prevalent in the 620°C data set, occurs at around 1 to 2 weight percent manganese. The reduced swelling at low manganese has been observed previously (see Figure 3) and is typical of behavior observed when a single element is added at the expense of Fe in 316 stainless steel.[1,13,14] We anticipate that the cold worked material may exhibit a higher fluence minimum similar to that of the solution annealed material.

Table 3 summarizes the percentage changes observed in all elements known or proposed to influence the radiation-induced swelling.[1,14] irradiation creep [13] or microchemical evolution,[15-17] of 316 stainless steel.

TABLE 2

INITIAL CONCENTRATION OF ELEMENTS IN AISI 316

Element	Initial Atomic Percent
Fe	64.3
Cr	18.5
Ni	13.0
Mn	1.65
Mo	1.30
Si	0.99
C	0.246
V	0.0109
N	0.0159
co	0.0094
cu	0.0044
S	0.0052
Al	0.0052
P	0.0036
Ta	0.0023
Nb	0.0003

In general the changes that occur in this steel when irradiated in EBR-II are quite small, with the largest, but probably insignificant, changes occuring in the cobalt and vanadium concentrations. This means that the influence of solid transmutants on the swelling data derived from EBR-II irradiations, can be considered to be negligible. A similar conclusion can be drawn for FFTF. However, in the mixed spectrum and fusion devices there are some rather consequential changes in composition.

5.4 Discussion

In both HFIR [18] and EBR-II [15] 50 dpa can be used as an exposure level at which swelling and creep have approached steady-state behavior for most relevant temperatures. At this displacement level, irradiation in HFIR has resulted in the largest change in the major alloy constituent, iron, at +2%. All other

TABLE 3

PERCENTAGE CHANGES IN COMPOSITION* DUE TO TRANSMUTATIONS

			1 x 10^{23} n/cm^2 (total)												
Reactor	Position	dpa	Fe	Cr	Ni	Si	Mn	C	N	V	Co	Al	S	P	Cu
HFIR	A-2	17.5	.86	-2.16	- .23	- .01	-26	.51	-8.04	3730	158	-.97	.53	3.2	187.5
FFTF		28.8	.02	- .005	- .14	- .002	- .34	.006	- .24	16.7	92	.034	.026	.14	2.62
EBR-II	℄, Row 2	43.6	.028	.013	- .24	- .002	.3	.01	- .44	9.4	64	.05	.02	.04	1.20
UWMAK		85.6	-.49	- .298	-3.16	- .73	33	-.71	-1.17	1340	531	88	.02	-1.7	4.17
FMIT		200	-.55	- .80	-5.86	-1.33	38	-1.47	-2.2	2530	3150	176	.006	-2.8	0.64
			3 x 10^{23} n/cm^2 (total)												
HFIR	A-2	52.5	2.36	-3.7	- .68	- .03	-60	1.5	-24	6470	315	-2.9	1.7	9.5	644
FFTF		86.4	.082	- .005	- .41	- .005	-1.04	.017	-.73	59	122	.10	.085	.397	8.08
EBR-II	℄, Row 2	131	.097	.074	- .727	- .005	.48	.03	-1.3	29	71	.15	.06	.13	3.93
UWMAK		257	-2.21	- .773	-9.34	-2.20	130	-2.1	-3.5	4040	741	265	.06	-5.0	24.1
FMIT		600	-1.68	-1.88	-17.5	-3.99	132	-4.4	-6.7	7830	4770	528	.02	-8.1	3.28

*All values are in units of percent of starting concentration for lot CN-13, FFTF first core heat of AISI 316. Molybdenum is not included in REAC library, but inspection of cross sections shows no probable transmutation problems.

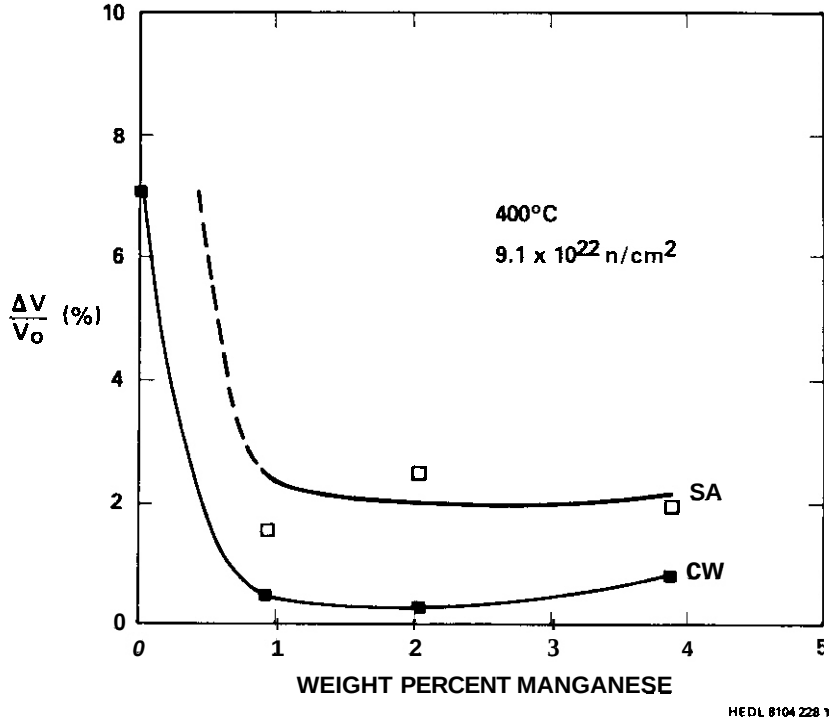

FIGURE 1. Effects of Manganese Content on Swelling in Both Annealed and 20% Cold Worked 316 at 400°C.

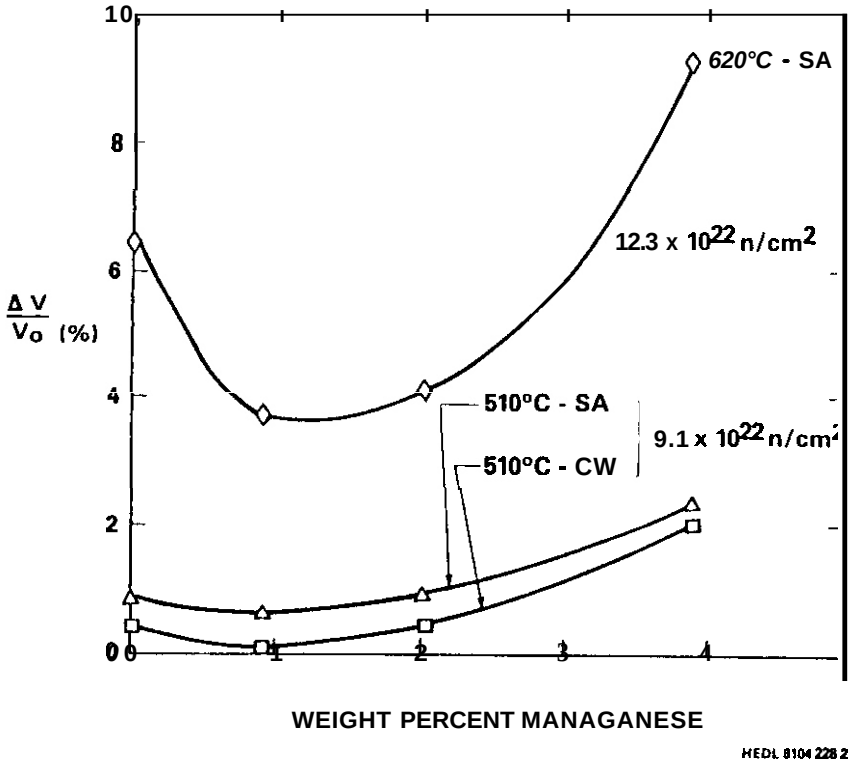

FIGURE 2. Effect of Manganese Content on Swelling in Both Annealed and 20% Cold Worked 316 at 510 and 520°C.

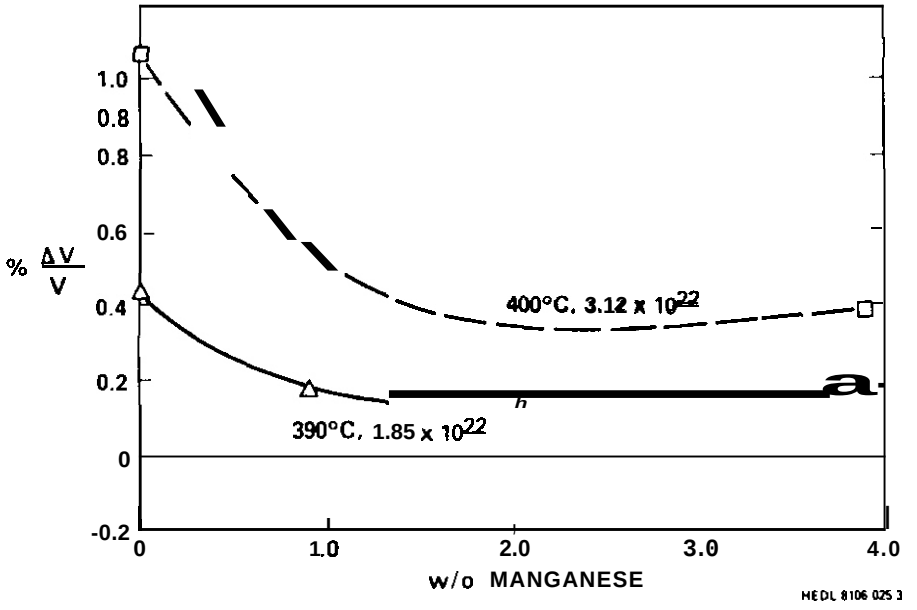

FIGURE 3. Effect of Manganese Content on Swelling of Annealed 316 at Low Temperatures and Low Fluence.(14)

reactors have much smaller changes in iron content. There has also been a 4% reduction in the original chromium concentration and a 0.7% change in the nickel content in HFIR. These changes are believed to be inconsequential.

There have also occurred relatively large changes in initially dilute elements whose roles in dimensional instabilities are uncertain. In the A-2 position of HFIR there are large increases in the cobalt and copper concentrations and a moderate decrease in the nitrogen concentration. More importantly the vanadium has increased by large factor to reach approximately 0.7%. This is a very large amount of vanadium, an element which is a strong MC-carbide former. Another study (19) has shown that strong MC formers, such as titanium, have large effects on swelling, and that the MC carbides formed in HFIR are quite rich in vanadium. As shown in Figure 4, no other reactor system studied will produce even one-fifth the amount of vanadium that is produced in HFIR at 50 dpa. The vanadium in HFIR arises primarily from $^{50}Cr\ (n,\gamma)\ ^{51}Cr \rightarrow\ ^{51}V$ while that in fusion devices is generated by $^{52}Cr\ (n,2n)^{51}Cr \rightarrow\ ^{51}V$ with the decay reaction having a 28 day half-life.

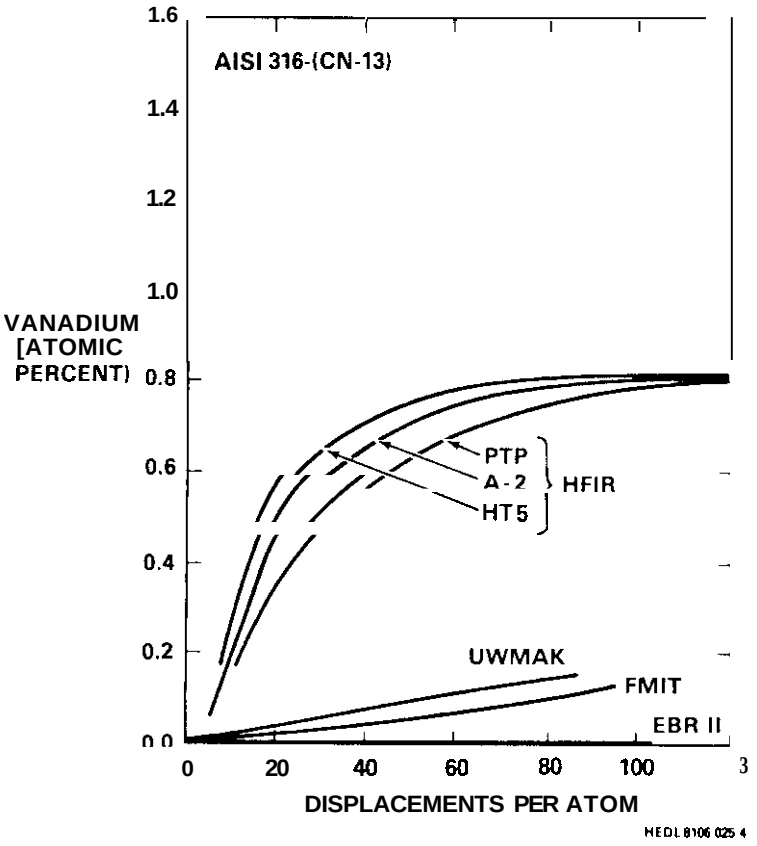

FIGURE 4. Vanadium Concentration as a Function of Exposure for Various Reactors. HT-5, A2 and PTP refer to different positions in HFIR. The saturation of vanadium at 0.814% in HFIR signals the complete burn-out of ^{50}Cr.

The next most consequential change in the AISI 316 composition during HFIR irradiation appears to be that of the manganese content which declines 60 to 70% at 60 dpa depending on which reactor position is chosen for study (see Figure 5). The manganese is seriously depleted during the void incubation stage of the swelling phenomenon. This means that the manganese depletion will have a significant effect on void swelling. Thermal reactors such as Oak Ridge Research Reactor (ORR) will induced a somewhat slower rate of decline since their thermal/fast neutron ratio is lower than that of HFIR.

The fusion devices studied are projected to increase the manganese content in 316 stainless steel (Figure 4). This difference in behavior between fusion devices and HFIR arises because of the relative shift in magnitude between fast and thermal reactions in the various reactors. In HFIR and ORR the dominant

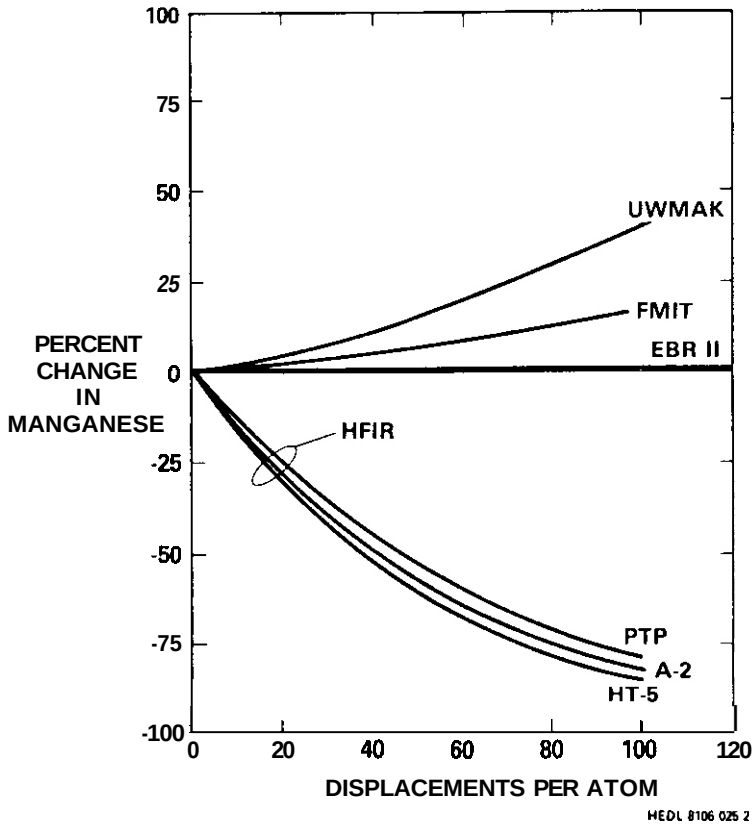

FIGURE 5. Change in Manganese as a Function of Exposure for Various Reactors. HT-5. A2 and PTP refer to different positions in, HFIR.

reaction is $^{55}Mn(n,\gamma)\ ^{56}Mn(t_{\frac{1}{2}} = 3\ hours) \rightarrow\ ^{56}Fe$. For fusion devices the following (n,p) and (n,2n) reactions tend to dominate:

$$^{54}Fe(n,p)\ ^{54}Mn(312\ days) \rightarrow\ ^{54}Fe$$

$$^{56}Fe(n,p)\ ^{56}Mn(3\ hours) \rightarrow\ ^{56}Fe$$

$$^{54}Fe(n,2n)\ ^{53}Fe(10\ min) \rightarrow\ ^{53}Mn\ (4 \times 10^{6}\ years) \rightarrow\ ^{53}Cr$$

$$^{55}Fe(n,2n)\ ^{55}Fe(3\ years) \rightarrow\ ^{55}Mn$$

$$^{55}Mn(n,p)\ ^{55}Cr(4\ min) \rightarrow\ ^{55}Mn$$

$$^{55}Mn(n,2n)\ ^{54}Mn(312\ days) \rightarrow\ ^{54}Fe$$

The magnitude of the various half-lives and abundancies of each isotope indicate that Mn tends not to burn out while Fe tends to transmute to Mn. In fast

reactors, the various burn-in and burn-out reactions tend to cancel each other and therefore no large change in manganese occurs. Although FMIT has a harder spectrum than does UWMAK, the transmutation rate to Mn is larger in UWMAK because the (n,p) cross section peaks around 10 MeV.

It was shown previously [2] that solution-annealed AISI 316 was somewhat sensitive to manganese content at low temperature and low fluences. Higher fluence data at 400°C (Figure 1) confirm this sensitivity, which is even more pronounced in cold worked steel. However, the increases in manganese content that would occur in fusion devices would not lead to much change in swelling at the lower temperatures. But, large decreases would lead to increased swelling at all temperatures. As indicated by Figure 2, differences in the swelling behavior at 620°C (relative to that of EBR-II) are expected in both HFIR and fusion devices. Another consequence of this analysis is that austenitic steels in which most of the nickel is replaced with manganese would be quite unstable in HFIR and probably revert to ferrite.

We are aware of no experiments performed on the effect of vanadium additions to AISI 316. Since vanadium will definitely influence the activity and availability of carbon it is expected that vanadium-modified steels may exhibit some of the same characteristics as titanium-modified steels. One investigation indicates that one may expect an increase in the low temperature swelling (400°C) and a decrease in the high temperature swelling (600°C). [15] Another investigation would suggest that since vanadium is an alpha-stabilizing element, increased concentrations might reduce the swelling. Chromium-rich carbides, such as $M_{23}C_6$, may evolve toward an MC type carbide. However if 0.7% vanadium is formed as free vanadium in the matrix, gross phase instabilities may be expected. [1]

The major elements thought to be important in the microchemical evolution of AISI 316 are nickel, carbon, and silicon. It is significant to note that no appreciable changes occur in any of these elements in any of the reactor systems studied.

5.5 Conclusions

Although solid transmutant effects in AISI 316 are minimal in breeder reactors, there will be significant changes in alloy composition in both fusion and thermal reactors. The elements normally thought to be instrumental in the microchemical evolution of this steel (Ni, Si, C) are not changed significantly in any reactor however.

The most significant changes with respect to the void swelling process occur in the manganese and vanadium concentrations. Whereas both elements will increase relatively slowly in fusion devices, the changes in reactors such as the High Flux Isotope Reactor (HFIR) are much more pronounced.

In HFIR the manganese will be essentially burnt out at doses below 100 dpa. Data on the swelling available from breeder reactor irradiations lead to the conclusion that the severe depletion in HFIR will lead to differences in swelling relative to that produced by both the breeder and fusion environment.

Steels which depend on manganese to stabilize the austenite will probably become ferritic in HFIR, as the manganese is transmuted to iron.

The large level of vanadium produced in AISI 316 at relatively low displacement levels in HFIR is expected to change the swelling, the phase stability and the mechanical properties of the alloy.

6.0 References

1. J. F. Bates and W. G. Johnston. "Effects of Alloy Composition on Void Swelling," Proc. of Conference-on Radiation Effects in Breeder Structural Materials, Scottsdale, AZ, June 1977, p. 625.

2. J. F. Bates. J. 0. Schiffqens and M. M. Paxton, "The Dimensional Stability of 316 SS as Affected by compositional Transmutations," Proc. of Conference on Radiation Effects and Tritium Technology for Fusion Reactors, Gatlinburg, TN, October 1975, Vol. 1, p. 519.

3. G. L. Kulcinski, D. G. Doran and M. A. Abdou, "Comparison of Displacement Rates in Current Fission and Future Fusion Reactors," ASTM-STP-570, February 1976, p. 329.

4. W. N. McElroy, J. L. Jackson, J. A. Ulseth and R. L. Simons, "EBR-II Dosimetry Test Data Analysis (Reactor Runs 31E and 31F)," BNWL-1402, Battelle Meaorial Institute, June 1970.

5. F. B. K. Kam and J. H. Swanks, "Neutron Flux Spectrum in the HFIR Target Region," ORNL-TM 3322, Oak Ridge National Laboratory, 1971.

6. The University of Wisconsin Fusion Feasibility Study Group, UWMAK-1, A Wisconsin Toroidal Fusion Reactor Design, University of Wisconsin, UWFDM-68, March 1974.

7. F. M. Mann, F. A. Schmittroth and L. L. Carter, "Neutron Environment in d + Li Facilities," Proceedings of Second Topical Meeting on Fusion Reactor Materials.

8. ENDF/B Summary Documentation (ENDF-201), 3rd Edition (ENDF/B-V), compiled by R. Kinsey, Brookhaven National Laboratory, BNL-NCS-17541, July 1979. ENDF/B is maintained at the National Nuclear Data Center at Brookhaven National Laboratory.

9. M. A. Gardner and R. J. Howerton, ACTL: Evaluated Neutron Activation Cross Section Library - Evaluation Techniques and Reaction Index, Lawrence Livermore National Laboratory, UCRL-50400, Vol. 18, October 1978.

10. E. D. Arthur and P. G. Young, Evaluated Neutron Induced Cross Sections for ^{54}, ^{56}Fe to 40 MeV, Los Alarnos National Laboratory, LA-8626-MS (ENDF-304), December 1980.

11. S. Pearlstein, "Neutron Cross Sections and Their Uncertainties Obtained from Nuclear Systematics," in Nuclear Cross Sections and Technology, Proceedings of a Conference, Washington DC, 1975. National Bureau *of* Standards Special Publication 425, October 1975.

12. C. M. Lederer and V. S. Shuley (Eds.), Table of Isotopes, Seventh Edition, John Wiley and Sons, Inc., New Yrok, 1978.

13. J. F. Bates, R. W. Powell and E. R. Gilbert, "Reduction of Irradiation-Induced Creep and Swelling in AISI 316 by Compositional Modifications," ASTM-STP-725, March 1981.

14. J. F. Bates, "Irradiation-Induced Swelling Variations Resulting from Compositional Modifications Type 316 SS, ASTM-STP-570, February 1976, p. 369.

15. F. A. Garner, "The Microchemical Evolution of Irradiated Stainless Steels," Proceedings of AIME Symposium on Irradiation Phase Stability, Pittsburgh, PA, October 5-9, 1981, (in press).

16. H. R. Brager and F. A. Garner, "Microchemical Evolution of Neutron-Irradiated 316 Stainless Steel," Effects of Radiation on Materials, ASTM-STP-725, D. Kramer, H. R. Brager and J. S. Perrin (Eds.), ASIM, 1981.

17. H. R. Braaer and F. A. Garner. "Dependence of Void Formation on Phase Stability in Neutron Irradiated Type 316 Stainless Steel," Effects of Radiation on Structural Materials, ASTM-STP-683, J. A. Sprague and D. Kramer, (Eds.), ASIM (1979), pp. 209-232.

18. P. J. Maziasz and M. L. Grossbeck, "Swelling and Microstructure of HFIR-Irradiated 20% Cold Worked Tvoes 316 Stainless Steel and 316 + 0.23% Ti," Alloy Development for Irradiation Performance Quarterly Progress Report, DOE/ER-0045/5, December 31, 1980, p. 43.

19. P. J. Maziasz, "Helium Trapping at Ti-Rich MC Particles in Neutron-Irradiated Type 316 + Ti Stainless Steel," Scripta Met., 14, 1980, pp. 1251-1256.

THE INCLUSION OF TRANSMUTANT EFFECTS ON DEVELOPMENT OF FISSION-Fusion Correlations

F. A. Garner and F. M. Mann (Hanford Engineering Development Laboratory)

1.0 Objective

The purpose of this study is to determine the impact of differences in generation rates of solid transmutants on the development of fission-fusion correlations.

2.0 Summary

The generation of both solid and gaseous transmutants is a strong function of neutron spectrum and neither can be ignored in the development of fission-fusion correlations of dimensional changes or mechanical properties. This report outlines the scope of a study designed to spotlight and assess potential areas where differences in transmutation rates will impact analysis of data and the development of correlations. The study focuses on four problem areas: trace element effects, major element effects, consequences of radiation-induced segregation on local helium deposition rates, and recoil effects on precipitate stability.

3.0 Program

Title: Irradiation Effects Analysis (AKJ)
Principal Investigator: D. G. Doran
Affiliation: Hanford Engineering Development Laboratory

4.0 Relevant DAFS Program Plan Task/Subtask

Subtask II.C.4 Effects of Solid Transmutants on Microstructure
Subtask II.C.10 Effects of Solid Transmutation Products on Fracture Behavior

5.0 Accomplishments and Status

5.1 Introduction

The development of fission-fusion correlations for the irradiation behavior of structural metals requires that the data analyst understand the differences in displacive and transmutational characteristics of the two types of neutron spectra, as well as the response of the metal to differences in preirradiation or irradiation history. The history effects aspect has been addressed elsewhere[1,2] as has the effect of gaseous transmutants[3,4]

More recently, however, it has become apparent that the differences in generation of solid transmutants in the various spectra cannot be ignored. This report outlines the scope and progress to date of a study designed to spotlight and assess potential areas where differences in transmutation rates might impact data analysis and the development of fission-fusion correlations.

5.2 Identification of Potential Problem Areas

5.2.1 Trace Element Effects

There are many alloy properties that have been found to be sensitive to low levels of various trace elements. This sensitivity is frequently accentuated in a radiation environment. A prime example of the latter is the radiation-induced increase in the ductile-brittle transition temperature that occurs in pressure vessel ferritic steels during irradiation in light water reactors[5]. This change has been correlated primarily to impurities such as copper and possibly phosphorus and nickel. Copper is produced in nickel-bearing alloys in reactors such as the High Flux Isotope Reactor (HFIR), but not in the Fusion Materials Irradiation Test (FMIT) facility[6]. As shown in Figure 1, many solutes affect the irradiation creep rate in AISI 316, with the sensitivity being most pronounced at very dilute solute levels.[7] A similar trend has been observed in the swelling of this steel.[8,9

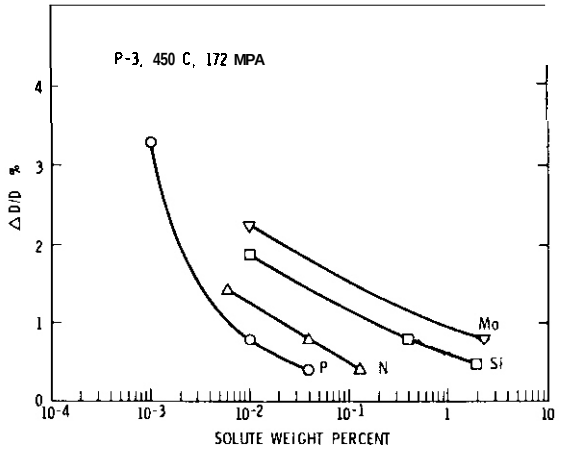

FIGURE 1. Effect of Solute Content on Irradiation Creep of 20% Cold-Worked AISI 316 at 450°C, 4.6 x 10^{22} n/cm^2 (E > 0.1 MeV) and 172 MPa Hoop Stress. The creep is expressed in percentage changes in tube diameter, % ΔD/D.(7)

A property such as ductility may be more sensitive to the differences in transmutation rates of such solutes produced in two different neutron spectra than it is to the differences in gaseous transmutants. An example of such behavior has been observed in the swelling of austenitic-stainless steels, where the swelling was more sensitive to the concentrated lithium produced by the B^{10} (n,α) reaction than it was to the less concentrated helium.(10) (The differences in concentration arise from the differences in range of the recoiling atoms).

The transmutants may exert their influence either as dissolved solutes, grain boundary segregants, or separate phases. Examples of the last mentioned are the silicon shells that form on voids in aluminum alloys irradiated in thermal reactors(11) or the insoluble calcium that will form in titanium during irradiation in fusion devices.

A survey is now being conducted to spotlight potential trace element problems Table 1 lists the results of an earlier unpublished study directed towards this goal. Transmutation of important elements is shown for the projected first wall environment of the UWMAK-I conceptual fusion device at a total flux of 1.5 x 10^{22} n/cm^2 - yr (14 MeV neutron wall loading of 1.25 MW/m2).

TABLE 1

TRANSMUTATION OF MATERIALS IN THE FIRST WALL
OF A FUSION REACTOR

The amount of transmutation is given in percent (for that transmutation greater than 0.001 percent) for a flux as given for the UWMAK-I. One hundred percent of the source element is assumed.

Element	30 Days	150 Days	1 Year	2 Years	3 Years	5 Years
Al						
H	0.05	0.24	0.60	1.2	1.8	3.0
He	0.05	0.28	0.69	1.4	2.1	3.5
Na	0.002	0.002	0.002	0.002	0.002	0.002
Mg	0.05	0.28	0.69	1.4	2.1	3.5
Ti						
H	0.041	0.202	0.497	0.994	1.502	2.509
He	0.013	0.053	0.129	0.259	0.39	0.653
Ca	0.01	0.47	0.095	0.156	0.211	0.319
Sc	0.019	0.047	0.105	0.211	0.326	0.555
V						
H	0.012	0.060	0.147	0.294	0.441	0.736
He	0.008	0.041	0.099	0.197	0.296	0.493
sc	0.001	0.001	0.001	0.001	0.001	0.001
Ti	0.037	0.185	0.452	0.904	1.355	2.258
Cr	0.014	0.072	0.176	0.352	0.527	0.879
C.r						
H	0.037	0.189	0.458	0.915	1.373	2.289
He	0.003	0.015	0.039	0.078	0.177	0.194
Ti	0.005	0.031	0.081	0.176	0.264	0.460
V	0.025	0.123	0.292	0.571	0.847	1.391
Cr	0.041	0.077	0.080	0.082	0.083	0.087
Mn						
H	0.029	0.147	0.358	0.717	1.075	1.792
He	0.009	0.043	0.105	0.211	0.317	0.528
V	0.002	0.009	0.023	0.045	0.068	0.113
Cr	0.051	0.354	1.205	3.199	5.543	10.608
Mn	0.164	0.722	1.417	2.046	2.326	2.505
	0.056	0.278	0.679	1.359	2.037	3.394
He	0.009	0.044	0.107	0.214	0.320	0.531
V	0.000	0.003	0.010	0.021	0.032	0.054
Cr	0.010	0.057	0.179	0.451	0.764	1.437
Mn	0.043	0.172	0.481	1.160	2.018	4.137
Fe	---	0.001	0.003	0.004	0.006	0.008
Co	---	---	---	---	0.001	0.001

Element	30 Days	150 Days	1 Year	2 Years	3 Years	5 Years
co						
H	0.025	0.126	0.305	0.612	0.917	1.529
He	0.012	0.062	0.152	0.304	0.456	0.759
Mn	0.005	0.023	0.055	0.111	0.166	0.27.7
Fe	0.058	0.294	0.717	1.483	2.152	3.586
Ni						
H	0.203	1.012	2.463	4.926	7.389	12.312
He	0.035	0.178	0.436	0.873	1.309	2.183
Mn	---	0.009	0.053	0.194	0.400	0.949
Fe	0.039	0.188	0.433	0.778	1.061	1.494
co	0.234	0.841	1.460	2.295	3.095	4.654
cu	---	---	---	0.001	0.001	0.003
Zr						
H	0.020	0.110	0.270	0.545	0.777	1.413
He	0.004	0.020	0.047	0.096	0.143	0.234
Sr	0.002	0.012	0.029	0.059	0.088	0.142
Y	0.076	0.417	1.070	2.081	3.082	5.144
Nb	0.013	0.189	1.663	1.519	2.377	4.094
Mo	---	0.010	0.093	0.244	0.395	0.699
Nb						
H	0.013	0.064	0.155	0.311	0.466	0.777
He	0.007	0.036	0.090	0.180	0.271	0.452
Y	0.001	0.001	0.001	0.001	0.001	0.001
Zr	0.019	0.100	0.245	0.491	0.737	1.229
Mo						
H	0.018	0.094	0.230	0.461	0.691	1.152
He	0.006	0.023	0.060	0.118	0.179	0.298
Y	0.001	0.003	0.008	0.016	0.025	0.042
Zr	0.005	0.017	0.042	0.079	0.117	0.193
Nb	0.019	0.102	0.246	0.492	0.738	1.230
Tc	0.010	0.058	0.144	0.290	0.435	0.726
Ru	0.004	0.019	0.047	0.095	0.143	0.238
Hf						
H	---	0.004	0.010	0.019	0.028	0.048
He	---	0.001	0.006	0.010	0.014	0.024
Yb	---	0.001	0.004	0.008	0.012	0.021
Lu	0.004	0.080	0.297	0.700	1.105	1.918
W						
H	---	0.004	0.008	0.016	0.025	0.043
He	---	---	0.003	0.007	0.011	0.018
Hf	---	---	0.002	0.003	0.006	0.009
Ta	0.013	0.272	1.189	3.183	5.284	9.537
Re	0.027	0.480	1.815	4.322	6.852	11.913

Table 1 shows the identity and percentage of elements generated for (n,p), (n,d), (n,α), (n,2n) and (n,np) reactions for a variety of pure metals. In this effort, no concentrations less than 10 ppm were recorded. Note that the concentrations of transmutants in this table cannot always be added to determine the loss of the original element. In some cases the transmuted element decays back to the original element. An example is $^{58}Ni(n,p)58Co \rightarrow ^{58}Ni$

Reference 6 contains a tabulation of the trace elements expected to either form in or change concentration in AISI 316 irradiated in a variety of breeder thermal and fusion devices. More effort is needed to complete the assessment of trace element effects.

5.2.2 Major Element Effects

The changes in composition induced by solid transmutant reactions are not always small. As shown in Figures 2 and 3, there are substantial changes in elements such as manganese and vanadium during irradiation of AISI 316 in various types of reactors. In a separate report[6], the consequences of such large changes in manganese are discussed, along with swelling data to demonstrate the potential sensitivity of swelling to changes in manganese level.

In some alloys, the depletion of manganese can actually threaten the phase stability of the alloy. Austenitic steels in which manganese at 11-14% has been substituted for most of the nickel will inevitably become ferritic as the manganese transmutes, primarily to iron in thermal reactors like HFIR.

The introduction to vanadium to levels approaching *0.8* atomic percent will probably have a pronounced effect on the phase stability of AISI 316[6]. It will probably affect properties such as swelling and creep which are sensitive to the activity of carbon.[1,12] The tendency of vanadium to form MC-carbides may also have important consequences on the high temperature strength of the alloy.

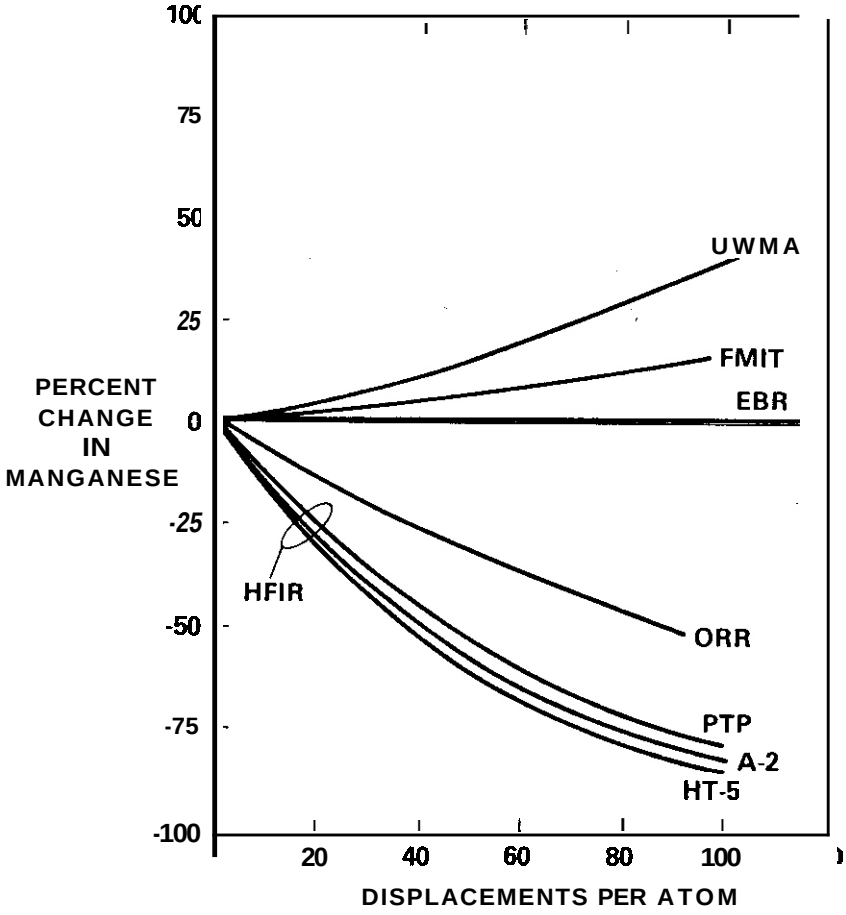

FIGURE 2. Changes in Manganese Concentration in AISI 316 as a Function of Exposure for Various Reactors. HT-5, A2 and PTP refer to different positions in HFIR. The curve for ORR was not included in reference 6.

A survey has been completed of the transmutation behavior of elements thought to be important in the microchemical evolution of AISI 316.[1] No significant changes were found in the levels of carbon, silicon and nickel in any reactor studied.[6] (Carbon and silicon exist at levels too large to designate as trace elements and too low to designate as major elements, but their influence in the microchemical evolution is a major one.)

5.2.3 Consequences of Segregation on Local Helium Production Rates

When correlating property change data with helium/dpa ratio, the appropriate helium deposition rate may not be the bulk-averaged value. A common feature

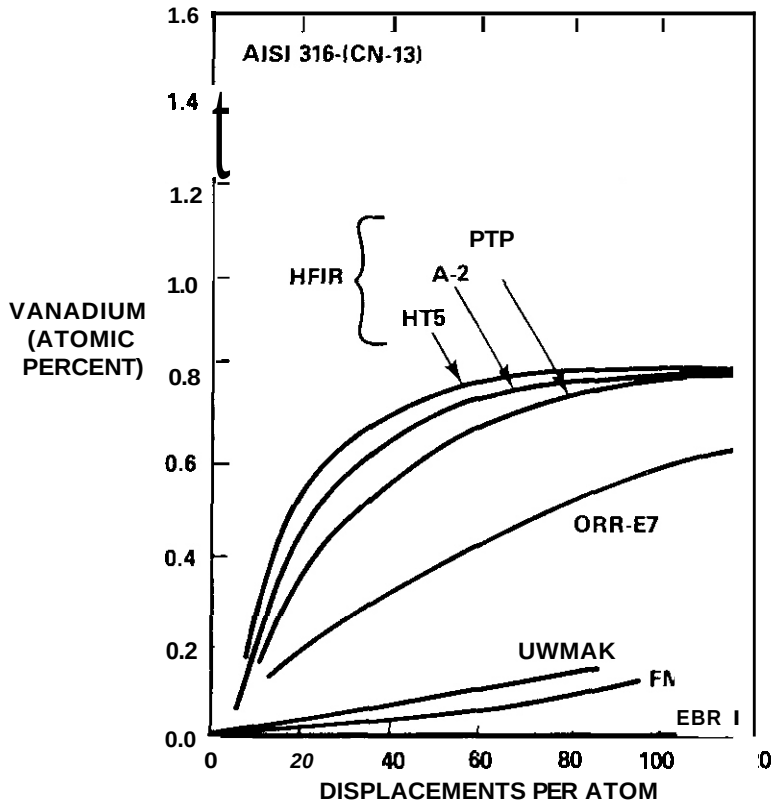

FIGURE 3. Vanadium Concentration in AISI 316 as a Function of Exposure for Various Reactors. The saturation of vanadium at 0.814% in HFIR signals the complete burn-out of ^{50}Cr. The curve for ORR was not included in reference 6.

of radiation-induced precipitation in 316 stainless steel is the concentration of nickel into most phases with a concurrent depletion in the alloy matrix. Although the matrix nickel content drops only 30%, the precipitate concentration of nickel can be as large as six times that of the preirradiation matrix level.

Nickel is one of the major contributors (50-70%)of helium in austenitic stainless steels irradiated in breeder reactor spectra, even though nickel accounts for only 13-14%of AISI 316. In thermal reactor spectra, Ni^{58} and its reaction product Ni^{59} provide essentially all of the helium. Therefore, a nonhomogeneous distribution of nickel will lead to a corresponding inhomogeneity in helium generation and deposition. Since nickel also segregates

to grain boundaries during irradiation, the helium/dpa ratio characteristic of such regions will be higher than that of the bulk.

If the failure process or property change of interest is associated with such a region, then the appropriate helium/dpa ratio for correlation purposes will be that associated with the region and not that of the bulk. Both this ratio and its difference from the bulk value will be sensitive to the specific reactors involved.

The possible consequences of nickel segregation on local helium production are now under study. There are possibly other similar processes to be studied. For instance, in fusion spectra carbon becomes a major contributor to the helium generation. Carbon is known to segregate at grain boundaries in both ferritic and austenitic alloys. In thermal and breeder spectra, the carbon contribution to helium generation is known to be negligible.

5.2.4 Recoil Effects on Precipitate Stability

Some precipitates such as γ' (Ni_3Si) in AISI 316 exist in a narrow regime of displacement and temperature.[11] Others, such as TiC, are composed of relatively insoluble components such as titanium. In reactors where transmutation rates are large, the stability of the precipitate may be altered by the recoil that occurs upon decay. This possibility is now being investigated.

5.3 Conclusions

It is apparent that an important element of any fission-fusion correlation effort is the influence of solid transmutant effects.

6.0 References

1. F. A. Garner, "The Microchemical Evolution of Irradiated Stainless Steels," Proceedings of the AIME Symposium on Irradiated Phase Stability, October 5-9, 1980, Pittsburgh, PA (in press).

2. F. A. Garner, "Extrapolation of Stress Affected Swelling Models Into Compressive and Cyclic Stress States," DAFS Quarterly Report DOE/ER-0046/5; also, D. L. Porter and F. A. Garner, "The Influence of Microchemical Evolution on the Swelling of AISI 316 and Its Dependence on Stress, Temperature and Heat Treatment", ibid, p. 141.

3. K. Farrell, "Experimental Effects of Helium on Cavity Formation During Irradiation - A Review," Radiation Effects, 1980, Vol. 53, pp. 175-194

4. R. E. Gold, et al, "Materials Technology for Fusion: Current Status and Future Requirements," Nuclear Technology/Fusion, Vol. 1, 1981, pp. 169-237.

5. L. E. Steele, Nuclear Safety, 17, No. 3, 1976, p. 327.

6. J. F. Bates, F. A. Garner and F. M. Mann, "The Effects of Solid Transmutation Products on Swelling in 316 Stainless Steel," this report.

7. J. F. Bates, R. W. Powell and E. R. Gilbert, "Reduction of Irradiation-Induced Creep and Swelling in AISI 316 by Compositional Modifications," Effect of Radiation on Materials: Tenth Conference, ASTM STP 725, D. Kramer, H. R. Brager and J. S. Perrin, American Society for Testing and Materials, 1981, pp. 713-734.

8. J. F. Bates and W. G. Johnston, "Effects of Alloy Composition on Void Swelling", Proceedings of Conference on Radiation Effects in Breeder Reactor Structural Materials, M. L. Bleiberg and J. W. Bennett, Eds., June 19-23, 1977, Scottsdale, AZ, p. 625.

9. J. F. Bates, "Irradiation-Induced Swelling Variations Resulting From Compositional Modifications of Type 316 Stainless Steel," Properties of Reactor Structural Alloys After Neutron or Particle Irradiation, ASTM STP 570, 1975, pp. 369-386.

10. D. S. Gelles and F. A. Garner, "An Experimental Method to Determine the Role of Helium in Neutron-Induced Microstructural Evolution," J. Nucl. Mat., 85 and 86, 1979, p. 689.

11. K. Farrell, J. Bentley and D. N. Braski, Scripta Met, 11, 1977, p. 243.

12. F. A. Garner, "The Influence of Dislocation Density on Carbon Activity and Phase Development in AISI 316," DAFS Quarterly Report, DOE/ER-0046/4, p. 89.

DISTRIBUTION

UC-20 (119)

UC-20c (77)

DOE-HQ/Office of Reactor
Research and Technology
NE-530
Washington, DC 20545

PB Hemmig, Safety & Physics

DOE-HQ/Office of
Fusion Energy (3)
ER-70
Washington, DC 20545

JF Clark JF Decker
NA Davies

DOE-RL/Office of Asst Manager For
Projects and Facilities Management (2)

GM Chenevert, FMITPO
LA Pasquini, Proj Manager, FMITPO

DOE-RL/Office of Asst Manager
for Advanced Reactor Programs

AR DeGrazia, Physical Scientist,
Technology Development

Argonne National Laboratory (4)
9700 South Cass Avenue
Argonne, IL 60439

LR Greenwood APL Turner
A. Taylor H. Wiedersich

Battelle Memorial Institute (3)
Pacific Northwest Laboratorv
P.O. Box 999
Richland, WA 99352

JL Brimhall
AB Johnson
LC Schmid

Brookhaven National Laboratory
Associated Universities
Upton, Long Island, NY 11973

Chairman, Nuclear Energy Oept

Columbia University
Plasma Physics Laboratory
New York, NY 10027

RA Gross

General Atomic Company (2)
P.O. Box 81608
San Diego, CA 92138

GR Hopkins
JR Gilleland

INESCO
11011 Torreyana Rd
San Oiego, CA 92121

RD Stevenson

Lawrence Livermore Laboratory (2)
P.O. Box 808
Livermore, CA 94550

MW Guinan
CM Logan

Los Alamos National Laboratory (2)
P.O. Box 1663
Los Alamos, NM 87544

DJ Dudziak
CR Emigh

Massachusetts Institute of Technology (4)
77 Massachusetts Avenue
Cambridge, MA 02139

L. Lidsky NJ Grant
IW Chen DB Montgomery

DISTRIBUTION (Cont'd)

McOonnell-Douglas Astronautics
P.O. Box 516
St. Louis, MO 63166

O. Kummer

Mound Laboratory
P.O. Box 32
Miamisburg, OH 45342

Manager, Tech Appl & Development

National Bureau of Standards
Gaithersburg, MO 20760

CO Bowman

Naval Research Laboratory (2)
Metallurgy Division,
Code 6390,
Washington, OC 20375

I. Manning
JA Sprague

North Carolina State University
Department of Nuclear Engineering
Raleigh, NC 26707

JR Beeler, Jr.

Oak Ridge National Laboratory (8)
P.O. Box X
Oak Ridge, TN 37830

Director, Thermonuclear Div,
(Bldg 9201-2)
RJ Colchin, Bldg 9201-2
FG Perey
M. Roberts, Bldg 9204-1
J. Sheffield
JO Stiegler
C. Weisbin
FW Wiffen

Princeton University (2)
Plasma Physics Laboratory
Forrestal Campus
P.O. Box 451
Princeton, NJ 08540

K. Wakefield
H. Furth

Rockwell International
Energy Systems Group
P.O. Box 309
Canoga Park, CA 91304

O. Kramer

Sandia Laboratories (2)
P.O. Box 5800
Albuquerque, NM 87115

FL Vook

Sandia Laboratories
Livermore, CA 94550

WO Wilson

University of California
Los Angeles, CA 90024

RW Conn

University of Michigan
Nuclear Engineering
Ann Arbor, MI 48105

T. Kammash

University of Missouri
Mechanical & Aerospace Engineering
1006 Engineering Bldg
Columbia, MO 65211

M. Jolles

DISTRIBUTION (Cont'd)

University of Virginia
Charlottesville, VA 22901

WA Jesser

University of Wisconsin
1500 W. Johnson Drive
Madison, WI 53706

WG Wolfer

Westinghouse
Research and Development Center (2)
1310 Beulah Road
Pittsburgh, PA 15235

S. Wood
JA Spitznagel

Commission for the European Communities
200, Rue de la Loi
B-1049 Rrussels, Belgium

J. Darvas

(ECN)
Energieonderzoek Centrum Nederland
Westerdionweg 3
NL-1755 ZG Petten, NH, The Netherlands

B. Van Der Schaaf

(EIR)
Swiss Federal Institute
For Reactor Research
CH-5303 Wuerenlingen, Switzerland

WV Green

EURATOM
Joint Research Center Ispra
Materials Science Division
1-21020 Ispra, Varese, Italy

P. Schiller

Hahn-Meitner Institute
für Kernforschung
Glienickerstrasse 100
D-1000 Berlin,
Federal Republic of Germany

H. Wollenberger

Japan Atomic Energy Research Institute

Division of Nuclear Fuel Research
Fukoku Seimei Bldg
2-2, Uchisaiwai-cho 2-chome, Chiyoda-ki,
Tokyo 100, Japan

K. Shiraishi

(KFA-IFF)
Kernforschungsanlage Jülich GmbH
Postfach 1913
D-517 Julich,
Federal Republic of Germany

H. Ullmaier

(KFK-JMF II)
Kernforschungsanlage Karlsruhe
Institüt für Reaktorbauelemente
Postfach 3640
D-7500 Karlsruhe I,
Federal Republic of Germany

K. Ehrlich

National Research Council
Montreal Road
Ottawa, Canada

EV Kornelson

(SCK/CEN)
Studiecentrum voor Kernenergie
Centre d'Etude de l'Energie Nucléaire
Boeretang 200
R-2400 Mol, Belgium

J. Nihoul

(UKAEA-Harwell)
United Kingdom Atomic Energy Authority
Atomic Energy Research Establishment
Metallurgy Division
Building 388
Oxfordshire, OX11 ORA, UK

DR Harries

HEDL (39)

HR Brager	W/A-64	EK Opperman	W/A-58
WL Bunch	W/C-47	NF Panayotou	W/A-65
LL Carter	W/C-47	EF Parker	W/E-17
DG Doran (5)	W/A-57	RW Powell	W/A-64
EA Evans	W/C-23	RJ Puigh	W/A-58
FA Garner	W/A-57	FH Ruddy	W/C-39
DS Gelles	W/A-64	FA Schmittroth	W/A-4
R. Gold	W/C-39	WF Sheely	W/C-62
HL Heinisch	W/A-57	RL Simons	W/A-57
DL Johnson	W/A-4	AL Trego	W/E-15
GD Johnson	W/A-65	GL Wire	W/A-58
NE Kenny	W/C-115	HH Yoshikawa	W/C-44
FM Mann	W/A-4	Central Files (5)	W/C-110
WN McElroy	W/C-39	Publ Services (2)	W/C-115
RE Nygren	W/A-58	Doc Management	W/C-125